The Pennsylvania State University
The Graduate School

PDF MODELING OF HIGH-PRESSURE TURBULENT SPRAY COMBUSTION UNDER DIESEL-ENGINE-LIKE CONDITIONS

A Dissertation in
Mechanical Engineering
by
Subhasish Bhattacharjee

Submitted in Partial Fulfillment
of the Requirements
for the Degree of

Doctor of Philosophy

December 2012

The dissertation of Subhasish Bhattacharjee was reviewed and approved* by the following:

Daniel C. Haworth
Professor of Mechanical Engineering
Dissertation Advisor, Chair of Committee

Stephen R. Turns
Professor of Mechanical Engineering

André L. Boehman
Professor of Mechanical Engineering

Savas Yavuzkurt
Professor of Mechanical Engineering

Karen A. Thole
Professor of Mechanical Engineering
Head of the Department of Mechanical and Nuclear Engineering

*Signatures are on file in the Graduate School.

Abstract

This thesis is focused on understanding the extent to which turbulent fluctuations in composition and temperature influence global ignition characteristics (e.g., ignition delays and liftoff lengths) and flame structure for high-pressure, transient, autoigniting spray flames under diesel-engine-like conditions. Turbulent spray flames for two single-component fuels (n-heptane and n-dodecane) are simulated. The modeling framework is a hybrid Lagrangian-particle/Eulerian-mesh probability density function (PDF) method. This framework allows for arbitrarily large chemical mechanisms, and features Lagrangian-based spray breakup and dispersed-phase models, soot models, and an optically thin radiation model. The influence of turbulent fluctuations is explored by comparing results from the PDF method (which explicitly accounts for turbulent fluctuations) with those from a model that neglects the influence of turbulent fluctuations on local mean chemical reaction rates (a well-stirred reactor WSR model) for the same chemical mechanism. Computed results are compared with experimental measurements that are available through the Engine Combustion Network [1]. Here a 40-species mechanism [2] has been adopted for n-heptane, and a 103-species chemical mechanism [3] for n-dodecane.

Overall, it is found that for conditions that correspond to robust diesel combustion (e.g., high initial temperatures, high initial pressures and/or high oxygen concentrations) the computed liftoff lengths and ignition delays for the WSR and PDF models are close to each other, and both are in good agreement with experiments. For less robust conditions (e.g., low initial temperatures and/or low oxygen concentrations), the computed liftoff lengths and ignition delays from the two models can be significantly different, and the results from the PDF model are generally in better agreement with measurements. The differences between the two models are especially apparent for n-dodecane at low initial temperatures. For n-dodecane at an initial temperature of 800 K, the WSR model fails to ignite, while the PDF

model shows a distinct two-stage autoignition process and the computed ignition delay and liftoff length are within 30% of the experimental values. For n-dodecane at an initial temperature of 900 K, the WSR model predicts an ignition delay that is three times higher than the measured value, while the PDF model prediction is within 5% of the measurement. For both fuels and for all initial conditions, the WSR and PDF models produce significantly different turbulent flame structures, and the differences are greater for lower initial temperatures and/or oxygen concentrations. The WSR model produces a laminar-like flame structure, whereas the PDF model produces a broader turbulent flame brush that is qualitatively more consistent with what is expected for a turbulent flame, and with what is observed in the experiments.

While it has been shown in the literature that some global characteristics (e.g., ignition delays and liftoff lengths) of high-pressure turbulent spray flames can be captured using a WSR model and a chemical mechanism that has been tuned for this purpose, the present results suggest that this approach effectively amounts to changing a model for one physical process (chemical rate coefficients) to account for deficiencies in modeling a different physical process (turbulent fluctuations in composition in temperature). It is expected that by properly accounting for turbulent fluctuations, it will be possible to develop a model that can be applied over a broad range of engine-relevant conditions without changing the model coefficients.

Table of Contents

List of Figures

List of Tables

List of Symbols

Variables

A_s	Surface area of a droplet, m^2,
C_a	Coagulation rate constant,
C_d	Coefficient of drag of a droplet,
$c_{p\alpha}$	Constant pressure specific heat of species α, J/kg-K,
$c_{v\alpha}$	Constant volume specific heat of species α, J/kg-K,
c_β	Molar concentration of species β, kmol/m^3,
$C_{b1}, C_{b2}, C_s, T_{strp}$	Empirical constants for breakup model,
Da	Damköhler number,
D_d	Droplet diameter, m,
D_{inj}	Droplet diameter, mm,
E_A	Activation energy, J/kmol,
f	Mixture fraction,
f_v	Soot volume fraction,
f_ϕ	Probability denity funtion for composition space, $1/\phi$,
g	Acceleration due to gravity, 9.81 m/s^2,
h	Gas-mixture enthalpy, J/kg,

h_s Equivalent enthalpy, J/kg,

h_{fg} Enthalpy of vaporization, J/kg,

$h^0_{f,\alpha}$ Enthalpy of formation of species α, J/kg,

J^α Molecular flux of species α, kg/s-m^2,

J^h Molecular flux of enthalpy α, J/s-m^2,

K_g Mass transfer coefficient, s/m,

K_p Planck-mean absorption coefficient, 1/m,

$k_{l,f}$ Forward reaction rate for reaction l,m^3/kmol-s,

$k_{l,r}$ Reverse reaction rate for reaction l,m^3/kmol-s,

k Turbulent kinetic energy, m^2/s^2,

L Total number of reactions,

M_α Chemical species symbol,

M_{C_s} Molar weight of carbon atom,

M_r r-th soot moment,

m_d mass of a droplet, kg,

m_p mass of a particle, kg,

N_A Avogadro's Number,

N_s Number of species,

N_ϕ Number of composition variables,

p Gas-phase pressure, N/m^2,

$p_{v,\infty}$ Partial vapor pressure in the surrounding gas, N/m^2,

$p_{v,s}$ Partial vapor pressure at the droplet surface, N/m^2,

p Gas-phase pressure, N/m^2,

Pr Prandtl number,

$\dot{Q}_{rad}$ Radiation source term per unit volume, W/m^3,

R_u Universal gas constant, 8314.5J/kmol-K,

Re Reynolds number based on gas velocity,

Re_d Reynolds number based on droplet diameter,

S_α Chemical source term for species α, kg$_\alpha$/kg-s,

Sc Schmidt number,

Sh Sherwood number,

t Time, s,

T Gas-phase temperature, K,

T_d Droplet temperature, K,

T_∞ Free-stream gas-phase temperature, K,

T_m Mean film temperature, K,

$\underline{u}$ Gas-phase velocity vector, m/s,

$\underline{u}_d$ Droplet velocity vector, m/s,

u_τ Friction velocity, m/s,

V_d Volume of a droplet, m^3,

W_α Molecular wieght of species α, kg/kmol,

W Molecular wieght of gas-mixture, kg/kmol,

W Vector of isotropic Weiner process, s$^{1/2}$,

We Weber number,

x_i $i-th$ co-ordinates, m,

X_α Mole fraction of species α,

Y_{C_s} Mass fraction of carbon atom,

Y_α Mass fraction of species α.

Greek variables

κ Boltzmann constant, J/K,

τ Instantaneous viscous stress-tensor, N/m^2,

τ_T Turbulent stress-tensor, N/m^2,

τ_b Breakup time, s,

ρ Gas-phase density, kg/m^3,

ρ_{C_s} Density of soot, kg/m^3,

μ Dynamic viscosity, kg/m-s,

μ_T Turbulent viscosity, kg/m-s,

$\nu'_{l\alpha}$ Stoichiometric coefficients of species α reaction l,

$\nu''_{l\alpha}$ Stoichiometric coefficients of species α reaction l,

ν Kinematic viscosity, m^2/s,

ϵ Dissipation rate of turbulent kinetic energy, m^2/s^3,

δ_{ij} Cronecker delta,

σ Stefan-Boltzmann constant, $W/m^2 - K^4$

ϕ Composition space variable,

Φ Viscous dissipation rate, $N/m^2/s$,

ψ Sample space variable of composition space,

ω Turbulent frequency,

$\dot{\omega}_\alpha$ Molar production rate of species α.

Operators

$\sim$ Density weighted average (Favre average),

$\langle\rangle$ Conventional average, or ensemble average.

Superscripts

$''$ Fluctuations over Favre average,

$*$ Any notional particle.

Abbreviations

CFD Computational fluid dynamics,

CI Compression ignition,

DISI Direct injection spark ignition,

ECN Engine Combustion Network,

EGR Exhaust gas recirculation,

EMST Euclidean minimum spanning tree,

FV Finite volume,

HCCI Homogeneous charge compression ignition,

IEM Interaction by exchange with mean,

ISAT *In situ* adaptive tabulation,

LES Large eddy simulation,

LMSE Linear mean-square estimation,

LPEM Lagrangian-particle/Eulerian-mesh,

MEPDF Multi-environment probability density function,

MOMIC Method of moments with interpolative closure,

PCCI Premixed charge compression ignition,

PDF Probability density function,

PPM Parts per million,

RAS	Reynolds averaged simulation,
RCCI	Reactivity controlled compression ignition,
SI	Spark ignition,
TCI	Turbulence chemistry interactions,
TRI	Turbulence radiation interactions,
WSR	Well-stirred reactor.

Acknowledgments

Over the last five years, my journey to this Ph.D. that started back in 2007, when I joined the computational research laboratory of Dr. Daniel Haworth as a graduate student, has been a memorable experience. I would like to take this opportunity to acknowledge a few individuals for all the help and support they provided over this period of time.

First of all, I would like to express my gratitude to my advisor, Professor Daniel Haworth, for his encouragement, support and guidance that helped me overcome the research roadblocks while working towards my Ph.D. His guidance has always been invaluable and has helped me towards ideas that enhanced my understanding and research. I would also like to thank the members of my dissertation committee: Dr. Stephen Turns, Dr. André Boehman and Dr. Savas Yavuzkurt for their insightful inputs and suggestions. I would also like to acknowledge the help and support I received from my fellow labmates.

I deeply admire the support I received from my parents in fulfilling my dream. It is their love, guidance and unrelenting support that helped me grow stronger in difficult times. Finally, I would like to thank my dear wife Rashmi whose unwavering support and patience motivated me to stay focused at difficult times and overcome the challenges.

Chapter 1

Introduction

The research work presented in this thesis is focused on simulating turbulent spray flames under diesel-engine-like conditions using a transported probability density function (PDF) method, including systematic validation of results from the computational model with experimental measurements over a wide range of conditions. This chapter begins with introductory discussions on background and motivation (Sec. 1.1) for the current research, which includes key challenges and future directions of engine combustion, and the role of computational fluid dynamics (CFD) modeling in addressing these needs. The key objectives that connect the current research with the challenges of turbulent combustion in engines are addressed in the next section (Sec. 1.2).

1.1 Background and Motivation

Turbulent combustion has been a major area of research over several decades, primarily because of the complexity of the processes that are yet to be understood completely. The chemical reactions that control the heat release and species formation interact with the hydrodynamics of the flow, resulting in a strong coupling between the two. Understanding and controlling turbulent combustion have presented significant theoretical and experimental challenges. Turbulence, by itself, remains a fundamental unresolved problem, and is characterized by a wide spectrum of temporal and spatial scales that govern the energy transfer and mixing processes through complex interactions between the scales. The scales represent

widely different flow characteristics that are difficult to model. The large scales include the most energetic eddies that interact with each other, and eventually break down to smaller eddies which are more dissipative in nature. Within the framework of available computational resources, it has been challenging to model the key attributes that capture all the characteristics of turbulent flow on sound physical and mathematical grounds. Combustion, on the other hand, is a process that leads to rapid release of heat and formation of a large number of species through a series of chemical reactions. Like turbulence, a combustion process is also characterized by a wide range of chemical scales that determine the production/destruction of each of the species. The reactions that characterize the rapid heat-release rates may have much shorter chemical time scales compared to reactions that contribute to the formation of key pollutants, such as NOx. The time scales of the reactions change rapidly with the physical state of the system, which, in turn, depends on the combustion process. It has been a challenging task to model all the processes that govern the key physical attributes of combustion.

Most engineering applications of combustion occur in a turbulent flow environment. Typical examples include industrial burners, internal combustion engines and gas turbine engines. The addition of turbulence with combustion increases the complexity of modeling far beyond the complexity of each of the individual disciplines. Therefore, turbulent combustion remains a key area of research for understanding and modeling of key physical aspects that control the combustion processes in these applications.

1.1.1 Emissions from Internal Combustion Engines

Internal combustion engines constitute a significant proportion of combustion devices for transportation purposes. Approximately 28% of the USA's total energy resources are consumed by transportation [4], and this is expected to grow further in the next 20 years (Fig. 1.1). Of the transportation energy resources, approximately 97% comes from petroleum, of which 65% is consumed by gasoline engines, 20% by diesel engines, and the remainder (12%) by jet engines. Approximately 12% of the world's population owned automobiles in 2000, and that number is projected to increase to 15% by 2020 [5, 6]. The turbulent combustion processes

in these engines convert the chemical energy of the fuel to thermal energy through

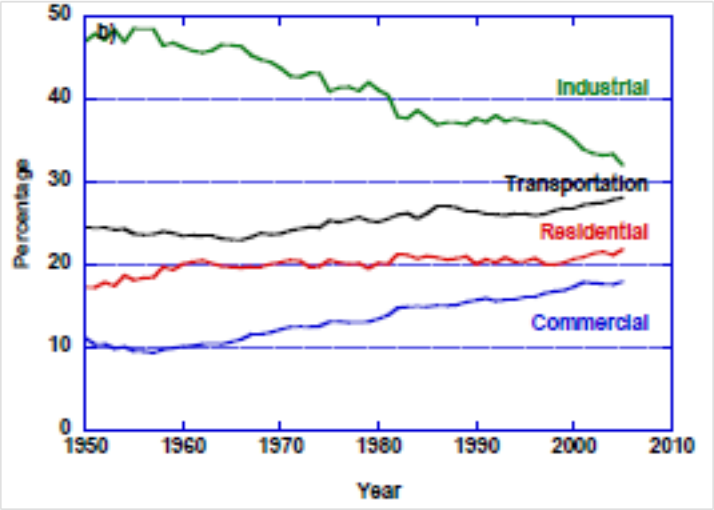

Figure 1.1. Growth in energy consumption over the last 60 years in different categories - industrial, transportation, residential, and commercial [4].

a series of chemical processes that lead to the oxidation of the fuel to form combustion products. Over the years, some combustion products have come to be recognized as major threats to the preservation of the environment [7]. Therefore, much emphasis has been given recently to reduce the emission of the combustion products that are potential contributors to climate change [8] or that are health threats. Unburned hydrocarbons (UHC), CO, NOx, and particulate matter (PM) are the primary regulated pollutants from engines. Of all the global emissions, 32% of total CO_2 emissions and 55% of NOx emissions are combustion products from engines [9]. Reducing pollutant formation and converting pollutants to more environment-friendly products has been a primary challenge that drives research efforts in turbulent combustion.

1.1.2 Emissions Control Strategies

The need to sustain a pollution-free environment has driven government agencies to enforce regulations that are reviewed and revised regularly, and have become stricter over the years. In particular, the regulation standards have tightened up significantly for heavy-duty diesel engines. Heavy-duty diesel engines are of major concern because of difficulties in controlling the combustion processes, leading

to large volumes of NOx and soot emissions. The USA Environment Protection Agency (EPA) set new emissions standards in 2007 [10] that required a significant reduction in NOx and PM (soot) emissions for heavy-duty vehicles. By the end of 2010, the heavy-duty diesel manufacturers had to reduce PM emission levels to 10% of the regulation standards in 2004 [4]. The regulations for heavy-duty vehicles are relatively less aggressive in Europe. To comply with the USA regulation standards, manufacturers need additional NOx and soot reduction systems. One approach is aftertreatment of the combustion products. Selective catalytic reduction (SCR) and diesel particulate filters (DPF) are examples of aftertreatment systems that reduce NOx through a series of catalytic reactions to nitrogen, and remove soot using a filter, respectively. The SCR aftertreatment systems reduce NOx emissions by 90%, and are currently in use in heavy-duty trucks. Although the aftertreatment strategies have provided wider operational flexibility for heavy-duty diesel engines, the efficiency, durability, operational cost, and mobility of the aftertreatment systems remain to be seen over a long period of time. With the likelihood of the current emission regulations being tightened up further in the near future, it is believed that aftertreatment alone will not be sufficient to address future emissions requirements. Much of the recent research effort has been directed towards exploring novel combustion strategies, alternative fuels, and advanced injection strategies that provide better control over the combustion process to reduce emissions. The goal is to move towards cleaner and more efficient combustion systems. The new combustion strategies evolve around mixed combustion modes that are significantly different from the typical diesel and gasoline engine combustion strategies. This leads to the development of a new generation of IC engines, which rely on low-temperature, fuel-lean or dilute combustion.

1.1.3 Advanced Combustion Strategies for Future Emissions Control

One promising strategy has been to move towards homogeneous-charge compression-ignition (HCCI) [11, 12], and this has received considerable attention in the research community. It has been recognized that the high levels of soot and NOx emissions in diesel engines arise from high temperature, inhomogeneous combus-

tion. The local inhomogeneity of the fuel-air mixture produces pockets of fuel-rich and fuel-lean mixture. Locally fuel-rich combustion results in high soot formation and high temperatures. The high-temperature combustion produces high levels of NOx. HCCI engines offer an attractive solution to this problem by introducing a leaner or diluted homogeneous-charge combustible mixture. The lean or dilute mixture keeps the temperature low and thereby reduces the thermal NO by a significant margin, and the fuel-lean mixture produces significantly lower soot. A homogeneous lean charge can be produced in multiple ways: premixing the air and fuel in a separate chamber, partial mixing of air and fuel in a separate chamber followed by direct injection of the remaining fuel into the combustion chamber, or direct injection of fuel at early stages of combustion to allow longer time for the liquid fuel to produce a more homogeneous mixture [13]. The low NOx- and soot-emissions HCCI engines have the potential to meet the emission regulations with reduced reliance on aftertreatment systems. Moreover, HCCI engines are expected to retain the high thermal efficiency that is characteristic of diesel engines, due to efficient burning of fuel. It should be emphasized here that HCCI-like strategies have been explored with both compression-ignition (CI) and spark-ignition (SI) engines with direct fuel injection. The main idea is to create a homogeneous or near-homogeneous charge to aid low-temperature combustion (LTC) with a globally fuel-lean and/or diluted mixture. Detailed discussions on low-temperature combustion in CI and SI engines are left for Chapter 2. A related development in gasoline engines has been direct-injection spark-ignition (DISI) engines [6, 14, 15], which operate on the principle of stratification of the fuel-air mixture. The stratification results in significant improvement of the flame propagation for a globally fuel-lean mixture and contributes to significant reduction of emissions and higher efficiency compared to typical gasoline engines.

1.1.4 Fuel Flexibility for Advanced Engines

The development of novel combustion strategies to improve efficiency and reduce emissions is occurring simultaneously with the exploration of new classes of fuels, known as alternative fuels. Demand for petroleum products in the energy sector is on the rise, and is expected to grow significantly in the next 30 years. A large

proportion of the growth is expected to come from emerging economies, as shown in Fig. 1.2. With limited oil resources, fast-changing global economies and steady

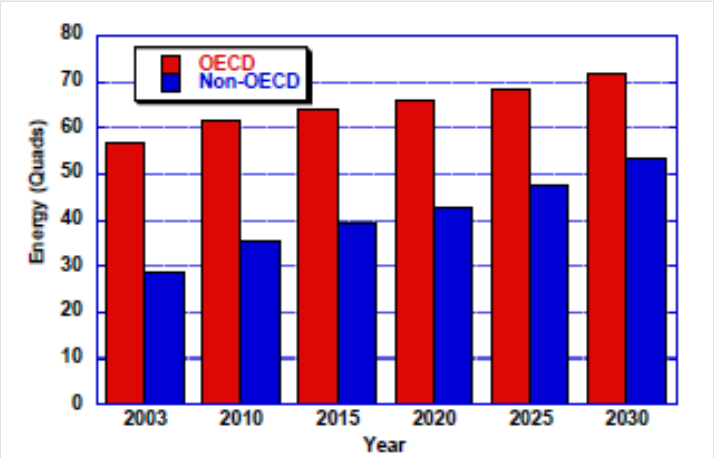

Figure 1.2. Projected worldwide transportation energy use in Quads from 2003 to 2030. OECD is the Organization for Economic Cooperation and Development. OECD member countries represent the developed world and non-OECD member countries the developing world [16].

increases in fuel consumption, research efforts have been directed to look beyond petroleum-based fuels and to replace them with alternative fuels that can be produced using other natural resources. At the commercial level, the possibility to replace petroleum-based fuels with alternative fuels has been explored with varying degrees of success. Biodiesel, ethanol, and synthetic gas are a few examples [17, 18] of alternative fuels that have been explored for transportation purposes. However, in the long term, the usefulness of alternative fuels is yet to be fully explored. The physical and chemical properties of these fuels are widely different from typical gasoline and diesel properties. This opens up the opportunity to explore new engine designs that offer wider fuel flexibility for efficient and clean combustion strategies. Conventional diesel and gasoline engines may be unsuitable for these fuels, since these engines have been highly optimized for petroleum use only. The possibility of a fuel-flexible engine design also has led to the exploration of dual-fuel engines, where a fuel of one class of reactivity is carefully blended with a fuel of different reactivity. Dual-fuel combustion has been a recent subject of engine research to control the combustion staging and heat-release processes that drive the efficiency and pollutant formation [19, 20, 21, 22]. Such multi-staged

combustion strategies demand advanced fuel injection strategies, highly turbulent flow structures, faster liquid breakup, and evaporation strategies to produce the desired local equivalence ratio distribution for optimum engine performance. The performance of these engines over a wide range of operating conditions remains to be investigated. The diversified fuel properties along with new combustion strategies offer new challenges, because engine performance for advanced combustion strategies is expected to be largely dependent on local fuel composition, and is even more sensitive to changes in fuel composition than those in conventional diesel and gasoline engines [4, 6].

1.1.5 Computational Fluid Dynamics Modeling of Turbulent Combustion

Over the years, computational fluid dynamics (CFD) has evolved as a promising tool toward a validated, predictive, multiscale combustion modeling capability to optimize the design and operation of advanced engines with evolving fuels for transportation applications [4]. With continuously improving numerical methods, physical modeling, and high-performance computational resources, CFD has emerged as an attractive design tool to provide realistic predictions for in-cylinder turbulent combustion processes, and to explore a wider design space than is accessible experimentally.

1.1.5.1 Turbulence-Chemistry Interactions

In all practical combustion devices, turbulence and chemical kinetics remain fundamental challenges for computational fluid dynamics. In highly turbulent combustion, the hydrodynamics of turbulent flow strongly interacts with the kinetics, giving rise to a new class of problems driven by highly non-linear turbulence-chemistry interactions (TCI). TCI are characterized by a strong coupling between the turbulence and kinetics, and reflect the effects of turbulent fluctuations in species and energy of the combustion system. The role of TCI becomes progressively more important as the combustion strategies move towards increasingly fuel-lean or dilute, low-temperature combustion. The relative importance of TCI is often characterized using a Damköhler number (Da), which is a ratio of hydrodynamic

to chemical time scales. For high Da, chemical time scales are significantly shorter compared to turbulent scales. The primary role of turbulence in high Da flames is to transport species and enthalpy ahead of and behind the flame, producing a rapid mixing and wrinkling of the flames. The turbulent scales are too large to produce any significant impact on the local flame structure, which is characterized by a very narrow high-temperature zone. Most of the past modeling developments have been for high Da flames [23, 24, 25, 26], with the assumption of an essentially laminar flame structure embedded in a turbulent flow field. The validity of this high Da assumption for engine combustion over a wide range of operating conditions is questionable [27]. Low Da flames, on the other hand, have relatively slow chemical scales and are characterized by a thick distributed reaction zone, where the turbulent eddies exist inside the flame core. In the limit $Da \rightarrow 0$, turbulence mixing controls the reaction process for such flames. The most computationally challenging flame configurations are intermediate Da flames, that span much of the combustion regime in IC engines [27]. In the intermediate Da regime, chemical and turbulent scales are comparable, resulting in strong interactions between the two. The low-temperature, highly turbulent, lean or dilute combustion regimes that drive the development of low-emissions next-generation engines, are often characterized by low-to-intermediate Da. In that case, local and global combustion characteristics are strongly influenced by TCI, and there are large differences between results from CFD models that consider TCI and those from models that neglect TCI. An example of the difference in computed turbulent flame structure with and without consideration of TCI is illustrated in Fig. 1.3. The transported probability density function (PDF) method [28, 29, 30, 31, 32, 33] has evolved as a promising modeling approach that accommodates TCI for CFD modeling of turbulent combustion. TCI are expected to be important for the low-temperature, fuel-lean or dilute, mixed-mode combustion that is expected to prevail in next-generation engines.

1.1.5.2 Modeling for Near-Atmospheric Pressure Statistically Stationary Flames

Much of the turbulent combustion modeling effort over the last 10-20 years has focused on development and validation of models using experimental measurements

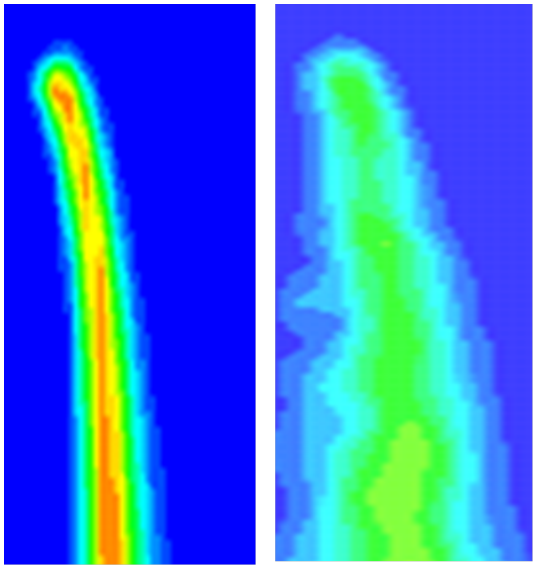

Figure 1.3. Favre-averaged OH mass fraction contour for a lifted n-heptane spray flame with TCI (right) and without TCI (left). Detailed comparisons are provided in Chapter 5.

for laboratory-scale, near-atmospheric-pressure, statistically stationary, nonluminous canonical flame configurations. Typical examples include turbulent nonpremixed flames that have been targeted by the Turbulent Nonpremixed Flame (TNF) Workshop [34] led by Sandia National Laboratories; that includes simple jet flames, piloted jet flames, bluff-body flames and swirl flames (Fig. 1.4). The TNF library includes multiscalar and velocity data for flames with progressively increasing complexity of the chemistry and the flow field. Over the last 15 years, the TNF Workshops have fostered collaboration among experimental and computational researchers to address the fundamental issues of turbulence-chemistry interactions in gaseous flames. These flames have been studied widely to explore the ability of models to capture local and global combustion behavior such as local extinction and reignition, lifted reaction zones, autoignition, flow recirculation, and swirl. The transported probability density function methods have been successful in capturing the local and global flame characteristics of these flames. For the piloted jet flames that are on the verge of extinction (Sandia E and F flames), the PDF method was able to capture the local extinction effects [35], which have not been captured using other models. Other laboratory turbulent jet flames that have been subjects of modeling studies include luminous ethylene-air

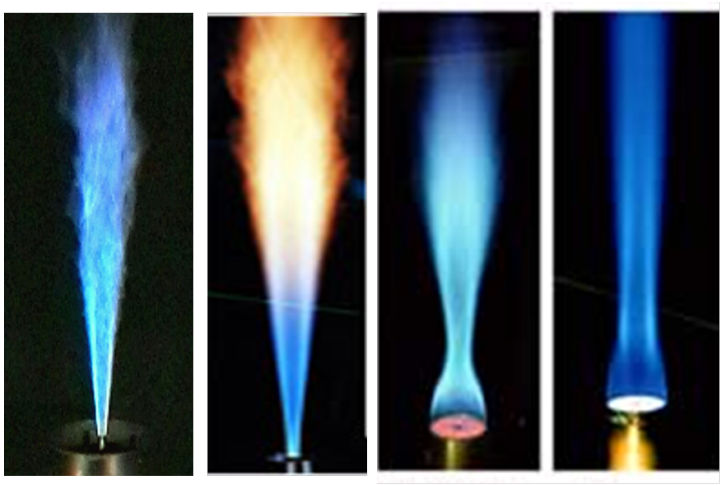

Figure 1.4. Turbulent nonpremixed flames addressed at the TNF Workshop [34]. From left to right: simple jet flame for $CH_4/H_2/N_2$, piloted jet flame for natural gas, swirl-stabilized flame for CH_4/H_2, and bluff body flame for CH_4/H_2.

flames by Coppalle and Joyeux [36] and Kent and Honnery [37]. These flames are moderately sooting flames, and are often used for soot and radiation studies. Transported PDF methods have proved to be powerful in producing reasonable agreement with the measurements with detailed soot and radiation modeling that captures the turbulence-radiation interactions, along with turbulence-chemistry interactions [38]. The Combustion Research Facility (CRF) of Sandia National Laboratories has been instrumental in conducting experiments in turbulent flames that span premixed, partially premixed and non-premixed flames to understand the role of TCI in flame stability and species formation. Another key research group has been the Engine Research Center at the University of Wisconsin-Madison, who has been instrumental in investigating the fundamental thermochemical processes with a major focus on low-temperature combustion modes for IC engines.

1.1.5.3 Existing Modeling Approaches and Challenges for High-Pressure Autoigniting Flames in Engines

High-end computational models with capabilities to capture TCI have been promising in capturing the key local and global behavior of turbulent flames in canonical laboratory-scale statistically stationary flame configurations. The application of transported PDF methods to non-stationary, autoigniting flames in engines has not

yet been explored in detail. The primary difficulty is lack of comprehensive and reliable experimental data that can provide insight into thermochemical processes under engine-like conditions. The complicated geometric shapes of a real engine make in-depth experimental measurements too complicated. In the absence of in-depth measurements, much of the modeling effort reported to date using transported PDF methods has emphasized the global ignition and combustion characteristics, and comparison between results obtained using the PDF methods to predictions with models that neglect TCI [39, 13, 40]. Most current state-of-the-art CFD simulations for real engines employ computational models that neglect TCI [41, 42, 43]. A recent example of a no-TCI model is a multi-zone kinetic model applied to premixed-charged compression-ignition (PCCI) engines by Aceves *et al*. [42]. The modeling framework included two stages. In the first stage, a CFD code was used to determine mean temperature and equivalence ratio distributions as functions of crank angle under motored conditions. In the second stage, the in-cylinder mass was divided into multiple zones based on temperature and composition, and a detailed chemical kinetic model was used in each zone to solve for the chemistry. This model provided reasonable predictions for pressure-rise and global heat-release rates for some operating conditions. However, the prediction of autoignition was problematic, since autoignition strongly changes with the transition between the two stages. The crank angle that determined the transition between the stages was tuned to match the measurements, and the tuning criteria needed to be recalibrated for each operating condition, which casts doubts over the predictability of autoignition using this model. A similar multi-zone computational model has been applied to HCCI engines, with emphasis on mixture-fraction-based transition between the two stages [43], instead of the temperature-based transition used by Aceves *et al*. While some of these computational models were partially successful in predicting the global combustion characteristics, the model predictions in real engines lack consistency in predictions. The apparent success of CFD models that ignore TCI may be due to tuning of one physical model (chemical kinetics) to compensate for deficiencies in modeling the TCI.

The application of TCI models in real engine configurations has been limited by computational resources: the transported PDF method demands much higher computational resources compared to models that completely ignore TCI. Therefore,

the benefit of accurately accounting for TCI to produce more accurate predictions needs to be carefully monitored for different combustion systems. In typical diesel engine configurations, the degree to which TCI influence autoignition and emissions is expected to vary with operating conditions. It would be appropriate to identify the conditions where TCI can safely be neglected (thereby speeding up the CFD computations significantly), and conditions where TCI must be accounted for explicitly. A detailed discussion of the role of TCI in compression-ignition engines is provided in Chapter 2.

1.1.5.4 PDF Modeling for High-Pressure Autoigniting Flames in Diesel-Like Conditions

The research presented here is based on a high-end CFD-based model that accommodates arbitrarily large kinetic models for chemistry and turbulence-chemistry interactions. A hybrid particle/finite-volume based method is used to solve a modeled transport equation for the joint PDF of the composition variables (species mass fraction and enthalpy) that describe the thermochemistry. The hybrid method retains the primary benefit of PDF-based modeling to capture TCI explicitly within reasonable computational time.

The present work is an extension of transported PDF methods from atmospheric-pressure, unconfined stationary flames to transient spray flames under diesel-engine-like conditions. We seek to establish the extent to which the turbulence-chemistry interactions are, or are not, important for conditions that are representative of those in compression-ignition engines. Sensitivities of results to variations in key physical and numerical parameters are explored. The major contribution of this work is to isolate and quantify differences between results obtained with versus without the transported PDF method to establish the relative importance of TCI, and to do so over a wide range of conditions within the framework of the available gas-phase chemical mechanisms. In addition to a transported PDF method to capture TCI, the model features Lagrangian-parcel-based fuel injection and spray models to account for realistic spray processes in diesel engines, and particle-based soot models to provide realistic soot prediction. An optically-thin radiation model is used to determine the extent to which results are affected by radiation heat transfer and turbulence-radiation interactions (TRI).

1.2 Objectives

The primary objective of the current research has been to apply a transported PDF method to study high-pressure transient spray combustion systems under diesel-engine-like conditions. The CFD models provide a powerful tool to study the complex turbulence-chemistry and turbulence-radiation interactions, soot formation and liquid fuel sprays. The particle PDF method has been integrated with the physical submodels for sprays, soot and radiation to produce realistic predictions for diesel combustion systems. It also provides a promising modeling framework to explore a wider design space for next-generation engines with different fuels.

The key objectives of the thesis are as follows.

- The extent to which turbulence-chemistry interactions influence ignition, combustion and emissions under diesel-engine-like conditions are established by comparing results from a model where TCI are considered using a transported PDF method with results from a model where TCI are neglected.
- Conditions under which TCI can and cannot be neglected are established.
- Quantitative comparisons between model and experiment are made for constant-volume turbulent spray combustion chambers under diesel-engine-like conditions.

Chapter 2

Turbulent Combustion in Direct-Injection Compression-Ignition Engines

This chapter begins with a review of the diesel combustion process (Sec. 2.1) in conventional compression-ignition (CI) engines. The working principles and key emissions challenges in conventional CI engines are discussed. The emissions challenges lead to the conceptual development of advanced combustion strategies, with increased focus on low emissions, high thermal efficiency, and alternative fuels (Sec. 2.2). The next section (Sec. 2.3) includes discussions on characteristics of fuels, including a review of the chemical kinetics for fuel components that are representatives of key fuel classes for CI engines. The need for experimental and computational studies using surrogate fuels is discussed, along with underlying challenges to reproduce real-fuel properties using a limited number of surrogate components. The next section (Sec. 2.4) discusses CFD modeling challenges for turbulent combustion in engines, beginning with the development of the transported PDF method applied to laboratory-scale, near-atmospheric-pressure, quasi-stationary turbulent flames. The challenges in transitioning these high-end computational models from laboratory-scale flames to turbulent spray flames under diesel-engine-like conditions are discussed. The current state-of-the-art computational models for engine simulation are reviewed, and their limitations are discussed. Finally, this section addresses how this thesis proposes to extend the

applicability of transported PDF methods from laboratory-scale well-characterized flames to transient, high-pressure, turbulent spray flames under diesel-engine-like conditions.

2.1 The Diesel Combustion Process

Diesel engines are highly effective for heavy-duty vehicles, largely due to their higher efficiency compared to gasoline engines. The gain in fuel efficiency of diesel engines is primarily due to their higher compression ratios and lack of throttling losses. While the application of spark-ignition gasoline engines is limited to low-to-intermediate compression ratios due to engine knock, diesel engines operate with higher compression ratios, which make diesel engines a natural choice for heavy-duty applications. The working principle of a conventional diesel engine is based on autoignition of the air-fuel mixture at high-temperature, high-pressure ambient conditions that are achieved by high volumetric compression of the air. In typical diesel engines, the compression ratio ranges from 15 to 22, and peak cylinder pressures are approximately 40 to 45 bar. A high-pressure common-rail fuel injector is used to inject a high-velocity liquid spray into the hot compressed air towards the end of the compression stroke (a few crank angle degrees before the piston reaches top dead center). The fuel pressure is raised to the desired level using a pump that feeds the liquid fuel to multiple injectors. For a given engine speed, the engine load is adjusted by controlling the amount of fuel injected. The high-velocity fuel jet penetrates through the high-pressure and high-temperature ambient gas, and breaks down to small droplets that evaporate by the heat and mass transfer with the surroundings. The evaporated fuel mass mixes with the surrounding oxidizer and produces a combustible mixture that autoignites and oxidizes fuel to products.

2.1.1 Ignition Delay

The combustion process begins with the autoignition of the combustible air-fuel mixture. The autoignition characteristics depend on the physical and chemical properties of the fuel. Ignition delay is a key measure of the autoignition. Au-

toignition in typical spray combustion occurs in two steps. The first step is controlled by the physical properties of the spray to create a combustible air-fuel mixture through the processes of evaporation and mixing. The time required for the spray to form a combustible mixture from the time of injection is referred to as the "physical delay". The physical properties of the fuel that control the physical delay include density, viscosity, surface tension, specific heat, boiling point and enthalpy of vaporization [44]. In-cylinder flow structures have significant influences on the physical delay. The small- and large-scale hydrodynamic structures drive the entrainment of the air into the liquid jet, which causes the break-down of the liquid jet by aerodynamic interactions, and evaporation of the spray by interactions with the ambient air in a turbulent environment. The second step of autoignition is controlled by the chemical properties of the fuel that govern the kinetics leading to ignition of the mixture. The time required to ignite the mixture after the completion of the physical process of mixing is referred to as the "chemical delay". The chemical properties that control the chemical delay include molecular structures, adiabatic flame temperature, C/H/O ratio, and sooting propensity [45]. The overall ignition delay is the sum of physical and chemical delays.

2.1.2 Chemical Kinetics

The chemical kinetics that lead to autoignition of the fuel-oxidizer mixture are complicated processes that consist of a large number of simultaneous reactions [46]. Autoignition occurs with a large heat-release rate that causes a rapid rise in temperature and pressure. The chemical mechanism that drives this heat-release process consists of chain initiation, chain propagation and chain termination processes. The chain initiation begins the chain reaction by building a pool of radicals or intermediate species from the reactants [44, 47, 48, 49, 50]. The radicals react with each other and with stable species to create more radicals, resulting in chain propagation reactions. The chain propagation reactions include chain branching reactions, which are responsible for a self-propagating flame and are essential ingredients for combustion [47]. Chain branching reactions involve formation of more radicals than are consumed by the reactions, and can have an explosive effect on a combustion system by producing radicals that dominate the overall reaction rate.

Finally, the chain reactions are terminated with the formation of stable products in chain termination reactions. The chain reactions are a complex set of simultaneous chemical reactions that, in addition to the chemical properties of the fuel, also strongly depend on the physical state of the mixture, such as pressure and temperature.

2.1.3 Two-Stage Autoignition

In low-temperature diesel-like conditions, the ignition occurs in two stages [51, 52]. The first-stage ignition is dominated by low-temperature chemistry [50, 53] and shows a small peak in heat-release rate. The pressure rise is slow due to low reactivity of the mixture. This ignition region is labeled as the negative temperature coefficient (NTC) region [54]. The small rise in temperature and pressure indicates the beginning of chain reactions. However, the low reactivity of the mixture prevents the chain reactions from propagating further due to formation of relatively stable intermediate species. For typical diesel combustion, low-temperature autoignition occurs at approximately 750 K. The NTC behavior changes from one fuel to another, and largely depends on the chemical properties of the fuel as well as the physical state of the mixture, such as pressure and temperature. The second-stage of ignition is dominated by high-temperature chemistry that favors the rapid chain branching reactions leading to rapid heat-release rate, high temperature and high pressure-rise rate. At high initial temperatures (approximately 1000 K), the chemistry is dominated by high-temperature chemistry pathway, and thereby suppresses the NTC behavior. The NTC region has been the subject of experimental and modeling studies with single-component fuels, such as n-heptane [54]. In typical diesel-spray applications, NTC behavior is likely to occur due to evaporative local cooling by the spray, which makes available the pathway to low-temperature kinetics. Two-stage autoignition has been desirable for efficient combustion in diesel engines. A main issue over the years for diesel combustion has been how to control the autoignition process and heat-release rates over a wide range of operating conditions, with minimum emissions and high efficiency.

2.1.4 Conceptual Model for Diesel Combustion

After the mixture autoignites, the combustion process inside the cylinder occurs in two phases: a premixed-controlled combustion, and a mixing-controlled combustion [55, 56, 57]. Premixed-controlled combustion occurs in a fuel-rich region, with an approximate equivalence ratio of four [56, 57], and produces partially oxidized fuel fragments that diffuse outward and lead to the mixing-controlled diffusion flame that surrounds the premixed core region. The first stage of heat-release and temperature rise occurs in a fuel-rich premixed mode. The premixed flame is followed by a diffusion flame or mixing-controlled flame that oxidizes the rich combustion products of the premixed flame. The overall heat-release rate is primarily controlled by the rate of mixing of fuel and oxidizer. The quasi-steady combustion process in a typical diesel engine is conceptually presented in Fig. 2.1. As the cold liquid jet penetrates through the domain, it entrains the surrounding hot oxidizer. The liquid spray is heated up and evaporation occurs at the boundary of the spray

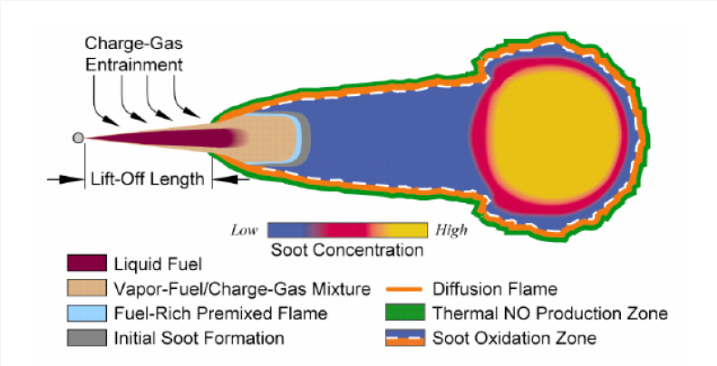

Figure 2.1. Schematic of a conceptual model of direct-injection (DI) diesel combustion [55, 58].

and oxidizer. As more air penetrates into the spray jet, the evaporation inside the jet core increases. The combustion begins when the fuel-oxidizer mixture reaches a particular equivalence ratio. The maximum temperature occurs in the diffusion region of the flame. The diffusion layer of the flame is identified by OH chemiluminescence [57]. The high-temperature diffusion layer has been the primary location for thermal NO production. However, the diffusion layer also oxidizes much of the soot that was formed in the fuel-rich zone.

2.1.5 Emissions

A principal advantage of combustion in diesel engines is the significant improvement in efficiency compared to gasoline engines at part-load conditions. Moreover, the direct injection of the fuel into the combustion chamber eliminates the throttling losses that are encountered in gasoline engines. This enables diesel engines to attain a peak brake-thermal efficiency of approximately 44% compared to approximately 30% for gasoline engines [44]. However, this benefit in efficiency often comes at the cost of high levels of emissions. The key pollutants from diesel engines are NOx and PM (or soot). Depending on the engine load conditions, diesel engines produce significant amounts of NOx, of which the majority is nitric oxide (NO) and nitrogen dioxide (NO_2). The key mechanisms that are responsible for NOx formation are: thermal NO, fuel-bound nitrogen, prompt NO, and N_2O-intermediate. In typical diesel combustion, thermal NO (via the Zeldovich mechanism) dominates the NOx formation. Thermal NO is produced by the oxidation of N-radicals that are created in the high-temperature diffusion layer of the flame. NOx from fuel-bound nitrogen comes from nitrogen compounds present in the fuel. Prompt NO (via the Fenimore mechanism) formation occurs in the flame zone when the CH radicals in a hydrocarbon flame rapidly react with atmospheric nitrogen [59]. The N_2O-intermediate mechanism is important for NOx production in low-temperature, fuel-lean combustion processes.

The soot formation, on the other hand, occurs in the fuel-rich zone and evolves inside the region surrounded by the thin diffusion layer (Fig. 2.1). Two key gas-phase kinetics that are important for soot formation are acetylene-based [60], and polycyclic aromatic hydrocabrons (PAHs)-based reactions [61, 62]. Soot formation begins with the formation of elemental carbon particles which agglomerate to form soot particles. The particles grow/deplete by surface reactions. Strategies to control NOx and soot emissions from engines are, unfortunately, not straightforward. The high-temperature diffusion flame increases thermal NO production, whereas the fuel-rich combustion results in soot production. One strategy to bring down the NOx level is exhaust gas recirculation (EGR), where a part of the combustion products is recirculated back to the engine. The recirculated gas provides a cooling effect that reduces thermal NO production. However, higher EGR concentration may lead to higher soot formation due to lack of oxygen to oxidize the soot. In

general, strategies that bring down the emissions level of one pollutant (soot or NOx) may tend to increase the other. The soot-NOx tradeoff is critical in diesel engines [58, 63, 64, 65].

2.2 Advanced Diesel Combustion

Driven by the need to reduce emissions from diesel engines, significant research efforts have been directed to the development of novel combustion systems that drastically reduce NOx and soot production without compromising fuel efficiency. The soot formation rate is controlled by the locally fuel-rich mixture that results from insufficient mixing due to limited air entrainment upstream of the lift-off length of the diffusion flame. A lean and homogeneous fuel-air mixture has the potential to reduce soot formation. The fuel-lean mixture results in higher fuel efficiency and comparatively lower combustion temperature, which in turn reduces the thermal NO production. This has lead to the development of HCCI-like combustion systems [11, 12] that operate on autoignition of homogeneous or quasi-homogeneous, lean or dilute fuel-air mixtures, and have the potential to comply with forthcoming emission norms with reduced reliance on aftertreatment [4].

2.2.1 Homogeneous Charge Compression-Ignition

HCCI operation requires the air and fuel to mix at the molecular level to produce a homogeneous mixture before combustion, similar to spark-ignition (SI) engines. However, while SI engines depend on an electric spark to initiate and propagate a premixed flame through the combustible mixture, HCCI relies on autoignition of the combustible mixture. SI engines are limited to low-to-moderate ranges of compression ratio to avoid knocking, whereas the HCCI engines operate with higher compression ratios that increase the thermodynamic efficiency of the system. Moreover, the homogeneous combustion mode retains the benefit of SI engines to produce low NOx and soot. Therefore, HCCI engines combine the benefits of both the SI and CI engines. The HCCI combustion concept is shown in Fig. 2.2, where it is compared with conventional diesel and gasoline combustion modes.

The engine load in HCCI engines, as in traditional diesel engines, is controlled

by the amount of fuel that is injected, with an approximately constant air flow rate (no throttling). The ignition delay strongly depends on the in-cylinder temperature, and weakly depends on the equivalence ratio of the mixture [66]. However, the heat-release rate, pressure-rise, and emissions strongly depend on equivalence ratio. Over the years, a primary challenge with HCCI engines has been to control combustion at low- and high-load conditions. At moderate loads, CO and UHC emissions are low and the combustion efficiency is high. At low-load conditions, due to small fuel mass, the mixture becomes too lean, unless the air is diluted significantly with high EGR. When the equivalence ratio of the mixture drops below 0.2, the combustion efficiency suffers significantly [58, 67], with increased levels of CO and UHC emissions. The higher CO and HC emissions occur because the mixture is too lean for the gas-phase reactions to complete [58, 68]. At high-load conditions, on the other hand, HCCI operations are limited by excessive pressure-rise rate, which can incur significant damage to the engine components. The high rate of pressure-rise also increases the noise level significantly. Therefore, key areas of research with HCCI engines have been to develop strategies to operate the engine with high efficiency and low emissions over a wide range of loads. To meet these requirements, additional investigations are needed to explore the potential of alternative fuel mixtures over the HCCI operating range.

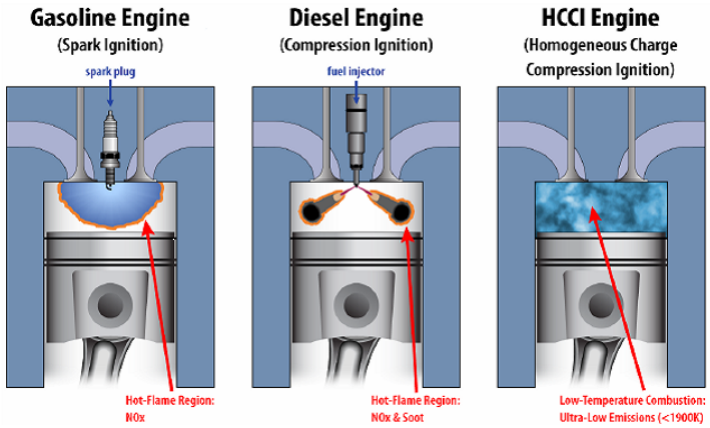

Figure 2.2. Combustion concepts in current and next-generation engines, [4].

To address these HCCI issues at low- and high-load conditions, developments have been made with novel injection strategies that involve changing the injection timing based on load conditions. At low-load conditions, the mixture becomes

too lean to produce complete combustion. To avoid this problem, the start of injection (SOI) is delayed until the air is compressed partially (e.g., SOI at 35 CAD before the end of compression [58]). This is in contrast with a pure-HCCI strategy that requires very early injection of fuel (during the intake stroke) to allow sufficient time for a homogeneous mixture to be realized. The late injection of fuel produces a globally lean stratified mixture, with pockets of local fuel-rich mixture followed by local fuel-lean mixture. The local fuel-rich mixture produces partial oxidation of the fuel and creates rich fuel fragments that diffuse ahead of the flame. The diffusion of the species and radicals towards the local fuel-lean region results in flame propagation faster than that expected from the same equivalence ratio without stratification [69]. The stratification of the charge widens the lean flammability limit, and thereby avoids local flame extinction due to extremely low equivalence ratio. The local rich mixture burns faster to produce high temperature that increases the thermal efficiency and reduces CO and UHC emissions. Stratification also proves to be effective at high-load conditions, where control over high pressure-rise rate has been achieved through thermal stratification of the charge. The thermal stratification occurs due to wall heat transfer, turbulent mixing, and the mixing of EGR with the fresh charge [70, 71]. The combustion occurs in a sequential autoignition processes, where the hottest zone autoignites first followed by other zones. This sequential process keeps the pressure-rise rate under control. Moreover, the stratification of equivalence ratio allows the engine to operate efficiently and cleanly with a higher equivalence ratio than that of an ideal homogeneous mixture.

2.2.2 Direct-Injection Spark-Ignition

A parallel development in spark-ignition (SI) engines with stratified charge is direct-injection spark-ignition (DISI) engines [6, 14, 15] that work on the principle of direct injection of fuel into the cylinder during the compression stroke. Direct injection has the potential to eliminate the throttling losses of a conventional SI engine, and therefore offers higher efficiency. A globally fuel-lean stratified mixture is created, through which a spark-initiated flame propagates [14]. The stratification of charge adds stability to the flame. The engine load is primarily controlled

by the injection timing and amount of fuel injected. For high-load conditions, the fuel is injected early (during the intake stroke) [6], allowing higher mixing time for the fuel-air mixture. The injection pressure is raised to a high value (5 - 20 MPa) to produce finely atomized spray and faster evaporation. The in-cylinder flow structure driven by a contoured piston surface and/or variable swirl and tumble at the intake enhances the mixing, allows the engine to operate with a nearly homogeneous charge [6] at full load, and retains the benefit of high fuel economy and low emissions.

2.2.3 Low-Temperature Combustion in Diesel Engines

Inspired by the high efficiency and low emissions potential of HCCI engines, significant research efforts have been invested in low-temperature combustion (LTC) in diesel-fueled compression-ignition engines, with emphasis on more nearly homogeneous charge formation [58, 72, 73, 74]. However, the initial attempts to achieve diesel-fueled HCCI-like mixing were not very successful with intake-port fuel injection strategies. The low volatility of diesel fuel causes accumulation of the fuel in the intake system and results in significant NOx and soot due to mixture inhomogeneities [72, 73, 74]. To avoid this problem, significant preheating is required, which coupled with the high cetane number of diesel fuel, requires lower compression ratio to avoid excessive pressure-rise rate. The early direct-injection of diesel fuel into the cylinder to allow for homogeneous mixing has been problematic with the current state-of-the-art injectors. The low volatility of the fuel coupled with lower cylinder pressure and temperature results in wall wetting, which becomes a source of higher UHC emissions and low combustion efficiency. Moreover, the high cetane number of the fuel results in early autoignition. Many of the control strategies to control autoignition have been centered on dilution of the fresh charge with high EGR concentrations [75, 76]. Other control strategies include variable intake-valve closing to control the effective compression ratio. Many of the LTC strategies in diesel engines rely on high pressure, late injection with fast mixing, delayed autoignition and high EGR rate. Even with all these strategies, these engines do not meet the 2010 NOx regulations. Although LTC in diesel engines has been of limited success to date, diesel fuel operations are still desirable at high load

conditions, due to superior efficiency. While conventional diesel combustion has a long history of development, HCCI/LTC engine combustion is relatively new and has not yet been fully explored with the alternative fuels of interest at high-load conditions.

2.2.4 Reactivity-Controlled Compression-Ignition

Another interesting strategy that has gained much attention recently is reactivity-controlled compression-ignition (RCCI) [19, 20, 21, 22]. A primary limitation of HCCI engines has been identified as limited operability range, since the autoignition process is difficult to control in CI engines. RCCI is a variant of HCCI that provides much-needed control with significant reduction in emissions of NOx and soot. RCCI combustion works on a dual-fuel strategy, where two fuels with different reactivities are injected into the cylinder with multiple injectors to control the total amount of fuel injected. The combustion phases are controlled by the injection of the two fuels. The fuel with high reactivity is introduced into the cylinder towards the end of compression. The high-reactivity fuel ignites first, leaving a mixture of air, low-reactivity fuel and recirculated exhaust gas which produces the second phase of combustion. The injection rate and the blend ratio of the high-reactivity fuel control the rate of pressure-rise in the cylinder. RCCI has been demonstrated using a wide range of fuel mixtures that include diesel and gasoline mixtures, ethanol and diesel, etc. A small amount of additives is often added to boost the cetane number of the fuel mixtures. The key benefits of RCCI combustion include lower levels of NOx and soot emissions, significant increases in fuel economy, and reduced heat losses and therefore higher brake-thermal efficiency. Preliminary engine studies with RCCI have reported a brake-thermal efficiency of 55% [22]. The RCCI combustion strategy provides a viable means to meet the 2010 emissions requirements for heavy-duty diesel engines with reduced dependence on aftertreatment. However, the application of RCCI needs to be explored in a wider design space. The blending of two fuels with widely different chemical and physical properties leads to complicated thermochemical processes that need to be better understood.

2.2.5 Soot and NOx Regimes

Figure 2.3 shows an equivalence ratio (ϕ) versus temperature plot for combustion under diesel engine conditions. Soot formation occurs in a region where the equivalence ratio is higher than two, within a temperature range of 1600 - 2400 K. The NOx formation region, dominated by the thermal NO formation, begins at 2200 K and occurs for relatively lean mixtures. A conventional diesel combustion process starts with fuel-rich premixed burn, which lies inside the sooting zone. The high-temperature diffusion flame then falls into the NOx region on the $\phi - T$ map. For high EGR, the curve shifts to the left, and therefore avoids the high soot and NOx zones. However, the brake-specific fuel consumption, and therefore the fuel economy, suffers significantly when the EGR concentration becomes too high. Low-temperature combustion attempts to operate in a region that minimizes both soot and NOx formation, and maximizes the fuel efficiency. This leaves a very narrow operating zone for LTC combustion. Controlling the engine combustion in this narrow range of conditions for a wide range of engine speeds and loads is an enormous challenge that requires in-depth understanding of the combustion in these systems.

2.2.6 Challenges for Low-Temperature Combustion

LTC strategies primarily rely on the detailed chemical kinetics of the fuel-air mixture for autoignition [77]. Understanding of these chemical processes has become essential for the study of detailed combustion characteristics of these engines. The sensitivity of the ignition timing to the fuel-specific physical and chemical properties creates multiple challenges for the emerging diversified fuel compositions. Over a wide range of operating conditions, the control of combustion processes becomes difficult. The lack of fundamental knowledge on flame propagation through an extremely lean charge at low-load conditions, the cycle-to-cycle variability, and control of fuel-air and temperature stratification are some of the key issues that need to be resolved.

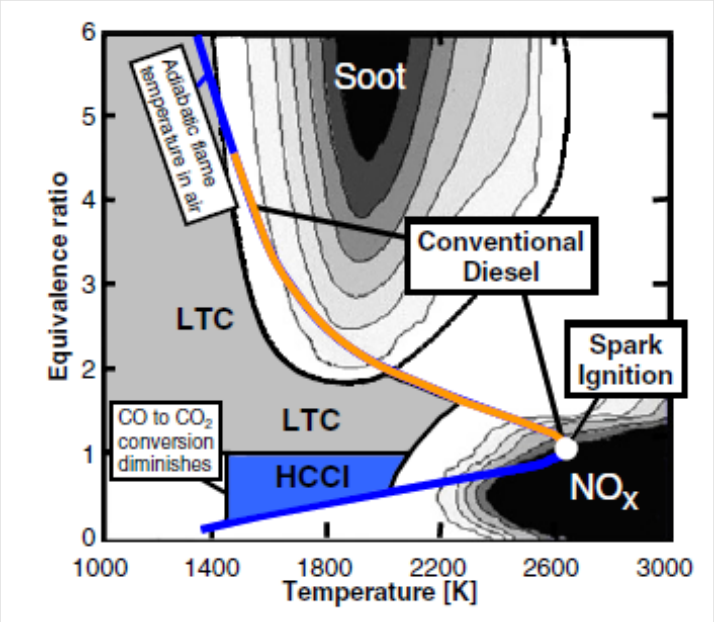

Figure 2.3. Diagram showing the equivalence-ratio-temperature ranges for soot and NOx formation, and the regions corresponding to conventional diesel, SI, HCCI, and diesel LTC engines [63, 64, 65, 58].

2.3 Fuels

Much of the recent research effort in engine combustion has been guided by the exploration of existing and new fuels, beyond the traditional petroleum-based gasoline and diesel fuels. The three major petroleum-based classes of fuels widely used in transportation are gasoline, diesel and jet fuel. Each of these classes has specific physical and chemical characteristics that make them suitable for specific engine applications. A typical SI engine uses gasoline as the fuel, and a key fuel characteristic that measures the performance of a gasoline fuel is the octane number. The octane rating of a gasoline fuel measures the resistance of the fuel to autoignite, and thus to prevent engine knock. In a typical SI engine the ignition is initiated with a spark, which establishes a flame kernel that propagates through a premixed, near-stoichiometric air-fuel mixture to produce rapid rise of pressure and temperature. Autoignition of the air-fuel mixture in SI engines causes a premature combustion, which results in abnormal rise in pressure that can cause severe engine damage. Higher octane number is preferred for gasoline fuels to prevent engine knocking. CI engines, on the other hand, work on the principle of autoignition of the fuel.

Diesel fuel is used for CI engines. The performance of CI engines depends on autoignition characteristics of the fuel, which are measured by the cetane number. The higher the cetane number, the faster is the autoignition of the fuel. The main differences between conventional diesel- and gasoline-based combustion processes are in how the combustion is initiated (spark versus CI) and how load is controlled. While gasoline-based SI engines rely on throttling of air to control the load, diesel-based CI engines control load by amount of fuel injection. Although engine fuels are typically composed of many compounds, gasoline fuels tend to contain more iso-alkanes or branched alkanes, whereas diesel fuels are predominantly based on straight-chain or normal alkanes.

2.3.1 Engine-Fuel Components and Properties

A typical diesel fuel is a blend of hundreds of compounds that belong to different classes, the most common class being alkanes. The relative amounts of various chemical classes in typical diesel fuel are shown in Fig. 2.4. The primary classes of species in diesel fuel are n-alkanes, iso-alkanes, cycloalkanes and aro-

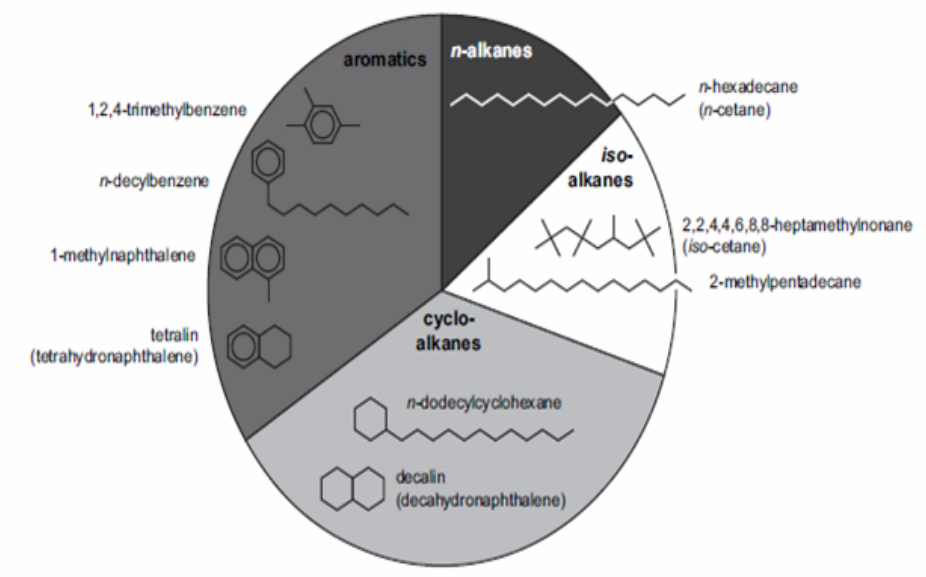

Figure 2.4. Relative amounts of chemical classes in diesel fuel and possible surrogate-compounds to represent these chemical classes [45].

matics. Each class consists of a large number of hydrocarbons, the proportion

of which varies from one country to other, one location to other, and even from one refinery to another [78]. N-alkanes, which are the primary components of high-cetane-number diesel fuel, are straight-chain compounds with single carbon-to-carbon bonds, and carbon-to-hydrogen bonds. Iso-alkanes, on the other hand, have one or more branched methyl groups, and are more suitable for SI engines. Cyclo-alkanes are typically composed of one or more rings, with multiple alkyl side chains. Aromatics are similar in structure to cyclo-alkanes, but have carbon-carbon double bonds in the ring structure. The typical number of carbon atoms in the different fuel components varies widely; a typical average value is approximately 14 - 15 [45]. Each component of the fuel has its own set of kinetics, which results in widely different reactivities for the different components of the mixture. The physical properties of the components also vary widely. The variations in physical properties result in significant differences in physical behaviors and the combustion processes. For engines with direct injection of liquid fuel into the cylinder, the physical properties control the fuel breakup, evaporation, species transport, and the reaction. The breakup and atomization characteristics of a fuel spray strongly depend on flow and fuel properties that include density, viscosity, diffusivity, molecular weight and surface tension. The evaporation of sprays and the species transport depend on specific heat, boiling point, density, thermal conductivity and other properties. The reactivity of fuel is controlled by molecular structure, formation enthalpy, C/H ratio and other properties.

With the new combustion strategies that are of interest recently, much of the research effort has been focused on exploring the capabilities of diesel and gasoline fuels for HCCI/DISI/RCCI/LTC combustion conditions. Gasoline has been one of the most commonly used fuels in HCCI; there the high volatility of gasoline has been an advantage over diesel. The low volatility of diesel fuel has proved to be disadvantageous to produce a homogeneous charge. On the other hand, the low cetane number of gasoline requires a high temperature for autoignition. Unlike diesel that shows a two-stage autoignition, gasoline-like fuels exhibit a single-stage ignition. Research has shown that for HCCI conditions, it may be advantageous to use fuels with properties and autoignition characteristics lying in between those of traditional gasoline and diesel [58]. A higher volatility is desirable for a homogeneous charge, and relatively higher cetane number with two-stage ignition is

necessary for efficient combustion.

2.3.2 Surrogate Fuels

Detailed chemical mechanisms are important to build the foundation for realistic CFD predictions to enable the optimization of practical devices and explore a wide design scope. Development of such kinetic mechanisms is extremely challenging for real fuels due to the presence of hundreds of components, each having its own characteristic set of reactions. A chemical mechanism based on all these reactions is prohibitively expensive for CFD modeling. A simplified, yet realistic, approach is to use surrogate fuels, which essentially consist of a single pure compound or a small number of compounds. The behavior of the surrogate fuel needs to match that of the target fuel. The surrogate fuel needs to represent the overall physical and chemical properties of the target fuel so as to predict not only the combustion characteristics, but also to reproduce the spray breakup, evaporation and mixing processes of the target fuel. Key physical properties of a surrogate fuel include boiling point, density, viscosity, surface tension coefficient, thermal conductivity, molecular diffusivity and molecular weight. Key chemical properties include ignition behavior, molecular structure, adiabatic flame temperature, C/H ratio, and sooting propensity.

Recent developments in detailed kinetic studies of single- and multi-component surrogate fuels have been reviewed in [45]. Detailed kinetic mechanisms for surrogate fuels remain large, and therefore, much of the recent modeling effort has been directed to reduction of the size of mechanisms based on optimized reduction tools. Small- to moderate-sized mechanisms are suitable choices for multi-dimensional combustion simulations in engines. To make the CFD predictions reliable, the kinetic models need to be validated with experimental measurements under engine-like conditions of interest. This requires well-coordinated efforts between experimentalists and modelers to provide validation of the kinetic models with the measurements. Over the years, much of the experimental research has been focused on providing measurements for the key ignition characteristics of a wide range of surrogate fuels with well-known properties. The geometric configurations for experimental studies have been extended from simple homogeneous reac-

tors or shock tubes to simplified and realistic engine configurations. With current state-of-the-art laser diagnostics and imaging techniques, engine measurements [67, 70, 79] have provided instantaneous and time-averaged images of autoignition, flame shape, and emissions that contribute to understanding the qualitative nature of the combustion process as a whole.

2.3.3 Chemical Kinetics for Diesel Surrogate Fuels

Progress towards the development of diesel surrogate fuels has been reviewed by Farrel *et al*. [78], and Battin-Leclerc [80]. More recent developments have been discussed by Pitz and Mueller [45]. There has been significant progress over the last decade towards building kinetic models relevant to diesel fuels. Most of these are based on single-component n-alkane kinetics from n-C_8 to n-C_{16} [81, 82, 83]. You *et al*. [84] have provided detailed mechanisms for n-dodecane and n-decane for temperatures above 850 K. Recent work includes high-temperature n-heptane to n-hexadecane mechanisms for premixed flames [85, 84] that include formation of key unsaturated soot-precursor species. All the chemical mechanisms have been validated with experimental measurements that provide the much needed insight into the behavior of these fuels. The key measurements include ignition delay, laminar flame speed, and pyrolysis/fuel-cracking for large alkanes using a wide range of experimental configurations that include shock tubes, jet-stirred reactors and plug-flow reactors. A recent experiment by Shen *et al*. [86] has provided comprehensive shock-tube measurements for ignition delay and laminar flame speed using large n-alkanes over a temperature range of 786 - 1398 K, a pressure range of 9 - 58 atm, and equivalence ratios of 0.25, 0.50 and 1.00.

2.3.3.1 Chemical Kinetics for Binary Surrogate Fuels

A primary difficulty that has been encountered in representing diesel fuel with a single-component surrogate has been to reproduce all the physical properties correctly with single component. To overcome this shortcoming, a significant amount of work has been carried out with binary surrogate fuels. A typical example of this includes a mixture of 70% n-decane and 30% 1-methyl-napthalene by volume. This fuel was formulated as a part of the Integrated Diesel European Action (IDEA)

[87] project, to specify a surrogate fuel with heavier compounds to facilitate numerical simulations for diesel combustion. The cetane number of this fuel is 55. A detailed n-decane mechanism had been suggested for the IDEA fuel by Pitsch and Peters [88]. Several other binary surrogate fuels had been evaluated to match the design targets for jet fuels and diesel fuels in the early 2000. One example of this is a binary mixture of n-decane and aromatic species (toluene, n-propylbenzene, 1,2,4-trimethylbenzene) that resulted from a coordinated effort between industry and academics called Computational Fluid Dynamics for Combustion (CFD4C) [89]. More recently, a blend of n-heptane and iso-octane (primary reference fuel - PRF) as surrogates of diesel and gasoline, respectively, has been evaluated as a reference for wide class of fuel properties. By changing the proportion of these two components, PRF has been able to reproduce realistic fuel behavior. PRFs have been subject to many experimental and modeling studies [90, 91]. One example is PRF80 that consists of a mixture of 80% iso-octane and 20% n-heptane [90]. PRF80 demonstrated a two-stage ignition process that includes a low-temperature heat-release by n-heptane followed by a high-temperature heat release. Experimental studies with PRF80 under HCCI conditions demonstrated potential for high power output, improved combustion phasing, low cycle-to-cycle variations, and low NOx.

2.3.3.2 n-Heptane Kinetics as a Single-Component Surrogate Fuel

Among all the single-component surrogate diesel fuels, much of the development has been centered on n-heptane. The cetane number of n-heptane is approximately 55, which is close to typical European and Japanese diesel fuels [78]. The cetane number of typical diesel fuel ranges from 40 to 56 in the USA. The primary benefit of using n-heptane as a diesel surrogate is that the detailed kinetics for n-heptane oxidation for low, intermediate and high temperatures have been explored widely [83]. Reduced kinetic models with a relatively small number of species and reactions are available, which make n-heptane a relatively easy choice for CFD computations. Of all the large-carbon-number alkanes considered, the kinetics of n-heptane is, perhaps, the best described. In a recent modeling effort for HCCI combustion, Maroteaux and Noel [77] provided a 25-species, 26-reaction reduced mechanism that was developed from a detailed mechanism of 2446 reactions and

544 species developed by the Lawrence Livermore National Laboratory (LLNL) through a systematic reduction process. Other reaction mechanisms for n-heptane include a 48-species, 248-reaction mechanism by Peters *et al.* [92], a 41-species, 130-reaction mechanism by Ra and Reitz [93], a 40-species, 165-reaction mechanism by Golovitchev [2], a 29-species, 52-reaction by Patel [94], and a 52-species, 48-reaction by Lu *et al.* [95] among others.

2.3.3.3 n-Dodecane Kinetics as a Single-Component Surrogate Fuel

Lately, much of the research effort on surrogate diesel fuel has been directed to the development of chemical kinetics of n-dodecane. The average carbon content in typical diesel fuel is much higher than n-heptane (7), and is closer to that of n-dodecane (12). Carbon content is an important parameter that determines the properties of the fuel. Therefore, n-dodecane may be more suitable as a diesel surrogate fuel. The cetane number of n-dodecane is approximately 45, which is below the European standard, but is more realistic for diesel fuel used in the USA. However, the kinetic models for n-dodecane are more complex compared to n-heptane. A detailed kinetic model for n-dodecane has been developed by You *et al.* [84], which essentially models the kinetic behavior of heavier n-alkanes up to n-dodecane. Another kinetic model includes a detailed mechanism for oxidation of n-alkanes from n-octane to n-hexadecane by Westbrook *et al.* [82]. Recently, a reduced mechanism with 103-species and 370-reactions has been suggested by Som *et al.* [3]. This mechanism includes low-temperature kinetics, and showed reasonable agreement with the measurements when validated for autoigniting flames under diesel-engine-like conditions, jet-stirred reactor and counterflow flames. Although a few reduced n-dodecane kinetics are available for near-atmospheric-condition jet flames [96, 97], not many are available for diesel-like conditions. Other single-component fuel surrogates that have been studied over the years include n-decane [98, 99, 100] and n-hexadecane [101, 102] in the normal-alkane class, iso-octane and iso-cetane in the branched-chain alkanes, methylcyclo-hexane of cyclo-alkanes, toluene, benzene, methyl-naphthalene in the aromatic class, and others.

2.3.3.4 Limitations of Single-Component Surrogate Fuels

It is widely recognized that a single-component surrogate fuel can not mimic all the properties of diesel fuel. This can result in significant differences in ignition characteristics between actual and surrogate fuels at different load/speed operating conditions. This is particularly true with n-heptane, which has higher volatility than diesel fuel. The higher volatility causes the spray to penetrate less, and to evaporate faster than diesel. This results in significant differences in in-cylinder distribution of local air-fuel ratio and subsequent combustion. The differences in combustion characteristics become particularly large for mixing-controlled combustion. However, even if the evaporation characteristics and the equivalence ratio match with those of diesel, the ignition characteristics may differ widely. This is because the first stages of heat-release at low temperatures for n-heptane and diesel fuel are likely to be different [78]. The n-heptane kinetics do not describe the complex pyrolysis break-down of diesel fuel. The presence of cyclo-alkanes, iso-alkanes and aromatics also is not considered. And the simplified kinetics for n-heptane may not be able to reproduce the key pollutant formation processes for diesel fuel. However, these problems with surrogate fuels apply not only to n-heptane, but also to other single-component surrogate fuels. Nevertheless, the single-component surrogate fuels are attractive choices for three-dimensional engine simulations, primarily because of the simplified and reduced kinetics models that are available, and well-characterized physical and chemical properties that make the CFD simulations useful to gain insight into the in-cylinder processes.

2.4 CFD for Turbulent Spray Combustion

The success of high-end computational models in engine combustion largely depends on how accurately the models can capture the physical processes that govern turbulent combustion in engines. For the purposes of physical understanding and model development, the CFD models are validated for simple flames.

2.4.1 Near-Atmospheric Pressure Statistically Stationary Turbulent Flames

Most of the modeling efforts to date have been directed towards laboratory-scale, near-atmospheric-pressure canonical flames with simple geometric configurations, where the thermochemical conditions are well known, and ample measurement data are available. Examples of such flames include the Sandia C, D, E and F flames [103, 104], which are non-luminous, turbulent nonpremixed piloted methane-air flames. The Sandia flames have been the subject of many modeling studies over the years. Key parameters of these flames are the speeds of the central fuel-air jet, the pilot mixture, and the co-flow air. The fuel jet and pilot velocities increase from flame C to F. These flames exhibit increasing local extinction effects as the fuel-jet and pilot velocities increase: flame D exhibits mild flame extinction effects, whereas flame F is on the verge of global extinction. These flames are suitable for modeling studies of turbulence-chemistry interactions (TCI). The importance of TCI is often characterized by Damköhler number, which is defined as the ratio of hydrodynamic to chemical time scales. Low-to-intermediate Damköhler number flows are of particular interest here, since they represent conditions where TCI are expected to be important. Recently, the development of modeling approaches to capture TCI has been reviewed by Haworth [33]. The importance of TCI was demonstrated by Zhang [13] in his Ph.D. work, for example. Zhang compared the results for a hybrid Reynolds-averaged-simulation (RAS)/PDF model that explicitly accounts for TCI, and a well-stirred reactor model that neglects TCI in the mean chemical source terms, with experimental measurements. The RAS/PDF model showed significant improvement of prediction capability compared to the model that neglected TCI. A number of modeling studies have been reported with PDF-based models, that illustrate the need to improve the modeling capabilities by exploring variants of transported PDF modeling (e.g. composition PDF, velocity-composition-joint PDF) [32, 31, 30, 29, 105, 106], advanced mixing models [107, 108], improved and faster numerical algorithms [109], parallelization strategies, radiation modeling [110] and detailed chemistry [111]. The turbulence modeling and flow structures for these configurations have been studied using both RAS [32, 31, 30, 29] and large-eddy simulation (LES) [105, 106] approaches. A

filtered density function (FDF) method is the analogue of a PDF method for LES. A recent development in modeling of turbulent jet flames has been a deterministic multi-environment Eulerian-field PDF method (MEPDF) [112, 113] that appears to be an encouraging alternative to particle-based Monte Carlo methods with lower computational cost, while retaining the benefits of transported PDF methods.

Bluff-body-stabilized flames have also been the subject of modeling studies with PDF methods. The geometric configuration includes a fuel jet issuing from the center of a cylinder, and a co-flow air at the outer diameter of the cylinder. This configuration is more complex than simple jet flames because of the presence of an annular recirculation zone that increases the complexity of the flow structure. Methane and hydrogen have been used as fuels. Modeling studies for these flames include RAS/PDF [112, 114], LES/FDF [115, 116], and MEPDF [112] methods. Detailed modeling studies with these methods include comparisons of transported PDF versus presumed PDF methods, effects of mixing models, effects of chemical mechanisms, effects of boundary conditions and numerical parameters, studies on particle/mesh consistency in hybrid Lagrangian-particle/Eulerian-mesh (LPEM) methods, and comparisons of turbulence models. Nonpremixed swirling flames have also been the subject of modeling studies with transported PDF method, with more emphasis on comparing results between transported PDF and presumed PDF methods [117], [118].

Premixed turbulent flames are of interest because of their relevance in spark-ignited IC engines. Modeling studies of premixed turbulent flames have been reported with canonical, near-atmospheric-pressure, simple geometric configurations that range from bluff-body-stabilized flames to Bunsen-burner flames. Cannon *et al.* [119] applied a transported velocity-composition joint PDF method to a laboratory-scale methane-air bluff-body-stabilized flame [120]. More recent modeling comparisons in turbulent premixed flames were provided by Lindstedt and Vaos [121] and Stollinger and Heinz [122] for stoichiometric, piloted methaneair Bunsen flames [123]. The measurements covered a range of Damköhler numbers (Da) that range from a distributed flame region (low-Da) to a flamelet region (high-Da). The composition PDF method captured the flame structure with reasonable accuracy over a wide range of Da.

The modeling studies with PDF methods have been extended to atmospheric-

pressure, laboratory-scale, luminous, non-premixed turbulent jet flames. These flames have been the subjects of modeling studies focused on soot and radiation. Lindstedt *et al.* [124] reported a modeling study of these flames using a composition PDF method that includes an optically-thin grey-radiation model, along with a soot model and a 14-species chemical mechanism for gas-phase chemistry for ethylene-air flames. Reasonable quantitative agreement has been observed with experimental measurements. Mehta [125, 126, 38] used a composition PDF method with a 33-species chemical mechanism for ethylene and methane/ethylene turbulent jet flames to integrate a method-of-moments-based detailed soot model and a detailed spectral photon Monte Carlo radiation model to explore interactions between gas-phase chemistry, soot, and radiation. Turbulence-radiation interactions (TRI) were investigated along with turbulence-chemistry interactions (TCI). The comparison of results with and without TRI demonstrated better agreement with the measurements when TRI were considered.

Table 2.1. Examples of computational studies with the transported composition PDF method for laboratory-scale, atmospheric pressure, statistically stationary turbulent flames from the TNF Workshop.

Configuration	Focus of study	References
Piloted CH_4/air jet flames	TCI, mixing model, chemical mechanisms, emissions, radiation and TRI, local extinction effects	[124], [109], [127], [128], [110]
Bluff-body stabilized H_2/CH_4-air flames	TCI, mixing model, Da effect, numerical accuracy, comparison of turbulence models	[129], [130], [114], [131], [132], [133]
Nonpremixed swirling flame	TCI, transported vs presumed PDF, mixing model	[117], [118]

The modeling efforts discussed up to now have been for near-atmospheric-pressure, laboratory-scale, statitically stationary, canonical flame configurations, where the model predictions are compared with experimental data. A summary of computational studies with the transported composition PDF method for the flame configurations discussed above is presented in Table 2.1. The strength of the transported PDF methods has been explored and validated for these flames, where the thermochemical processes are relatively well-known due to availability

of a wide range of high-quality experimental data.

2.4.2 High-Pressure Turbulent Spray Flames

Direct extension of the high-end computational models from the simple laboratory scale statistically stationary turbulent flames to turbulent combustion in IC engines is not straightforward. Accurate capturing of turbulent combustion in engines requires high temporal and spatial resolution to capture the transient ignition characteristics. The high-end computational models that have demonstrated improvement in predictions for well-characterized stationary flames, remain to be investigated for high-pressure, transient, autoigniting flames that involve multiple combustion modes: premixed, mixing-controlled, and kinetically-controlled combustion. Liquid fuel injection and subsequent two-phase flow increase the complexity of in-cylinder processes in direct-injection engines. Moreover, the lack of reliable detailed experimental measurements for real engine configurations limits in-depth understanding of the in-cylinder processes.

2.4.2.1 State-of-the-art Engine Modeling

Efforts to apply the RAS/PDF method to simulate engine combustion for premixed turbulent flames under near-stoichiometric conditions have been reported by Taut *et al.* [134] for a spark-ignited two-stroke engine. Although the CFD predictions could only provide qualitative agreement with the measurements, this work illustrated the feasibility of a time-dependent, three-dimensional engine simulation using PDF methods. PDF-based simulations have been reported for HCCI engines to study the autoignition and emissions using skeletal chemical mechanisms for single-component surrogate fuels (n-heptane and iso-octane) [39, 6, 13, 40]. In the absence of comprehensive experimental measurements, the modeling studies focused on the difference between results obtained with versus without consideration of TCI. In a more recent work with low-temperature combustion in diesel engines [58, 79], chemiluminescence images revealed that OH was broadly distributed throughout the combustion zone downstream of the fuel jet, as opposed to that in a thin diffusion flame around the jet periphery as in conventional diesel combustion (Fig. 2.5). These qualitative images emphasize the need to include

TCI models for future development of combustion strategies that are significantly different from traditional diesel combustion.

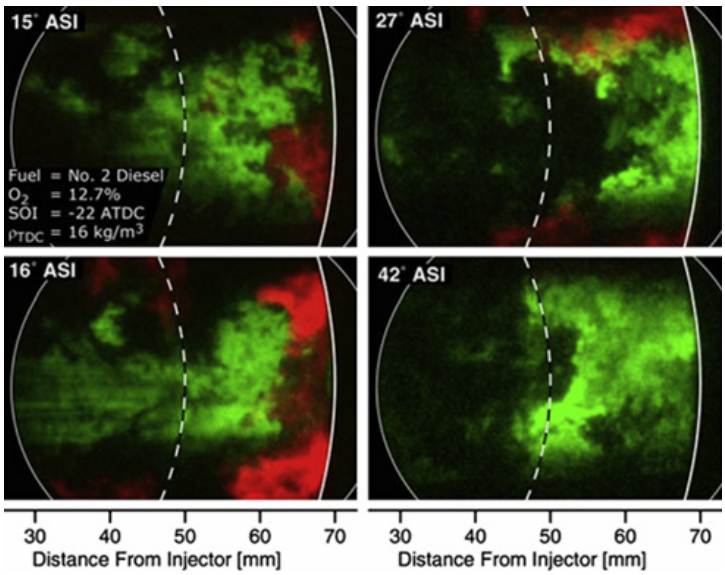

Figure 2.5. Sequence of simultaneous OH (green) and soot (red) luminescence images for low-temperature combustion in a diesel engine [58, 79].

2.4.2.2 Modeling Challenges for Turbulent Spray Combustion for Diesel-Like Conditions

The degree of complexity of a turbulent-spray-combustion process is intensified by the high cylinder pressures that are anticipated for next-generation LTC engines. Most of the physical phenomena that govern the turbulent spray combustion processes are built on theories and experimental observations at atmospheric pressure. At extremely high pressures, the physical processes of spray breakup, droplet evaporation, two-phase heat and mass transfer, chemical kinetics, flame propagation and other transport properties may require models that are fundamentally different from those at near-atmospheric pressure. The strong coupling between the high-pressure flow, molecular transport and chemistry may require consideration of different spatial and temporal scales that demand improved physical and computational models for LTC engines. To explore the capability of transported PDF methods in producing realistic predictions for ignition and emissions characteristics under such conditions, the modeling efforts need to be supported by

a comprehensive set of experimental measurements that characterize the detailed thermochemical processes under conditions that are expected in advanced diesel combustion systems. A recent effort to address this issue is the Engine Combustion Network (ECN) [1] of the Sandia National Laboratories. ECN provides a much-needed platform to bridge the gap in modeling strategies between canonical laboratory-scale flames and practical diesel engines by providing a reliable experimental database for well-characterized turbulent spray flames for diesel-engine-like conditions. For detailed discussion of ECN, the readers are referred to Chapter 4 of this thesis.

Along with the emphasis on TCI for realistic predictions, other key modeling areas that are addressed in the present work include modeling of turbulent sprays. While more emphasis has been given to autoignition of homogeneous or near-homogeneous charges for improved engine performance, advanced injection strategies hold the key to producing the desired homogeneous/near-homogeneous mixtures. Capturing the sensitivity of engine performance to small changes in the physical state of the combustible mixture demands accurate modeling of injector and spray processes for realistic CFD predictions. In particular, a key challenge is modeling of the spray near the injector, where a liquid core disintegrates to ligaments of liquid and finally to droplets through a sequence of instabilities that are created by complex interactions of the liquid with the gas phase. This region of the spray, referred to as the dense-spray region (also referred as primary atomization region), has been subject of many modeling and theoretical studies over the years [135, 136]. The physical processes that lead to the formation and growth of instabilities on the liquid surface have not yet been fully understood. Moreover, the lack of sound experimental techniques to resolve the physical characteristics of the spray has limited our ability to improve the theoretical understanding. Although a few modeling approaches have been reported in the literature to describe the spray behavior statistically [135, 136, 137, 138, 139, 140], the absence of experimental measurements does not allow rigorous validation of these models. The ad-hoc modeling strategies that are currently in use are based on tuning the model coefficients to match measurements relatively far downstream of nozzle. However, far downstream of the nozzle, the spray is relatively well behaved, and the physical characteristics are relatively better known. This region is referred to as the

dilute-spray region. The modeling of spray/droplet behavior in dilute sprays, and two-phase interactions between droplets and the gas-phase, have been the subjects of many computational studies [141]. Several Eulerian- and Lagrangian-based approaches are available to model this. Lagrangian-based dispersed-phase modeling is the more popular of the two for engine spray modeling. This model is based on the computational approach suggested by Dukowicz [141], with a strongly coupled Eulerian-based gas-phase modeling. The interactions of the dispersed-phase droplets with the strong turbulent flow are the key factors that control the evaporation and heat transfer rates to/from the droplets. Most of the Lagrangian modeling strategies for droplet evaporation are based on uniform droplet properties, with the approximation that the droplet internal circulation is infinitely fast. The characterization of droplets with uniform properties that evolve with time is a reasonable approximation for the dilute spray regime in engine applications. The modeling aspects of single-component droplets are discussed in detail in Chapter 3.

Due to growing interest in multi-component fuels, multi-component droplet evaporation also has been a subject of modeling studies. Many of the earlier multi-component vaporization studies have approximated the droplet evaporation as a vaporization sequence of single components controlled by their volatility differences. However, studies have revealed that for components with widely different mass diffusivities, the evaporation rates of the components may potentially be limited by the rate at which the low-diffusivity component is transported to the droplet surface [142, 143]. In the limiting case where the mass diffusivity drops to zero, the vaporization rates of the individual species no longer depend on the volatility of the components. In practical applications of interest, the droplet evaporation occurs due to the combined effects of volatility and mass diffusion of the components. Most of the engine spray modeling to date neglects the diffusive transport inside the droplets. However, care should be taken in extending these models to a low-temperature, low-pressure environment, where the low-evaporation rate of spray can result in wall film formation. The transient heating of the wall film and differential mass diffusion of the liquid components can significantly alter the evaporation rates, and result in different emissions characteristics.

The availability of high-speed computational resources has increased the de-

mand and scope of improvement in the numerical predictions significantly. Faster and more robust numerical algorithms, and significant improvements in parallel computing resources have opened up opportunities to introduce more detailed physical models to improve the CFD predictions. However, understanding of the fundamental complex physical processes holds the key to the development of physical models that are needed for accurate predictions. The physical models should be explored with simple, yet realistic, flame configurations representative of engine combustion, where the model performance can be evaluated against experimental data without introducing geometric complexities. The ultimate goal is to build up efficient, reliable and accurate CFD-based models that can be used in complete engine simulations.

Chapter 3

Mathematical Formulation, Physical Models and Numerical Methods

In this chapter, a comprehensive review of the mathematical formulation, physical and numerical models is provided, and the models used in the present work are discussed. The chapter begins with the governing equations for instantaneous (unaveraged, unfiltered) flow variables and thermochemical properties (Sec. 3.1). The turbulent flow equations are presented next (Sec. 3.2), with discussions of closure modeling for the Reynolds-averaged equations for mean flow variables. A two-equation turbulence model is discussed next (Sec. 3.3), including the near-wall modeling. The concept of a composition-PDF within the framework of Lagrangian stochastic modeling follows next (Sec. 3.4). Section 3.5 discusses the Lagrangian-particle/Eulerian-mesh (LPEM) method, with emphasis on a consistent numerical algorithm for mean density computation. The remaining physical submodels employed in the present work are discussed in the subsequent sections: gas-phase chemistry (Sec. 3.6) for detailed kinetic modeling of gas-phase reactions, soot modeling (Sec. 3.7) using a two-equation model or method of moments with interpolative closure (MOMIC), liquid fuel-spray modeling (Sec. 3.8) including secondary breakup and dispersed-phase models, and radiation modeling (Sec. 3.9) using an optically-thin treatment. The final section (Sec. 10) summarizes the numerical strategies, including parallelization of the computational methods.

3.1 Governing Equations

The instantaneous partial differential equations (PDE) for a gas-phase multi-component reacting system with N_s chemical species are given in Eq. (3.1) [33] using Cartesian tensor notation. For the purpose of brevity, the terms representing multi-phase transport are not shown here. The multi-phase terms, in general, appear as source terms on the right-hand sides of the transport equations, and are discussed later in the context of dispersed-phase modeling and the particle-PDF method.

$$\begin{aligned}
\frac{\partial \rho}{\partial t} + \frac{\partial \rho u_i}{\partial x_i} &= 0, \\
\frac{\partial \rho u_i}{\partial t} + \frac{\partial \rho u_i u_j}{\partial x_j} &= -\frac{\partial p}{\partial x_i} + \rho g_i + \frac{\partial \tau_{ij}}{\partial x_j}, \\
\frac{\partial \rho Y_\alpha}{\partial t} + \frac{\partial \rho u_j Y_\alpha}{\partial x_j} &= -\frac{\partial J_i^\alpha}{\partial x_i} + \rho S_\alpha, \\
\frac{\partial \rho h}{\partial t} + \frac{\partial \rho u_j h}{\partial x_j} &= -\frac{\partial J_i^h}{\partial x_i} + \frac{Dp}{Dt} + \tau_{ij}\frac{\partial u_j}{\partial x_i} - \dot{Q}_{rad}.
\end{aligned} \tag{3.1}$$

Here u_i is the i-th component of velocity vector $\underline{u}$ (i =1,2,3), Y_α is the mass fraction of species $\alpha(\alpha = 1, 2, ..., N_s)$, and h is the mixture specific enthalpy. Mixture mass density, pressure and body force per unit mass are denoted by ρ, p and $\underline{g}$, respectively. The viscous stress tensor is τ_{ij}, and the molecular fluxes of species and enthalpy are denoted by $\underline{J}^\alpha$ and $\underline{J}^h$, respectively. The chemical production rate for species α is given as $\rho S_\alpha = W_\alpha \dot{\omega}_\alpha$, where W_α and $\dot{\omega}_\alpha$ are the molecular weight and molar production rate of species α.

It is noted that enthalpy is the energy variable used here. However, other forms of the energy equation can also be used. The enthalpy presented here is the absolute enthalpy, which includes sensible and formation enthalpy of the gas mixture.

The thermodynamic state variables are related by thermal and calorific equations of state. Assuming the gas mixture to be an ideal gas, these equations are specified as

$$p = \rho(R_u/W)T, \qquad h = \sum_{\alpha=1}^{N_s} Y_\alpha \Big(h_{f,\alpha}^0 + \int_{T_0}^{T} c_{p\alpha}(T')dT' \Big). \tag{3.2}$$

For a pressure-based solver, the mixture density and temperature are computed from the ideal-gas law and calorific equation of state, respectively. Here $h^0_{f,\alpha}$ and $c_{p\alpha}$ denote the formation enthalpy and specific heat at constant pressure for species α, and R_u is the universal gas-constant. An elementary chemical reaction mechanism involving L reactions and N_s species is represented as

$$\sum_{\alpha=1}^{N_s} \nu'_{l\alpha} M_\alpha \rightleftharpoons \sum_{\alpha=1}^{N_s} \nu''_{l\alpha} M_\alpha, l = 1, 2, ..., L. \tag{3.3}$$

Here $\nu'_{l\alpha}$ and $\nu''_{l\alpha}$ denote stoichiometric coefficients and M_α is a chemical species symbol. The molar production rate of species α then is given as,

$$\dot{\omega}_\alpha = \sum_{l=1}^{L} \Big((\nu''_{l\alpha} - \nu'_{l\alpha}) \Big[k_{l,f}(T) \prod_{\beta=1}^{N_s} c_\beta^{\nu'_{l\beta}} - k_{l,r}(T) \prod_{\beta=1}^{N_s} c_\beta^{\nu''_{l\beta}} \Big] \Big). \tag{3.4}$$

Here c_β is the molar concentration of species β, and $k_{l,f}$ and $k_{l,r}$ are the forward and backward reaction rates, which usually are specified using the modified Arrhenius expression:

$$k_{l,f}(T) = A_{l,f} T^b exp\Big(- E_{Al,f}/(R_u T) \Big), \tag{3.5}$$

where $A_{l,f}$ is the pre-exponential factor, b is the temperature exponent, and $E_{Al,f}$ is the activation energy for the forward reaction rate of reaction l. The reverse rate is related to the forward rate through an equilibrium constant.

3.2 Turbulent Flow Equations

The instantaneous flow equations given in the previous section are averaged over multiple realizations to provide transport equations for mean flow variables that include velocity, pressure, enthalpy, and species mass fractions. A combination of density-based averaging and conventional averaging is introduced for the variables of interest. The conventional average of a random variable $Q = Q(\underline{x}, t)$ is defined

as,

$$\langle Q \rangle = \langle Q(\underline{x}, t) \rangle = \int_{-\infty}^{+\infty} Q(\underline{\psi}) f_Q(\underline{\psi}; \underline{x}, t) d\underline{\psi}, \tag{3.6}$$

where the probability density function (PDF) of Q is denoted by $f_Q(\underline{\psi}; \underline{x}, t)$. The density-based average (Favre average) of Q is defined as,

$$\tilde{Q} = \tilde{Q}(\underline{x}, t) = \frac{1}{\langle \rho \rangle} \int_{-\infty}^{+\infty} \rho(\underline{\psi}) Q(\underline{\psi}) f_Q(\underline{\psi}; \underline{x}, t) d\underline{\psi}. \tag{3.7}$$

A random variable can, in general, be expressed as the sum of an average component and a fluctuation component with respect to the average:

$$Q = \langle Q \rangle + Q', \tag{3.8}$$

or,

$$Q = \tilde{Q} + Q''. \tag{3.9}$$

By using these decompositions, the instantaneous equations (Eq. 3.1) can be recast by replacing the instantaneous variables with average and fluctuating terms, and averaging the resulting equations to develop transport equations for the mean flow variables (Eq. 3.10). This set of equations is is the basis for Reynolds-averaged simulation (RAS):

$$\begin{aligned}
\frac{\partial \langle \rho \rangle}{\partial t} + \frac{\partial \langle \rho \rangle \tilde{u}_i}{\partial x_i} &= 0, \\
\frac{\partial \langle \rho \rangle \tilde{u}_i}{\partial t} + \frac{\partial \langle \rho \rangle \tilde{u}_i \tilde{u}_j}{\partial x_j} &= -\frac{\partial \langle p \rangle}{\partial x_i} + \langle \rho \rangle g_i + \frac{\partial \left(\langle \tau_{ij} \rangle + \tau_{Tij} \right)}{\partial x_j}, \\
\frac{\partial \langle \rho \rangle \tilde{Y}_\alpha}{\partial t} + \frac{\partial \langle \rho \rangle \tilde{u}_j \tilde{Y}_\alpha}{\partial x_j} &= -\frac{\partial \left(\langle J_i^\alpha \rangle + J_{Ti}^\alpha \right)}{\partial x_i} + \langle \rho \rangle \tilde{S}_\alpha, \\
\frac{\partial \langle \rho \rangle \tilde{h}}{\partial t} + \frac{\partial \langle \rho \rangle \tilde{u}_j \tilde{h}}{\partial x_j} &= -\frac{\partial \left(\langle J_i^h \rangle + \langle J_{Ti}^h \rangle \right)}{\partial x_i} + \frac{D \langle p \rangle}{Dt} + \Phi - \langle Q_{rad} \rangle.
\end{aligned} \tag{3.10}$$

Here Φ is the viscous dissipation rate of kinetic energy to heat and is given by $\Phi = \langle \tau_{ij} \frac{\partial \tilde{u}_j}{\partial x_i} \rangle$, τ_{Tij} is the turbulent stress tensor, and $\underline{J}_T^{\alpha}$ and $\underline{J}_T^{h}$ are the turbulent fluxes of species and enthalpy, respectively. For a pressure-based CFD solver, a transport equation for mean pressure field is solved:

$$\frac{\partial^2 \langle p \rangle}{\partial x_j \partial x_j} = \frac{\partial^2 \langle \rho \rangle}{\partial t^2} - \frac{\partial^2 \langle \rho \rangle \tilde{u}_i \tilde{u}_j}{\partial x_i \partial x_j} + \frac{\partial^2 \big(\langle \tau_{ij} \rangle + \langle \tau_{Tij} \rangle \big)}{\partial x_i \partial x_j} + g_j \frac{\partial \langle \rho \rangle}{\partial x_j}. \quad (3.11)$$

It is worth mentioning that the turbulent stress tensor, and turbulent fluxes of species and enthalpy terms appear in unclosed form in the mean flow equations. This is the well known "closure problem" of turbulence for RAS. To solve the equations for mean flow variables, closure models are needed for the turbulent transport terms. The most common form of closure model that has been used for the turbulent transport is the eddy viscosity/gradient transport model, which expresses the turbulent transport of scalars as the product of the gradient of the mean quantity multiplied with an isotropic turbulent viscosity:

$$\tau_{Tij} = -\langle \rho \rangle \widetilde{u_i'' u_j''} = \mu_T \left(\frac{\partial \tilde{u}_j}{\partial x_i} + \frac{\partial \tilde{u}_i}{\partial x_j} \right) - \frac{2}{3} \langle \rho \rangle \, k \delta_{ij} - \frac{2}{3} \mu_T \frac{\partial \tilde{u}_m}{\partial x_m} \delta_{ij}, \quad (3.12)$$

$$J_{Ti}^{h} = \frac{\mu_T}{Pr_T} \frac{\partial \tilde{h}}{\partial x_i}, \quad (3.13)$$

$$J_{Ti}^{\alpha} = \frac{\mu_T}{Sc_{T\alpha}} \frac{\partial \tilde{Y}_{\alpha}}{\partial x_i}. \quad (3.14)$$

The mean molecular stress tensor is given as,

$$\langle \tau_{ij} \rangle = \mu \left(\frac{\partial \tilde{u}_j}{\partial x_i} + \frac{\partial \tilde{u}_j}{\partial x_i} \right) - \frac{2}{3} \mu \frac{\partial \tilde{u}_m}{\partial x_m} \delta_{ij}, \quad (3.15)$$

and is often neglected compared to the turbulent stress for a high-Reynolds-number turbulent flow away from a wall.

Here μ is the molecular viscosity, μ_T is the turbulent viscosity, k is the turbulent kinetic energy, and Pr_T and $Sc_{T\alpha}$ are the turbulent Prandtl and Schmidt numbers, respectively. The closure model for the RAS equations then reduces to modeling of the turbulent viscosity (μ_T) and turbulent kinetic energy (k). The models for these two turbulent quantities are discussed in the next section.

The mean density is given by the ideal-gas equation-of-state:

$$\langle \rho \rangle = \frac{\langle p \rangle}{R_u \langle \frac{W}{T} \rangle}. \tag{3.16}$$

Here the influence of pressure fluctuations on the mean density has been ignored, which is appropriate at low Mach number.

Here the averaging of instantaneous variables has been interpreted as ensemble averaging. Depending on the application of interest, other forms of averaging may be appropriate. For example, in statistically stationary flows, time-averaging would be appropriate. This approach is particularly useful when the flow is statistically stationary after a brief transient period, and the modeling goal is to capture the statistically stationary flow characteristics, without any need to resolve the transient characteristics. However, for flows that demand accurate capturing of transient characteristics, time-averaging may be unsuitable. For IC-engines, for example, key flow characteristics evolve over an engine cycle and are repeated over multiple cycles. Therefore, phase-averaging is more appropriate. The averaged equations presented here are generic in nature, and apply to both statistically stationary and transient flows.

3.3 The k-ϵ Turbulence Model

A standard two-equation $k-\epsilon$ turbulence model [144, 145] is used for turbulence closure. In this model, modeled transport equations are solved for turbulent kinetic energy (k) and for the viscous dissipation rate of turbulent kinetic energy (ϵ). The derivation of the equations is provided in [144]:

$$\begin{aligned}
\frac{\partial \langle \rho \rangle k}{\partial t} + \frac{\partial \langle \rho \rangle \tilde{u}_i k}{\partial x_i} &= \frac{\partial}{\partial x_j}\left(\left[\mu + \frac{\mu_T}{\sigma_k}\right]\frac{\partial k}{\partial x_j}\right) + \tau_{Tij}\frac{\partial \tilde{u}_j}{\partial x_i} - \langle \rho \rangle \epsilon, \\
\frac{\partial \langle \rho \rangle \epsilon}{\partial t} + \frac{\partial \langle \rho \rangle \tilde{u}_i \epsilon}{\partial x_i} &= \frac{\partial}{\partial x_j}\left(\left[\mu + \frac{\mu_T}{\sigma_\epsilon}\right]\frac{\partial \epsilon}{\partial x_j}\right) + C_{\epsilon 1}\frac{\epsilon}{k}\tau_{Tij}\frac{\partial \tilde{u}_j}{\partial x_i} \\
&\quad - C_{\epsilon 2}\langle \rho \rangle \frac{\epsilon^2}{k} + C_{\epsilon 3}\langle \rho \rangle \epsilon \frac{\partial \tilde{u}_j}{\partial x_j}.
\end{aligned} \tag{3.17}$$

The ϵ equation has three model constants that are connected to turbulent

production, dissipation and compressibility, respectively. The standard model constant values are $C_{\epsilon 1}$=1.44, $C_{\epsilon 2}$=1.92, $C_{\epsilon 3}$=1.44, σ_k=0.9, and σ_ϵ=1.219. The turbulent viscosity is computed as,

$$\mu_T = C_\mu \langle \rho \rangle k^2/\epsilon, \tag{3.18}$$

where C_μ is a model constant, whose standard value is C_μ=0.09.

The $k-\epsilon$ model has shown reasonable prediction for simple flows. For round jet flows, the model coefficients for the ϵ equation may need to be tuned to predict the correct jet spread rate. However, for flow with strong pressure gradients and/or curvature, the predictions from this model become unreliable. The current work is for a relatively simple geometric configuration with a weak pressure gradient. Therefore, within the current turbulence modeling framework, the standard $k-\epsilon$ model is suitable.

For a wall-bounded flow, to account for the effects of the turbulent boundary layer, a standard wall-function approach [144] is used in the near-wall region. The region very close to the wall is characterized by steep normal gradients that span a small wall-normal distance. The wall-function method has proven to be a computationally efficient method that eliminates the need to resolve this region with extremely refined computational cells. The mean velocity in this region is given as,

$$\frac{U}{u_\tau} = \frac{1}{\kappa} \ln y^+ + B, \tag{3.19}$$

where $y^+ = u_\tau y/\nu$, $u_\tau^2 = C_\mu^{1/2} k$ and $\epsilon = u_\tau^3/(\kappa y)$. Here y is the wall-normal distance, u_τ is the friction velocity, y^+ is the non-dimensional distance from the wall and U is the mean velocity component parallel to the wall. κ and B are the log-law constants, given as κ=0.41 and B=5.41.

The simplicity and computational economy of the wall-function model make it useful for many engineering applications. However, for certain flow conditions (e.g., strong pressure gradient, or recirculating flow), the wall-function approach produces poor accuracy in predicting the mean flow quantities. In the current work,

the bulk of the turbulent flow occurs far away from the wall. Near the wall, the flow velocity and pressure gradient are low, resulting in a weak turbulent structure. Therefore, within the current turbulence modeling framework, the standard wall-function approach is suitable.

3.4 Probability Density Function (PDF) Method

Equations (3.10) - (3.17) provide a complete set of transport equations that can be solved for a gas-phase chemically reacting system. This set of equations can, in principle, be solved using a finite-volume (FV) method. In this method, the flow region is divided into a large finite number of cells and the equations are discretized spatially and temporally to a finite-number of algebraic equations that are solved for the quantities of interest at the centers of the cells. A principal drawback of this method is that the mean chemical source term in the species equation remains unclosed, and needs to be modeled. This term involves a coupling between flow and flame structures, and therefore generalization of this term to complex flow and multi-regime turbulent combustion has been a major issue. Different modeling approaches have been suggested over the decades to provide a closure model for this term. Among these, the transported PDF method has proven to be the most robust approach available to date. The strength of the PDF method is that the chemical source term appears in a closed form, and therefore this method eliminates the need for direct modeling of the mean chemical source term.

Multiple versions of transported PDF methods have been developed for turbulent combustion, including composition PDF, velocity-composition joint PDF, and velocity-composition-frequency PDF [28] methods. The composition PDF is, perhaps, the most tractable and computationally efficient approach, while the most comprehensive model is the velocity-composition-frequency joint PDF. The latter eliminates the need for modeling of transport by turbulent velocity fluctuations, and completes the turbulence modeling with an equation for turbulent frequency. The velocity-composition joint PDF, like the velocity-composition-frequency joint PDF, provides closure for turbulent transport; however, a modeled ϵ equation is required to prescribe the turbulent time scales. The composition PDF method requires models for turbulent transport terms; the probability density function

is defined on the composition space (species mass fraction and mixture specific enthalpy), and therefore requires a $k-\epsilon$ model (or other turbulence model) to describe the turbulence scales. All three transported PDF methods provide complete closure of the chemical source terms, and need a model to account for molecular mixing. However, the number of computational particles needed to represent the flow system adequately increases significantly from the composition PDF method to the velocity-composition-frequency PDF method for the same statistical accuracy. The composition PDF method provides a reasonable tradeoff that retains the key benefits of the PDF methods.

The present work is based on the transported composition PDF method. In this method, a transport equation is solved for the one-point, one-time composition PDF. The derivation of this equation is provided in [28]. The equation is given as,

$$\frac{\partial \rho f_\phi}{\partial t} + \frac{\partial \rho f_\phi \tilde{u}_j}{\partial x_j} + \frac{\partial \rho f_\phi S_\alpha}{\partial \psi_\alpha} = -\frac{\partial}{\partial x_i}\left[\langle u_i'' | \underline{\psi}\rangle \rho f_\phi\right] + \frac{\partial}{\partial \psi_\alpha}\left[\left\langle \frac{\partial J_j^\alpha}{\partial x_j} | \underline{\psi} \right\rangle f_\phi\right] \quad (3.20)$$

The first term on the left-hand side is the time rate of change of the composition PDF with time, and the second term describes transport in the physical space by the mean velocity. The third term represents the transport of the composition PDF by reaction in composition space. All the terms that are on the left-hand side of the above equation are in closed form. The terms on the right-hand side need to be modeled. The first term on the right-hand side is the transport of the composition PDF by turbulent fluctuations in physical space, and the last term represents transport of composition PDF in the composition space by the molecular fluxes. The turbulent transport term is modeled using a gradient diffusion hypothesis, while the molecular flux is modeled using a mixing model. In the gradient transport model,

$$-\frac{\partial}{\partial x_i}\left[\langle u_i'' | \underline{\psi}\rangle \rho f_\phi\right] = \frac{\partial}{\partial x_i}\left[\Gamma_T \frac{\partial}{\partial x_i}\left(\frac{\rho f_\phi}{\langle \rho \rangle}\right)\right]. \quad (3.21)$$

The simplest mixing model is interaction-by-exchange-with-mean (IEM), where:

$$\left\langle \frac{\partial J_j^\alpha}{\partial x_j} | \underline{\psi} \right\rangle f_\phi = \frac{1}{2}\rho(\underline{\psi}) C_\phi \omega \left(\phi_\alpha - \tilde{\phi}_\alpha\right). \quad (3.22)$$

Here $\omega = \epsilon/k$, $\Gamma_T = \mu_T/\sigma_\phi$, C_ϕ is a model constant, and σ_ϕ is constant for all the species. For a flow where the density changes significantly, it is appropriate to use Favre averaging (density-weighted averaging). The Favre-averaged PDF is defined as $\rho f_\phi = \langle\rho\rangle \tilde{f}_\phi$. The conventional and Favre averages of $Q(\underline{\psi})$, defined in terms of the conventional- and Favre-averaged PDF, respectively, are given as,

$$\langle Q \rangle = \int_{-\infty}^{+\infty} Q(\underline{\psi}) f_\phi(\underline{\psi}; x, t) d\underline{\psi}, \tag{3.23}$$

$$\tilde{Q} = \int_{-\infty}^{+\infty} Q(\underline{\psi}) \tilde{f}_\phi(\underline{\psi}; x, t) d\underline{\psi}. \tag{3.24}$$

The modeled PDF transport equation is a N-dimensional (3-space + 1-time + N_s-species + 1-enthalpy) equation, and therefore cannot be solved using traditional finite-volume or finite-difference numerical methods. Monte-Carlo approaches are useful for this application. There the flow is represented by a large number of stochastic particles whose evolution follows the same one-point one-time Eulerian PDF transport equation as the real fluid system (Eq. 3.20). The evolution of the stochastic particles is governed by stochastic equations. The principal idea is that if the fluid particles and stochastic particles evolve by the same PDF transport equation, and the initial and boundary conditions for the stochastic particles are the same as those for the fluid particles, then the statistical averages computed from the stochastic particles are the same as those computed from fluid particles. This is the foundation for the current PDF model. The stochastic evolution equations for a particle at position $\underline{x}^*$ and composition $\underline{\phi}^*$ are given as,

$$\begin{aligned} d\underline{x}^*(t) &= \left[\tilde{\underline{u}} + \frac{\nabla \Gamma_T}{\langle\rho\rangle}\right]_{\underline{x}^*(t)} dt + \left[\frac{2\Gamma_T dt}{\langle\rho\rangle}\right]^{1/2}_{\underline{x}^*(t)} \underline{\eta}, \\ d\phi^*_\alpha(t) &= S_\alpha(\underline{\phi}) dt - \frac{1}{2} C_\phi \omega \left(\phi^*_\alpha - \tilde{\phi}_\alpha\right) dt, \alpha = 1, 2, ..., N_\phi. \end{aligned} \tag{3.25}$$

Here N_ϕ is the number of composition variables ($N_\phi = N_s + 1$), $\underline{\eta}$ is a vector of three independent standardized Gaussian random vectors, and C_ϕ is a model constant. The first term on the right-hand side of the equation for particle location represents the change in the particle location due to the mean flow velocity, and the last two terms represent changes in the particle location due to advection by

turbulent velocity fluctuations ("turbulent-diffusion") corresponding to a gradient transport model. The first term on the right-hand side of the particle composition equation gives the change in the particle composition due to reaction, and the final term represents the mixing of particles in the composition space corresponding to the IEM [146, 108] mixing model. For the enthalpy equation, there is no chemical source term, as the total enthalpy (sensible plus formation enthalpy) is considered here. For constant-volume combustion, an additional $D\langle p\rangle/Dt$ term is included to account for the enthalpy change due to pressure rise. For open flames, this term may be neglected.

The weakest link of the PDF method is, perhaps, the modeling of the scalar mixing term [33]. The mixing of scalars and enthalpy controls the rate at which particles at the molecular level exchange their compositions locally. Fast mixing of particles creates a local homogeneity of compositions at the cell level. In the limit, this is equivalent to a well-stirred reactor model, which corresponds to computing the chemistry using the mean composition and enthalpy, and thereby ignoring turbulent fluctuations in composition and enthalpy. Over the years, many mixing models have been developed within the framework of Lagrangian-based particle methods. These models need to meet certain constraints to ensure the realizability of the predictions. Three basic constraints have been identified, and every mixing model needs to satisfy these conditions to ensure physical consistency of the predictions [147, 148, 107]. These conditions are: 1. The mean scalar should remain unchanged after the mixing; 2. The scalar variance evolves consistent with experimental observations for constant-density homogeneous flow; and 3. The scalar quantities should remain bounded.

The interaction-by-exchange-with-mean (IEM) [146, 108], also known as the linear-mean-square estimation (LMSE) model is, perhaps, the simplest of all mixing models. IEM is a deterministic model, in which the particle compositions relax to the local mean values at a rate determined by the local turbulent time scale ($\tau = 1/\omega$). This model is continuous in time, and produces the same mixing rate for all the scalars, since the model does not recognize differential diffusion of species and energy. Although this model meets the basic constraints of a mixing model, it does not retain the notion of locality in composition space [149]. Moreover, IEM retains the shape of the distribution. The particle distribution, initialized from an

arbitrary distribution, does not relax to a Gaussian distribution in homogeneous isotropic turbulence, as is observed in a physical system. Another widely used mixing model is the coalescence-dispersion (CD) model [150], which is an example of a stochastic mixing model. The CD model works on the principle of mixing between two particles selected at random with a probability that is proportional to the ratio of the computational time step to the local turbulent time scale. The scalar values of the two particles after mixing are equal to the weighted average of the two particle values prior to mixing. This model preserves the mean of the distribution and predicts the correct decay rate for the scalar variance. However, the CD model is not continuous in time. The IEM and CD mixing models have been modified, over the years, to address their limitations. This has lead to the development of the modified Curl (MC) model, and the interaction by exchange with the conditional mean (IECM) model [151, 152], among others. Overall, these mixing models have shown reasonable success in low-to-intermediate Damköhler number flames. One major deficiency of the IEM and CD models is their inability to capture effects that require locality in composition space. This has been highlighted by Pope [149, 107] for high-Damköhler-number flames, where a narrow flame separates the burnt and unburnt regions. For these flames, IEM and CD models may produce mixing between burnt and unburnt particles, which may result in unphysical behavior. This issue has been addressed by the Euclidean-minimum-spanning-tree (EMST) model [107], which produces preferential mixing between particles based on their proximity in composition space, and therefore retains the property of locality. The EMST model also satisfies the basic constraints of mixing model, and is generally considered to be one of the best currently available mixing models for PDF methods.

3.5 Hybrid Lagrangian-Particle-Eulerian-Mesh (LPEM) Method

Solving the composition PDF equation, or equivalently, the stochastic particle equations, requires mean velocities and turbulent time scales at the particle locations, and therefore the composition PDF does not by itself provide a complete

description of the turbulent combustion system. The mean velocities and turbulent scales are fed to the particle-PDF side by solving the RAS system of equations for mean-pressure, velocity and turbulence. This solution strategy is known as a hybrid particle/finite-volume PDF method [33, 153, 154, 13], where Lagrangian-based evolution equations of stochastic particles in the composition space are solved simultaneously with finite-volume-based RAS computations for the mean velocity field and turbulence quantities. The mean density provides the main feedback from the particle system to the FV system. The mean density is estimated from Eqn. (3.16) where the denominator is evaluated as the average over the particles in a cell. The coupling of a particle PDF method with a finite-volume-based RAS through the mean density has shown promising results for quasi-steady problems where the flame attains a statistically stationary configuration. In a stationary system, time-blending can be used to ensure that the change in mean density over a time step is small enough to avoid significant oscillations in the finite-volume calculation. For a flame that is not steady in time, this method cannot be used. Without time blending, statistical noise arising from the particle-based computation of $\langle \frac{W}{T} \rangle$ can induce undesirable oscillations in the CFD code. An alternative approach was suggested by Moradoglu [154], where a transport equation is solved on the finite-volume side for "equivalent enthalpy" using particle-derived source terms for mixing and reaction. The equivalent enthalpy is defined by Eqn. (3.26). The mean density then is evaluated from the mean equivalent enthalpy using Eqn. (3.27):

$$h_s = \frac{\gamma}{\gamma - 1} \frac{p}{\rho} = \frac{\gamma}{\gamma - 1} \frac{R_u T}{W}, \tag{3.26}$$

$$\langle \rho \rangle \;\; = \;\; \frac{\gamma}{\gamma - 1} \frac{\langle p \rangle}{\widetilde{h_s}}, \tag{3.27}$$

where γ is the ratio of the specific heat at constant pressure to the specific heat at constant volume of an ideal diatomic gas (γ=1.4). It is noted here that a constant value of γ does not imply any restriction of constant properties to this formulation.

The transport equation for mean equivalent enthalpy [154] is given as:

$$\frac{\partial \langle\rho\rangle \tilde{h}_s}{\partial t} + \frac{\partial \langle\rho\rangle \tilde{u}_j \tilde{h}_s}{\partial x_j} = \langle\rho\rangle \tilde{\dot{q}} - \frac{\partial \langle\rho\rangle \widetilde{h_s'' u_j''}}{\partial x_j}. \tag{3.28}$$

It is noted that equivalent enthalpy is not same as enthalpy, and it should not be seen as an energy variable. The mean equivalent enthalpy can, in principle, be evaluated from mean pressure and composition variables, and is interpreted as a scalar that is used to provide a consistent numerical algorithm to compute cell-mean density. The transport equation of mean equivalent enthalpy (Eqn. 3.28) includes the time-rate of change of mean equivalent enthalpy (first term on the left-hand side), transport by the mean flow (second term on the left-hand side), a mean source term due to chemical reaction (first term on the right-hand side), and transport by turbulent fluctuations (second term on the right-hand side). The left-hand-side of the equations appears in closed form, and the turbulent transport is modeled using the gradient-transport hypothesis. However, the mean source term due to reaction remains to be modeled. Modeling of this term is difficult on the FV-side. However, this term appears in closed form on the particle side. Therefore, the source term due to reaction is computed at the particle level using a corresponding stochastic particle equation for equivalent enthalpy of stochastic particles, and the mean source term is passed to the FV-side. Using this hybrid interface, the solution algorithm for mean equivalent enthalpy retains the key benefit of PDF modeling (closure of the mean chemical source term).

For any quantity Q which is a function of the composition variable $\underline{\psi}$, the Favre average of Q is estimated from particle values as,

$$\tilde{Q} = \frac{\sum_{p=1}^{n_p} m_p Q_p(\underline{\psi})}{\sum_{p=1}^{n_p} m_p}. \tag{3.29}$$

Here n_p is the number of particles in a FV cell, and m_p is the mass of a particle.

3.6 Gas-Phase Chemistry

The reliability of the model predictions depends on the accuracy of the physical models. One of the key physical models of interest here is the chemistry modeling.

A typical combustion process is characterized by a large number of chemical species that may include stable compounds, ions, radials and intermediate species. Accurate capturing of a combustion process, therefore, requires a detailed chemistry model that includes all the important reactions and species. However, such a chemical mechanism may be prohibitive for CFD-based modeling because it requires enormous computational resources that can not be achieved even with current state-of-the-art computational facilities. Therefore, a reasonable-sized chemical mechanism is essential for providing the much-needed balance between computational accuracy and efficiency. Reasonable-size "CFD-friendly" mechanisms are derived as a subset of larger detailed mechanism using optimization methods that essentially capture the key reaction and species needed to provide realistic CFD predictions within a reasonable computational time over a prescribed set of conditions. Constructing mechanisms that reproduce realistic chemical behavior over a wide range of operating conditions has proven to be a challenge. The important reaction pathways often change significantly with temperature, pressure, equivalence ratio and other physical parameters. For example, in a typical diesel engine that operates at high temperatures, the NOx chemistry is dominated by thermal NO; however, for lean low-temperature HCCI combustion, low-temperature NOx pathways may become more important than thermal NO [155, 48, 156, 157]. Also, at low temperatures, negative temperature coefficient (NTC) effects which are not observed at high-temperature conditions are needed to describe autoignition [53, 54]. The reactions and species that drive the heat release and key pollutants, such as CO or NOx, at high temperatures behave differently at low temperatures. Therefore capturing the representative chemical processes with limited number of species and reactions over a wide range of operating conditions has proven to be a challenging undertaking.

In this work, three skeletal mechanisms are considered for n-heptane. The simplest one is a 29-species, 52-reaction skeletal mechanism [94] that has been used widely by different research groups for diesel-engine-like conditions. N-heptane is a single-component surrogate for diesel fuel, and this mechanism is intended to be representative of diesel combustion to study the transient combustion characteristics. Being small in size, this skeletal chemistry is suitable for CFD simulations. However, this reaction mechanism does not include any acetylene and nitrogen-

containing compounds that are the key species for soot and NOx modeling. Therefore, the use of this chemistry model is limited to quantitative comparison of global transient combustion characteristics that include flame lift-off length, ignition delay and rate of pressure rise. Next is a 34-species, 74-reaction skeletal mechanism [94] that is an extension of the 29-species mechanism and includes acetylene and key nitrogen compounds to account for the soot and NOx chemistry, respectively. In the absence of any NOx measurements for the configurations of interest here, no NOx chemistry is considered in the third skeletal mechanism; this is a 40-species, 165-reaction mechanism [2]. The details of the mechanisms are provided in Appendix A. This work also includes simulations of n-dodecane spray flames. n-Dodecane is another single-component surrogate for diesel that provides a more realistic reproduction of physical and chemical properties of diesel fuel compared to n-heptane. The chemical mechanism for n-dodecane is a 103-species, 370-reaction skeletal kinetics mechanism [3] (Appendix B).

The literature is rich with many n-heptane mechanisms with sizes ranging from 20 species to over 1000 species. The smaller mechanisms are typically derived from a detailed mechanism to represent the chemical processes over a limited range of operating conditions that are specific to the applications of interest. However, only a few n-dodecane mechanisms are available in literature; most of them have large numbers of species and reactions that are too high for use in multidimensional CFD. The 103-species, 370-reaction mechanism [3] adopted here is one of the few relatively "CFD-friendly" mechanisms available for diesel-like conditions to date.

3.7 Soot Models

In non-premixed combustion, soot formation is a common phenomenon. For typical diesel engines, soot formation has been observed to occur within a temperature range of 1300 to 1700 K under locally fuel-rich conditions. The complexity of the soot formation process makes soot prediction extremely difficult. Simplistic models for soot prediction are based on empirical rate coefficients that are functions of key gas-phase species concentrations. The simplicity of this modeling approach makes it suitable for CFD computations. More advanced physics-based models have also been attempted, which aim to maintain the computational efficiency of the simpler

models.

An example of a simple soot model is a semi-empirical two-equation soot model. There are multiple versions of two-equation soot models in the literature. The one that has been adopted here is the model by Lindstedt *et al.* [60]. This is a simplistic soot model, yet it captures the essential physical processes that lead to soot formation and oxidation in non-premixed combustion. The soot modeling is characterized by two soot variables: soot number density, and soot mass fraction. The volume fraction of soot then is estimated from the soot mass fraction. The overall soot formation in this model is split into a three-step, four-reaction process. The three steps are nucleation, coagulation and surface reaction. The soot formation begins with the nucleation process that initiates the growth of soot particles from acetylene, which is taken to be the soot precursor. The coagulation process causes the soot particles to coalesce into larger particles; this reduces the soot number density, and leaves the soot mass fraction unchanged. The final step is the surface reaction, which accounts for an increase in soot mass fraction due to surface growth by adsorption of acetylene, and depletion of soot mass-fraction by oxidation at the surface of the soot particles. The four reactions are summarized below:

$$C_2H_2 = 2C(s) + H_2, \tag{3.30}$$

$$C_2H_2 + nC(s) = (n+2)C(s) + H_2, \tag{3.31}$$

$$C(s) + 1/2O_2 = CO, \tag{3.32}$$

$$nC(s) = C_n(s). \tag{3.33}$$

The reaction rates for soot are summarized below.

- Nucleation rate:

$$R_1 = k_1(T)[C_2H_2] \qquad [\text{kmol/m}^3\text{/s}], \tag{3.34}$$

where $k_1(T)$ is the reaction rate coefficient given as:

$$k_1(T) = 0.1 \times 10^5 exp[-21000/T] \qquad [1/\text{s}]. \tag{3.35}$$

Here $[C_2H_2]$ is the acetylene concentration.

- Soot surface growth by adsorption of C_2H_2 is given as:

$$R_2 = k_2(T)[C_2H_2]\sqrt{\pi\left(\frac{6M_{C_s}}{\pi\rho_{C_s}}\right)^{2/3}\left[\frac{\rho Y_{C_s}}{M_{C_s}}\right]^{1/3}[\rho N]^{1/6}} \qquad [\text{kmol/m}^3/\text{s}], \quad (3.36)$$

where the reaction rate coefficient $k_2(T)$ is given as:

$$k_2(T) = 0.6 \times 10^4 exp[-12100/T] \qquad [\text{m}^{3/2}/\text{m(soot)/s}]. \quad (3.37)$$

Here ρ_{C_s}, Y_{C_s}, M_{C_s}, N are the density, mass fraction, molar weight of a C-atom, and soot number density [particles/kg-mixture], respectively. ρ is the density of gas-mixture [kg/m^3].

- Surface oxidation of soot is given by:

$$R_3 = k_3(T)S[O_2] \qquad [\text{kmol/m}^3/\text{s}], \quad (3.38)$$

where $k_3(T)$ is the reaction rate coefficient given as:

$$k_3(T) = 0.1 \times 10^5 T^{1/2} exp[-19680/T] \qquad [\text{m}^3/\text{m}^2\text{(soot)/s}]. \quad (3.39)$$

Here S is the surface area of soot per volume of mixture [m^2/m^3], and is given as: $S = \pi d_p^2 \rho N$, where the particle diameter d_p is calculated as:

$$d_p = \left(\frac{6Y_{C_s}}{\pi\rho_{C_s}N}\right)^{1/3}. \quad (3.40)$$

- The rate of soot formation due to coagulation is given as:

$$R_4 = -2C_a d_p^{1/2}\left(\frac{6\kappa T}{\rho_{C_s}}\right)^{1/2}(\rho N)^2 \qquad [\text{kmol/m}^3/\text{s}], \quad (3.41)$$

where C_a is an coagulation rate constant (C_a=9.0), and κ is the Boltzman constant (κ=1.38x10^{-23} J/K)

The total source term for soot number density is given as:

$$S_N = 2\frac{R_1}{C_{min}}N_A + R_4, \tag{3.42}$$

where N_A is Avagadro's number [particles/kmol], and C_{min} is a model constant for Nucleation (C_{min}=100). The source term for soot mass fraction is given as:

$$S_y = (2R_1 + R_2 - R_3)M_{C_s}, \tag{3.43}$$

This two-equation model considers acetylene as the only pathway for soot formation. However, experimental evidence suggests that there are multiple paths to soot formation, and that soot from polycyclic aromatic hydrocarbons (PAHs) is especially important.

An example of a more detailed and comprehensive soot model that has been proved to be promising is one based on a method of moments with interpolative closure (MOMIC) [158] for soot aerosol dynamics. This model is based on a more rigorous mathematical and physical formulation that aims to capture the key physical processes, and includes soot aerosol dynamics based on the "Smoluchowski Master Equation" (Eqn. 3.44) for Brownian coagulation. The equation of evolution of the particle moments is presented by:

$$\begin{aligned} \frac{dN_1}{dt} &= -\sum_{j=1}^{\infty}\beta_{1,j}N_1N_j, \\ \frac{dN_i}{dt} &= \frac{1}{2}\sum_{j=1}^{i-1}\beta_{j,i-j}N_jN_{i-j} - \sum_{j=1}^{\infty}\beta_{i,j}N_iN_j. \end{aligned} \tag{3.44}$$

Here N_i denotes the particle number density of particles of size i, with N_1 being the number density of the smallest particles, and $\beta_{i,j}$ is the collision coefficient between particles of size i and j. In general, $\beta_{i,j} = \beta_{i,j}(N_i, N_j, m_i, m_j)$, where m_i is the mass of particle of size i. The concentration moment of particle number

density function is given as,

$$M_r = \sum_{j=1}^{\infty} m_i^r N_i. \tag{3.45}$$

The zero-th moment M_0 is proportional to soot number density, and the first moment M_1 is the total mass of the soot particles per unit volume. The soot volume fraction f_v is directly related to the first moment as $f_v = M_1/\rho_{C_s}$, where ρ_{C_s} is the soot density. The higher moments lack simple physical interpretations. For practical purposes, the first few moments characterize most of the quantities of interest. Multiplying the Smoluchowski equation with m_i^r and summing over all size classes, the moment equations for coagulation are given as:

$$\begin{aligned}
\frac{dM_0}{dt} &= -\sum_{j=1}^{\infty} \beta_{1,j} N_1 N_j, \\
\frac{dM_1}{dt} &= 0, \\
\frac{dM_2}{dt} &= -\sum_{i=1}^{\infty}\sum_{j=1}^{\infty} ij\beta_{i,j} N_i N_j, \\
\frac{dM_3}{dt} &= 3\sum_{i=1}^{\infty}\sum_{j=1}^{\infty} ij^2\beta_{i,j} N_i N_j, \\
&\ldots
\end{aligned} \tag{3.46}$$

(3.47)

Generalizing the moment equations by addition nucleation and surface reaction, the equation for the r-th moment can be expressed as:

$$\frac{dM_r}{dt} = R_r + G_r + W_r, \tag{3.48}$$

where R_r, G_r and W_r are nucleation, coagulation and surface reaction terms, respectively, for the r-th moment.

This method provides a system of equations that can, in principle, more completely describe the soot evolution. The number of moments required to describe the soot variables of practical interest within a reasonable computational cost may

vary from one condition to another. In the current computations, six moments are used. The reaction pathway that has been implemented with this method is a hydrogen-abstraction, acetylene-addition (HACA) pathway [158]:

$$
\begin{aligned}
C_s - H + H &\rightleftharpoons C_s^* + H_2, && (3.49)\\
C_s - H + OH &\rightleftharpoons C_s^* + H_2O, && (3.50)\\
C_s^* + H &\longrightarrow C_s - H, && (3.51)\\
C_s^* + C_2H_2 &\longrightarrow C_s - H + H, && (3.52)\\
C_s + C_2H_2 &\longrightarrow C_s^* + H, && (3.53)\\
C_s^* + O_2 &\longrightarrow 2CO + Products, && (3.54)\\
C_s - H + OH &\longrightarrow CO + Products. && (3.55)
\end{aligned}
$$

The nucleation, coagulation and surface reactions are provided in [158]. It should be emphasized here that the soot models are implemeted on the particle side of the LPEM model. The molecular diffusion of soot is neglected, since the density of soot is significantly higher compared to that of gas-phase species.

3.8 Liquid Fuel-Spray Models

Different modeling approaches are available to account for multiphase flow in spray flames. These include Eulerian-Eulerian approaches, Eulerian-Lagrangian approaches and volume of fluid (VOF) methods. In Eulerian-Eulerian and Eulerian-Lagrangian approaches, the gas-phase is modeled using an Eulerian approach. The difference between the two is that, for the former, the dispersed liquid-phase is modeled with an Eulerian approach, whereas for the latter the liquid-phase is modeled with a Lagrangian-based, discrete-phase modeling of droplets. The most commonly used approach for engines currently is the Eulerian-Lagrangian method, which is especially suitable for modeling dilute sprays. However, in the near-injector dense-spray region, this model as usually implemented is not suitable. In the near-injector region, the particle interactions become strong due to collision and coalescence of droplets, which are not completely understood to date.

The Eulerian-Eulerian approach perhaps has the potential to provide a more accurate description of near-injector multiphase flow by treating each size group of droplets as a separate phase and solving conservation equations for each phase. However, this approach requires significantly higher computational resources. For this work, the Eulerian-Lagrangian approach has been applied [159, 160, 161], with a breakup model to account for the dense-spray region. In this method, the liquid phase is represented by a large number of computational parcels, with each parcel representing a group of droplets that have the same properties. The number of computational parcels required for the statistical description of the liquid-phase is significantly smaller than the actual number of droplets. Each parcel carries information about droplet diameters, velocity, mass, temperature and the number of droplets in each parcel. For multi-component fuel sprays, additional information, such as evaporation rate of each component, differential diffusivity, etc., are required [162]. The physical processes that lead to the atomization and breakup of the liquid spray into droplets are modeled for each computational parcel.

3.8.1 Breakup Models

Within the framework of a Lagrangian spray model, the spray processes near the injector are modeled using breakup models, which include primary and secondary breakup processes. The primary breakup occurs very close to the injector, whereas the secondary breakup occurs further downstream of the injector nozzle (Fig. 3.1). The primary breakup region is characterized by a large volume fraction of liquid. As the liquid flows out of the nozzle, the surrounding ambient gas is entrained into

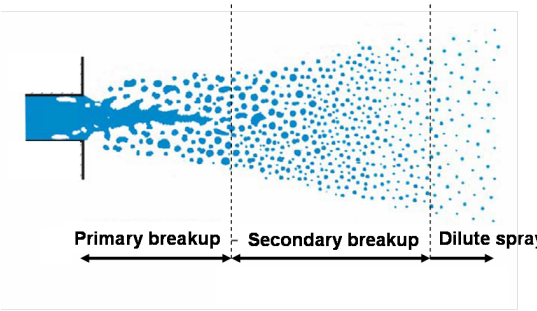

Figure 3.1. Conceptual model for liquid spray injection near the injector (primary and secondary breakup) and further downstream.

the liquid core, forming an air core inside the liquid. In this process, the liquid core is disintegrated by dual liquid-liquid and liquid-gas interactions. The strong aerodynamic effects and nozzle-generated turbulence generate instabilities on the liquid surface, which grow further downstream and result in disintegration of the liquid to ligaments and droplets. The droplets in this region strongly interact with each other through droplet coalescence and collision.

Available modeling approaches in the near-injector region within the framework of a Lagrangian method are: 1. Description of the spray with statistical distributions [163, 164], and 2. Breakup modeling [135, 139, 136]. Of the two methods, the first one is simple to model; a presumed statistical distribution is used for the droplet diameters, velocities, and locations. The distributions, however, are required as input, typically from detailed experimental measurements. This method has been used in a number of modeling studies in the past. More recent modeling studies for diesel engines, driven by the need for more robust spray modeling for consistent and realistic predictions at high pressures, have relied on breakup models to produce a realistic statistical distribution of droplets with limited empirical input.

Different breakup models have been suggested in the literature. One example is a two-stage breakup model suggested by Bianchi and Pelloni [135]. This breakup model begins with the injection of "blobs", where Lagrangian parcels consist of blobs of liquid having diameters the same as the nozzle diameter. The first stage of the breakup process, referred to as primary breakup, is modeled using dual effects of turbulence and aerodynamic instability. The turbulent forces acting on the surface of the liquid column emerging from the nozzle induce a perturbation that grows with characteristic time and length scales defined by the nozzle turbulence. The aerodynamic instability effects are modeled using characteristic time scales estimated from the theory of wave growth. When the disturbance wave-length grows beyond a cut-off value, new droplets are formed. Huh and Gosman [136] used a wave dispersion equation to estimate the aerodynamic time scale, whereas Bianchi and Pelloni [135] used an aerodynamic time scale that had been derived from Kelvin-Helmholtz instability theory. The primary breakup model gives a distribution of droplets starting from liquid blobs.

Once the droplets are formed by the primary breakup processes, the droplets

may further break into smaller droplets due to the aerodynamic interactions that are induced by the relative motion between droplets and air. This process is referred to as secondary breakup. A variety of models has been suggested to model the secondary breakup process. These include the Reitz-Diwakar (RD) model [140], the Taylor-analogy breakup (TAB) model [165], the Pilch and Erdman model [137], and the Hsiang and Faeth model [138]. All these models share reasonable success in reproducing experimental measurements, as long as the model constants are tuned properly.

In the current work, the overall breakup process is modeled using the secondary breakup model only. The breakup model considered here is the Reitz-Diwakar (RD) model. In this model, two modes of breakup are considered: bag breakup, and stripping breakup. Bag breakup occurs when the pressure distribution around the droplet causes the droplet to expand and eventually disintegrate when the aerodynamic effect overcomes the surface tension. Stripping breakup occurs when liquid is sheared off the droplet surface. The two breakup regimes are characterized by the Weber number and Reynolds number of the parent droplet. For the high injection pressures that are characteristic of typical diesel engines, the stripping breakup dominates over the bag breakup. In any secondary breakup model, the size of the newly formed droplets from the parent droplets is given by,

$$\frac{dD_d}{dt} = -\frac{D_d - D_{d,stable}}{\tau_b}, \tag{3.56}$$

where $D_{d,stable}$ is the stable droplet diameter, D_d is the droplet diamter, and τ_b is the breakup time. The specifications of $D_{d,stable}$ and τ_b change from one breakup mode to another. If the droplet diameter is larger than the stable droplet diameter, new droplets are formed from the parent droplets.

For the Reitz-Diwakar breakup model considered for the present work, the criteria for droplet breakup are based on specification of critical Weber numbers for two breakup regimes: bag breakup and stripping breakup.

- For bag breakup,

$$We = \frac{\rho|\underline{u} - \underline{u}_d|^2 D_d}{2\sigma_d} \geq C_{b1}, \tag{3.57}$$

where $\underline{u}$ is the gas-phase velocity, $\underline{u}_d$ is the droplet velocity, σ_d is the surface tension coefficient, and C_{b1} is an empirical model constant (C_{b1}=6.0) [140]. The stable droplet size satisfies the equality of the above condition. The corresponding characteristic time for breakup is given as:

$$\tau_b = \frac{C_{b2}\rho_d^{1/2} D_d^{3/2}}{4\sigma_d^{1/2}}, \tag{3.58}$$

where $C_{b2} = \pi$, and ρ_d is the density of droplet.

- For stripping breakup,

$$\frac{We}{\sqrt{Re}} \geq C_s, \tag{3.59}$$

where C_s is an empirical constant (C_s=0.5), and the characteristic time scale is:

$$\tau_b = \frac{T_{strp}}{2}\left(\frac{\rho_d}{\rho}\right)^{1/2} \frac{D_d}{|\underline{u} - \underline{u}_d|}, \tag{3.60}$$

where T_{strp} is an empirical constant whose value lies between 2 and 20 [140].

3.8.2 Droplets Dispersed Phase

The primary and secondary breakup processes lead to the formation of sparse small droplets that characterize the onset of the dilute spray region. The volume fraction of droplets in this region is negligible, and the droplets are separated by a large distance compared to the characteristic droplet dimensions. The interaction between the droplets becomes weak. This regime of spray is known as the dispersed phase, where the physical processes that lead to the evolution of the spray are relatively well defined. Within the framework of Lagrangian modeling, the spray parcels are tracked through the computational cells. The transport of each parcel within the computational domain is governed by a set of ordinary differential equations that govern the mass, momentum and energy of the parcel. The weak interaction between the droplets and a strong coupling between the dispersed phase and the continuous gas phase drives the mass, momentum and energy exchange between the two phases. The turbulent structure of the gas-flow increases the heat- and

mass-transfer between the two phases. In typical diesel-engine-like conditions, the gas-phase temperature is much higher than the droplet temperature, causing the droplets to heat up and evaporate faster in the process of transport though the domain.

The modeling approach that has been usually applied to multiphase flow for engines is based on rapid circulation theory [166, 167]. In this approach, the circulation internal to the droplets is assumed to be infinitely fast compared to the transient changes in droplet properties. This is a sufficiently accurate model for most practical applications of interest. The infinitely fast transport results in uniform droplet properties [166]. However, the properties vary with time. The heat and mass transfer of droplets due to evaporation result in changes in droplet temperature and mass. The change in droplet temperature results in changes in the molecular properties of droplets, including thermal conductivity, viscosity and surface tension [168]. The present work is based on single-component fuels, and therefore homogeneity of the physical properties of droplets with characteristic dimension of 10 micron is a reasonable assumption. However, for multi-component droplets, this model should be applied with caution, particularly with two components having a large difference in evaporation rates. Large differences in boiling points of two components may result in micro-explosions within the droplets causing further disintegration of droplets. These effects are not included for the present study.

The computational models for the dispersed phase do not attempt to solve the full Navier-Stokes equations for each droplet/parcel. Such an attempt would be prohibitively expensive. Instead, the computational model uses standard correlations for drag, heat and mass transfer rates for the dispersed phase. The gas-phase equations are the standard transport equations, with corrected molecular properties and additional source terms to account for exchanges with the liquid phase.

In this work, the droplets are assumed to be spherical of diameter D_d. Radiation heat transfer to/from the droplets is neglected in comparison to convective heat transfer. The momentum equation for the droplets in the Lagrangian framework is:

$$m_d \frac{d\underline{u}_d}{dt} = \frac{1}{2}\rho C_d A_d |\underline{u} - \underline{u}_d|(\underline{u} - \underline{u}_d) - V_d \bigtriangledown p - \frac{1}{2}\rho V_d \frac{d(\underline{u} - \underline{u}_d)}{dt} + m_d \underline{g} \quad (3.61)$$

Here the first term on the right-hand side is the drag force experienced by a droplet due to the relative motion of the droplet with respect to the ambient gas, the second term is the pressure force, the third term is the virtual mass force required to accelerate the surrounding gas entrained by the droplet, and the last term is the body force term due to gravity. The droplet is characterized by diameter D_d, velocity $\underline{u}_d$, surface area A_d, volume V_d and mass m_d. In general, all the droplet properties are indicated by a subscript d, while non-subscripted quantities refer to the gas phase. The drag coefficient C_d is specified as a function of Reynolds number as follows:

$$\begin{aligned} C_d &= 24\left(1+0.15Re_d^{0.687}\right)/Re_d, Re_d \leq 1000 \\ &= 0.44, \qquad\qquad\qquad\qquad Re_d > 1000, \end{aligned}$$

where Re_d is the droplet Reynolds number defined as:

$$Re_d = \frac{\rho|\underline{u}-\underline{u}_d|D_d}{\mu}.$$

The equations for mass and heat transfer rates of the droplet are:

$$\frac{dm_d}{dt} = -A_s K_g p_t ln\left[\frac{(p_t - p_{v,\infty})}{p_t - p_{v,s}}\right], \tag{3.62}$$

$$m_d c_{p,d}\frac{dT_d}{dt} = -A_s h(T_d - T) + h_{fg}\frac{dm_d}{dt}, \tag{3.63}$$

where A_s is the droplet surface area, and K_g is the mass transfer coefficient; p_t, $p_{v,\infty}$ and $p_{v,s}$ are the gas pressure, partial vapor pressure in the surrounding gas and partial vapor pressure at the droplet surface, respectively. The droplet is at a uniform temperature of T_d. Assuming equilibrium between the liquid and gas phase, the partial vapor pressure at the droplet surface is the saturation vapor pressure at T_d. For the temperature equation, h denotes the heat transfer coefficient, $c_{p,d}$ denotes the droplet specific heat and h_{fg} is the enthalpy of vaporization. The heat transfer coefficient is evaluated from the following Ranz-Marshall correlation for non-evaporating droplets, which is then multiplied by a correction factor Z:

$$h = \frac{k_m Nu Z}{(e^Z - 1)D_d}, \tag{3.64}$$

$$Nu = 2(1 + 0.3Re_d^{1/2}Pr^{1/3}), \tag{3.65}$$

$$Z = -\frac{c_p(dm_d/dt)}{\pi D_d k_m Nu}, \tag{3.66}$$

where Nu is the Nusselt number, and c_p and k_m are the specific heat and thermal conductivity of the gas at the mean film temperature T_m given as $T_m = T_d + \frac{1}{3}(T_\infty - T_d)$. Similarly, the mass transfer coefficient is defined as,

$$K_g = \frac{D_m Sh}{R_m T_m D_d}, \tag{3.67}$$

$$Sh = 2(1 + 0.3Re_d^{1/2}Sc^{1/3}), \tag{3.68}$$

where Sh, Sc, D_m and R_m are the Sherwood number, Schmidt number, vapor diffusivity and gas mixture constant, respectively. The last two quantities are defined at a mean film temperature.

The gas-phase velocity that has been used in Eqns. (3.61-3.68) is the total gas velocity, which includes mean and fluctuating components. The interactions of turbulent fluctuations with droplets result in turbulent dispersion of droplets. This effect is modeled using a stochastic approach called the "random-walk" model [169].

The equations for the PDF stochastic particles described in the previous section were for single-phase particles. Additional considerations are required for multi-phase flow, where additional mass and energy are deposited into the gas-phase due to evaporation of droplets. This requires additional considerations for mass and energy sources in the computational cells. Within the framework of the LPEM method, the stochastic particles should reflect this change in a local or aggregate sense within each computational cell. Two approaches have been suggested to account for this [39]. The first approach is to distribute the evaporated mass and enthalpy in a computational cell over the existing particles in proportion to the particle mass [170]. This method is easy to implement, and preserves the cell mean values of compositions. The second approach is to create new stochastic particles corresponding to the vaporized liquid [40]. Since the new particles correspond to freshly evaporated liquid, these new particles contain pure fuel only. The latter method is particularly promising in capturing the local effect of turbulent fluctuations in compositions. However, under certain conditions, this method can yield

unphysical temperatures [39]. The creation of new particles of pure fuel completely ignores the mixing of the vaporized mass, which typically occurs at the gaseous boundary layer around the liquid droplets. For a high-temperature gaseous environment, with little entrainment of air inside the spray, the unity mass fraction of the new particle proves to be a reasonable approximation. However, for high entrainment of air, this approximation can lead to unreliable predictions. As the entrainment of the hot air becomes significant, the droplets are heated up quickly and the droplet surrounding is enriched with hot oxidizer. This results in significant change in liquid properties as compared to the properties for droplets with low entrainment of air. For the present modeling purpose, the first approach is adopted to avoid any unrealistic spray characteristics that could arise from the second approach due to high air entrainment.

It should be emphasized here that injector modeling has not been considered here. The injection is modeled as a point injection process that adds the injected liquid into the domain from a user specified injection point at a prescribed rate.

3.9 Radiation Heat Transfer Models

Thermal radiation can have a strong impact on the prediction of mean flame temperature and emissions. For laboratory-scale atmospheric-pressure nonluminous flames, inclusion of a radiation model reduces the flame temperature by approximately 100 K [38]. The reduction of local temperature affects the NOx chemistry, in particular. However, detailed treatment of radiative heat transfer in turbulent combustion is generally too expensive. Here, TCI are the primary interest. The extent to which radiation influences the results is determined by comparing results obtained with no radiation model to those obtained using an optically thin model [171, 172, 173, 174].

The complex turbulence-radiation interactions (TRI) in a participating gas-phase medium and soot radiation can be modeled using a spectral photon Monte Carlo method (PMC) [125, 126, 38]. The PMC method is based on tracing photon bundles which represent a fixed amount of radiative energy. The photon bundles travel through the domain undergoing absorption, scattering and reflection processes until they leave the computational domain or are completely absorbed in

the domain [175]. However, PMC is computationally intensive.

Here an optically thin radiation model has been implemented at the stochastic particle level, with consideration of radiation from four gaseous species (CO_2, CO, CH_4, and H_2O) and soot. The radiative heat loss for a particle due to radiation is expressed as [176]:

$$q_r = -4\sigma K_p\left(T^4 - {T_\infty}^4\right) - C f_v T^5, \tag{3.69}$$

$$K_p = p\sum \chi_i K_{pi}, \tag{3.70}$$

where, σ is the Stefan-Boltzmann constant, K_p is the Planck-mean absorption coefficient of the gas mixture, and T_∞ and p, respectively, denote the environmental temperature and pressure, and K_{pi} and χ_i are the Planck-mean absorption coefficient and mole fraction of the i-th emitting gas species. The Planck-mean absorption coefficients of the emitting gas species were obtained by polynomial fits as specified in the TNF website [34]. The quantity f_v is the soot volume fraction, and C is a constant equal to 3.334x10^{-10} W/m^3-K^5 [176].

3.10 CFD Implementation

The hybrid particle-PDF/Eulerian-RAS method has been implemented using STAR-CD [177], a commercial CFD code. A schematic diagram of the overall algorithm is presented in Fig. (3.2). The mean Eulerian fields are obtained from STAR's inbuilt CFD solver, whereas the particle-PDF method is implemented through the user interface of STAR-CD. For the Eulerian part, the computational domain is decomposed into large number of computational cells. A pressure-based PISO [178] algorithm is used to solve the coupled set of transport equations at the cell-centers. A spatially second-order scheme and a first-order temporal discretization schemes are used to produce a set of linearized discretized equations which is solved using a coupled, pressure-based, segregated iterative solver that is iteratively implicit in time.

The computational domain is initialized with approximately the same number of notional particles in each computational cell (20-50). This ensures a uniform

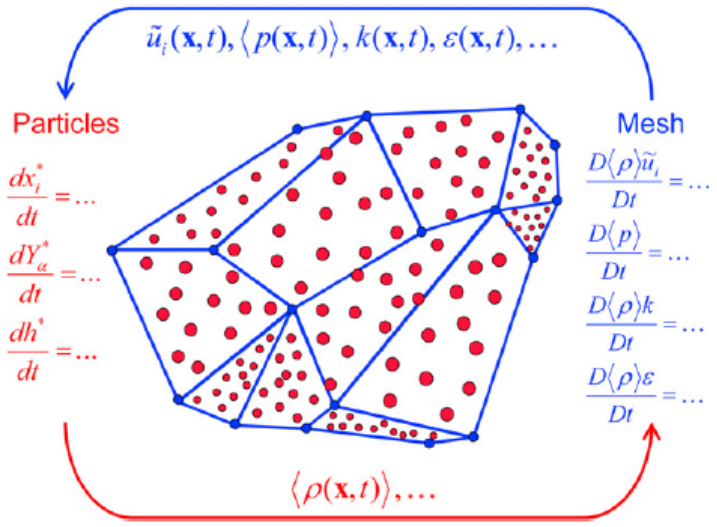

Figure 3.2. Schematic of a hybrid Lagrangian particle/Eulerian mesh composition PDF method, illustrating a two-dimensional slice through an arbitrary three-dimensional unstructured finite-volume mesh. Blue lines represent finite-volume cell edges, and red circles represent notional PDF particles [33, 39].

distribution of statistical error in the computational domain [33]. The cell-based average mass fraction of species and enthalpy are computed from mass-based averages of the particle compositions. The numerical computations on the particle side correspond to the physical processes that are carried out sequentially over the computational time-step. That is, the updates in particle compositions due to mixing, chemical reaction, and evaporation are all carried out sequentially. This "operator splitting" approach is formally first order in time. The specific order of the physical processes is of secondary importance here [33]. The mixing occurs through the interaction of particles in a computational cell. The particle-interaction mixing models leave the mass-weighted cell mean values unchanged. However, some of the interaction models (e.g., IEM) require mean particle compositions at the particle locations. The interpolation scheme that is used to compute the mean compositions at the particle locations must ensure that the mean values remain unchanged after the mixing. One convenient choice is to use the cell mean values as the estimates of mean values at the particle location. The chemistry is solved at the particle level using a stiff ordinary differential equation (ODE) solver using a CHEMKIN/DARS [179] interface. The computational time-step used for the simulations of particle motion is usually large compared to chemical time scales.

Therefore, the changes in particle compositions due to chemistry are computed by solving a set of stiff coupled ODEs. This is the most expensive computational step, especially for chemical mechanisms with large numbers of species [33]. The effects of evaporation of liquid fuel are accounted for by distributing the evaporating mass and energy in a computational cell over the existing particles in proportion of their masses.

The computational time-step is one of the most significant parameters that determine numerical accuracy. The computational time step must be smaller than the integral scales of turbulence, and small enough to keep the particle Courant numbers less than one. Different particle tracking algorithms are available [180, 181, 13, 182, 183] to track the particles through the finite-volume cells. The one that has been used here is based on face-to-face tracking of particles. This method is suitable for arbitrary shaped computational cells. The particles are also tracked across the processor boundaries for parallel simulations. When a particle reaches a processor boundary during a computational time-step, the particle crosses the processor and the tracking continues for the rest of the computational time step. The spatial distribution of the particles in a computational cell is maintained within acceptable bounds by forcing the number of particles per cell to remain within specified maximum and minimum limits. If the number of particles in a cell drops below the acceptable minimum, the particles with large masses are each split into two particles with half the mass and the same compositions as the original particle. This method is called "cloning". Cloning retains the averages and the shape of the particle distribution. On the other hand, if the particle number in a cell exceeds the maximum allowed, particles are selectively removed, with preference given to low-mass particles, and the mass and physical properties associated with the removed particle are distributed among the retained particles. This process is called "annihilation" of particles. Annihilation does not preserve all the properties of the particles. The simple annihilation algorithm used here changes the particle distribution by introducing "artificial mixing".

Maintaining consistency between the Lagrangian and finite-volume sides has been an important factor that determines the robustness of a LPEM method. One basic requirement for this method is that the expected value of the particle mass in a computational cell should be equal to the finite-volume fluid mass. This

requirement is met for the initial distribution of the particles inside the computational cells. However, as the particles are transported across the computational domain, the accuracy to which this criterion is satisfied depends on the accuracy of the tracking algorithm and the interpolation scheme that gives a mean velocity field consistent with the mean continuity equation at the particle locations. Even with these algorithms, deviations between the particle mass distribution and finite-volume mass distribution can develop over a period of time and additional mass consistency algorithms are required to keep the mass distribution same between the two.

The numerical errors of the LPEM method can be divided into statistical error, bias error, temporal discretization error, and spatial discretization error [184]. The first two come from stochastic particle method. The statistical error arises due to using a finite number of particles. The statistical error scales as $N_p^{-1/2}$, and is referred to as random error. The bias error is a deterministic error that arises due to using a finite number of particles, and scales as N_p^{-1}. With an increase in the number of particles, the bias error decreases more rapidly than statistical error. The spatial and temporal errors depend on the spatial and temporal resolution of the numerical algorithm.

Parallelization of the numerical algorithm is key to keeping the computational time for the LPEM method within reasonable and affordable limits. A major part of the overall computational time is consumed in the chemistry solver. While the FV method employs a discretized linear algebraic set of equations for mean velocities, pressure and turbulence quantities at each cell center, the particle methods solve stochastic ODEs for particle properties. There are typically 20-40 particles per finite-volume cell. This suggests that the particle calculations will dominate the CPU time. Therefore, to bring down the computational expenses, the chemistry computations need to be accelerated. Use of multiple processors is one strategy to bring down the computational time, by distributing the cells equally to all the processors. However, the scalability of this algorithm is often difficult to ensure, particularly when the chemistry is predominantly limited to a small region that belongs to only a few processors. This creates an unbalanced load between processors, where one low-load processor completes computations faster than a high-load processor, and then waits for the high-load processor to complete the chemistry

computations before proceeding to the next time-step. One simple strategy to avoid this problem is a "round-robin" algorithm that redistributes particles from each processor to all other processors based on particle number just before the chemistry computations. After the chemistry computations, the particles are returned back to their original processors. This algorithm has been effective in producing reasonable parallel scalability for large chemical mechanisms, and has been employed for this work.

Chapter 4

Constant-Volume Turbulent Spray Combustion

The modeling efforts summarized in Chapter 2 have primarily been focused on comparisons for laboratory-scale, near-atmospheric-pressure, canonical, statistically stationary turbulent jet flames with gas-phase reaction. However, transition of modeling efforts from these flames to high-pressure mixed-mode transient spray flames in engines is not straightforward and introduces significant modeling challenges that evolve around the complex interactions between turbulence and chemistry, and between turbulence and sprays, in extremely high-pressure environments. To bridge the gap in modeling between the canonical laboratory-scale flames and practical diesel engines, a reliable experimental database is required for well-characterized turbulent spray flames for diesel-engine-like conditions. Practical engine configurations are too complicated for this purpose. Complex fuel injector designs, a wide range of thermochemical conditions, and complicated geometric shapes are among the complications that limit the availability of a reliable experimental database. A recent effort to resolve this issue is the Engine Combustion Network (ECN) [1] of Sandia National Laboratory. The experimental configuration is a constant-volume cubical combustion chamber that can reach the desired thermochemical conditions representative of diesel combustion, without incorporating the geometric complexities of a real piston engine.

4.1 Engine Combustion Network

The Engine Combustion Network (ECN), much like the Turbulent Non-premixed Flame (TNF) Workshop, is an open forum for international collaboration between experimental and modeling groups. However, while the TNF workshop focused on canonical statistically stationary flame configurations, the ECN provides experimental measurements for turbulent spray flames at high pressure, diesel-engine-like conditions. The objectives of ECN are [1] to:

- Establish library of well-documented experimental measurements for model validation and development of understanding of combustion at conditions specific to engines;
- Provide a framework for collaborative comparisons of measured and modeled results;
- Identify priorities for further experimental and computational research.

ECN maintains a wide database of experimental measurements that include data for non-reacting and reacting sprays for diesel-engine-like conditions. The database of measurements continues to grow, and is expected to have more data for systematic validation of models in the near future.

The experimental set up (Fig. 4.1) consists of an optically accessible constant-volume combustion vessel at conditions representative of quiescent diesel engine conditions. The shape of the combustion vessel is cubic, and it has a characteristic dimension of 108 mm. Each side of the combustion chamber has a round port with a diameter of 105 mm. Figure 4.2 shows a schematic cross-sectional view of the combustion vessel. The fuel injector is located in one side port using a metal insert that forms the right wall of the combustion chamber. Two spark plugs and a mixing fan are mounted in another metal insert that forms the top wall of the chamber. Optical access is provided by four sapphire windows with clear apertures of 102 mm located in the other four ports. The mixing fan mounted at the center ensures nearly uniform ambient conditions at the beginning of injection. Intake and exhaust valves, or instruments such as pressure transducers or thermocouple inputs, can be mounted at the corners of the cubical-shaped combustion chamber.

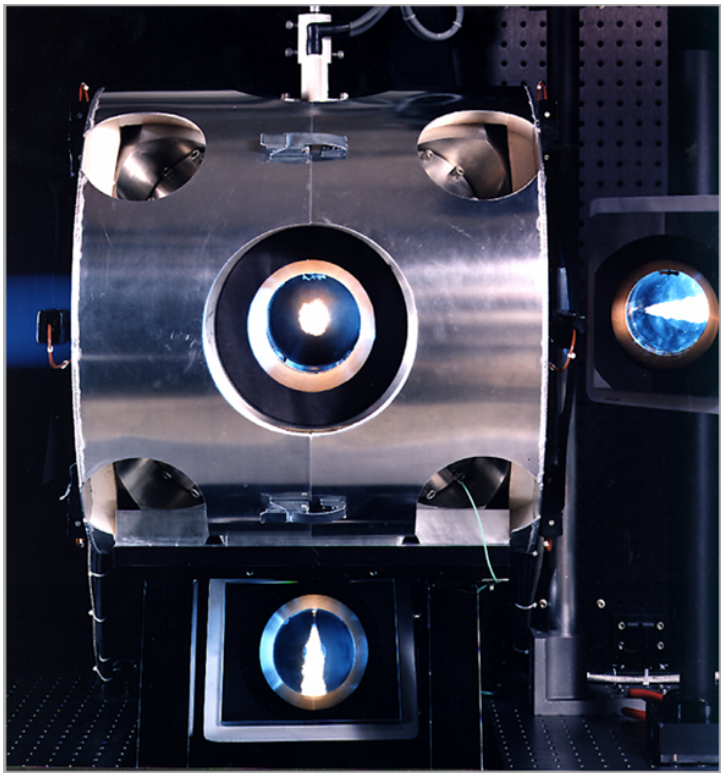

Figure 4.1. The experimental configuration for a constant-volume combustion chamber [1].

The vessel is designed to produce simulated diesel conditions by igniting a premixed fuel-lean mixture to completion. To begin each experiment, the vessel is filled with a premixed, combustible gas mixture of acetylene, hydrogen, oxygen and nitrogen, which is ignited with spark plugs. This creates a high-temperature, high-pressure environment. The products of combustion cool down over a relatively long time (approximately 1 s) due to heat transfer to the vessel walls, and the pressure slowly decreases. When the desired experimental conditions are reached, the diesel fuel injector injects liquid fuel that evaporates, mixes and autoignites to begin the combustion processes. The oxygen concentration for the diesel combustion is controlled by changing the oxygen level for the premixed combustion. The ambient gas temperature, density, and composition at the start of injection are determined by the pressure at the time of fuel injection and the initial mass and composition of gas within the vessel.

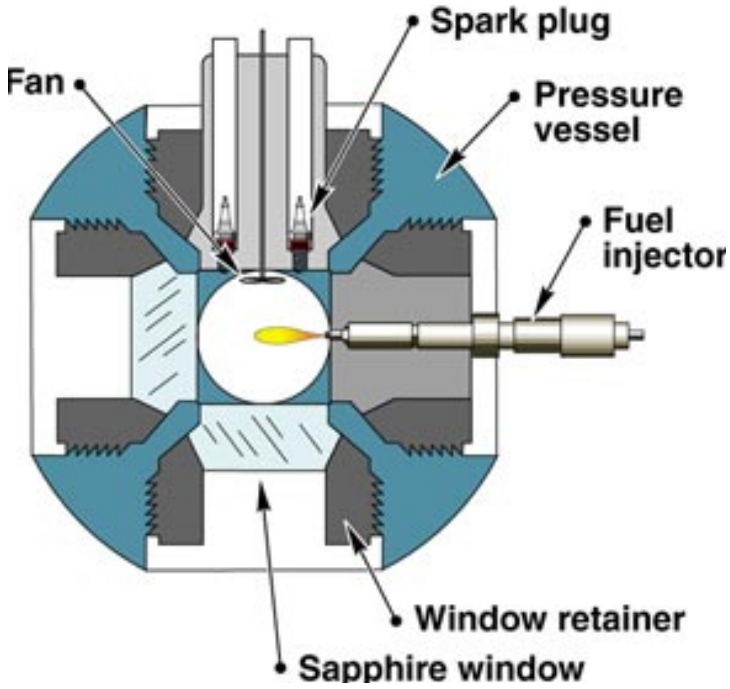

Figure 4.2. Schematic of the combustion vessel [1].

A Bosch second-generation common-rail injector equipped with a single-orifice, axial nozzle with mini-sac type injector tip was used for this study. The injection rate is maintained almost constant in time over the injection duration, resulting a top-hat injection profile. For details of the injector, the readers are referred to [185, 186]. Nozzles with different orifice diameters were also included in the test matrix.

The combustion vessel allows experiments over a wide range of operating conditions that are representative of in-cylinder diesel combustion. With full optical access, the vessel can reach initial temperatures of 450 to 1300 K, densities of 1 to 60 kg/m^3, oxygen mole fractions of 0% to 21%, and pressures up to 350 bar [187, 188, 189, 190, 185]. The measurements for low ambient temperatures/pressures/densities are representative of early injection strategies in engines. Higher initial temperatures/pressures/densities represent late injection. Effects of EGR are simulated with different levels of initial oxygen concentration. The experimental set-up offers measurements over a wide range of injector parameters that include injection pressures of 40 to 200 MPa above ambient pressure, and nozzle diameters from 0.05 to 0.5 mm. Measurements are provided for different

fuel compositions that include oxygenated fuels and hydrocarbon fuels (n-heptane, cetane, n-dodecane, 2,2,4,4,6,8,8 heptamethyl-nonane, and n-hexadecane).

4.2 n-Heptane Spray and Spray Flames

The first configuration that has been targeted for the current modeling studies is the baseline n-heptane spray configuration, also known as "Spray-H" on the ECN website. The physical conditions for the baseline n-heptane case include an initial ambient pressure of 44 bar, temperature of 1000 K, density of 14.8 kg/m^3, and oxygen mole fractions from 0% to 21%. The compositions of the ambient gas are listed in Table 4.1 for different O_2 levels. It is emphasized that the simulated ambient gas corresponds to the products of premixed combustion, and should not be confused with atmospheric air. The Spray-H/baseline-n-heptane spray includes measurements for non-reacting and reacting spray flames. The non-reacting spray data are for 0% O_2. The experimental diagnostics available for the non-reacting spray include liquid and vapor penetration lengths, radial profiles of mean mixture fraction at selected axial locations and times, radial profiles of variance of mixture fraction at selected axial locations and time, and time-averaged images of the vapor jet penetrating through the vessel. The liquid penetration length is computed from Mie-scattered light images acquired during the quasi-steady period of the spray development [185]. A 532-nm, continuous-wave laser was used to illuminate the spray while an image of the Mie-scattered light was acquired with an intensified camera orthogonal to the spray. The liquid penetration length is measured as the maximum axial distance in the spray where the light intensity was above a threshold equal to 3% of the light intensity range measurable with the camera. The vapor penetration measurements were computed from shadowgraph or Schlieren imaging [186] by tracking the vapor boundary of a penetrating jet. The boundary of the jet is determined through image analysis. The experimental diagnostics for the reacting spray flames include measurements for ignition delay, lift-off length, OH images, radial profiles for soot volume fraction at selected axial locations and time, and pressure rise. OH chemiluminescence images were used to determine the lift-off length of the combusting region of the fuel jet. Pressure measurements were used to estimate the time of autoignition relative to the start

of injection. A laser extinction technique and planar laser-induced incandescence (PLII) measurements were used to evaluate soot optical thickness across the fuel jet and qualitative visualization of the spatial location of soot, respectively. The measurements have also been extended beyond the baseline n-heptane spray configurations for additional model comparisons. The experimental configurations for the non-baseline conditions include variations of initial temperature from 750 to 1300 K, and ambient density of 30 kg/m^3 for different O_2 levels. The run matrix for the present modeling comparisons is provided in Table 4.2

Table 4.1. Molar percentages for constituents of the ambient gas for Spray-H.

O_2	N_2	CO_2	H_2O
21.0	69.33	6.11	3.56
15.0	75.15	6.22	3.63
12.0	78.07	6.28	3.65
10.0	80.00	6.33	3.67
8.0	81.95	6.36	3.69
0.0	89.71	6.52	3.77

Recently, the ECN baseline n-heptane spray configuration has been the subject of modeling studies that focus on liquid fuel injection, evaporation, mixing, autoignition, and emissions. The first ECN workshop was organized in 2011 to bring together different experimental and modeling groups to highlight the modeling needs and future developments for engine combustion. It was recognized that to bring all the modeling efforts under the same global framework, ECN requires a set of definitions to describe the key characteristics in a consistent manner. Following discussions and recommendations among different groups, definitions were established for the computation of liquid penetration, vapor penetration, and lift-off length. The modeling definitions that were recommended are as follows:

- Liquid penetration: Distance from the nozzle outlet to the farthest axial location where liquid volume fraction is 0.15%;
- Vapor penetration: Distance from the nozzle outlet to the farthest axial location where the fuel-vapor mass fraction (or mixture fraction) is 0.1%;

Table 4.2. Operating conditions for run matrix.

% O_2	Ambient gas density (kg/m^3)	Ambient temp. (K)	Injected fuel mass (mg)	Injection time (ms)	Injection temp. (K)
21	14.8	1000	17.8	6.8	373
15	14.8	1000	17.8	6.8	373
12	14.8	1000	17.8	6.8	373
10	14.8	1000	18.1	6.9	373
8	14.8	1000	18.1	6.9	373
0	14.8	1000	-	-	-
15	30.0	1000	18.0	6.8	373
12	30.0	1000	17.8	6.8	373
10	30.0	1000	18.0	6.8	373
8	30.0	1000	18.0	6.8	373
21	14.8	750	17.4	6.6	373
21	14.8	800	17.5	6.6	373
21	14.8	850	17.6	6.7	373
21	14.8	900	17.5	6.6	373
21	14.8	950	17.6	6.7	373
21	14.8	1000	17.8	6.8	373
21	14.8	1100	18.1	6.9	373
21	14.8	1200	18.1	6.9	373
21	14.8	1300	17.4	6.6	373
8	14.8	1000	18.1	6.9	373
8	14.8	1100	17.7	6.7	373
8	14.8	1200	17.9	6.8	373

- Flame lift-off length: Distance from the nozzle outlet to the first axial location where the Favre-averaged OH mass fraction reaches 0.00025.

Over the past year, the definitions for the global quantities have been reviewed and a new set of definitions has been suggested recently. The updated definitions are given below, although the comparisons presented in this thesis are based on the earlier set of definitions. One important addition in the updated definitions is the characterization of ignition delay, which was not available previously. For the modeling comparison, however, the time to realize a temperature rise of 400 K from the start of injection is used as the measure of ignition delay.

- Liquid penetration: Distance from the nozzle outlet to the farthest axial

location where liquid volume fraction is 0.1%, averaged over a volume of 1 mm in diameter and 1 mm in axial length;

- Vapor penetration: Distance from the nozzle outlet to the farthest axial location where the fuel-vapor mass fraction (or mixture fraction) is 0.1%;
- High-temperature ignition delay: Two different definitions are utilized. (1)First time at which Favre-average OH mass fraction reaches 2% of the maximum in the domain after a stable flame is established. (2) The time of maximum time rate of change in temperature;
- Lift-off length: First axial location of Favre-average OH mass fraction reaching 2% of its maximum in the domain.

The ECN workshop included discussions on different modeling approaches for injector modeling, atomization and breakup modeling, two-phase-flow/dispersed-phase modeling, kinetic modeling, and turbulence-chemistry interactions. Borghesi *et al*. [191] presented a conditional moment closure (CMC) model with a presumed PDF for mixture fraction to model turbulent spray combustion. The presence of droplets was taken into account for the mixture fraction PDF and scalar dissipation rate. Somers *et al*. [192] reported a large-eddy simulation (LES)-based Eulerian multiphase model with detailed flamelet-based n-heptane chemistry to study the autoignition characteristics. A numerical model with a "re-normalizing group" (RNG) $k-\epsilon$ turbulence model, and partially stirred reactor model with detailed chemistry has been suggested by Novella *et al*. [193] The spray characteristics have been studied in detail by Bajaj *et al*. [194]. Most of the modeling efforts presented in the first ECN workshop did not capture the turbulence-chemistry interactions. The spray modeling included different breakup models, including Kelvin-Helmholtz-Raleigh-Taylor (KH-RT), Reitz-Diwakar (RD), Bianchi, Eulerian and Lagrangian discrete phase models, droplet collision/coalescence models, drag, dispersion, and evaporation models. The kinetic modeling across the modeling groups included a wide range of mechanisms. A summary of the chemistry modeling is presented in Table 4.3, and a similar summary of turbulence and spray breakup models is shown in Table 4.4.

Table 4.3. Summary of chemistry and TCI modeling for the ECN n-heptane flames; ANL - Argonne National Laboratory, Cambridge - Cambridge University, CMT - CMT-Motores Trmicos (Valencia), Eindhoven - T.U. Eindhoven, ERC-UW - Engine Research Center-University of Wisconsin, Penn. State - Pennsylvania State University, POLIMI - Politecnico di Milano, Purdue - Purdue University, UNSW - University of New South Wales.

Group	Kinetic Model			Turbulence-Chemistry Interaction
	Reference	No. of Species	Type	
ANL	Lu *et al.* [95]	68	reduced	No model
	Golovitchev *et al.* [195]	42	skeletal	
Cambridge	Pitsch and Liu	23	reduced	CMC
CMT	Zeuch *et al.* [196]	110	skeletal	No model
	Ra and Reitz [93]	41	skeletal	
	Patel *et al.* [94]	29	skeletal	
Eindhoven	Peters *et al.* [92]	48		No model
ERC-UW				No model
Penn. State	Chalmers [2]	40	skeletal	Composition PDF
POLIMI	Lu *et al.* [95]	52	reduced	No model
	Seiser *et al.* [197]	159	skeletal	
	Patel *et al.* [94]	29	skeletal	
Purdue	Peters *et al.* [92]	37		Flamelet-based
	Seiser *et al.* [197]	159	skeletal	progress variable
UNSW	Patel *et al.* [94]	29	skeletal	Composition PDF

Table 4.4. Summary of other key physical models for the ECN n-heptane flames

Group	CFD Code	Turbulence Model	Break-up Model
ANL	CONVERGE	RNG k-ϵ, LES Smagorinsky	KH-RT
Cambridge	StarCD 4.1	RNG k-ϵ	RD
CMT	OpenFOAM	k-ϵ	KH-RT
Eindhoven	-	LES	-
ERC-UW	KIVA-3V	RNG k-ϵ	KH-RT
Penn. State	StarCD 4.12	Standard k-ϵ	RD
POLIMI	OpenFOAM	Realizable k-ϵ	Bianchi, KH
Purdue	In-house	k-ϵ	RD
UNSW	Fluent 13.0	Realizable k-ϵ	KH

It is observed that limited attempts have been made to capture turbulence-chemistry interactions (TCI) in the modeling studies reported to date. The importance of TCI can be seen in the OH contours [191], for example. Comparisons of computed OH contours with versus without TCI show significant differences in the turbulent flame structures. Models that include TCI provide a broader and distributed mean flame zone compared to models that completely ignore TCI. This difference has been seen in the CMC model results [191], for example, which models TCI using a presumed PDF shape for mixture fraction. A more recent study includes a transported PDF method, using a particle-based solution method by Pei *et al*. [198]. This method explicitly captures TCI. Another recent development in TCI modeling is the stochastic Eulerian field (SEF) PDF method [113]. Preliminary results with the SEF PDF method showed improved flame structures with consideration of TCI.

Along with TCI, the first ECN workshop emphasized the importance of kinetic models to capture the global ignition characteristics, such as ignition delay and flame lift-off length. The comparison of results over a wide range of O_2 levels, initial temperatures and densities suggested different degrees of agreement among the modeling groups with the measurements. The two primary reasons for the wide variability of predictions are differences in physical models (turbulence, and sprays) and kinetics. It was observed that for the same physical model and kinetics, the degree of agreement in predictions varies with the ambient conditions. Based on the modeling comparisons, two chemical mechanisms were suggested for future modeling studies: a 29-species skeletal mechanism by Patel *et al*. [94] and a 52-species reduced mechanism by Lu *et al*. [95].

4.3 n-Dodecane Spray and Spray Flames

The second spray configuration that has been the subject of extensive experimental and modeling studies is with n-dodecane fuel, also known as "Spray-A". It has been recognized that n-dodecane has fuel characteristics that are more representative of real diesel fuels compared to n-heptane. The evaporation characteristics and cetane number of n-dodecane are closer to diesel than those of n-heptane. The high volatility of n-heptane gives more rapid evaporation and more mixing time com-

pared to a typical diesel fuel. Therefore, much of the ECN effort has been directed to experimental and modeling studies for Spray-A. The experimental database for the Spray-A configuration has not yet been completed, and is expected to grow in the near future. The measurements that are currently available on the ECN website include two operating conditions: 0% O_2 for the non-reacting spray, and 15% O_2 for the reacting spray flame. The initial temperature, pressure and density in the vessel are 900 K, 87 bar, and 22.8 kg/m^3 (Table 4.5). The measurements for the non-reacting Spray-A include liquid and vapor penetration lengths, radial profiles of mean mixture fraction, and images of mixture fraction contours, whereas the measurements for the reacting spray include ignition delay, lift-off length, flame images, and radial profiles of soot volume fraction.

Table 4.5. Operating condition for the ECN n-dodecane spray.

Nozzle diameter	90 micron
Injection temperature	363 K
Injection duration	1.5 ms
Injected mass	3.5 mg
Ambient gas temperature	900 K
Ambient gas density	22.8 kg/m^3

The first ECN workshop addressed the modeling requirements for the Spray-A configuration. The preliminary results presented in the first ECN workshop had been for the non-reacting spray. Limited modeling studies are available to date for the reacting n-dodecane spay, primarily because of the lack of a validated chemical mechanism for this fuel under diesel-engine-like conditions. Recently, Argonne National Laboratory (ANL) in collaboration with Lawrence Livermore National Laboratory (LLNL) has developed a reduced skeletal mechanism that includes 103 species, and 370 reactions [3] for n-dodecane. Preliminary studies with this mechanism for the n-dodecane spray flames showed encouraging results; however, the capabilities of this mechanism to produce realistic agreement with the measurements over a wide range of conditions remain to be fully explored.

4.4 Computational Configuration

The experimental geometry is a cubic vessel with sides of 108 mm. For the computational study, an axisymmetric geometry with a 5° sector (Fig. 4.3) is used for computational expediency. The radial dimension of the computational domain is adjusted to ensure that the computational volume remains same as that for the real combustion vessel. The mesh has a total of 7952 hexahedral cells that are split into 112 cells along the axial direction, 71 cells in the radial direction, and a single layer of cells in the azimuthal direction. The cells are non-uniformly distributed in both axial and radial directions, with more cells close to the injector location. The characteristic cell dimension varies from 0.3 mm near the injector to 1.4 mm near the bottom wall. The injector is located at the center of the domain (r =0 and z =0), and is oriented along the axis of the domain. Initial compositions of the gas-phase are listed in Table 4.1. The details of the physical and modeling parameters for the spray model are discussed in the next Chapter (Table 5.1). The boundary conditions for the domain are symmetry conditions for the azimuthal planes and the axis (r =0), and walls for the top (z =0), bottom ($z = H$) and side planes ($r = R$). Here H and R are the axial height and the radius of the domain, respectively. The wall boundary conditions include no-slip and no-penetration for velocity components, zero-gradient for the scalars and adiabatic or isothermal for the energy variable. In the actual experiment, the wall temperature changes and the combustion products cool down over a period of time. Therefore, idealization of the wall as a constant wall-temperature or constant heat flux (zero for adiabatic) is an approximation. However, the preliminary results suggest that the flame remains away from the wall for most of the combustion event, and therefore it is believed that the wall boundary condition should not significantly affect the transient and quasi-steady characteristics of the flame. The current computations employ a constant wall temperature of 850 K. No spray-wall interaction models are required since the liquid spray evaporates before reaching the wall.

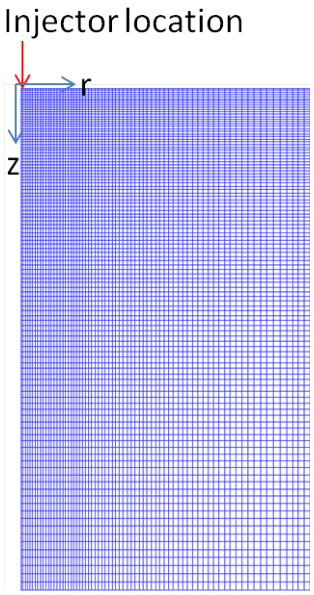

Figure 4.3. Axisymmetric geometry (5° sector) for the ECN n-heptane and n-dodecane spray flames.

Chapter 5

Results for n-Heptane Sprays and Spray Flames

In this chapter, the computational results for n-heptane sprays and spray flames are compared with experimental measurements using the axisymmetric geometry described in Chapter 4. Results from two models are compared to determine the extent to which turbulent fluctuations in composition and temperature influence the results: a PDF method and a well-stirred reactor model. Differences between results from the two models are manifestation of turbulence-chemistry interactions (TCI). The comparisons are divided into two sections: non-reacting sprays and reacting spray flames. Simulations for the non-reacting spray are limited to the baseline n-heptane condition (T=1000 K, ρ=14.8 kg/m^3) with 0% O_2. For reacting spray flames, the simulations are performed over a wide range of operating conditions, and the models are validated against a large pool of experimental data.

5.1 Non-reacting n-Heptane Spray

In the absence of chemical reaction, the key physical models are those that govern the liquid breakup, vapor penetration, mixing, and jet spread rate. The principal models used here are a high-Reynolds-number standard $k-\epsilon$ model [144, 145] with standard wall-functions to model near-wall turbulence, the Reitz-Diwakar [140] model to account for secondary breakup, and a dispersed-phase model [141] for dilute sprays. A number of parametric studies has been conducted to explore

the sensitivities of spray characteristics to the specification of the turbulence model constant ($C_{\epsilon 1}$ in the ϵ equation of the standard $k-\epsilon$ model), and the spray breakup-time constant (T_{strp}) for the secondary breakup process. The dispersed-phase model employs standard correlations for drag, heat and mass transfer coefficients, and is not varied in the parametric studies, since the model constants used in the correlations have long been validated and established as standard benchmark constants. The primary objective here is to establish a set of baseline model constants for the turbulence and breakup models that can then be used for reacting flows, under the assumption that the physical processes that lead to the liquid breakup, evaporation, and turbulent mixing of the air and fuel upstream of the lifted-flame remain largely unaffected by the flame at downstream locations.

The initial and boundary conditions for the gas-phase, and key physical attributes of the injector and spray, are listed in Table 5.1, and the model constants for turbulence and spray models are given in Table 5.2. Compositions of the gas mixture at the beginning of fuel injection are provided as inputs from the ECN measurements. The temperature of the liquid fuel during injection is maintained close to its boiling point (373 K). The spray modeling considers a high-pressure solid-cone spray, with only a 5° sector of the cone being considered in the computations. Spray modeling in the near-injector region includes a blob-injection model with a secondary breakup model. The diameter of the injected blobs is approximately the same as the nozzle diameter, after consideration of a suitable correction factor to account for the nozzle contraction coefficient. The maximum number of computational spray parcels per time step is maintained at 50. The initial turbulent kinetic energy is computed from the reported average RMS velocity (0.7 m/s), and the dissipation rate is evaluated based on a characteristic turbulence length scale which is one-fourth of the cube dimension. Table 5.2 presents the baseline model constants that have been used for this work. The table also includes the ranges of constants that have been explored for parametric studies of turbulence and spray breakup models. It is worth mentioning that, with the exception of $C_{\epsilon 1}$, all other constants for turbulence model are same as in the standard $k-\epsilon$ model [144]. The standard value of $C_{\epsilon 1}$ reported in [144] is 1.44, whereas a value of 1.50 has been adopted for the present work. The difference in predictions between these two values is left for later discussion. Key experimental diagnostics that are

Table 5.1. Initial gas-phase composition, boundary conditions, and injector and spray characteristics.

Computational time step	WSR (s) PDF (s)	5.0e-7 1.0e-7/2.0e-7
Injector and spray models	Injector location Injection rate, 360^0 equiv (kg/s) /constant or variable Number of parcels per time-step Injector model and key parameters Spray model key parameters	on-axis 0.0027/constant 50 constant-size blobs, inner cone angle=0^0, outer cone half angle= 6.3^0, Sauter mean diameter (SMD) = 9.27e-5 m, velocity = 700 m/s Temp = 373 K no primary breakup, Reitz secondary breakup, turbulent dispersion, no collision
Turbulence model	Type	Standard $k-\epsilon$
Initial conditions	Temperature (K) Pressure (Pa) Density (kg/m^3) O_2 mass fraction N_2 mass fraction CO_2 mass fraction H_2O mass fraction Turbulence kinetic energy (m^2/s^2) Turbulence dissipation rate (m^2/s^3)	1000 4290619.90 14.8 0.0 0.876270 0.100049 0.023681 0.735 3.5
Boundary conditions	Momentum Energy	no-slip walls, standard wall functions fixed T (850 K)

used to validate the model predictions for non-reacting spray are the liquid and vapor penetration lengths as functions of time, mean mixture fraction profiles, and mixture fraction variance profiles [185].

The results in this section are organized as follows. First, temporal evolutions of liquid and vapor penetration lengths are compared using a baseline well-stirred reactor (WSR) model (the baseline model constants are listed in Table 5.2). It

Table 5.2. Model constants for turbulence and spray.

Physical model	Baseline model constants	Range for parametric studies
Turbulence Model	Standard $k-\epsilon$	
	C_μ=0.09	-
	$C_{\epsilon 1}$=1.5	1.44 - 1.52
	$C_{\epsilon 2}$=1.92	-
	$C_{\epsilon 3}$=1.44	-
	κ=0.41	-
	σ_k=1.0	-
	σ_ϵ=1.219	-
Breakup Model	Reitz-Diwakar secondary breakup	-
	T_{strp} = 19.0	16 - 20
	T_{bag} = 3.1416	-
	We_{strp} = 0.6	-
	We_{bag} = 6.0	-
Spray Model	Dispersed Phase Model, Ranz Marshall correlation for heat/mass transfer	-

should be recognized here that the term "well-stirred reactor" is more suitable for reacting flow. In this thesis, results obtained using cell-level mean values of composition and temperature (neglecting turbulent fluctuations) are denoted as WSR. For non-reacting sprays, the mean chemical source term is zero, and the WSR model includes modeling of turbulent jet only. The sensitivities of computed penetration lengths to the variations in turbulence and breakup model constants are presented using the WSR model. The next set of results compares WSR model predictions for radial profiles of mean mixture fraction at selected axial locations and times with the experimental data. Based on these comparisons, the model constants that produce the best results are employed for the PDF model. The next set of results illustrates the differences in liquid and vapor penetration rates, and radial profiles of mean mixture fraction for the WSR and PDF models, and compares the predictions with measurements. Relatively small differences between WSR and PDF are found for the non-reacting spray, as expected, and for expediency, model constants were not recalibrated to give better agreement with the PDF model. The sensitivity of mean mixture fraction to variations in the

PDF mixing model constant (C_ϕ) then is investigated using IEM mixing model. The mixing model study includes sensitivity of computed radial profiles of mixture fraction variance. Finally, this section concludes with contours of mixture fraction mean and variance at different times to illustrate how the mean and variance of mixture fraction develop over time.

Computed (WSR) and measured liquid and vapor penetration lengths are compared in Fig. 5.1 using the baseline model constants. The computed penetration lengths are determined as explained in Chapter 4. Overall, the baseline model shows excellent agreement with the measurements. The computed penetration lengths grow somewhat faster during the early stage of injection. After approximately 0.5 ms, the liquid penetration reaches a quasi-steady state, whereas the vapor penetration continues to grow as the evaporated vapor-mass penetrates downstream. The qualitative shape of the vapor penetration curve matches with the earlier study of Naber and Siebers [186] that provides analytical measures of jet penetration length. Following the scaling-law analysis of Naber and Sieber [186], during the early part of jet penetration the vapor penetration grows linearly with time up to a certain distance beyond which the growth becomes slower (proportional to square root of time). Although the application of this scaling-law is

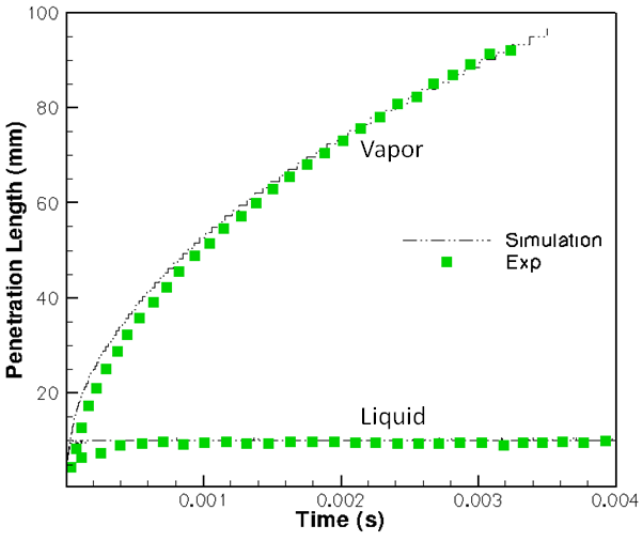

Figure 5.1. Computed (WSR model) and measured liquid and vapor penetration lengths versus time for the baseline models.

strictly limited to a non-evaporating spray, this still provides useful corroboration of the experimental and modeling results. The accurate prediction of jet penetration rate is a crucial factor for the computational model. Under diesel-engine-like conditions, it has been recognized that the location of the lifted premixed core of the flame is strongly influenced by the air that is entrained upstream of the lift-off location. The air-entrainment is a key factor that controls the speed at which the penetration tip propagates. Therefore, accurate prediction of vapor penetration is one of the key factors to capture the accurate entrainment of air, and subsequent autoignition characteristics.

It is observed from Fig. 5.1 that there are small differences between computed and measured penetration lengths at early times. This is due to the lack of appropriate physical modeling to capture the initial transient characteristics of the spray, which are governed by the gradual needle movement of the injector, and are neglected in the present modeling study. Here the injection rate is taken to be constant.

The sensitivity of computed liquid and vapor penetration lengths to variations in the turbulence model constant $C_{\epsilon 1}$ is illustrated in Fig. 5.2 for the WSR model. The standard value of $C_{\epsilon 1}$ is 1.44. However, it is well known that the standard value of $C_{\epsilon 1}$ produces significant overpredictions in jet spread rate for high-Reynolds-number turbulent round jets [147], and an overprediction in jet spread rate results in shorter jet penetration. This is often addressed in modeling studies by adjusting the value of $C_{\epsilon 1}$. The parametric study shows that the computed liquid penetration length is insensitive to the choice of $C_{\epsilon 1}$. This insensitivity of liquid penetration to the choice of $C_{\epsilon 1}$ is due to short interaction time between the liquid spray and gas-phase turbulence, which doesn't allow for any strong impact of gas-phase turbulence on the liquid penetration length. However, the vapor penetration changes significantly with $C_{\epsilon 1}$. The higher the value of $C_{\epsilon 1}$, the higher is the computed vapor penetration length. The standard value of $C_{\epsilon 1}$ produces significant underprediction of vapor penetration. The value of the model constant that produces the best match with the measurement is $C_{\epsilon 1}$=1.50.

The sensitivity of computed penetration lengths to the variations in breakup model constant is presented in Fig. 5.3. The breakup model used here is the Reitz-Diwakar model [140] that accounts for two primary modes of droplet breakup: bag

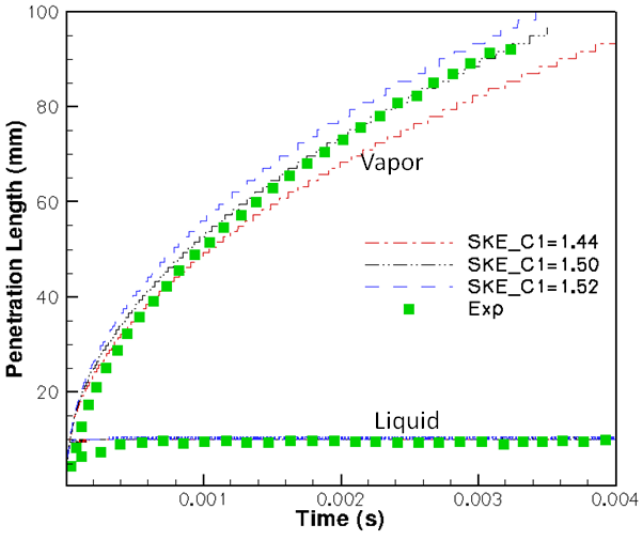

Figure 5.2. Sensitivity of computed liquid and vapor penetration lengths to variations in turbulence model coefficient $C_{\epsilon 1}$ for the WSR model. Three values of model constant have been considered: $C_{\epsilon 1}$=1.44, 1.50, and 1.52. The breakup constant is T_{strp}=19.

and stripping breakup. The stripping breakup is the predominant mode of breakup for high-pressure and high-velocity conditions that are typical characteristics of diesel engines. Here the sensitivity to variations in the breakup-time constant for stripping breakup (T_{strp}) is explored. Low values of T_{strp} result in faster breakup, and thereby to lower liquid penetration length. However, the vapor penetration length, being much larger than the liquid penetration length, is relatively insensitive to the choice of breakup model constant. Based on the comparison with the measurements, T_{strp}=19 produces the best match in liquid penetration length. Unless otherwise specified, T_{strp}=19 is used for the subsequent comparisons.

Figure 5.4 shows computed and measured radial profiles of mean mixture fraction from the WSR model and measurements at an axial location of z=17 mm and at t=0.49 ms after the start of injection. The injector tip is located at z=0. In the absence of chemical reaction, the mixture fraction is simply the fuel-vapor mass fraction. The maximum value of mean mixture fraction occurs on the centerline of the jet. This is due to the large amount of fuel vapor formed immediately downstream of the liquid column due to entrainment of hot surrounding gas. The mean fuel mass fraction decreases monotonically in the radial direction due to mixing

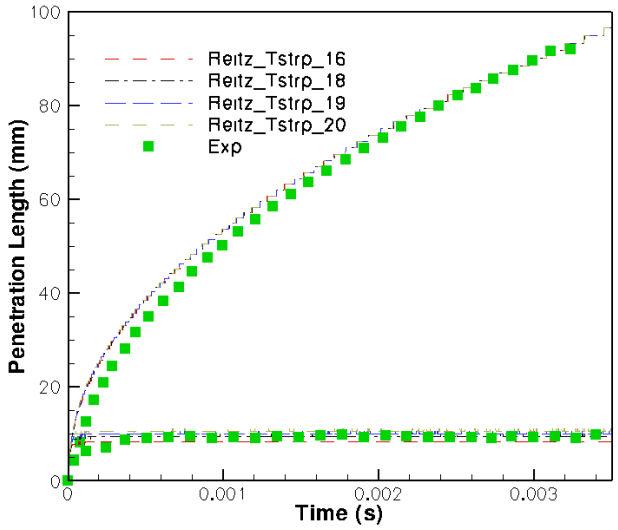

Figure 5.3. Sensitivity of computed liquid and vapor penetration lengths to variations in spray breakup model parameter T_{strp} for the WSR model. Four values of breakup time constant are considered: T_{strp}=16, 18, 19, and 20. The turbulence model used is the standard $k-\epsilon$ model with $C_{\epsilon 1}$=1.50.

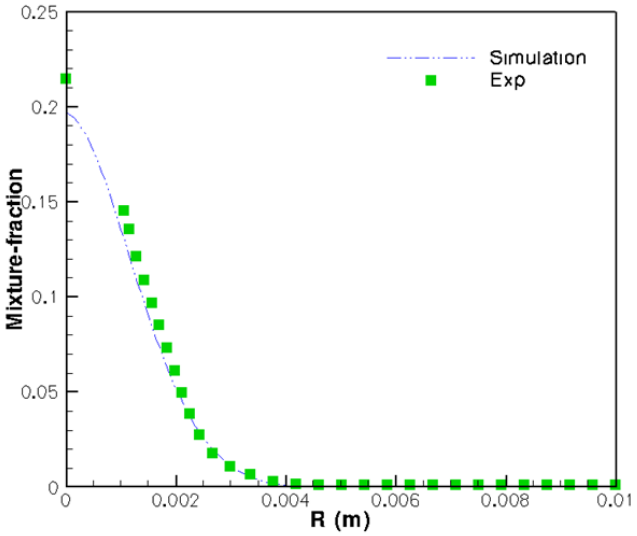

Figure 5.4. Computed (WSR model) and measured radial profiles of mean mixture fraction at axial location z=17 mm at time t=0.49 ms after start of injection for the baseline model.

with gas. The computational model shows good agreement with the data. The WSR model underpredicts the peak mixture fraction by approximately 5%, but the overall spreading rate is in excellent agreement with the experimental data. It is emphasized here that this is a key axial location, since it corresponds to the flame lift-off length for the 21% O_2 baseline n-heptane reacting-spray condition (as discussed in the next section, for reacting spray). The mean mixture fraction profile at this location is probably a good measure of how well the turbulence and spray models predict the correct mixing rate upstream of the flame.

The sensitivity of computed mean mixture fraction profiles to the variations in turbulence model constant $C_{\epsilon 1}$ is shown in Fig. 5.5. Four values of $C_{\epsilon 1}$ are considered: 1.44, 1.48, 1.50 and 1.52. The higher the value of $C_{\epsilon 1}$, the higher is the computed peak mean mixture fraction (on the injector axis). This is consistent to the earlier observation that higher $C_{\epsilon 1}$ results in higher vapor penetration length

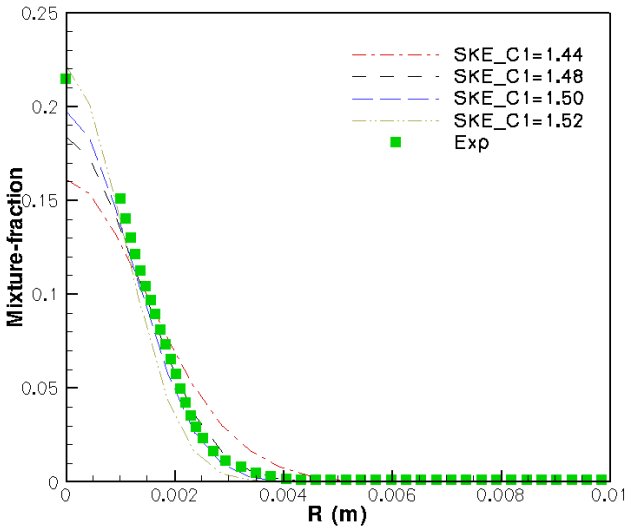

Figure 5.5. Sensitivity of computed radial profiles of mean mixture fraction at axial location z=17 mm at time t=0.49 ms after start of injection to variations in turbulence model constant $C_{\epsilon 1}$. Four values of model constant have been used: $C_{\epsilon 1}$=1.44, 1.48, 1.50, and 1.52. The breakup constant is T_{strp}=19.

(Fig. 5.2). The higher the vapor penetration, the narrower is the vapor column due to conservation of mass. The best match with the experiment is found for $C_{\epsilon 1}$=1.50, and since $C_{\epsilon 1}$=1.50 also provides the best match with the vapor penetration versus

time, this value is adopted for the rest of the computations.

We next compare results from WSR model with those from the PDF model.

Difference in the computed liquid and vapor penetration lengths between WSR and PDF models is presented in Fig. 5.6. The PDF model produces an excellent match in vapor penetration length with experimental data up to t=1.5 ms, and after 1.5 ms the model underpredicts the data. The WSR model, on the other hand, produces a better match with measurements at later times ($\geq$ 1.5 ms). Both models produce similar qualitative trends as that from the measurements.

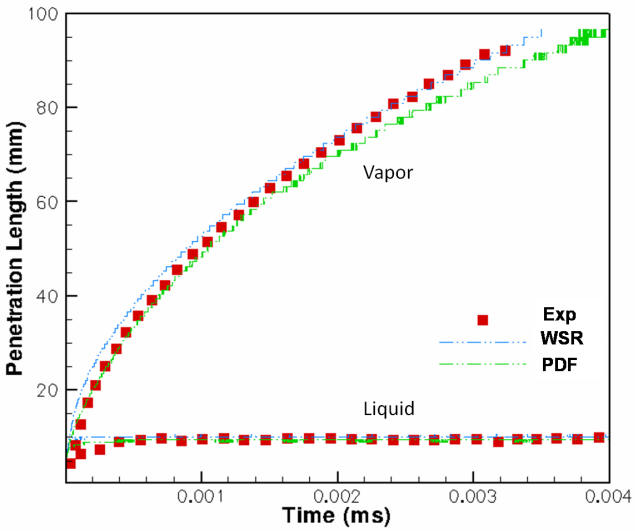

Figure 5.6. Comparisons of liquid and vapor penetration lengths versus time for the WSR and PDF models for the baseline model constants. For the PDF model, the IEM mixing model with C_ϕ=3.0 is used.

The WSR model shows some overprediction in vapor penetration length compared to the PDF model. It is noted here that the penetration length computations are based on distances from the nearest cell-center to the injector location. Therefore, the resolution of the computed penetration lengths is limited by the axial dimension of a cell. Moreover, computations for the PDF model are based on cell-mean values, which include fluctuations due to statistical noise. This noise is reflected in the small wriggles that can be seen in the vapor penetration. Both the WSR and PDF models predict liquid penetration reasonably well compared to the measurements.

Comparisons of radial profiles of mean mixture fraction between the WSR and

PDF models are presented in Fig. 5.7. The model predictions are compared with experimental measurements at an axial location of z=17 mm at time t=0.49 ms. While both the WSR and PDF models predict the jet spread rates in excellent agreement with the experimental data, the PDF model predicts the peak mean

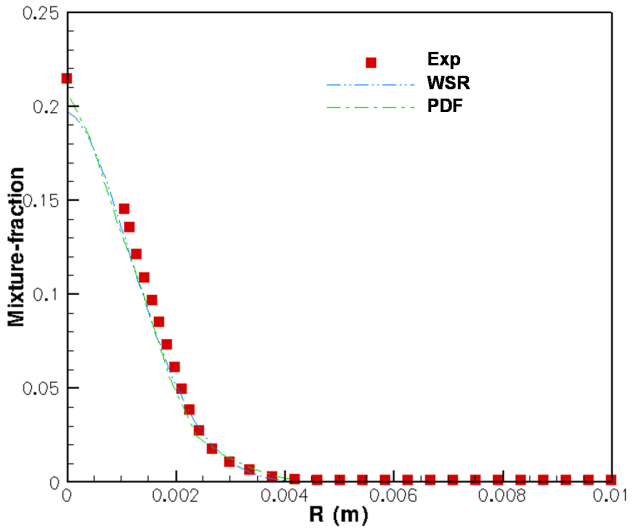

Figure 5.7. Comparison of radial profiles of mean mixture fraction at axial location z=17 mm at time t=0.49 ms after the start of injection for the WSR and PDF models, using the baseline model constants. For the PDF model, the IEM mixing model with C_ϕ=3.0 is used.

mixture fraction marginally better than the WSR model. The comparisons of radial profiles of mean mixture fraction are further investigated at axial locations, z=20 mm and z=40 mm at t=6 ms in Fig. 5.8 and 5.9, respectively. The PDF model shows a better match in mean mixture fraction profile with the measurements at z=20 mm and t=6 ms (Fig. 5.8). The centerline peak and the spread of the jet using the PDF model matches reasonably well with the measurements. However, the WSR model overpredicts the center-line peak and underpredicts the jet spread marginally. Figure 5.9 illustrates that further downstream (z=40 mm) at a later time (t=6 ms), the WSR model produces a closer match in mean mixture fraction with experiment than the PDF model. While the PDF model underpredicts the measurements at all radial locations, the WSR model produces the correct centerline peak. The tail of the radial profile becomes wider and the cen-

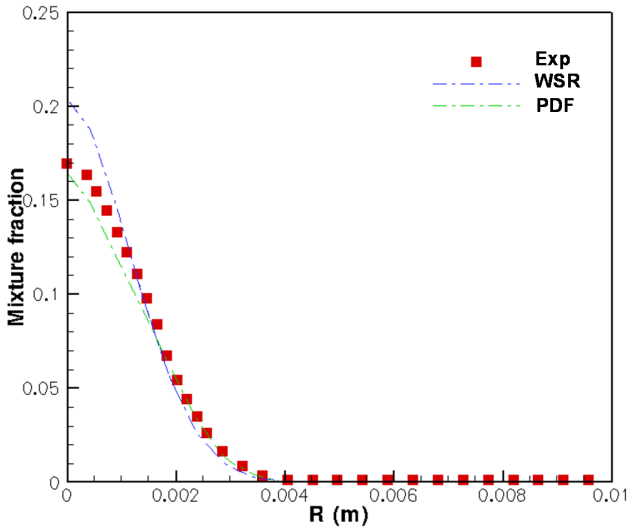

Figure 5.8. Comparison of radial profiles of mean mixture fraction at axial location z=20 mm at time t=6.0 ms after the start of injection for the WSR and PDF models, using the baseline model constants. For the PDF model, the IEM mixing model with C_ϕ=3.0 is used.

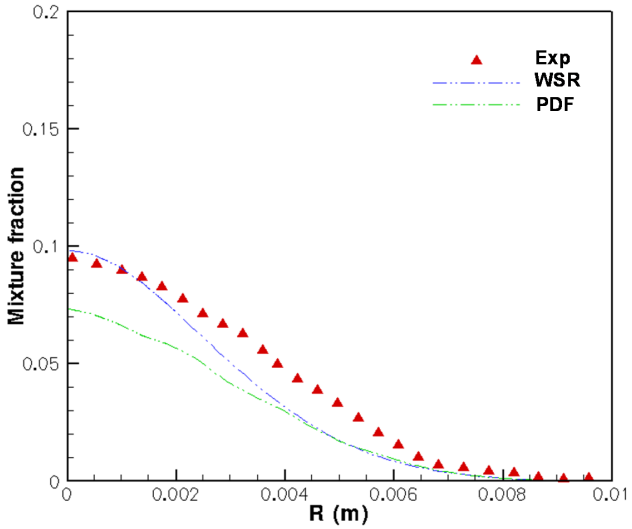

Figure 5.9. Comparison of radial profiles of mean mixture fraction at axial location z=40 mm at time t=6.0 ms after the start of injection for the WSR and PDF models, using the baseline model constants. For the PDF model, the IEM mixing model with C_ϕ=3.0 is used.

terline peak becomes lower for both the models, as the jet propagates downstream. The overprediction of peak mean mixture fraction by the WSR model compared to the PDF model is consistent with the difference in vapor penetration, as shown in Fig. 5.6. As time increases, the difference in vapor penetration increases. The higher vapor penetration of the jet for the WSR model results in a narrower jet width and a higher centerline value.

Figures 5.10 - 5.12 show the sensitivity of the computed radial mean mixture fraction profiles to the variations in the IEM mixing model constant C_ϕ for the PDF model. Comparisons are made with experimental measurements at axial location, z=17, 20 and 40 mm, and times t=0.49 and 6.0 ms. The WSR results are also included for comparison. Two values of C_ϕ are chosen for comparison: 2.0 and 3.0. At z=17 mm and t=0.49 ms, the two mixing model constants produce almost identical results. For C_ϕ =3.0, the center-line peak value is marginally closer to the WSR result than the value for C_ϕ =2.0. This trend continues at other locations (z=20 and 40 mm). At z=20 mm, C_ϕ =3.0 produces the closer match with the measurements, whereas C_ϕ =2.0 underpredicts. This observation is consistent

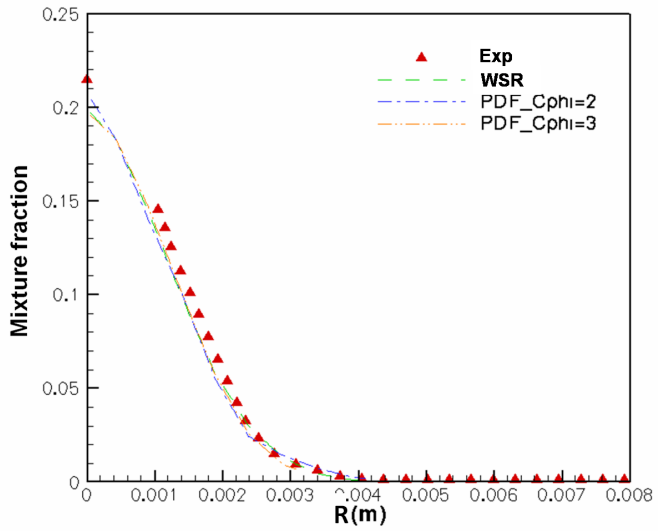

Figure 5.10. Sensitivity of computed mean mixture fraction profiles to variations in C_ϕ of IEM mixing (PDF model) at axial location z=17 mm and at t=0.49 ms after start of injection. Two values of C_ϕ are considered: C_ϕ=2.0 and 3.0. The WSR profile is also included for comparison.

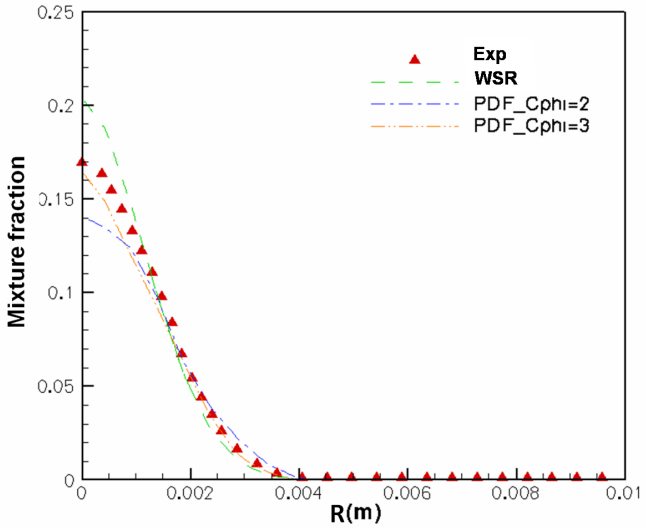

Figure 5.11. Sensitivity of computed mean mixture fraction profiles to variations in C_ϕ of IEM mixing (PDF model) at axial location z=20 mm and at t=6.0 ms after start of injection. Two values of C_ϕ are considered: C_ϕ=2.0 and 3.0. The WSR profile is also included for comparison.

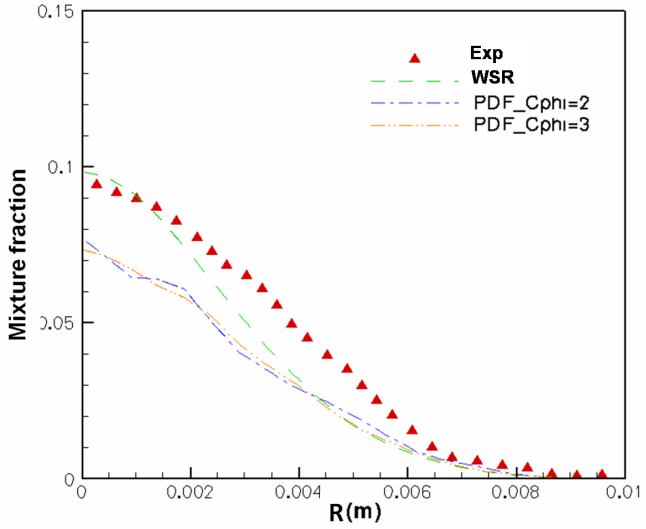

Figure 5.12. Sensitivity of computed mean mixture fraction profiles to variations in C_ϕ of IEM mixing (PDF model) at axial location z=40 mm and at t=6.0 ms after start of injection. Two values of C_ϕ are considered: C_ϕ=2.0 and 3.0. The WSR profile is also included for comparison.

with the physical modeling, which suggests that as C_ϕ increases, the particle values should relax to the cell mean values at a faster rate. In another words, the higher the value of C_ϕ, the closer the results from the PDF model should be to those from the WSR model, and the faster is the decay rate of mixture fraction variance. This is further supported by the radial profiles of mixture fraction variance shown in Fig. 5.13. Higher mixture fraction variance is observed at all radial locations for C_ϕ =2.0 compared to C_ϕ =3.0. The overall trend of the mixture fraction variance is similar for both values of the mixing model constant C_ϕ. For C_ϕ =2.0, the variance of mixture fraction is overpredicted compared with measurements, while C_ϕ =3.0 underpredicts the data at most of the locations. The peak value of variance of

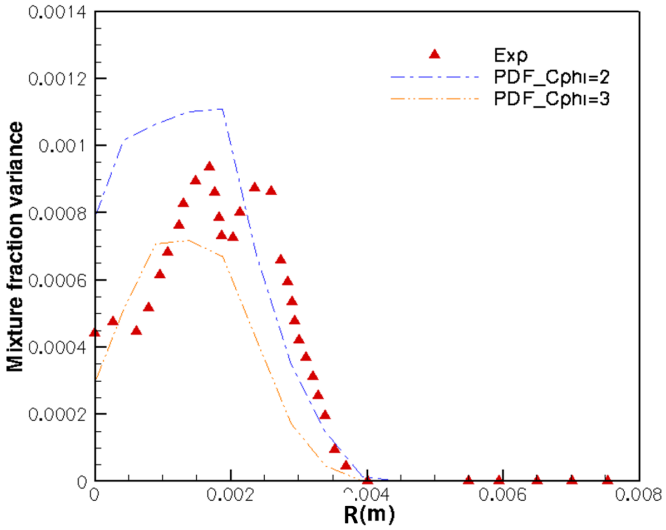

Figure 5.13. Sensitivity of computed mean mixture fraction variance profiles to variations in C_ϕ of IEM mixing (PDF model) at axial location z=17 mm and at t=0.49 ms after start of injection. Two values of C_ϕ are considered: C_ϕ=2.0 and 3.0. The WSR profile is also included for comparison..

mixture fraction occurs along the shear layer between the fast-moving vapor jet and the near-stationary gas surrounding the jet. Strong entrainment along the edge of the vapor jet enhances the turbulent mixing, which results in an increase in mixture fraction variance along this shear layer. The experimental measurements show two peaks away from the centerline of the jet, while the PDF model has shown one peak. The presence of two peaks in the measurement data is not well

understood, and may be attributed to the large uncertainties of measurements.

Time evolution of contours of computed mean mixture fraction and mixture fraction variance are shown in Figs. 5.14 and 5.15 for the PDF model using IEM mixing with C_ϕ=3. The mean mixture fraction grows axially with time, whereas the mixture fraction variance attains a quasi-steady profile and remains attached to a small region downstream of the injection point. This is the region where the mixture fraction variance is highest. Downstream of this region, the variance decays rapidly.

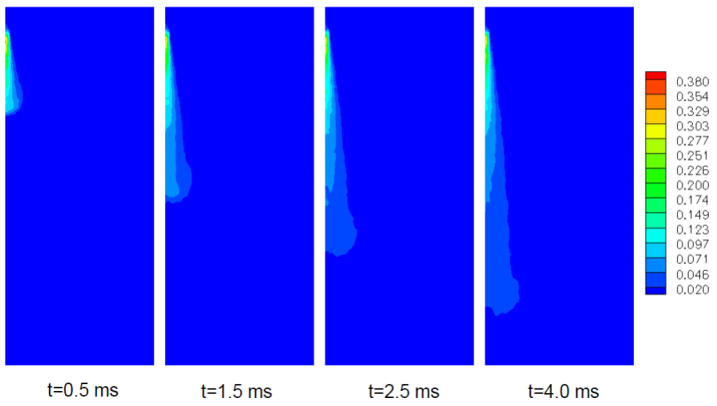

Figure 5.14. Computed contours of mean mixture fraction for the PDF model with IEM mixing (C_ϕ=3.0) at times t=0.5, 1.5, 2.5, 4.0 ms after the start of injection for baseline turbulence and spray models.

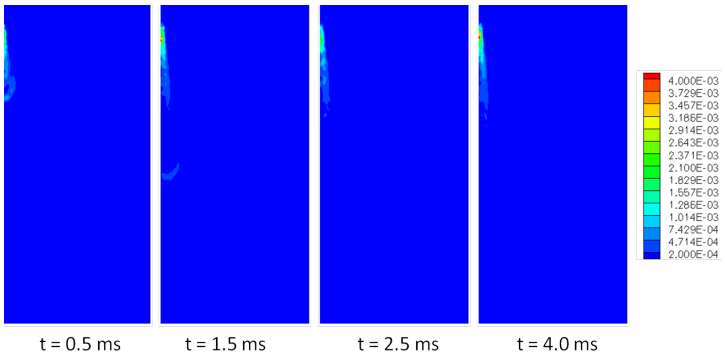

Figure 5.15. Computed contours of mixture fraction variance for the PDF model with IEM mixing (C_ϕ=3.0) at times t=0.5, 1.5, 2.5, 4.0 ms after the start of injection for baseline turbulence and spray models.

This completes the comparison of results for non-reacting evaporating n-heptane sprays between the WSR and PDF models. In the absence of chemistry, model

predictions have been validated with experimental measurements for both models and differences between the models are generally small. Sensitivity studies have been carried out to establish a set of baseline model constants for turbulence, breakup and mixing models. The capabilities of the WSR and PDF models have been evaluated by comparing the numerical results for penetration lengths, mean mixture fraction profiles, and mixture fraction variance profiles (the latter for the PDF model only) with those from experimental measurements. To ensure high accuracy of the numerical predictions, a relatively small time step of dt=2x10^{-7} has been adopted for the PDF method. Results using dt=2x10^{-7} s are also compared with those using a time step of dt=1x10^{-7} s, and the solutions are confirmed to be independent of dt (not shown). The PDF model is initialized with N_{Pc}=30 particles per cell to ensure the balance between expediency and accuracy of computations. For high velocity liquid blob-injection, the maximum droplet Courant number is set as 0.3 to ensure a good resolution for physical modeling of droplet motion. The results for the PDF model have been obtained using the IEM mixing model. Comparisons in predictions using different mixing models are left for the reacting spray flames.

5.2 Autoignition and Combustion for n-Heptane Spray Flames

In this section, computed and measured results are compared for the chemically reacting turbulent spray flames. Results from two modeling approaches are compared: a PDF model that explicitly accounts for TCI, and a WSR model that ignores TCI. In the model that neglects TCI the mean chemical source terms for the mean species transport equations are computed based on cell-based mean values that are computed from the RAS equations, thereby neglecting the effects of turbulent fluctuations. For the PDF model chemical source terms are computed for each stochastic particle from the local composition variables corresponding to that particle, thereby accounting for the effects of turbulent fluctuations. The comparison between the predictions using the WSR (no TCI) and PDF (with TCI) models is focused on understanding and exploring the degree to which TCI need to be

considered to reproduce realistic turbulent flame structures and combustion characteristics for thermochemical conditions representative of those in diesel engines. The primary combustion data that are available for the validation of computational models include ignition delay, flame lift-off length [66], OH-contours, and soot volume fraction distributions. Unlike the non-reacting spray, the validation of computational models for n-heptane spray flames covers a wide range of operating conditions (Table 4.2) and provides an opportunity to evaluate the accuracy and consistency of the computational models under different conditions.

The results in this section are organized as follows. First, results are shown for the baseline n-heptane spray flames, which are referred to as "Spray-H" in ECN data, and then the comparisons are extended to other conditions. The baseline conditions are characterized by an initial gas temperature of T=1000 K, density of ρ=14.8 kg/m^3, and variations in O_2 mole fraction from 8% - 21%. For non-baseline conditions, comparisons are presented for variations in initial temperature (800 - 1200 K), initial density (14.8 and 30.0 kg/m^3), and initial O_2 mole fraction (8% - 21%).

5.2.1 Baseline n-Heptane Spray Flames

For the baseline conditions, sensitivities of computed ignition delays and flame lift-off lengths first are investigated to variations in the chemical mechanism within the framework of the WSR model. Results for lift-off length and ignition delay are then compared with and without TCI (PDF versus WSR models). The differences in predictions between these two models are investigated using contours of OH mass fraction and temperature. The predictions are compared qualitatively with experimental chemiluminescence images of OH mass fraction. The sensitivity of the computed ignition delay and lift-off length to variations in the mixing model constant using the IEM mixing model is investigated within the framework of the PDF model. The study also includes comparison between two mixing models: (IEM and EMST) to explore the sensitivity of transient ignition/flame characteristics to the choice of mixing model. Next $\phi - T$ maps are presented with and without consideration of TCI. The $\phi - T$ maps are investigated both close to the time of autoignition and during the quasi-steady flame. Comparisons of computed

soot volume fractions with and without consideration of TCI are presented next. Radial profiles of soot volume fraction predicted by the models at selected locations are compared against the measurements. The role of the gas-phase kinetic model in soot prediction is also discussed. Soot results are compared for two soot models: a two-equation model and a MOMIC-based model. Finally results are compared with and without an optically-thin soot radiation model.

5.2.1.1 Autoignition and Combustion Diagnostics

Comparisons of computed ignition delays and lift-off lengths with measurements for different initial O_2 levels are presented for three different skeletal mechanisms without TCI (WSR model) in Figs. 5.16 and 5.17 respectively. The determination of ignition delays and lift-off lengths were discussed in Chapter 4. The lift-off length is defined as the first axial location where the computed Favre-averaged OH mass fraction reaches 0.00025. This is consistent with the general notion that a flame contour is often visually interpreted by the OH-mass-fraction. However, the criterion for ignition delay is not as straightforward, and several criteria are available; those include pressure-, temperature- and OH-mass-fraction-based criteria. Pressure-based criteria are, perhaps, most common for characterization of ignition delay in engine experiments. However, for the conditions of interests here, it has been recognized that pressure-based criteria are not appropriate. This is because, in contrast to an engine, the autoignition results in only a small rise of pressure compared to the initial pressure in the chamber, which imposes difficulties for the pressure sensors to isolate the effects of small changes in pressure due to the spray from the beginning of autoignition. For the present work, a temperature rise of 400 K is used as a criterion to compute the ignition delay. The ignition delay and lift-off length both decrease as the initial O_2 level increases. This is because the higher the O_2 level, the faster the fuel-air mixture reaches the desired composition for autoignition. The location of the lift-off position is primarily governed by the entrainment of the oxidizer into the fuel jet upstream of the rich premixed core that initiates the autoignition process. Typically the autoignition starts at an equivalence ratio of approximately four [56, 57] in the premixed region. For the baseline n-heptane conditions, the physical conditions of the air and fuel that control the entrainment remain approximately same. However, with decreasing

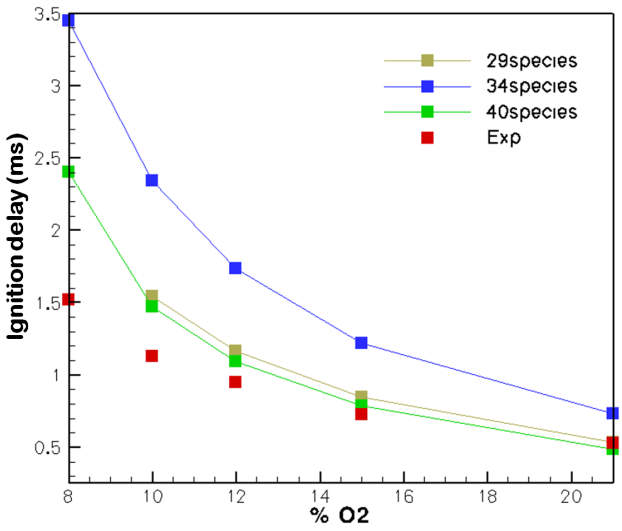

Figure 5.16. Computed and measured ignition delays versus O_2 level for 29-species, 34-species, and 40-species skeletal mechanisms for baseline n-heptane conditions using the WSR model.

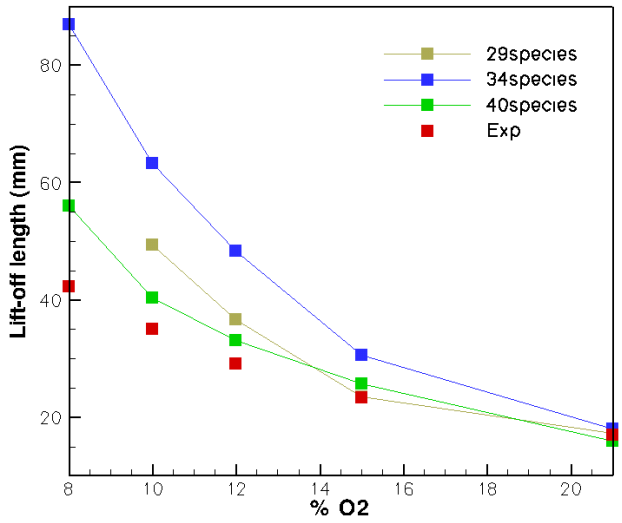

Figure 5.17. Computed and measured lift-off lengths versus O_2 level for 29-species, 34-species, and 40-species skeletal mechanisms for baseline n-heptane conditions using the WSR model.

O_2 level, the ambient gas becomes progressively diluted. Therefore, to reach the desired equivalence ratio, the jet has to travel further downstream. This increases the lift-off length, with a commensurate increase in ignition delay. All the kinetic models capture this trend. It is also observed that all the kinetic models show better match with the measurements for higher O_2 levels (15% and 21%). The level of agreement deteriorates as the O_2 level drops. However, for any O_2 level, the degree of agreement with the measurement varies within the kinetic models. For the 21% O_2 level, the best agreement is observed for 29-species mechanism [94], with the predicted ignition delay on top of measurement. The 40-species mechanism [2] underpredicts the ignition delay (by 20%), and the 34-species mechanism [94] significantly overpredicts (by 38%) the ignition delay. However, for the 21% O_2, the lift-off lengths for all the kinetic models do not show any appreciable differences, and are close to the measurements. For 15% or lower O_2 levels, the 40-species mechanism shows the best agreement in ignition delay, followed by the 29-species mechanism. These two mechanisms show almost parallel trends, with marginal overprediction by the 29-species mechanism for most O_2 levels. The 34-species mechanism deviates from the measurement significantly as the O_2 level drops below 15%. The same trend is observed for the lift-off length comparison, where the predictions diverge from the experimental data as the O_2 level drops, with the 34-species mechanism showing the maximum deviation. It is worth noting that for the 29-species mechanism, the computed OH-mass fraction never reaches the cut-off criteria for lift-off length (0.00025) for 8% O_2, although a flame is observed in the simulations.

The comparisons of ignition delay and lift-off length suggest that the quality of CFD predictions can vary widely from one kinetic mechanism to another. Moreover, the prediction capability changes significantly with the operating conditions. This is expected, because all three chemical mechanisms that are used here have been derived from a detailed chemical mechanism using highly optimized tools that make the kinetics suitable within a range of operating conditions. Outside of these conditions, these mechanisms may not perform well. Therefore, care needs to be taken in applying these mechanisms to extreme operating conditions. For the comparisons presented here (Fig. 5.16 and 5.17), it is evident that none of the mechanisms performs particularly well for low O_2 levels (8% or less). However, the

40-species mechanism performs better than the other two mechanisms, and therefore, this mechanism is used for the subsequent studies. The ECN-recommended 29-species mechanism is not used here, since it does not have key species (e.g., C_2H_2) that are required for the prediction of soot.

Figure 5.18 compares the computed ignition delays with versus without TCI (PDF versus WSR), and with the measurements for the baseline n-heptane flames. The comparisons include a range of O_2 levels from 8% to 21% at a constant ambient pressure of 42 bar and temperature of 1000 K. At 21% O_2, both the models (with and without TCI) underpredict the ignition delay, the margin of underprediction being approximately 20% for the PDF model and 8% for the WSR model. At 15% O_2, the PDF model produces a better match with the measurement compared to the WSR model. At this O_2 level, the PDF model underpredicts the measurement by approximately 4%, while the WSR model overpredicts by approximately 7.5%. As the O_2 level drops further, the PDF model overshoots the measurement, and both models deviate from the measurements. However, the trends for the two

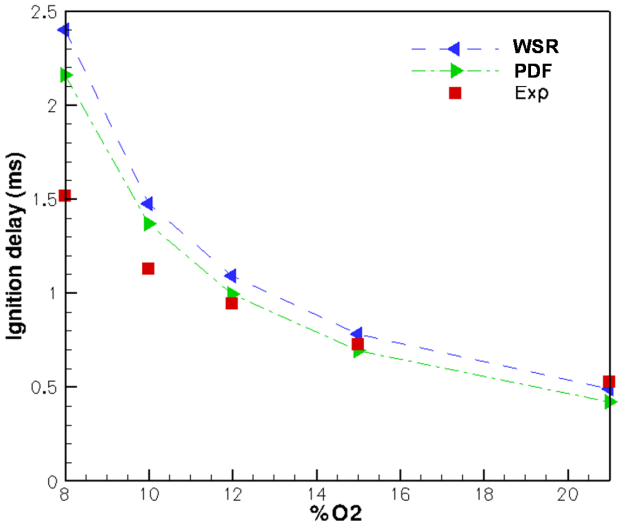

Figure 5.18. Computed and measured ignition delays versus O_2 level for baseline n-heptane conditions with the WSR and PDF models using a 40-species skeletal mechanism. For the PDF model, IEM mixing is used with C_ϕ=3.0.

models are almost parallel to each other, with the PDF model producing lower ignition delays compared to the WSR model. It should be recognized here that

apart from the fact that the PDF model accurately captures the influences of turbulent fluctuations in chemistry, there are differences in the implementation of the physical models for the two approaches. The PDF model uses a hybrid Lagrangian/Eulerian approach; the implementation of the molecular diffusion of species and energy occurs at the particle level. The particle-tracking algorithm, the stochastic nature of the particle evolution, and the coupling between Eulerian and Lagrangian sides through a consistent algorithm for mean density - all contribute to producing differences between the WSR and PDF models. However, the principal difference between the PDF and WSR models is in how the mean chemical source terms are computed. Larger differences between the models are found for low ambient temperatures (Sec. 5.2.2 below).

Figure 5.19 shows the differences in the computed lift-off lengths with and without consideration of TCI, and compares them with the measurements. The PDF model produces higher lift-off lengths than those produced by the WSR model. This is in contrast to the prediction of ignition delay, where the PDF model shows somewhat better agreement with the measurement data. Overprediction of lift-off length was also reported by Pei *et al.* [198] for the n-heptane ECN spray flames. The PDF model shows oscillations in lift-off length with time, even after a quasi-stationary flame is established. These oscillations are due to the stochastic nature of the method. The amplitudes of the oscillations vary with the O_2 level, and increase significantly as the O_2 level drops. The variation of lift-off length with time for 21% O_2 is shown in Fig. 5.20. The lift-off lengths presented in Fig. 5.19 have been averaged over time. For all the O_2 levels other than 8%, the time averaging is over 2.5 to 4 ms, and for 8% O_2, the averaging period is from 3 to 4 ms. The variation of the lift-off length with time for 8% O_2 is presented in Fig 5.21. The oscillations increase significantly from 21% to 8% O_2. As the O_2 level drops, the high-temperature diffusion flame progresses towards a more distributed reaction zone, where the flame characteristics become sensitive to small changes in thermophysical conditions, and a tight coupling between the chemistry and hydrodynamics is important for realistic model predictions. It is also worth mentioning here that the lift-off lengths presented here are cell-center distances from the injector location. Therefore, the numerical resolution of lift-off length corresponds to the axial distance between two adjoining cells. However, the

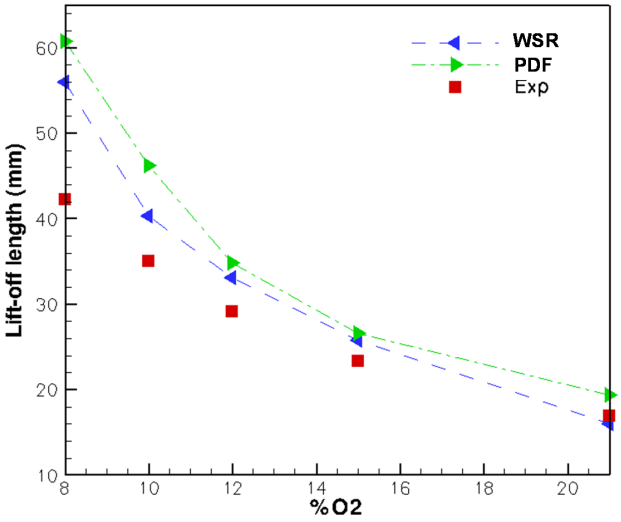

Figure 5.19. Computed and measured lift-off lengths versus O_2 level for baseline n-heptane conditions with the WSR and PDF models using a 40-species skeletal mechanism. For the PDF model, IEM mixing is used with C_ϕ=3.0.

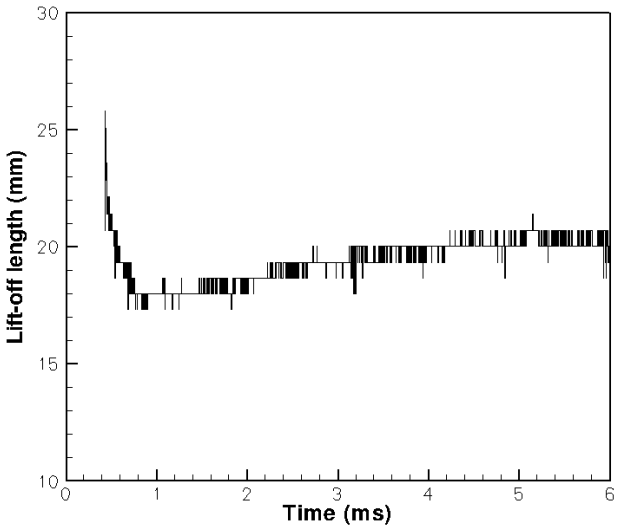

Figure 5.20. Computed lift-off length versus time for the 21% O_2 baseline n-heptane flame using the PDF model with IEM mixing. The mixing model constant is C_ϕ=3.0.

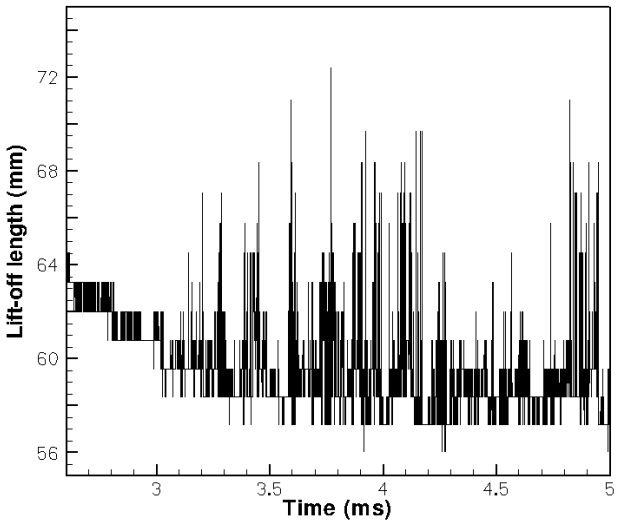

Figure 5.21. Computed lift-off length versus time for the 8% O_2 baseline n-heptane flame using the PDF model with IEM mixing. The mixing model constant is C_ϕ=3.0.

computational cells are nonuniform both axially and radially, with the smallest cells located near the injector. Further downstream of the nozzle, the computational cells become more coarse. This results in an apparently higher amplitudes of oscillations for lower O_2 levels, since for lower O_2 levels, the lifted flames lie in relatively the coarse-mesh region. Figure 5.20 also shows that the autoignition starts at a location downstream of the stable lift-off location, and the flame then travels upstream with time until a stable lifted flame is established. The WSR model shows similar characteristics for the lift-off length (Fig. 5.22). However, no oscillations are observed with the WSR model.

Figure 5.23 compares the temporal evolution of the mean OH-mass fraction contours for the PDF and WSR models for 21% O_2. OH is a key radical that characterizes the flame and heat-release processes. Accurate prediction of OH is important for the computational models to capture the key flame characteristics. The shape of the mean OH contour gives a visual representation of the mean flame brush of the turbulent flame. Figure 5.23 shows that the flame starts from a location downstream of the injection point and grows axially with time. During the early phase of flame development, a narrow OH contour is observed, which becomes broader as the flame travels downstream. It is observed that from the

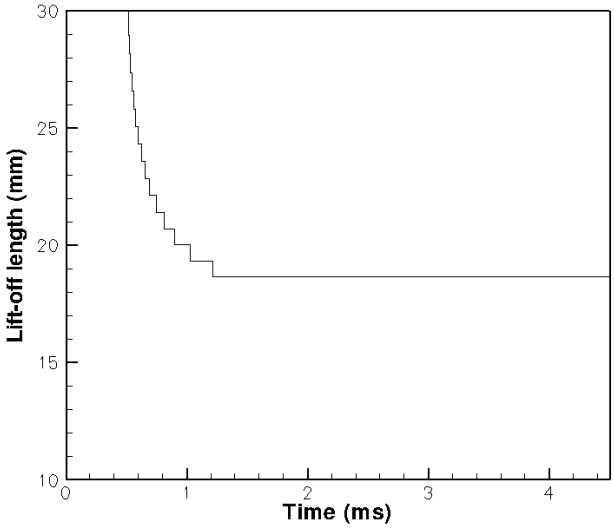

Figure 5.22. Computed lift-off length versus time for the 21% O_2 baseline n-heptane flame using the WSR model.

beginning of auto-ignition, the PDF model produces a broader mean reaction zone than the WSR model; the latter produces an extremely thin mean reaction zone with significantly higher peak OH than the PDF model. The experimental evidence from OH-chemiluminescence images suggest that the broader OH-contours similar to that observed with the PDF model are more realistic. The ability of the PDF model to explicitly account for the effects of turbulent fluctuations in the species mass fractions and enthalpy demonstrates a considerable advantage over the WSR model in producing a realistic turbulent flame structure, even in cases where the global lift-off lengths and ignition delays vary little between the two models.

Figure 5.24 compares computed mean temperature contours with and without considering TCI. The comparisons are similar to those for the mean OH-contour. The initial temperature of the domain is 1000 K. A lifted flame is observed downstream of the injector location. Near the injector location a low-temperature ($\sim$600 K) region is observed. This is due to the evaporative cooling of the liquid fuel. The initial development of the flame with the PDF model appears to be similar to that of the WSR model. However, at later time ($\geq$ 2 ms), the WSR model produces a longer and narrower high-temperature region compared to the PDF model. At about t=4 ms, the differences between the two models can be clearly

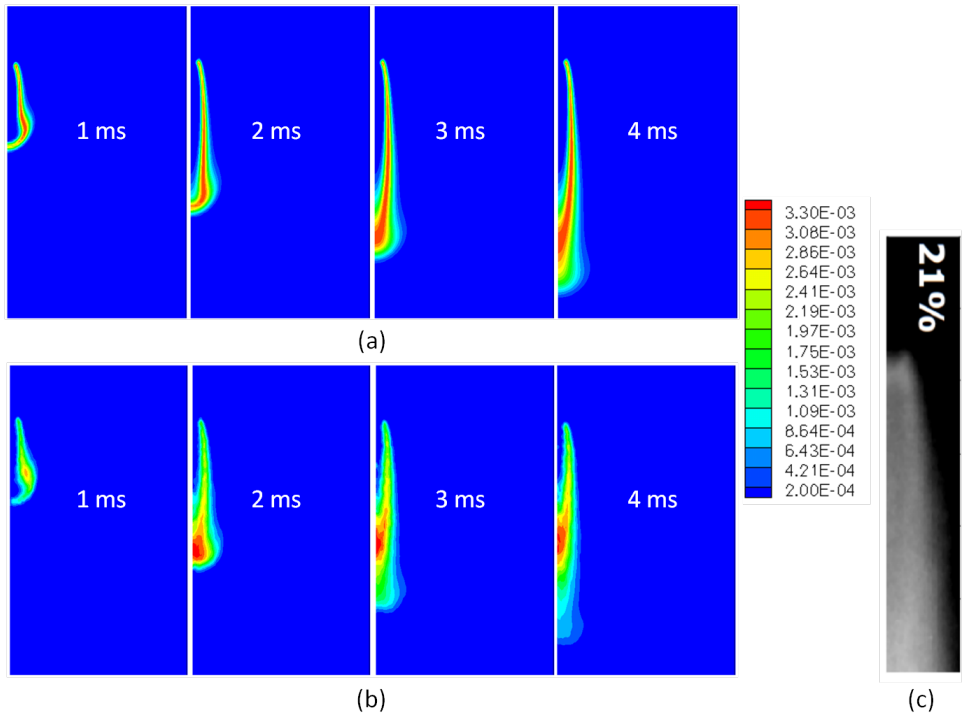

Figure 5.23. Computed mean contours of mean OH-mass fraction for the 21% O_2 baseline n-heptane flame (a) without TCI (WSR model) ,(b) with TCI (PDF model), and (c) experiment [1] at times t=1, 2, 3, and 4 ms after the start of injection. For the PDF model, IEM mixing is used with C_ϕ=3.0.

seen. The effect of turbulent fluctuations in the composition variables in the PDF model produces a mixing effect that eventually brings down the peak mean temperature and provides a more distributed flame zone. For the WSR model, the peak mean temperature is higher (by approximately 10 K) compared to the PDF model. This observation is consistent with Fig. 5.23 that shows a narrow strip of highly concentrated OH mass fraction for the WSR model and a more distributed mean OH-mass fraction contour for the PDF model. The narrow strip of OH-profile results in significantly higher local heat release rate and temperature values over a narrower region of the flame.

Figure 5.25 shows the differences in computed heat-release rates with and without TCI for baseline n-heptane fuel with 21%, 15%, and 8% O_2 levels, respectively. The WSR model shows higher peak in heat-release rate compared to the PDF model. This is consistent with the earlier observations (Fig. 5.18) that suggest shorter ignition delays for the PDF model compared to those from the WSR model.

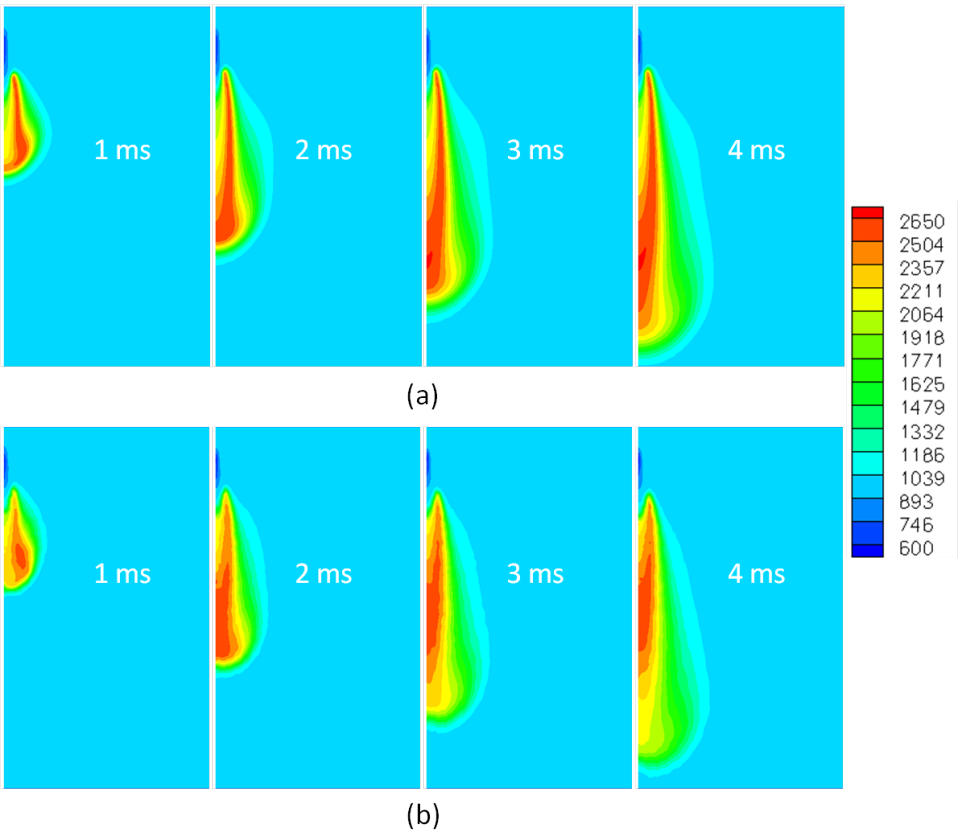

Figure 5.24. Computed contours of mean temperature for the 21% O_2 baseline n-heptane flame (a) without TCI (WSR model), and (b) with TCI (PDF model) at times t=1, 2, 3, and 4 ms after the start of injection. For the PDF model, IEM mixing is used with C_ϕ=3.0.

In general, earlier ignition broadens (in time) the heat-release rate, and results in a smaller peak for the PDF model. With the decrease in O_2, the differences in ignition delay increase between the two models, resulting in larger differences in heat-release rate.

An equivalence-ratio-temperature ($\phi - T$) map for the entire computational domain with the WSR model is presented in Fig. 5.26(a) for the quasi-steady flame. The equivalence ratio (ϕ) is computed from the mixture fraction using the equation,

$$\phi = \frac{f}{1-f}\left(\frac{A}{F}\right)_{st}, \tag{5.1}$$

where f is the mixture fraction computed from elemental carbon and hydrogen

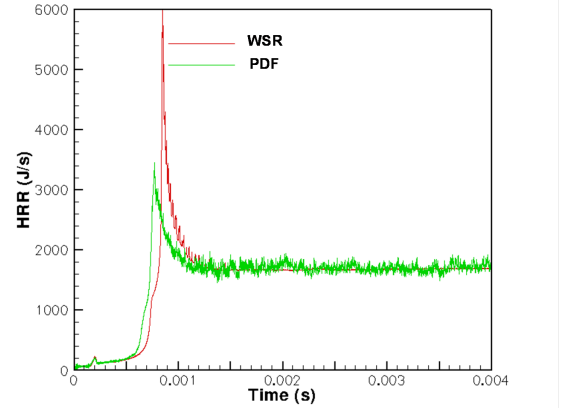

(a)

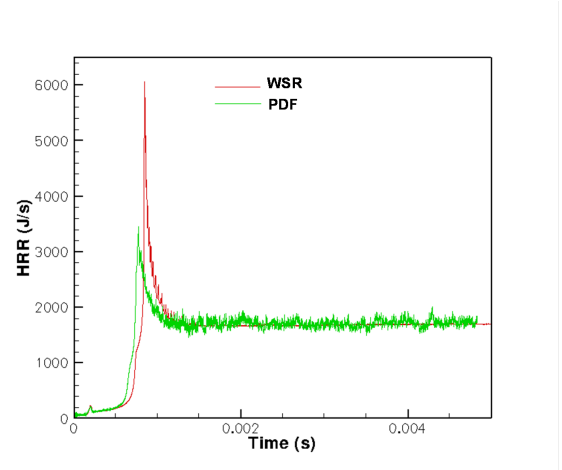

(b)

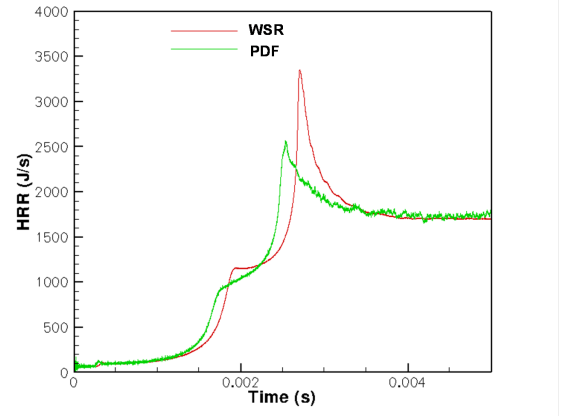

(c)

Figure 5.25. Computed heat-release rates versus time for the WSR and PDF models for (a) 21% O_2, (b) 15% O_2, and (c) 8% O_2 baseline n-heptane flames. With the PDF model, IEM mixing is used with C_ϕ=3.0.

mass fraction, and $(A/F)_{st}$ is the stoichiometric air-fuel ratio. The computed $\phi - T$ map is compared with a generic $\phi - T$ map for compression-ignition configuration (Fig. 5.26(b)) [199]. The simulated results demonstrate remarkable qualitative agreement with the trends in [199]. In an engine, the $\phi - T$ map strongly depends on injection timing: early injection timing results in near-homogeneous, low-equivalence-ratio mixture before combustion, and avoids the high-equivalence-ratio sooting zone [199]. The $\phi - T$ maps presented in Fig. 5.26(a) show that the computed results lie between the extreme limits of early and late injection in engines (Fig. 5.26(b)). The differences in computed $\phi - T$ maps between the PDF and WSR models are presented in Fig. 5.27 for 21% and 8% O_2 levels. For the WSR model, the $\phi - T$ values are the cell-center values from the finite-volume mesh, whereas for the PDF model, particle values are plotted. Both the models (PDF and WSR) predict similar distributions. The location of the peak-temperature increases towards higher ϕ as the O_2 level drops. As the O_2 level decreases, the ambient gas becomes more diluted. As a consequence, the stoichiometric air-fuel ratio increases, which in effect, increases the equivalence ratio (as defined here) even if the fuel mass fraction remains approximately the same. Higher dilution results in lower peak temperature. The maximum temperature occurs at the diffusion layer of the flame. Referring to Fig. 5.27, equivalence ratios above this point belong to the fuel-side of the diffusion-layer, and equivalence ratios below this point belong to the ambient-side of the flame. The different regimes of the turbulent spray flame are labeled for 8% O_2 level in Fig. 5.27. The shape of $\phi - T$ map that belongs to the ambient-side of the diffusion flame remains approximately the same for the PDF and WSR models. Similar observations are made in the near-injector region, which is characterized by high equivalence ratios and low temperatures ($\leq$ 1000 K). In this region, the evaporation of the liquid fuel reduces temperature of the gas mixture, and produces pockets of local fuel-rich mixture. It is observed that the only difference between the PDF and WSR models occurs on the fuel-rich side of the flame. On the fuel-rich side of the flame, the WSR model shows a temperature rise at higher equivalence ratio compared to the PDF model. The difference between the two models increases as the O_2 level drops from 21% to 8%. The narrow range of equivalence ratio over which the temperature rises on the fuel-rich side of the PDF model suggests to combustion with near-homogeneous or

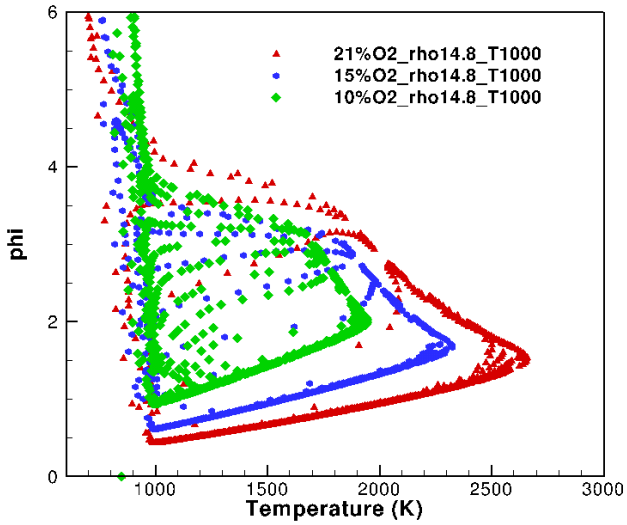

(a)

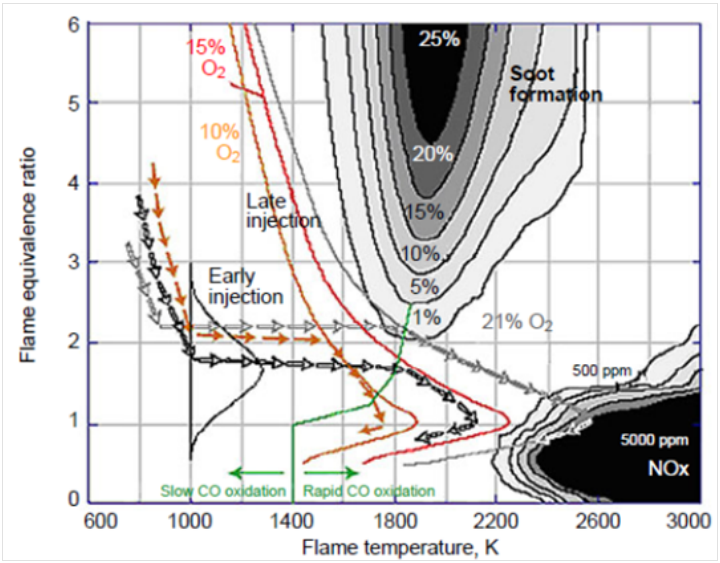

(b)

Figure 5.26. Comparison of $\phi - T$ maps between (a) the WSR model, and (b) Sandia data [199] for baseline n-heptane conditions with 21%, 15%, and 10% O_2 levels.

premixed combustion (Fig. 5.26(b)) that produces a steep temperature-rise while the mixture fraction/equivalence-ratio remains approximately constant. This region of the flame is recognized as the fuel-rich premixed region near the injector axis (Fig. 5.27(c)). A possible reason for the differences in $\phi - T$ maps between

the PDF and WSR models in the premixed zone is that the turbulence-chemistry interactions, which result in stronger mixing effect by accounting for turbulent fluctuations in chemistry. This effect is particularly observed on the fuel-rich side of the flame due to the high-gas velocity induced by the spray. On the ambient-side of the flame the gas velocity is significantly lower and the turbulent fluctuations are too low to make any contribution to the combustion process. The shape of the $\phi - T$ map changes from 21% t0 8% O_2. With 8% O_2, a longer premixed zone is noticed. This is probably due to the longer ignition delay for 8% O_2, which allows additional mixing time for the fuel-vapor prior to ignition. The $\phi - T$ map for the 21% O_2, due to faster chemistry, is closer to the classic flamelet profile. However, at 8% O_2 more data fill in between the fast-chemistry limit and the unburnt mixing line. It is worth mentioning that the equivalence ratio computed from local mixture fraction does not drop to zero at locations where fuel mass fraction is zero. This is because the initial gas composition includes water and carbon dioxide, which give non-zero mixture fraction, since mixture fraction is computed from elemental carbon and hydrogen mass fractions.

The $\phi - T$ maps provided in Fig. 5.26(a) and 5.27 are at time t=4 ms, when a quasi-steady flame is established. An example of the temporal evolution of the $\phi - T$ map through ignition is illustrated in Fig. 5.28. It is observed that during the early stages of ignition, the shape of the $\phi - T$ map changes gradually from low to high temperatures. Once the flame reaches the maximum temperature, the shape of $\phi - T$ profile remains approximately the same. This occurs at approximately 0.5 ms after the start of injection for the condition shown.

The results that have been presented above for the PDF model are with IEM mixing with C_ϕ=3.0. Recall that this choice of the model constant C_ϕ was based on a sensitivity study for a non-reacting n-heptane spray. For the reacting spray, the sensitivity of global ignition/combustion characteristics to variations in C_ϕ is explored for the 21% O_2, n-heptane baseline condition. Comparisons of lift-off lengths and ignition delays for two values of C_ϕ (2.0 and 3.0) are presented in Table 5.3. The computed ignition delay is insensitive to C_ϕ, while the lift-off length increases marginally as C_ϕ decreases. Lower C_ϕ corresponds to slower mixing processes, while as $C_\phi \to \infty$, the particle compositions relax to the cell mean values. Therefore the PDF results for higher C_ϕ approach those from the WSR model. Over

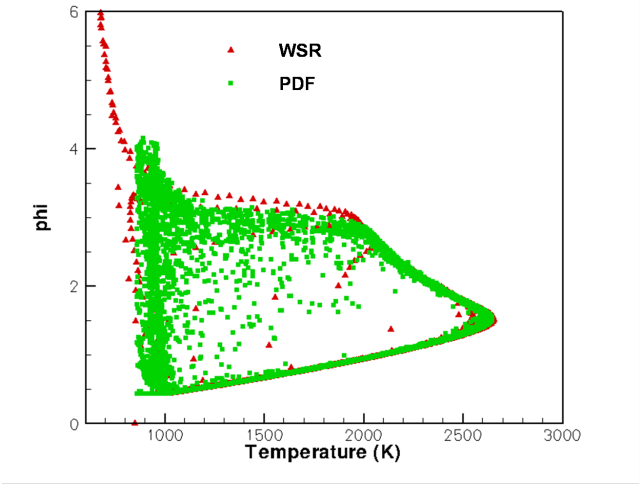

(a)

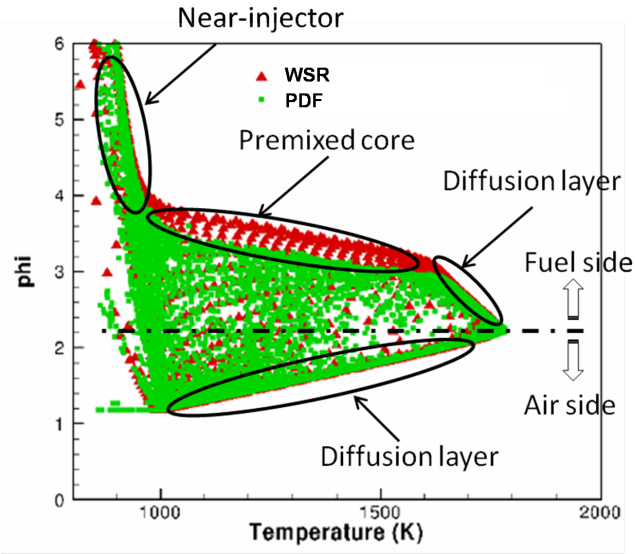

(b)

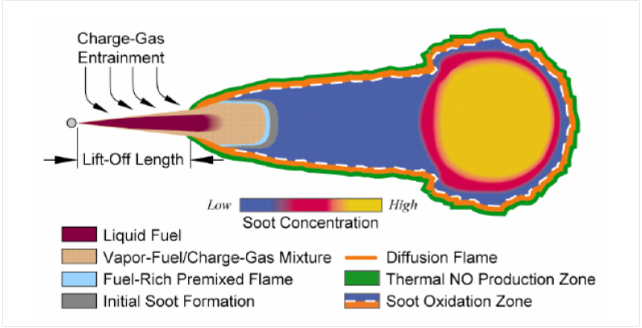

(c)

Figure 5.27. Comparisons of computed $\phi - T$ maps between the WSR and PDF models for baseline n-heptane conditions with (a) 21%, and (b) 8% O_2 levels. The conceptual model for diesel combustion is also included in (c) [55, 58]. With the PDF, IEM mixing is used with C_ϕ=3.0.

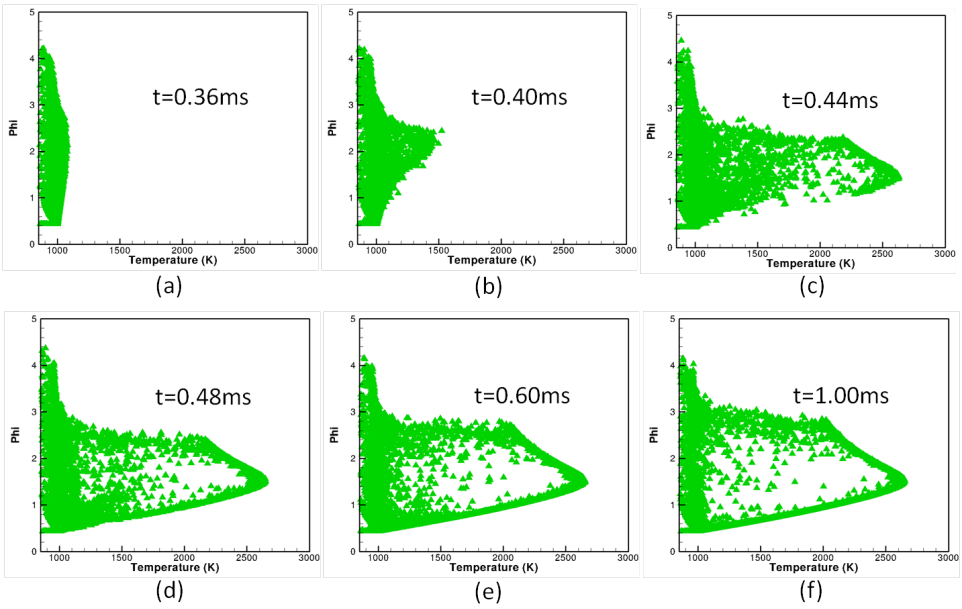

Figure 5.28. Computed $\phi - T$ maps for the 21% O_2 baseline n-heptane flame using the PDF model at times (a) t=0.36 ms, (b) t=0.40 ms, (c) t=0.44 ms, (d) t=0.48 ms, (e) t=0.60 ms, and (f) t=1.00 ms after the start of injection. The IEM mixing model is used with C_ϕ=3.0.

Table 5.3. Comparison of computed lift-off lengths and ignition delays for the PDF/IEM model with C_ϕ=2.0 and 3.0.

O_2%	TCI-C_ϕ=2		TCI-C_ϕ=3		Experiment	
	LOL(mm)	ID(ms)	LOL(mm)	ID(ms)	LOL(mm)	ID(ms)
21	21.94	0.427	19.36	0.422	17.00	0.530

the narrow range of C_ϕ explored here, the computed lift-off length is observed to marginally move toward that from the WSR model. Compared to measurements, C_ϕ=3 predicts the lift-off length somewhat better than C_ϕ=2. Comparisons in contours of mean OH-mass fraction and temperature between C_ϕ=2 and C_ϕ=3 are presented in Fig. 5.29 and 5.30, respectively. The mean OH-mass fraction contours are very similar for C_ϕ=2 and C_ϕ=3; however a difference is observed in the computed mean temperature contour at t=4 ms. The flame becomes narrower and longer for C_ϕ=2.0 compared to C_ϕ=3.0. Higher values of C_ϕ correspond to higher mixing rates, which in turn produces wider and shorter flame compared to lower C_ϕ values. For the remainder of the comparisons, C_ϕ=3 is used unless

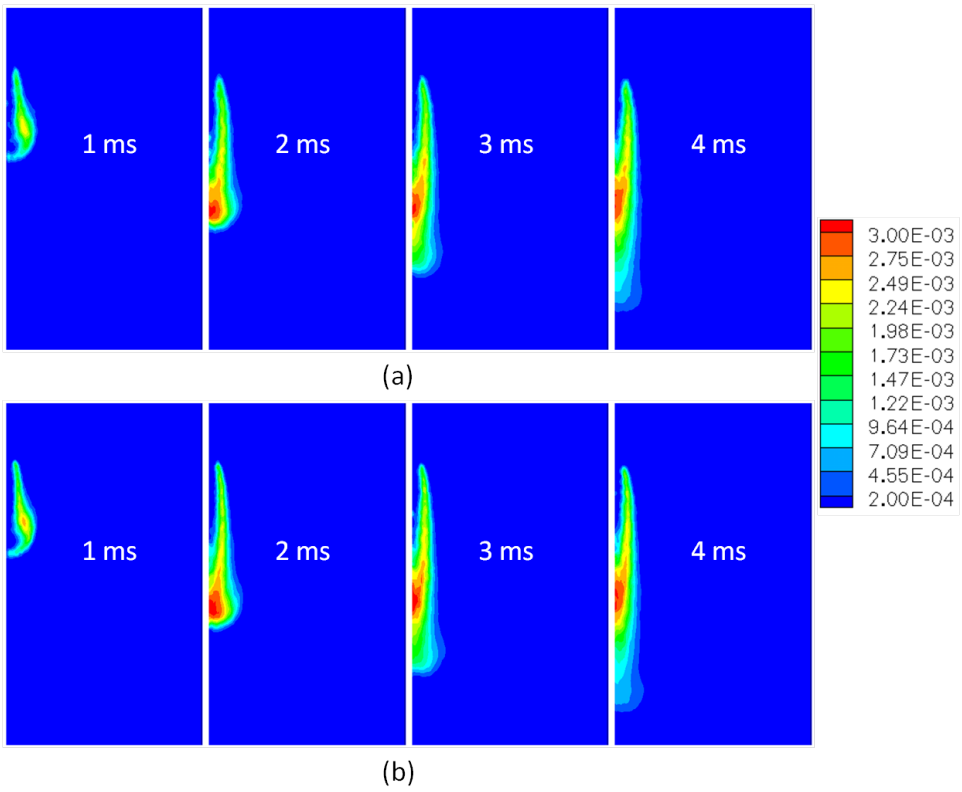

Figure 5.29. Computed contours of mean OH-mass fraction for the PDF model with IEM mixing with (a) C_ϕ=2, and (b) C_ϕ=3 at times t=1, 2, 3, and 4 ms after the start of injection.

specified otherwise.

The effects of the mixing model on the computed flame structure, and lift-off lengths and ignition delays are discussed next. For these comparisons, results are presented using two mixing models: IEM and EMST, within the framework of the PDF model. IEM is a weak particle interaction model that specifies mixing by the interaction of stochastic particles with the cell-mean values. EMST, on the other hand, enforces mixing of particles that are close in composition space. EMST is a strong particle interaction model that prevents mixing of unburnt and burnt particles by biased selection of particles based on their composition variables. This mixing model is more powerful than the IEM model, particularly for higher-Damköhler-number flames where burnt and unburnt particles may be separated over short distances in physical space. The differences between the two models in predicting the ignition delays and lift-off lengths are illustrated in Table 5.4

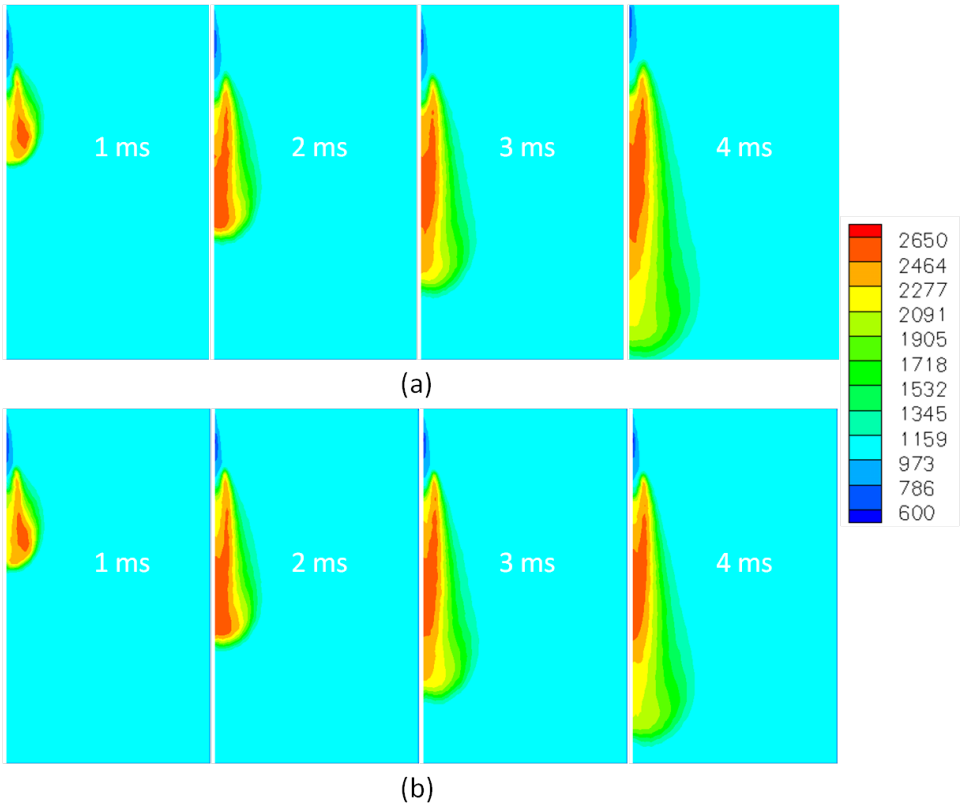

Figure 5.30. Computed contours of mean temperature (K) for the PDF model with IEM mixing with (a) C_ϕ=2, and (b) C_ϕ=3 at times t=1, 2, 3, and 4 ms after the start of injection.

for the 21% and 8% O_2 baseline n-heptane conditions. The EMST model shows some improvement in lift-off length predictions over the IEM model; however, the ignition delay is predicted better by the IEM model for 21% O_2. For 8% O_2, the lift-off lengths are approximately the same for both models, whereas the

Table 5.4. Comparisons of computed lift-off lengths and ignition delays for the PDF model with two mixing models: IEM and EMST.

O_2%	IEM-C_ϕ=3		EMST-C_ϕ=3		Experiment	
	LOL(mm)	ID(ms)	LOL(mm)	ID(ms)	LOL(mm)	ID(ms)
21	19.36	0.422	16.7	0.406	17.00	0.530
8	60.79	2.161	59.92	2.056	42.30	1.520

ignition delay is predicted marginally better by the EMST model. The overall flame structures for the two models for 21% O_2 are presented in Figs. 5.31 and

5.32 in the form of mean OH-mass fraction and temperature contours, respectively. There are no apparent visible differences between the contours from the two

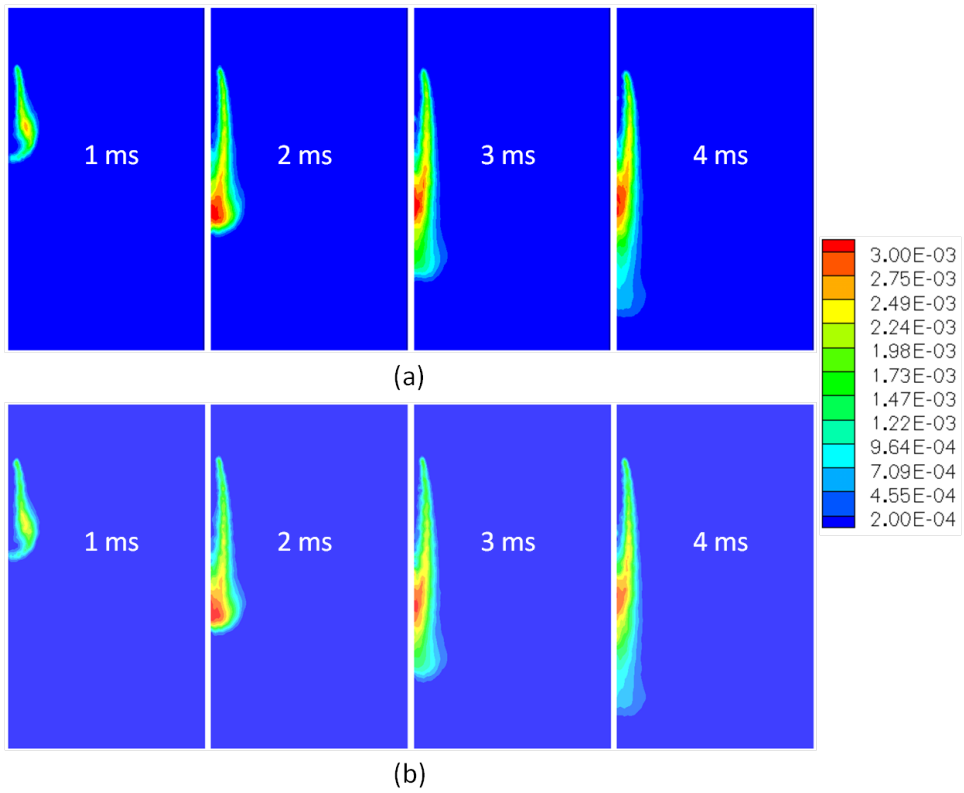

Figure 5.31. Computed contours of mean OH-mass fraction for the PDF model using the (a) IEM, and (b) EMST mixing at times, t=1, 2, 3, and 4 ms after the start of injection for 21% O_2.

models, although the global characteristics such as ignition delay and lift-off length suggested small differences between the two. A similar comparison is presented for 8% O_2 in Fig. 5.33 - 5.34. There small differences are observed in mean OH-mass fraction and mean temperature contours between the two mixing models at the beginning of autoignition (2.5 ms). The differences diminish as the flame propagates downstream. The shape and overall flame structures from the two mixing models are similar. The differences between the two mixing models are further explored in the context of soot modeling in the next subsection.

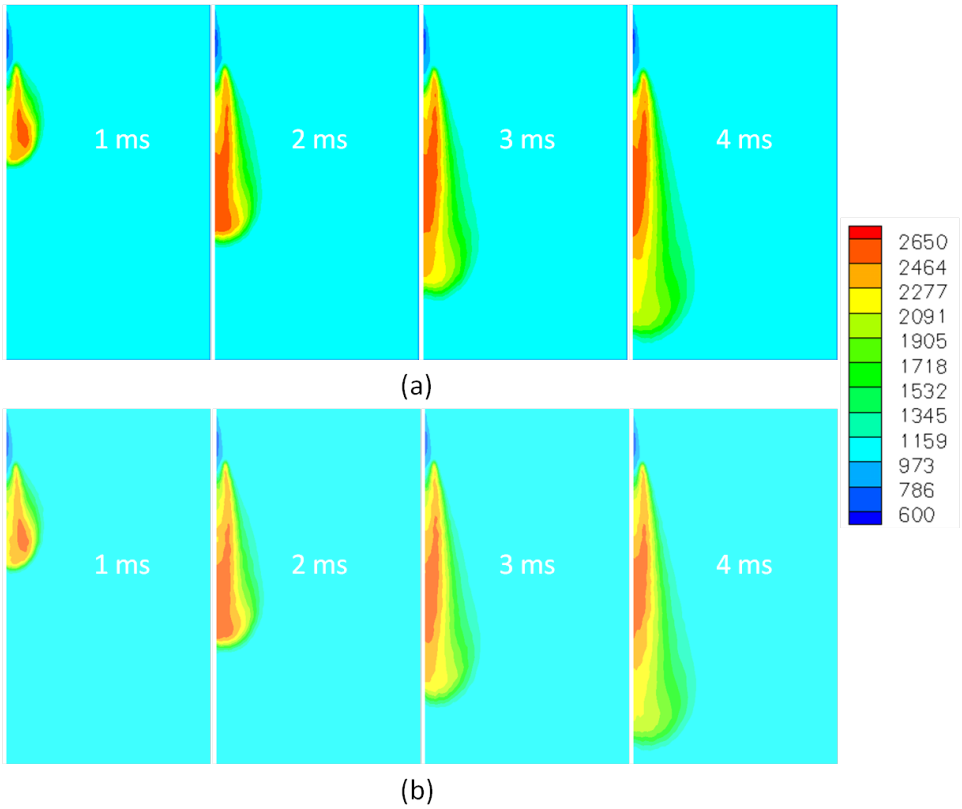

Figure 5.32. Computed contours of mean temperature for the PDF model using the (a) IEM, and (b) EMST mixing at times, t=1, 2, 3, and 4 ms after the start of injection for 21% O_2.

5.2.1.2 Soot Modeling

Two classes of soot models are considered here: a semi-empirical two-equation soot model, and a detailed model with a method of moments with interpolative closure (MOMIC) for soot aerosol dynamics. The results are compared with and without consideration of TCI (PDF versus WSR models). A detailed comparative study is provided first with the two-equation soot model, which also includes the sensitivity of computed soot volume fraction to the details of the coupling between the soot chemistry and the gas-phase chemistry. The results are compared between a two-way coupled soot- and gas-phase-chemistry interaction model and a one-way coupled model. The one-way coupling model allows the soot to grow without interfering with the gas-phase chemistry. In one-way coupling, soot depends on the gas-phase chemistry, but the gas-phase chemistry evolves independently of soot.

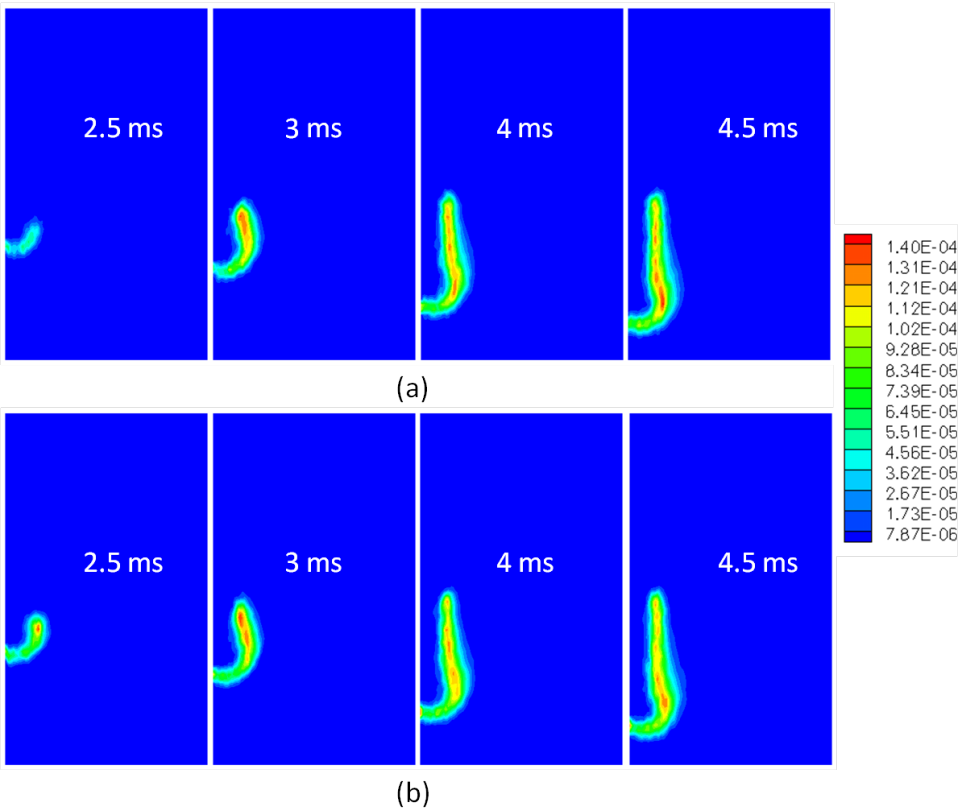

Figure 5.33. Computed contours of mean OH-mass fraction for the PDF model using the (a) IEM, and (b) EMST mixing at times, t=1, 2, 3, and 4 ms after the start of injection for 8% O_2.

In two-way coupling, the soot- and gas-phase-chemistry are strongly coupled. The role of mixing model in prediction of soot volume fraction is also explored by comparing results obtained with two mixing models: IEM and EMST. The soot results presented here include comparisons of contours of instantaneous mean mass fractions of key gas-phase species including acetylene and oxygen, contours of time-averaged and instantaneous mean soot volume fraction, and 2-D line plots of soot volume fraction and key gas-phase species mass fractions.

Comparisons of computed contours of mean acetylene mass fraction are presented in Fig. 5.35 between the PDF models with IEM and EMST mixing, and the WSR model. The results are presented for the 21% baseline n-heptane flame using the two-equation soot model. Within the framework of this soot model, acetylene is the precursor of soot, and therefore accurate prediction of acetylene is key to accurate prediction of soot. The contours for the PDF models are with one-way

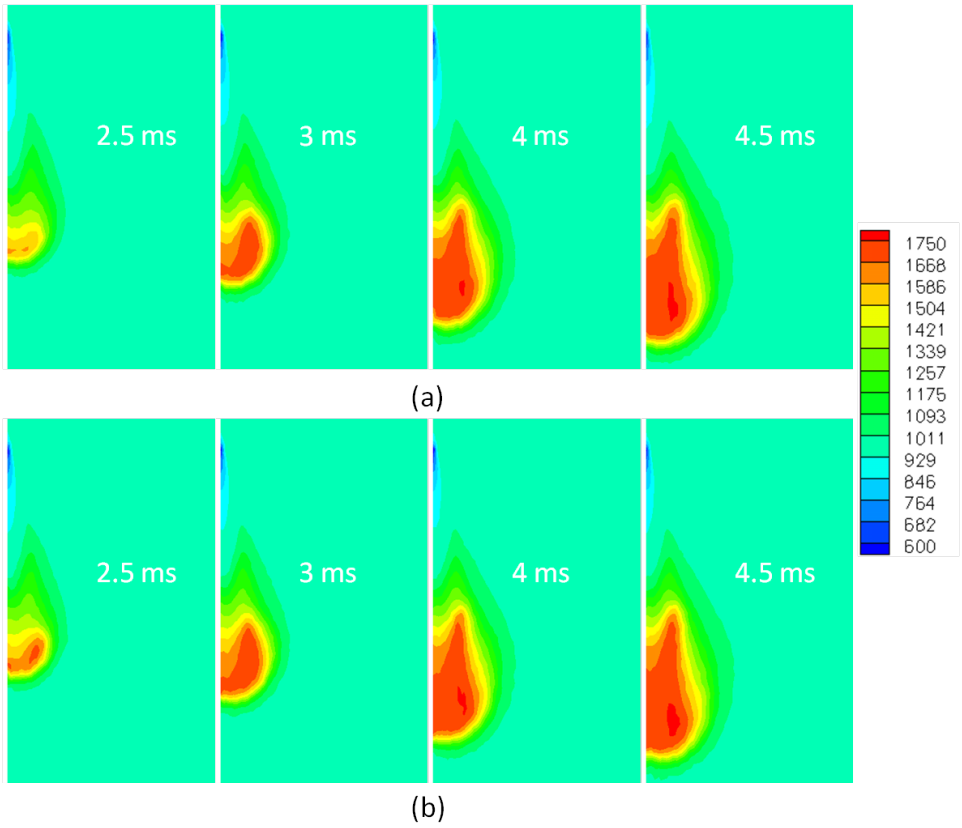

Figure 5.34. Computed contours of mean temperature for the PDF model using the (a) IEM, and (b) EMST mixing at times, t=1, 2, 3, and 4 ms after the start of injection for 8% O_2.

coupling between the soot and the gas-phase chemistry. The figure shows a significant difference in the shape, magnitude and spread of the acetylene contours between the PDF and the WSR models. The WSR model shows much higher mean acetylene mass fraction than the PDF models. The PDF model with EMST mixing produces more acetylene than with IEM mixing. The acetylene mass fraction contours show no appreciable change with time for the WSR model, whereas the PDF model with IEM mixing shows depletion of acetylene between 2 and 5 ms, and the shape of the acetylene contour shrinks as time increases.

The predictions of acetylene mass fraction using the PDF model depend strongly on the chemical mechanism. It has been observed that the 34-species chemical mechanism [94] results in one order-of-magnitude lower acetylene compared to the 40-species mechanism [2]. The lower acetylene mass fraction significantly alters

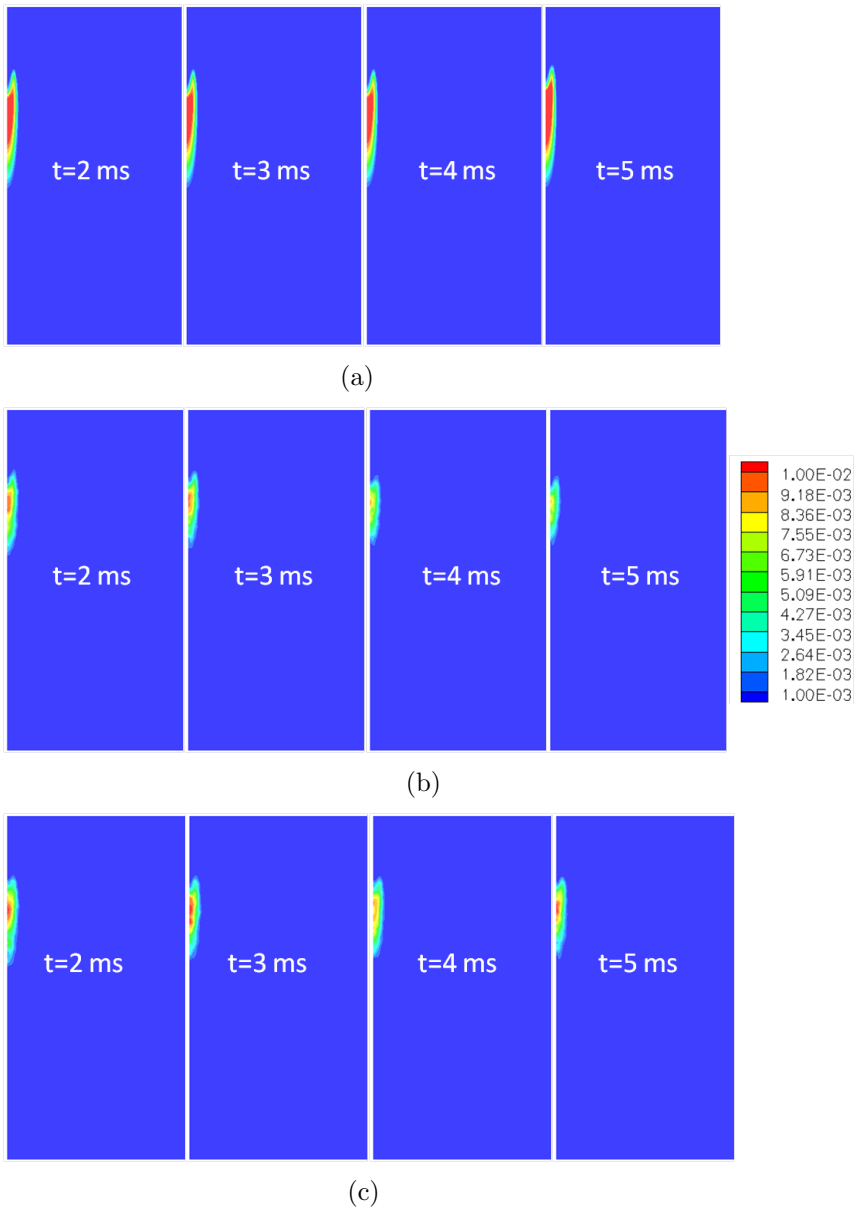

Figure 5.35. Computed contours of mean acetylene mass fraction for the baseline n-heptane flame with 21% O_2 using the (a) WSR, (b) PDF with IEM mixing model, and (c) PDF with EMST mixing model at times t=2, 3, 4, and 5 ms after the start of injection.

the soot formation process, and results in one-to-two orders of magnitude less soot than is observed in the measurements. The 40-species mechanism is more appropriate, since this mechanism produces soot levels that are comparable to those found in the experiment. All of the soot results shown in this section have been

obtained using the 40-species chemical mechanism.

Figure 5.36(a)- 5.36(c) compares the computed contours of mean soot volume fraction for the same conditions and models as Fig. 5.35. The corresponding contour obtained from the experimental chemiluminescence image is presented in Fig. 5.36(d). It is observed that the WSR model predicts a peak mean soot volume fraction of ∼2.5 ppm, approximately twice that from the measurements ∼1.2 ppm. The PDF models with IEM and EMST mixing predict peak soot volume fractions of ∼1.1 ppm, closer to measurements. The overprediction of soot by the WSR model compared to the PDF model is primarily due to the higher levels of acetylene given by the WSR model: higher acetylene results in higher nucleation and surface growth, which result in higher soot volume fractions for the WSR model. The PDF models produce a much shorter soot cloud than the WSR model. Both the PDF and the WSR models predict the location of peak mean soot volume fraction to be far upstream of where it is observed in the measurements. The comparison between IEM and EMST mixing models shows that EMST produces somewhat higher soot compared to IEM. This is consistent with the earlier observation in Fig. 5.35, which showed higher acetylene mass fraction with the EMST model.

Figure 5.37 illustrates radial profiles of time-averaged mean soot volume fraction for the PDF and WSR models, and compares them with experimental measurements at the same axial locations. The computed soot volume fraction profiles oscillate with time, even after a quasi-steady flame is established. Therefore, time-averaged values are presented here for comparison. Four axial locations are considered: z=40, 45, 50 and 55 mm. As observed earlier, the soot volume fraction is significantly overpredicted by the WSR model for all the locations considered here. The PDF models show earlier (upstream) formation of soot compared to the measurements. The experimental data suggest that the mean soot volume fraction attains a peak value of approximately 1.2 ppm at approximately z=60 mm on the injector axis, whereas the PDF models predict the peak mean soot volume fraction between z=40 to 45 mm. At z=40 mm, the PDF/IEM model produces the best match with the measurements. The PDF/EMST and WSR models predict mean soot volume fractions that are close to each other; however, both overpredict the mean soot volume fraction by approximately a factor of two. At z=45 mm, the EMST model produces the best agreement with the measurements, whereas the

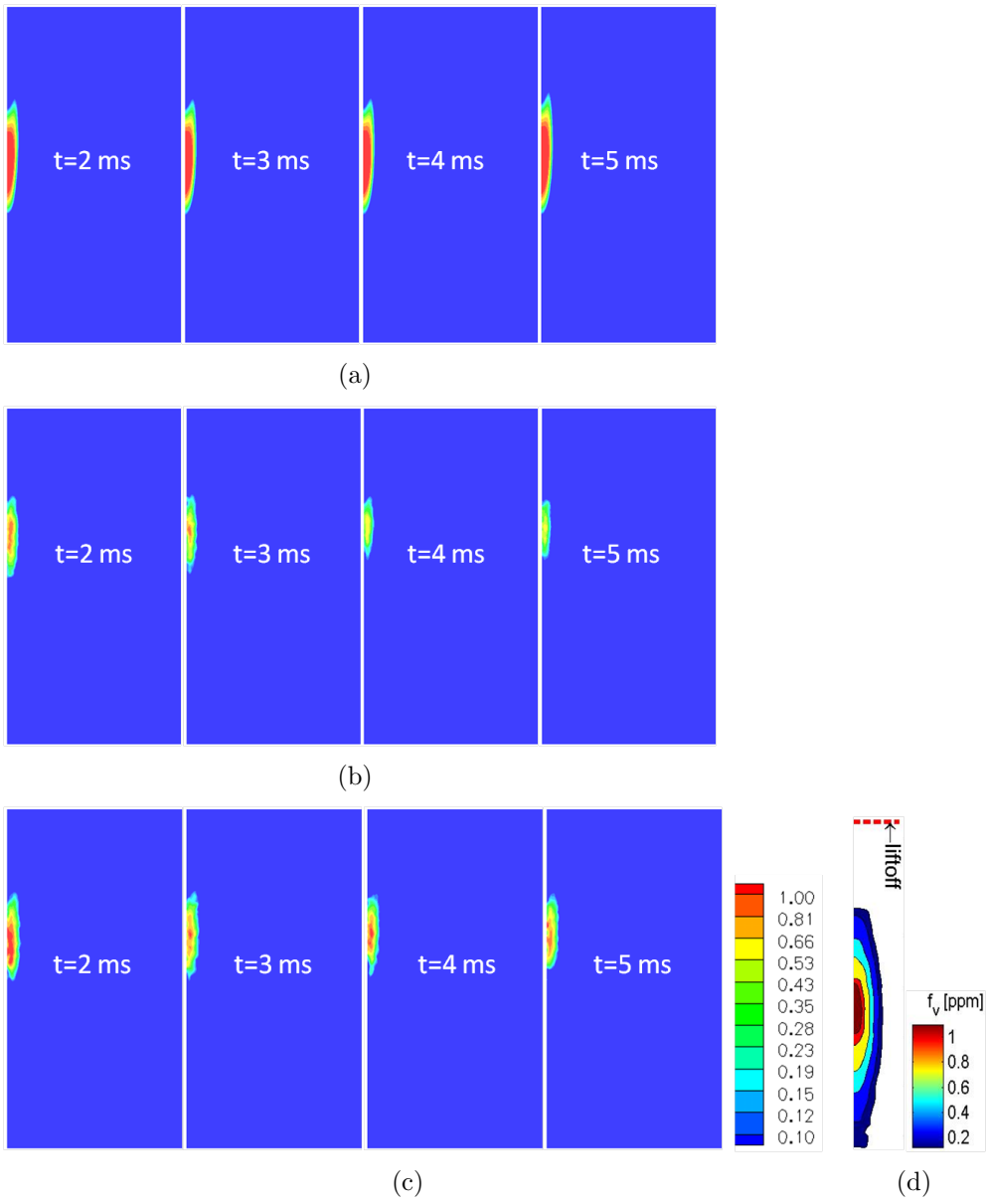

Figure 5.36. Computed contours of mean soot volume fraction for the baseline n-heptane flame with 21% O_2 using the (a) WSR, (b) PDF with IEM mixing, (c) PDF with EMST mixing, and (d) experimental image [1] at times t=2, 3, 4, and 5 ms after the start of injection.

IEM model underpredicts by approximately a factor of two. The WSR model continues to overpredict the mean soot volume fraction by a factor of two or more. At z=50 and 55 mm axial locations, all three models are far from the measurements; the PDF models underpredict the data and the WSR model overpredicts by a large

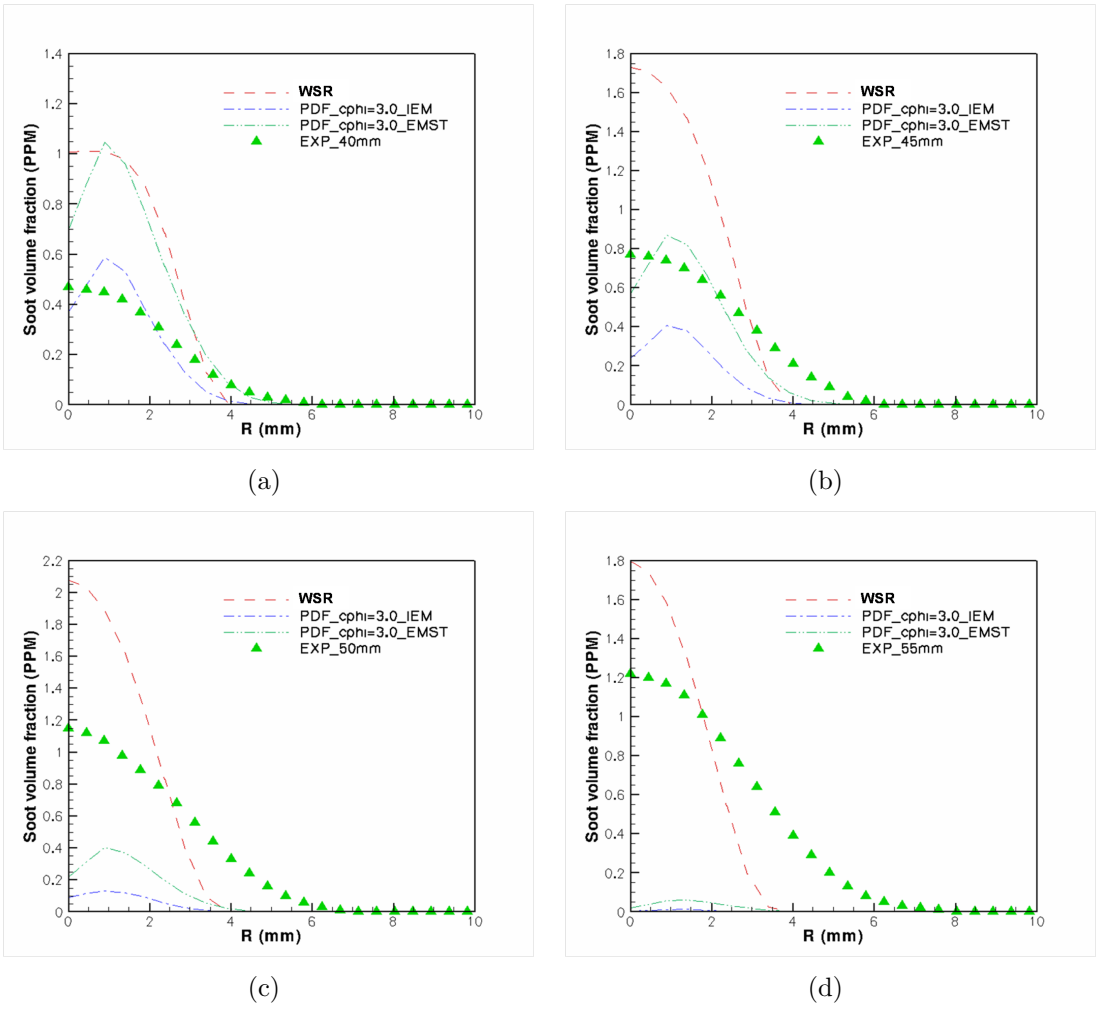

Figure 5.37. Computed and measured radial profiles of mean soot volume fraction for the 21% O_2 baseline n-heptane flame using the WSR, PDF with IEM mixing, PDF with EMST mixing, and experimental data at axial locations of (a) 40 mm, (b) 45 mm, (c) 50mm, and (d) 55 mm from the injector location.

margin. At axial locations downstream of z=60 mm, all three models underpredict the measurements. The computed values drop too rapidly for all the models as the distance along the nozzle axis increases. The WSR model predicts the peak mean soot volume fraction on the nozzle axis, whereas the PDF models show off-axis peaks. The measurements suggest that the peak occurs on the nozzle axis; however earlier soot measurements by Pickett *et al.* [187] showed a centerline dip and off-axis soot peaks. The large differences between the computational models and experiment are possibly due to the use of standard values of soot model con-

stants to model the nucleation, coagulation and surface reactions. The standard model constants [60] result in early soot formation and early oxidation than those observed in experiment. These model constants were calibrated based on specific flame configurations, and may require further tuning for diesel-like-conditions.

The overprediction of mean soot volume fraction by the WSR model is also consistent with the $\phi - T$ map (Fig. 5.27(a)), which suggests that the combustion regime for the WSR model penetrates more into the sooting zone (Fig. 5.26(b)). This is also supported by Fig. 5.38, which illustrates the region in the $\phi - T$ map where soot formation occurs. Figure 5.38 suggests that the soot formation begins in between the premixed and diffusion layer of the flame, where partially oxidized

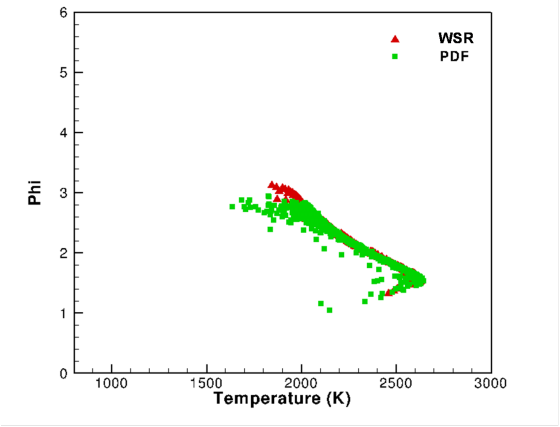

Figure 5.38. $\phi - T$ maps for the 21% O_2 baseline n-heptane flame using the PDF and WSR models. Only the regions where the computed mean soot volume fraction is greater than 0.01 ppm are shown.

rich fuel fragments are present. For the WSR model, the premixed combustion occurs at higher equivalence ratio compared to the PDF model. Therefore, soot levels are expected to be higher with the WSR model.

From the comparisons of mean soot volume fractions with the two PDF mixing models, it is observed that the choice of mixing model produces differences in soot prediction, while no appreciable differences were noticed between the mixing models for the global flame characteristics. However, compared to the differences with the measurements, the differences in predictions between the two mixing models is perhaps not significant. The qualitative nature of the soot predictions is same for both models.

The comparisons of soot volume fraction discussed above have been based on one-way coupling between the soot and the gas-phase chemistry. We next investigate the differences in soot predictions between one-way and two-way coupling within the framework of the two-equation model using IEM and EMST mixing models. Figure 5.39 compares the computed contours of time-averaged mean soot volume-fraction between one-way and two-way coupling using the IEM mixing model. The two-way coupling provides higher soot volume fraction compared to

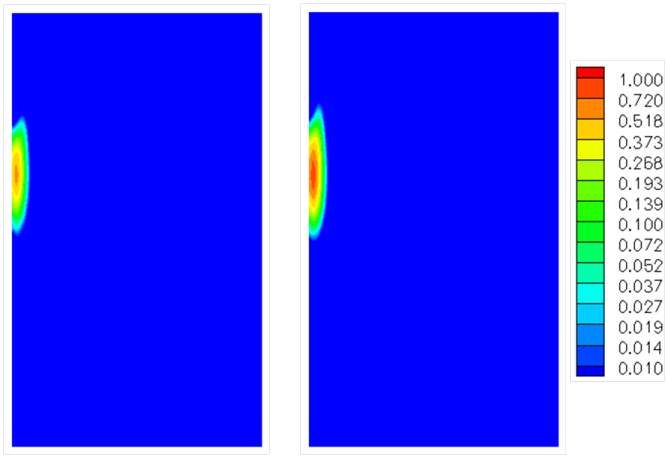

Figure 5.39. Computed contours of time-averaged mean soot volume fraction for the 21% O_2 baseline n-heptane flame using the PDF model with IEM mixing.(a) One-way coupling, and (b) two-way coupling. The time averages are computed over a period of 2 to 5 ms.

one-way coupling. The same trend has been observed with the EMST mixing model (Fig. 5.40), where the two-way coupling produces a longer soot cloud with higher peak mean soot volume fraction compared to one-way coupling.

The corresponding radial profiles of time-averaged mean soot volume-fraction are illustrated in Fig. 5.41 for one- and two-way coupling using the IEM mixing model. The comparisons are made at axial locations z=40, 45, 50, and 55 mm. Again the radial profiles suggest that the computational models predict early soot formation compared to measurements. The two-way coupling predicts significantly higher soot volume fraction than one-way coupling at all locations. Both one- and two-way coupling overestimate the peak mean soot volume fraction at an axial location of z=40, with one-way coupling being closer to the measurements. Downstream of z=40 mm, the soot volume fraction is underpredicted by both the

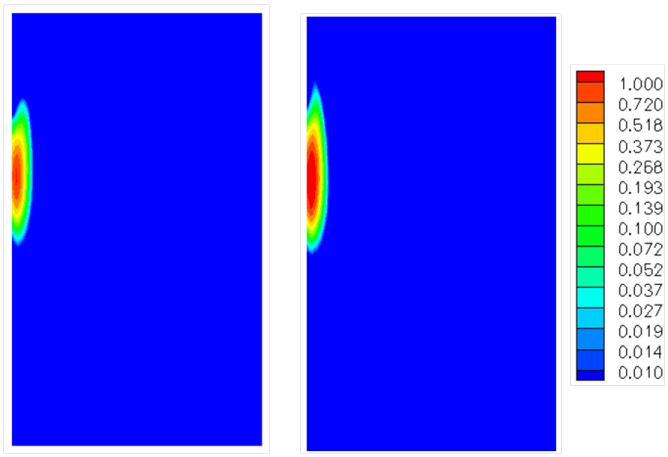

(a) (b)

Figure 5.40. Computed contours of time-averaged mean soot volume fraction for the 21% O_2 baseline n-heptane flame using the PDF model with EMST mixing. (a) One-way coupling, and (b) two-way coupling. The time averages are computed over a period of 2 to 5 ms.

methods (one- and two-way coupling). The margin of underprediction increases further downstream. A similar trend is observed with the EMST mixing model (Fig. 5.42). However, with EMST, higher soot volume fraction is observed.

All of the computational soot models investigated up to now showed significant differences in mean soot volume fraction contours with the measurements. The axial and radial extent of the computed sooting zone are both underpredicted by the models, and the soot cloud is too far upstream. While some of the models are able to predict the peak soot-volume fraction correctly, the location of maximum soot formation is upstream of the measurements in all cases. A possible explanation could be overestimation of the surface oxidation rate in the model, which typically dominates in sooting flames under these conditions. It is interesting to note that with both mixing models, two-way coupling produces more soot than one-way coupling. This may appear to be counter-intuitive. One-way coupling does not provide any feedback from soot to the gas-phase species, and therefore, it would be natural to assume that one-way coupling would produce more soot because acetylene is not depleted due to soot formation. Two-way coupling, on the other hand, includes feedback from the soot-chemistry to the gas-phase reactions, which is expected to reduce the acetylene mass fraction. Low acetylene is expected to reduce the nucleation and surface growth of soot. However, the computational

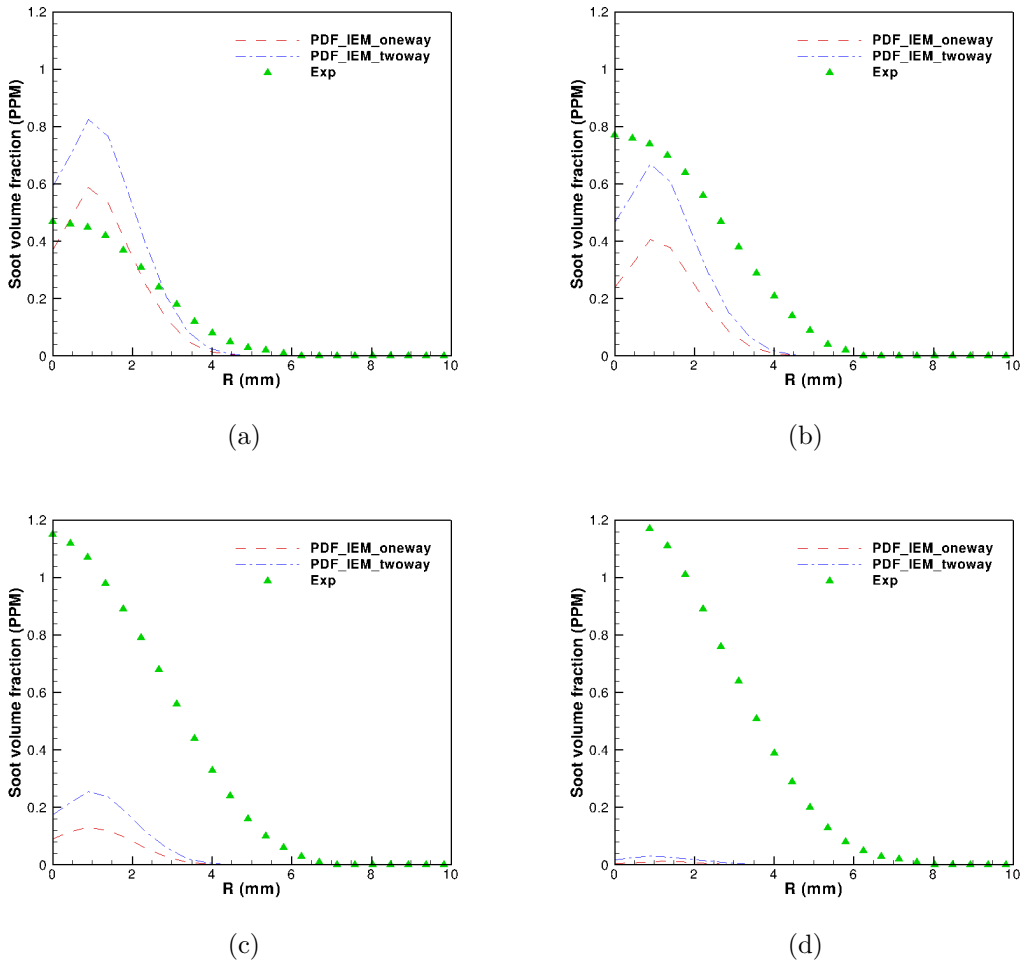

Figure 5.41. Computed and measured radial profiles of mean soot volume fraction for the 21% O_2 baseline n-heptane flame using the PDF/IEM model with one- and two-way couplings at axial locations of (a) 40 mm, (b) 45 mm, (c) 50 mm, and (d) 55 mm.

results have shown an increase in soot level with two-way coupling. The increase in soot level using two-way coupling might be explained in terms of surface oxidation. One-way coupling does not account for the decrease in O_2 level resulting from soot oxidation. The excess oxygen increases the surface oxidation of soot, and therefore tends to negate the effects of growth of soot due to nucleation and surface growth. In a strongly oxidizing environment where surface oxidation dominates the overall soot chemistry, one-way coupling may result in low soot mass. For two-way coupling, on the other hand, the local O_2 level decreases due to consumption by surface oxidation. The low O_2 level, in turn, reduces the surface oxidation and

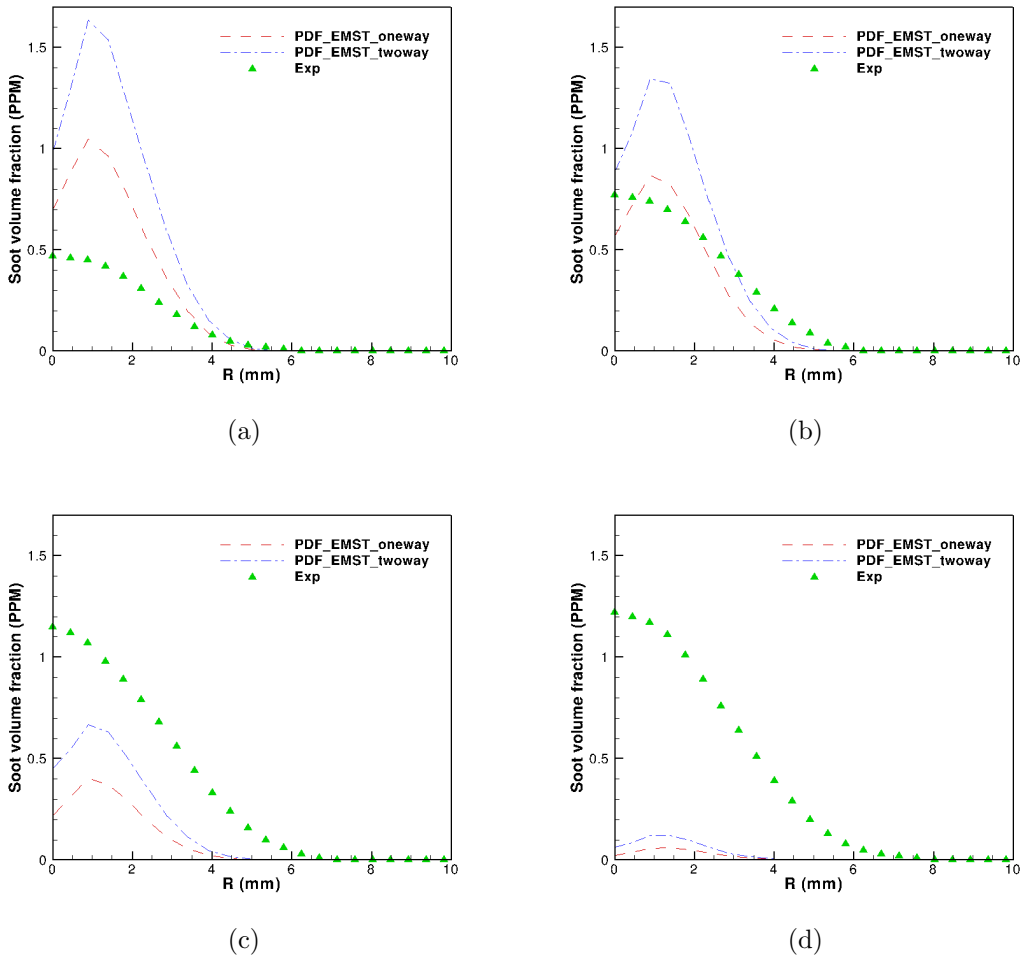

Figure 5.42. Computed and measured radial profiles of mean soot volume fraction for the 21% O_2 baseline n-heptane flame using the PDF/EMST model with one- and two-way couplings at axial locations of (a) 40 mm, (b) 45 mm, (c) 50 mm, and (d) 55 mm.

may result in higher soot levels. It should be recognized here that depending on the strength of the coupling between gas-phase and soot, the gas-phase chemistry may change. For example, changes in O_2 levels may alter the chemical pathways for oxidation of acetylene. The differences in O_2 levels between one- and two-way couplings are illustrated in the radial profiles of mean O_2 mass-fraction at different axial location with the EMST mixing model in Fig. 5.43. At axial locations of z=20, 30, and 50 mm from the injector location, one-way coupling results in higher O_2 mass fraction near the injector axis. This is consistent with the

lower soot volume fractions that are observed with one-way coupling. The higher

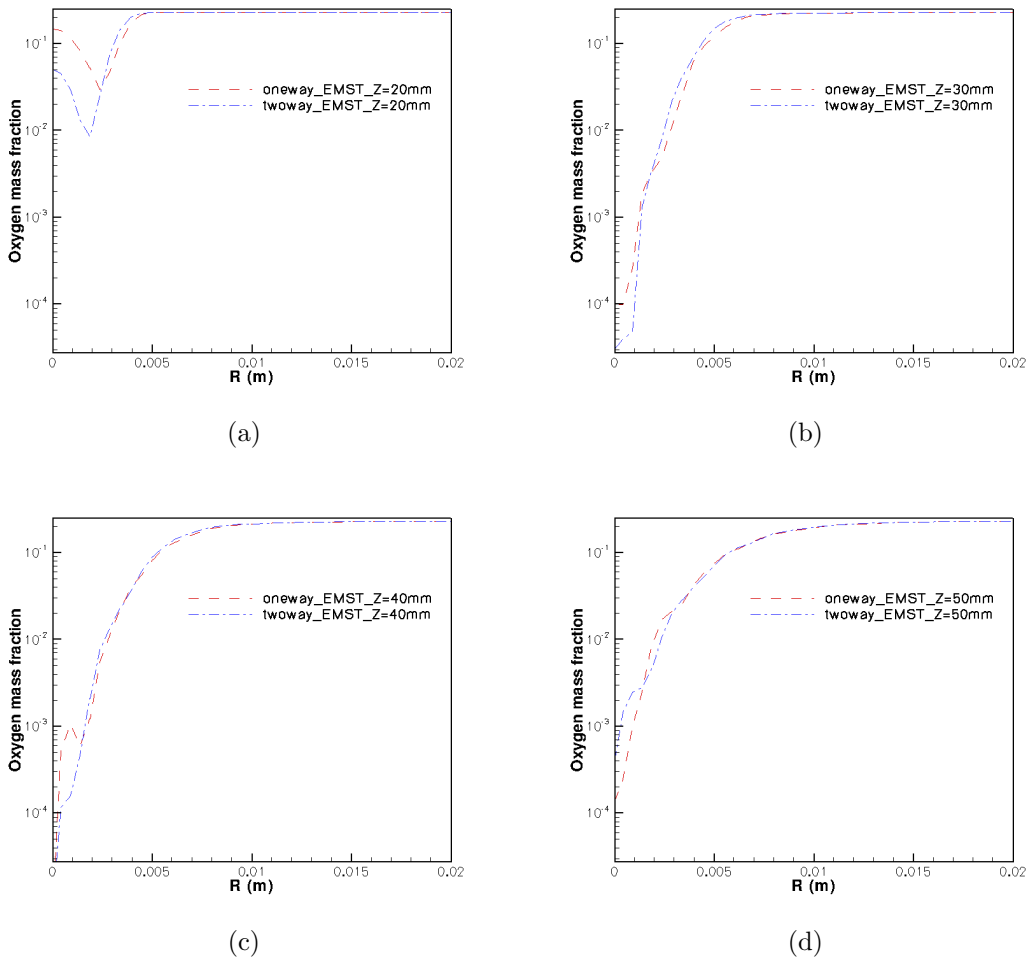

Figure 5.43. Computed radial profiles of mean O_2 mass fraction for the 21% O_2 baseline n-heptane flame at time t=3.0 ms after the start of injection using the PDF/EMST model. Comparisons are made with one- and two-way couplings at axial locations (a) z =20 mm, (b) z =30 mm, (c) z =40mm, and (d) z =50 mm.

O_2 mass fraction changes the gas-phase chemistry, resulting in more oxidation of acetylene, and thereby reducing the acetylene mass fraction available for nucleation and surface growth of soot. This is supported by Fig. 5.44, which shows lower computed acetylene mass-fractions with one-way coupling compared to two-way coupling near the injector axis. The lower nucleation and surface growth rates, coupled with higher surface oxidation, result in lower soot volume fractions with one-way coupling compared to two-way coupling.

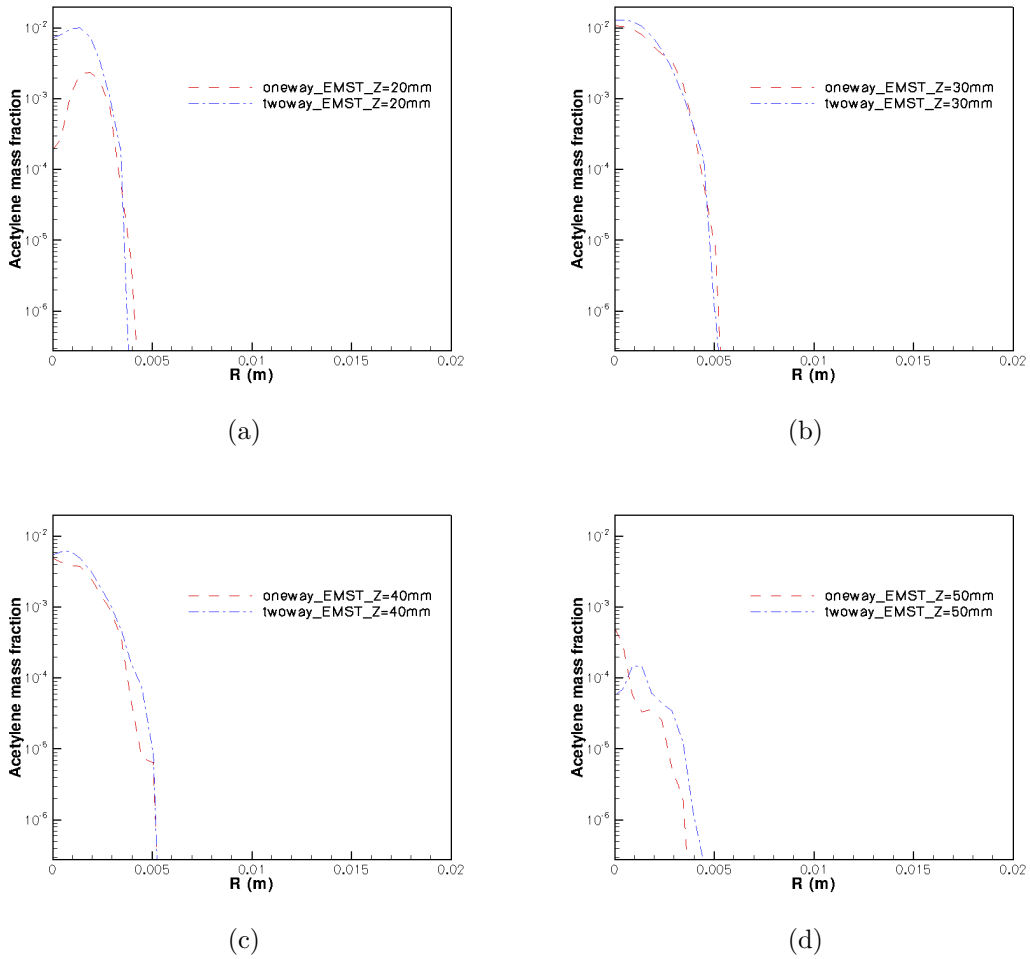

Figure 5.44. Computed radial profiles of mean C_2H_2 mass fraction for the 21% O_2 baseline n-heptane flame at time t=3.0 ms after the start of injection using the PDF/EMST model. Comparisons are made with one- and two-way couplings at axial locations (a) z =20 mm, (b) z =30 mm, (c) z =40mm, and (d) z =50 mm.

The role of surface oxidation on the overall soot prediction by the PDF models is further investigated by disabling surface oxidation of soot within the framework of the two-equation soot model. Computed contours of mean soot volume fraction using one- and two-way coupling are compared in Fig. 5.45. In the absence of surface oxidation, both one- and two-way coupling show wider and longer soot volume fraction contours that continue to grow in width and length with time, to become similar to the shape of the mean temperature contours. The total soot mass continues to increase with time due to nucleation and surface growth, and no steady state

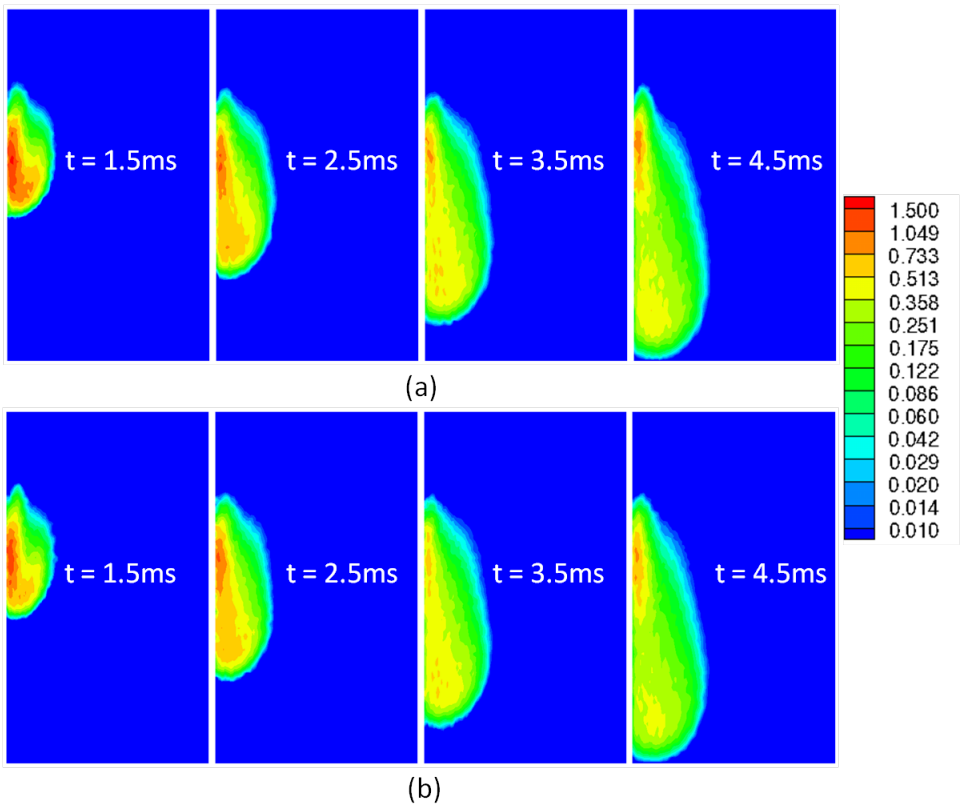

Figure 5.45. Computed contours of mean soot volume fraction for the 21% baseline n-heptane flame using the PDF/EMST model with C_ϕ=3.0 for (a) one-way coupling, and (b) two-way coupling at times, t=1.5, 2.5, 3.5, and 4.5 ms. The two-equation soot model with no surface oxidation is used.

is reached. The shapes of the contours for soot volume fraction without surface oxidation are closer to those from the experiment compared to the earlier results that included surface oxidation. With no mechanism to oxidize the soot, the soot mass is carried downstream, as has also been observed in experiments. However, with soot oxidation, the soot is quickly oxidized before propagating downstream. This suggests that it may be possible to improve the soot predictions by changing the model constants for surface oxidation in the semi-empirical two-equation model. This exercise is left out for future work.

Without surface oxidation, it is expected that one-way coupling should produce higher soot mass compared to two-way coupling. This is illustrated in Fig. 5.46, which compares computed total soot mass versus time for one- and two-way coupling without surface oxidation. With no surface oxidation present in the soot-

chemistry, one-way coupling gives higher acetylene mass fraction, which results in higher soot formation by nucleation and surface growth. The higher acetylene explains the higher soot mass in one-way coupling compared to two-way coupling, in the absence of soot oxidation.

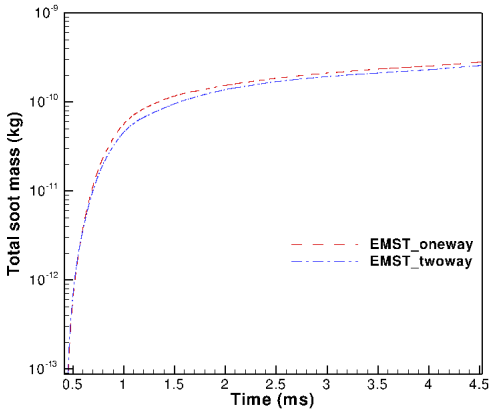

Figure 5.46. Computed total soot mass versus time for the 21% baseline n-heptane flame using the PDF/EMST model with C_ϕ=3.0 for (a) one-way coupling, and (b) two-way coupling. The two-equation soot model with no-surface-oxidation is used.

While some gas-phase reaction pathways and mass fraction of some of the gas-phase species change depending on the coupling between the gas-phase chemistry and soot, global autoignition and combustion characteristics including lift-off length, ignition delay, flame temperature remain essentially the same. The maximum difference in peak mean flame temperature between one- and two-way couplings is 2 K, which is negligible for practical purposes.

The comparisons presented up to now have been for a semi-empirical two-equation soot model suggested by Lindstedt [60]. Comparisons of computed mean soot volume fractions between the semi-empirical two-equation soot model and the detailed MOMIC-based model are shown in Fig. 5.47. For both soot models, the IEM mixing model has been used. The contours for the two models are compared at t=2 and 3 ms, using a two-way coupling between the gas-phase chemistry and soot chemistry. It is observed that MOMIC produces lower peak soot volume fraction compared to the two-equation model. The soot cloud is also shorter using the MOMIC model. However, the qualitative trends are similar: both models predict the peak mean soot volume fraction upstream of the location observed in

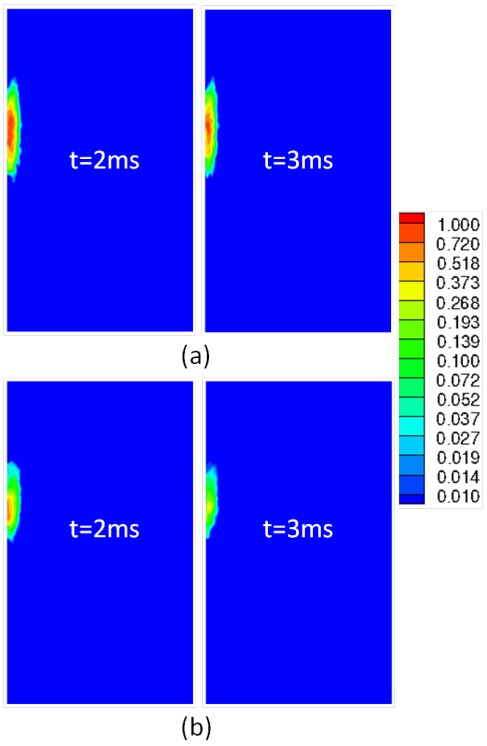

Figure 5.47. Computed contours of mean soot volume fraction for the 21% baseline n-heptane flame using the PDF/IEM model with C_ϕ=3.0 for (a) two-equation soot model, and (b) MOMIC soot model with six moments at times, t= 2 and 3 ms. Two-way coupling is used for both models.

the experiment, and a much more compact soot zone.

Comparisons of soot volume fractions for different soot models are extended to the 15% O_2 baseline n-heptane flame in Fig. 5.48. The results are compared between the WSR and PDF models using the two-equation model and two-way coupling. For the PDF model, EMST mixing is used. Figure 5.48 shows significant differences in time-averaged contours between the WSR and PDF models. The trends for 15% O_2 are generally similar to those for 21% O_2. While the WSR model continues to overpredict the peak mean soot volume fraction, the PDF model underpredicts the peak soot volume fraction. The measurement shows a peak mean soot volume fraction of 0.74 ppm, while the WSR model predicts ∼1.1 ppm, and the PDF model predicts ∼0.5 ppm. The shape of the soot cloud volume fraction is longer for the WSR model compared to the PDF model. The corresponding comparisons of radial profiles of mean soot volume fraction using the WSR and

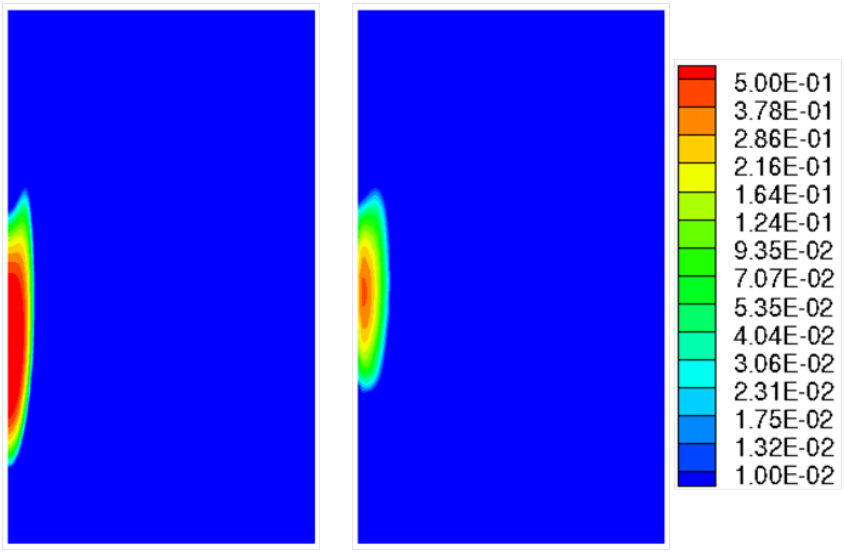

(a) (b)

Figure 5.48. Computed contours of time-averaged mean soot volume fraction for the 15% O_2 baseline n-heptane flame using the (a) WSR model, and (b) PDF model with EMST mixing and two-way coupling. The time-averages are computed over a period of 2.5 to 4.5 ms. The two-equation soot model is used.

PDF models are shown in Fig. 5.49.

5.2.1.3 Radiation Modeling

The effects of radiation on the overall flame characteristics is investigated by comparing results between the PDF model without radiation and the PDF model with an optically-thin radiation model that accounts for emission by four species (CO, CO_2, CH_4, and O_2) and soot. The comparisons are presented for 21% O_2, since both the flame temperature and soot volume fraction are maximum for 21% O_2. Therefore, it is anticipated that the maximum differences between with versus without radiation should be seen for this O_2 level. Figure 5.50 shows the differences in computed mean OH-mass fractions with versus without radiation. The shape and time-evolution of the mean OH-mass fraction contours remain essentially the same. However, with radiation marginally lower OH-mass fraction are found near the nozzle axis compared to the model without radiation. Figure 5.51 compares the computed mean temperature contours for the PDF model with versus without radiation. As for the mean OH-mass fraction contours, the shape and time evolu-

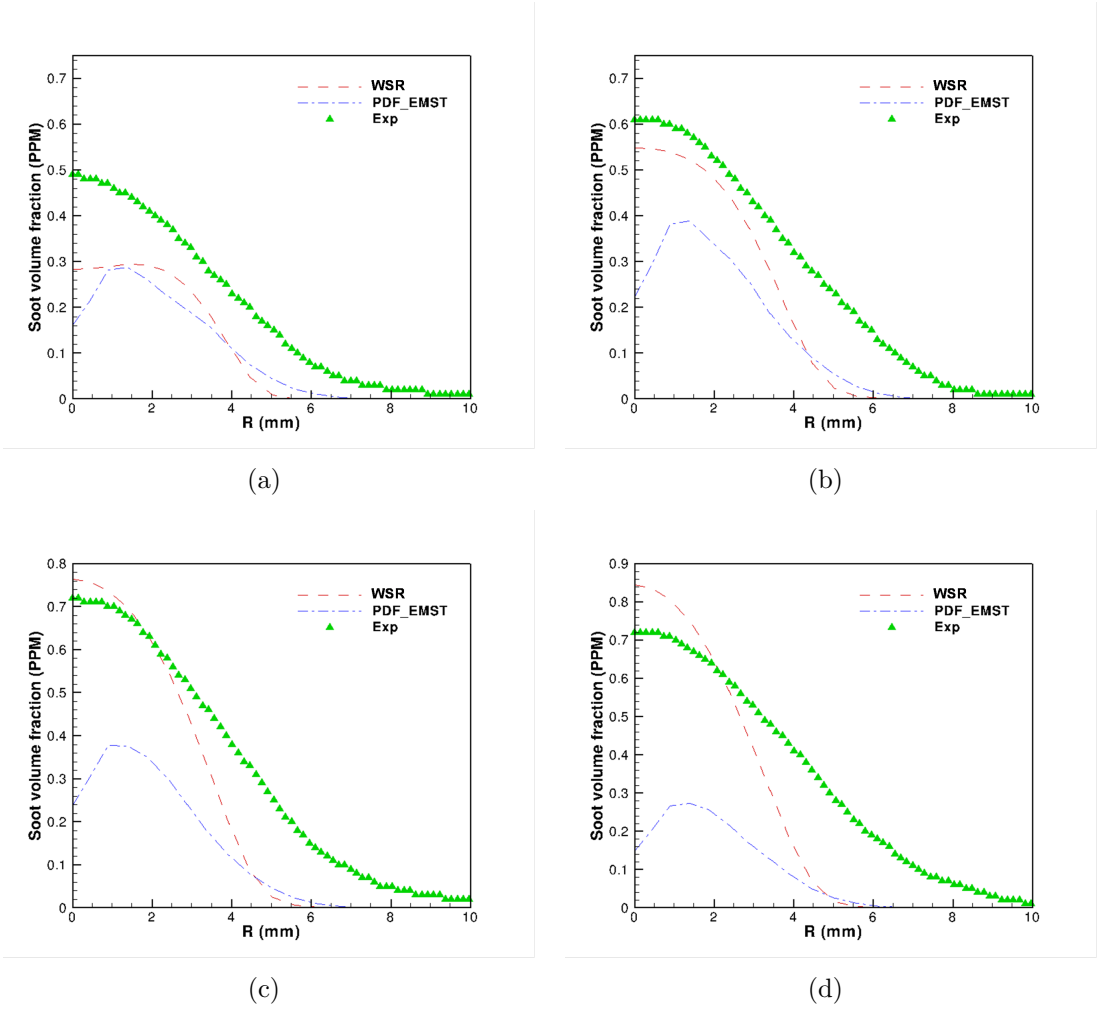

Figure 5.49. Computed and measured radial profiles of time-averaged mean soot volume fraction for the 15% O_2 baseline n-heptane flame using the WSR model and PDF model with EMST mixing and two-way coupling at axial locations of (a) 50 mm, (b) 55 mm, (c) 60 mm, and (d) 65 mm. The time averages are computed over a period of 2.5 to 4.5 ms. The two-equation soot model is used.

tions of mean temperature are essentially the same. The model without radiation predicts a marginally higher peak mean flame temperature (by 5 K) compared to the radiation model. The comparisons presented in Figs. 5.50 - 5.51 show that an optically thin radiation model does not contribute to any significant difference in the flame structures. Therefore, radiation can safely be neglected for the rest of the computations.

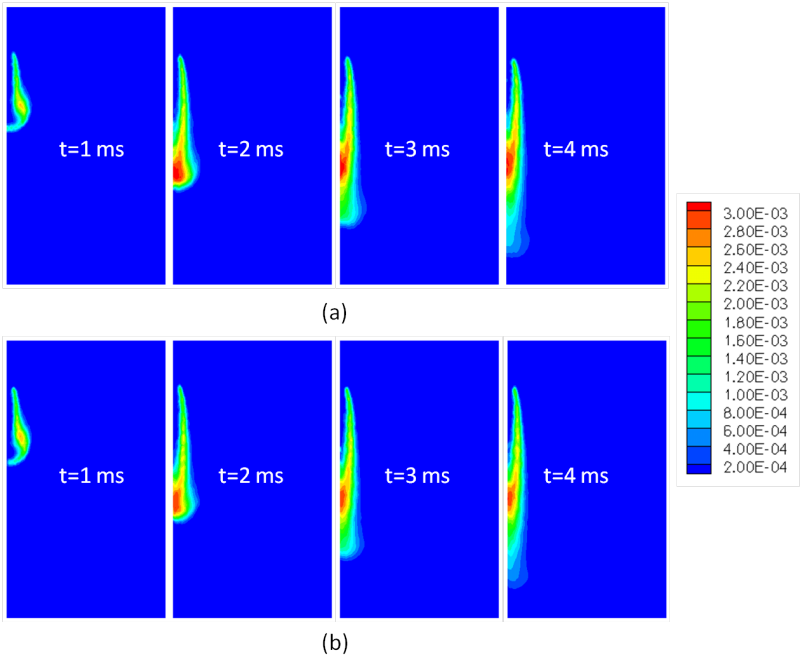

Figure 5.50. Computed contours of mean OH-mass fraction for the 21% O_2 baseline n-heptane flame using the (a) PDF model without radiation, and (b) PDF model with an optically thin radiation model at times t=1, 2, 3, and 4 ms after the start of injection.

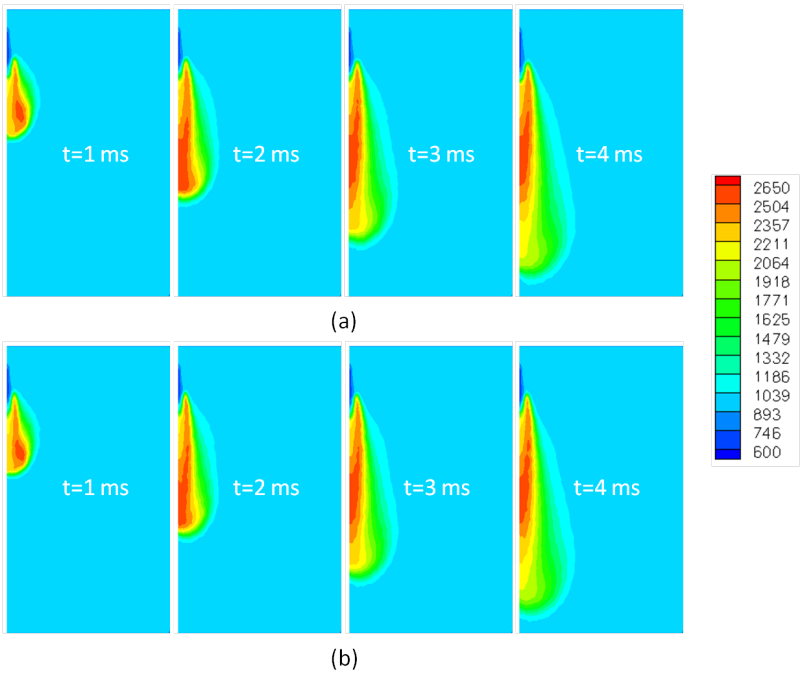

Figure 5.51. Computed contours of mean temperature (K) for the 21% O_2 baseline n-heptane flame using the (a) PDF model without radiation, and (b) PDF model with an optically thin radiation model at times t=1, 2, 3, and 4 ms after the start of injection.

5.2.2 Non-baseline n-Heptane Spray Flames

The comparisons between the PDF and WSR models for the baseline n-heptane flames demonstrates that TCI have a strong influence on the computed turbulent flame structure, and affect the global characteristics (ignition delay, lift-off length) to varying extents, most noticably at lower O_2 levels. The difference between the two models is further investigated for non-baseline n-heptane flames, which include variations in initial temperature, density and O_2 level. The purpose of the study is to determine the conditions where TCI are or are not important.

The sensitivity of computed ignition delays to variations in the initial temperature is compared between the PDF and WSR models, and with the measurements in Fig. 5.52(a). The initial temperature range for this study is from 800 to 1000 K, while the O_2 level and density are fixed at 21% and 14.8 kg/m^3, respectively. The study is focused on initial temperatures less than 1000 K, since below 1000 K, TCI are expected to contribute significantly due to the relatively slow chemistry. Above 1000 K, the reaction rates become significantly faster and contributions of TCI are expected to become progressively weaker. The PDF model demonstrates significant improvement in the prediction of ignition delay for low initial temperatures. At 800 K, while the WSR model produces significant overprediction in ignition delay ($\sim$ 60%), the PDF model underpredicts approximately by 5%. As the temperature increases, the difference in predictions between the two models decreases. The PDF model shows some underprediction of ignition delay compared to measurements over the selected temperature range. The WSR model, on the other hand, starts with a large overprediction in ignition delay at 800 K, and underpredicts for temperatures above 900 K. The variation of lift-off length with initial temperature with and without TCI is compared with the measurements in Fig. 5.52(b). The PDF model overpredicts the lift-off length, while the WSR model underpredicts. In contrast to the comparison of ignition delay, the lift-off length is better predicted overall by the WSR model, especially at low initial temperatures. However, the PDF predictions improve as the initial temperature increases. The differences between the PDF and WSR models decrease rapidly as the initial temperature increases beyond 900 K.

Comparisons of computed mean OH-mass fraction and temperature contours between the PDF and WSR models for an initial temperature of 850 K, with 21%

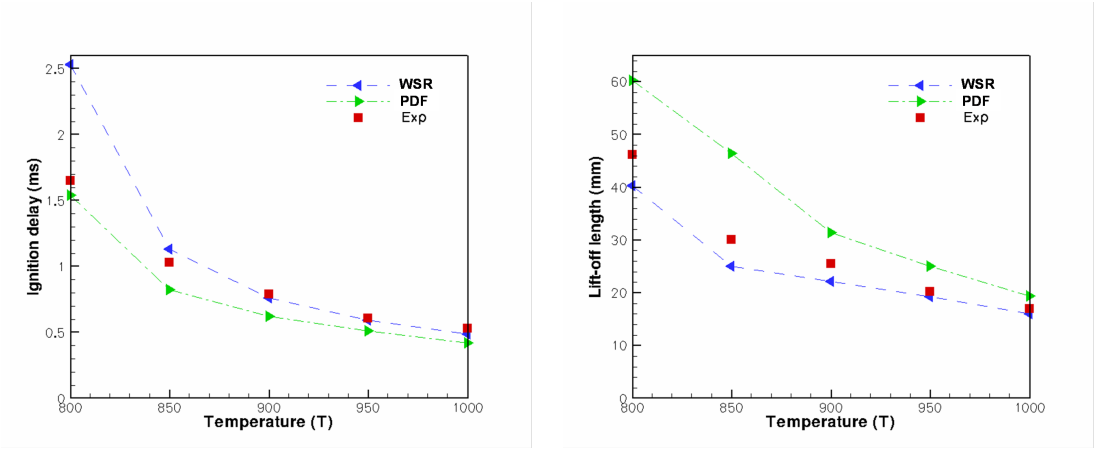

(a) (b)

Figure 5.52. Comparisons of (a) ignition delay (ms) versus initial temperature (K) (b) lift-off length (mm) versus initial temperature (K) using the PDF model and WSR model for the 21% O_2 n-heptane flames.

O_2, at time t=3.0 ms are presented in Fig. 5.53. The PDF and WSR contours are significantly different from each other: the PDF model shows significantly higher lift-off length compared to the WSR model. The shape of the contours also shows significant differences between the two models. While the WSR contour is similar to that for the baseline conditions, the PDF model contours significantly differ from that of baseline conditions. The comparison of computed mean temperature contours (Fig. 5.53(b)) reveals that the PDF mean temperature profiles are more diffuse, with a slower rise in temperature axially, which results in a more distributed combustion regime compared to the WSR model. In absence of temperature measurement for this flame, it is difficult to conclude which model produces the more realistic flame structure. However, this comparison illustrates that TCI make significant differences in the computed mean flame shape for low initial temperature conditions.

Figure 5.54 compares the heat-release rates for the WSR model for four different initial temperatures from 800 K to 950 K. As the initial temperature decreases, a distinct low-temperature heat-release zone becomes apparent. This is due to the negative temperature coefficient (NTC) behavior that is typically observed for low-temperature chemistry. With increasing initial temperature, the main heat-release shifts to earlier times, and the first-stage heat-release peak gradually diminishes.

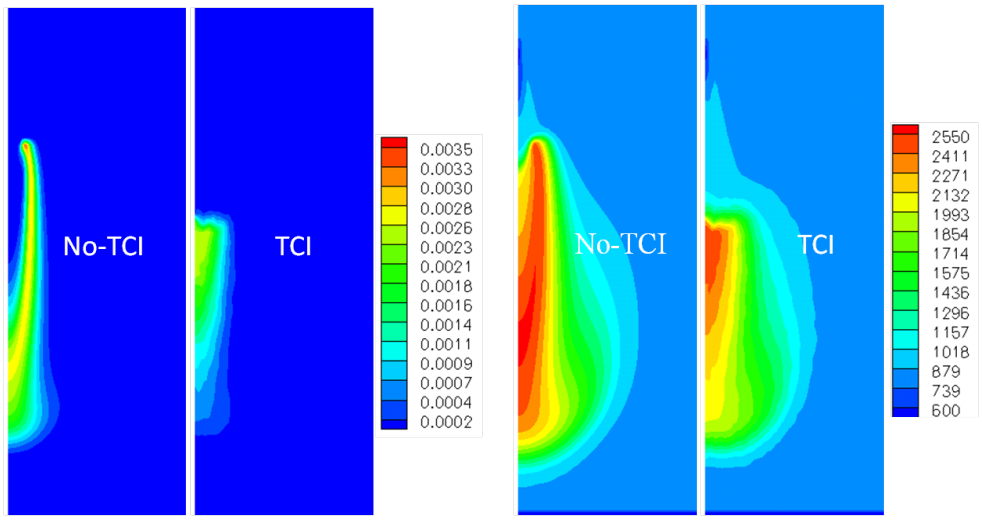

(a) (b)

Figure 5.53. Computed contours of (a) mean OH-mass fraction (b) mean temperature using the WSR and PDF models for the 21% O_2, 850 K initial temperature and 14.8 kg/m^3 initial density n-heptane flame. The comparisons are made at t=3.0 ms.

For temperatures at and above 1000 K, the first-stage heat-release can hardly be

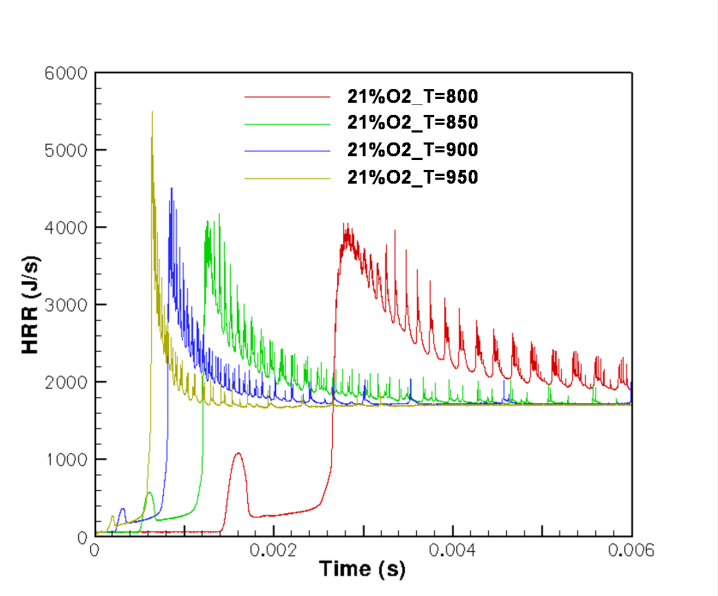

Figure 5.54. Computed heat-release rates versus time for the 21% O_2 n-heptane flame with 800 K to 950 K initial temperatures and 14.8 kg/m^3 initial density using the WSR model.

observed. The first-stage heat-release is followed by the large main heat-release

that characterizes the main combustion regime. The ignition delay, which is defined based on the onset of the main heat-release zone, becomes longer for lower temperatures. Low temperatures result in late second-stage (main) heat-release. The peak of the second-stage heat-release decreases with reductions in the initial temperature. At low temperatures, the chemistry becomes significantly slower and therefore results in incomplete combustion products.

The differences in computed heat-release rates between the PDF and WSR models are shown in Fig. 5.55 for initial temperatures of 800 K and 850 K. The PDF model predicts the first- and second-stage heat-release earlier than the WSR model. For both temperatures, the WSR model shows a higher peak than the PDF model; at later times, the heat-release rates for the two models are essentially the same, in time. The PDF model shows a more uniformly distributed heat-release. The differences between the PDF and WSR models decrease from 800 K to 850 K; at higher temperatures, as shown for the baseline n-heptane conditions (Fig. 5.25), the heat-release rates for the two models are close to each other.

Figure 5.56 shows the variations of ignition delay with temperature with and without TCI, and compares them with the measurements for the 8% O_2 n-heptane flames. It was observed earlier that for the baseline conditions, the model predictions show maximum deviation from the measurements for the lowest O_2 level (8% O_2). Differences are also observed between the two models (PDF and WSR). This is an extreme conditions that corresponds to high EGR and low O_2, where the fuel-vapor mixture requires a longer time to produce the desired equivalence ratio for autoignition. The longer ignition delay provides more time for the turbulent fluctuations to interact with the chemical scales. Therefore, this condition is expected to be one where differences between the PDF model and WSR model would be large. The comparison of computed ignition delays between the PDF and WSR models shows that overall the PDF model predicts the ignition delays better than the WSR model. The WSR model starts with a significant overprediction at T=1000 K and ends with an underprediction at T=1200 K. The PDF model, on the other hand, shows a more consistent overprediction of ignition delay, and the margin of overprediction decreases with increasing temperature. At T=1200 K, the PDF prediction lies on top of the measurement.

Comparisons of computed ignition delays between the PDF and WSR models

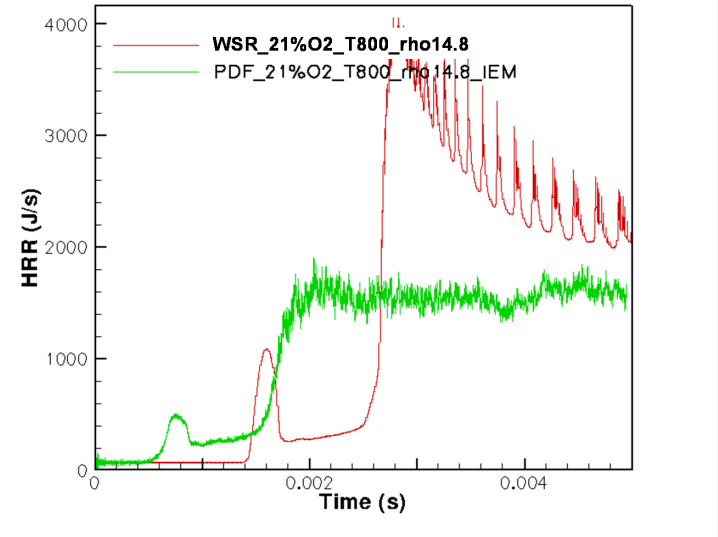

(a)

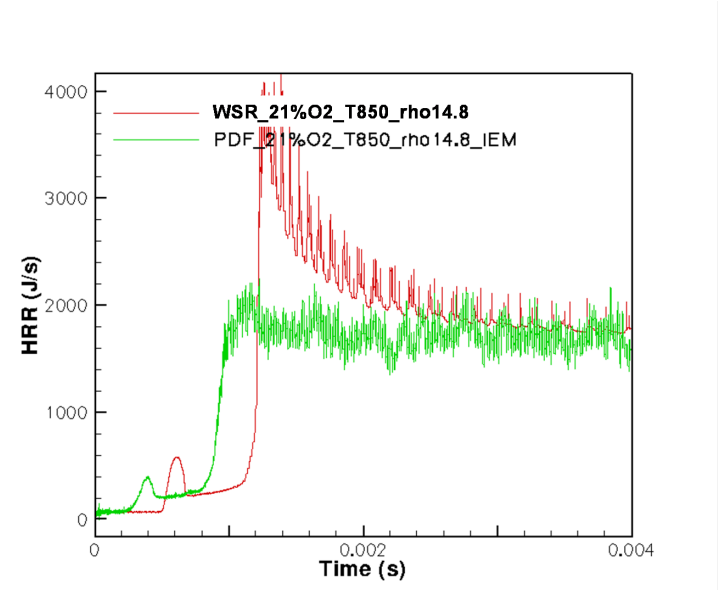

(b)

Figure 5.55. Computed heat-release rates versus time for the 21% O_2 n-heptane flame with initial temperature of (a) 800 K and (b) 850 K using the PDF and WSR models.

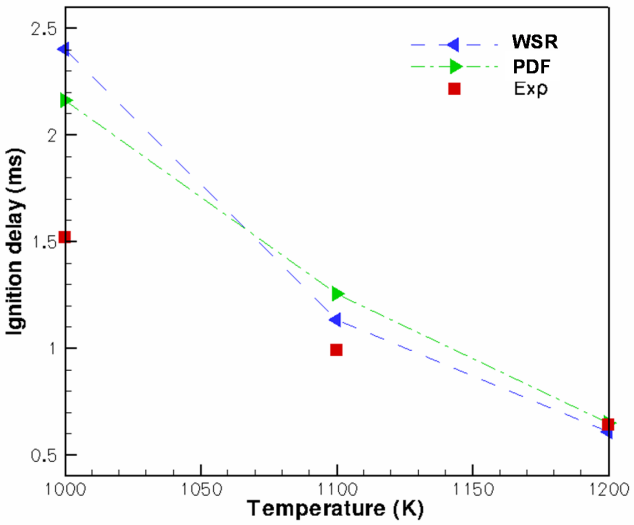

Figure 5.56. Comparisons of computed ignition delay (ms) versus initial temperature (K) using the PDF and WSR models for the 8% O_2, 14.8 kg/m^3 initial density n-heptane flames.

are shown in Fig. 5.57 for two O_2 levels (8% and 15%) at an ambient density of 30.0 kg/m^3 and temperature of 1000 K. The PDF and WSR predictions are identical. The higher ambient density results from higher vessel pressure, which in turn increases the reaction rates for the combustible mixture. As the chemistry becomes faster, the coupling between the turbulent fluctuations and chemistry becomes progressively weaker, and TCI become relatively less important. This is also evident in the heat-release profiles for 8% O_2 level at high ambient density shown in Fig. 5.58, where the WSR and PDF models coincide, in contrast to results shown earlier at lower pressures. However, as shown earlier, there are still significant differences in the computed turbulent flame structures with versus without consideration of TCI.

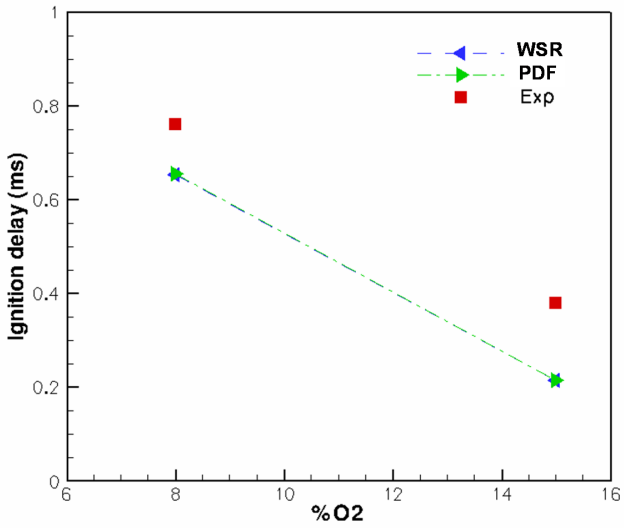

Figure 5.57. Comparisons of computed ignition delay (ms) versus O_2 using the PDF and WSR models for 1000 K initial temperature, 30.0 kg/m^3 initial density n-heptane flames.

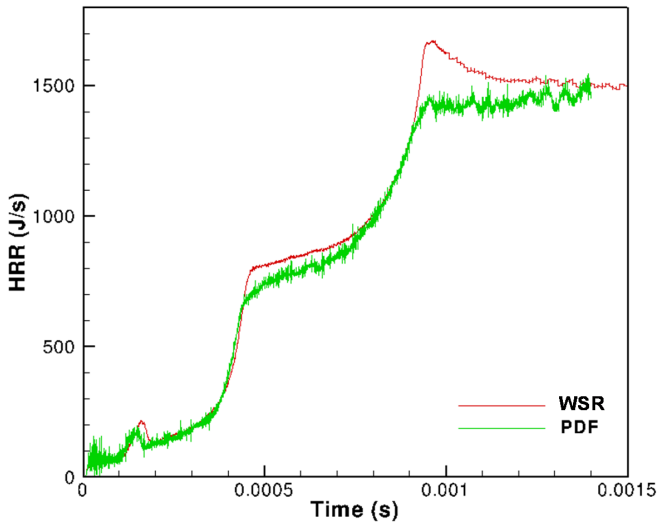

Figure 5.58. Computed heat-release rates versus time using the PDF and WSR models for the 8% O_2 n-heptane flame with 1000 K initial temperature and 30.0 kg/m^3 initial density.

Chapter 6

Results for n-Dodecane Sprays and Spray Flames

In this chapter, results are presented for n-dodecane sprays and spray flames (Spray-A), using the same axisymmeytric geometry and boundary conditions that were described in Chapter 4. The organization of results for n-dodecane in this chapter follows that for n-heptane in Chapter 5. Results first are presented for a non-reacting evaporating spray. These are followed by results for reacting spray flames over a range of operating conditions where experimental measurements are available.

6.1 Non-reacting n-Dodecane Spray

Key experimental diagnostics available are the time evolution of liquid and vapor penetration lengths, radial profiles of mean mixture fraction at selected axial locations and times, and images of mean mixture fraction contours. The physical models that are used in this section are same as those used for n-heptane fuel: high-Reynolds-number standard $k-\epsilon$ model [144, 145] with standard wall functions for turbulence, Reitz-Diwakar [140] model to account for secondary break-up and dispersed-phase model [141] for the dilute spray. The turbulence and break-up model coefficients are initially carried over from those used for the baseline n-heptane flames ($C_{\epsilon 1}$=1.50, T_{strp}=19). However, it is anticipated that due to the higher boiling point of n-dodecane compared to n-heptane and differences in molec-

ular and thermodynamic properties, the evaporation and mixing characteristics of n-dodecane may significantly differ from those of n-heptane. The higher boiling point of n-dodecane (approximately 100 K higher than n-heptane) can slow down the evaporation and the subsequent mixing processes. This may require a different set of model coefficients for the turbulence and break-up models to match the measurements. Therefore, a parametric study is conducted to explore the sensitivity of the spray characteristics to the choice of turbulence model constant $C_{\epsilon 1}$ for the ϵ equation, and breakup time constant T_{strp} for the secondary breakup model.

The results in this section are organized as follows. First, computed liquid and vapor penetration lengths are compared with the experiment using a baseline WSR model. The sensitivities of the computed penetration lengths to the specification of turbulence and break-up model constants are investigated. Next, radial profiles of computed mean mixture fraction are compared with measurements over a range of values for the model constants. Based on these comparisons, a baseline set of model constants is selected for the rest of the computations. Then results are compared between the WSR and PDF models. As was the case for the baseline n-heptane non-reacting sprays, the emphasis is on accurate prediction of penetration lengths and mean mixture fraction profiles, to ensure that the numerical model predicts the correct mixing and evaporation of the spray prior to reaction. The initial conditions, boundary conditions and model parameters for the spray and gas-phase are listed in Table 6.1, and the model constants specific to the turbulence and spray models are listed in Table 6.2. It is noted that the initial conditions are different from the baseline n-heptane spray conditions. The initial temperature is 100 K lower and the initial pressure is approximately 45% higher compared to the baseline n-heptane spray. The spray-A nozzle diameter (0.09 mm) also is smaller than the one used for the n-heptane spray (0.1 mm), and the injection temperature is 10 K lower than for the n-heptane spray. The gas-phase initial compositions, initial turbulence, and boundary conditions remain the same. However, the turbulence and spray model constants are adjusted to produce the correct mixing and evaporation rates.

Figure 6.1 shows comparisons of the liquid and vapor penetration lengths computed using the WSR model with experimental measurements. Three values of the turbulent model constant $C_{\epsilon 1}$ (=1.52, 1.53, and 1.54) are considered. The details

Table 6.1. Model specification for n-dodecane sprays

Computational time step	WSR (s) PDF (s)	5.0e-7 1.0e-7/2.0e-7
Injector and spray models	Injector location Injection rate, 360^0 equiv (kg/s) /constant or variable Number of parcels per time-step Injector model and key parameters Spray model key parameters	on-axis 0.0027/constant 50 constant-size blobs, inner cone angle=0^0, outer cone half angle= 6.3^0, SMD = 8.37e-5 m, velocity = 700 m/s Temp = 363 K no primary breakup, Reitz secondary breakup, turbulent dispersion, no collision
Turbulence model	Type	Standard $k-\epsilon$
Initial conditions	Temperature (K)	900
	Pressure (Pa) Density (kg/m^3) O_2 mass fraction N_2 mass fraction CO_2 mass fraction H_2O mass fraction Turbulence kinetic energy (m^2/s^2) Turbulence dissipation rate (m^2/s^3)	5948886.00 22.8 0.0 0.876270 0.100049 0.023681 0.735 3.5
Boundary conditions	Momentum Energy	no-slip walls, standard wall functions fixed T (850 K)

of the model constants are provided in Table 6.2. Compared to measurements it is found that the liquid penetration length is insensitive to $C_{\epsilon 1}$, and is overpredicted for all values of $C_{\epsilon 1}$. The insensitivity of computed liquid penetration length to $C_{\epsilon 1}$ is attributed to the short interaction time between the liquid spray and the gas-phase turbulence, which eliminates any strong impact of gas-phase turbulence on the liquid penetration length. The vapor penetration length, much like that for the n-heptane spray, is sensitive to variations in $C_{\epsilon 1}$, with higher vapor penetra-

Table 6.2. Model constants for n-dodecane spray.

Turbulence Model	Standard $k-\epsilon$	Range for parametric studies
	C_μ=0.09	-
	$C_{\epsilon 1}$=1.54	1.50 - 1.54
	$C_{\epsilon 2}$=1.92	-
	$C_{\epsilon 3}$=1.44	-
	κ=0.41	-
	σ_k=1.0	-
	σ_ϵ=1.219	-
Breakup Model	Reitz-Diwakar secondary breakup	-
	T_{strp} = 18.0	12 - 18
	T_{bag} = 3.1416	-
	We_{strp} = 0.6	-
	We_{bag} = 6.0	-
Spray Model	Dispersed Phase Model,	-
	Ranz Marshall correlation	
	for heat/mass transfer	

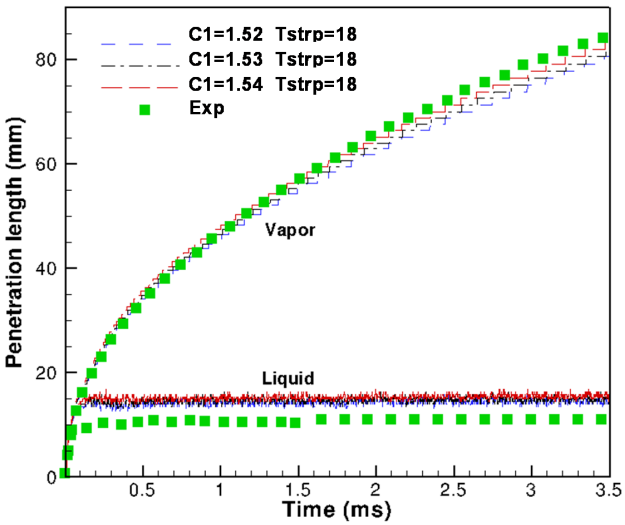

Figure 6.1. Sensitivity of computed liquid and vapor penetration lengths to variations in turbulence model coefficient $C_{\epsilon 1}$ for the WSR model. Three values of model constant have been considered: $C_{\epsilon 1}$=1.52, 1.53, and 1.54. The breakup constant is T_{strp}=18.

tion length observed for higher $C_{\epsilon 1}$. The computed vapor penetration length for the WSR model produces the closest match with the measurements for $C_{\epsilon 1}$=1.54. The sensitivity of computed liquid and vapor penetration lengths to variations in breakup model constant T_{strp} is illustrated using the WSR model in Fig. 6.2. Three values of T_{strp} (=12, 16, 18) are considered for comparison; $C_{\epsilon 1}$ is kept constant at 1.54. it is observed that the liquid penetration length is overpredicted for all values of T_{strp}, with T_{strp}=12 producing marginal improvement compared to the

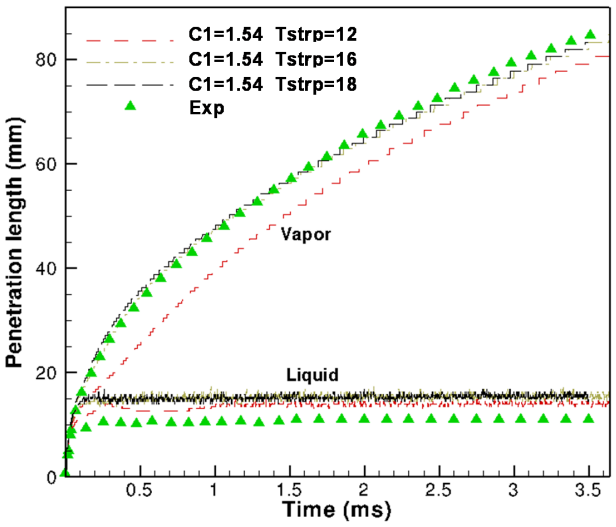

Figure 6.2. Sensitivity of computed liquid and vapor penetration lengths to variations in spray breakup model parameter T_{strp} for the WSR model. Three values of breakup time constant are considered: T_{strp}=12, 16, and 18. The turbulence model used is the standard $k-\epsilon$ model with $C_{\epsilon 1}$=1.54.

other two values. However, the vapor penetration is significantly underpredicted with T_{strp}=12, while the other two values (T_{strp}=16 and 18) produce a reasonable match with the measurements and are essentially identical. The earlier study with Spray-H showed that the vapor penetration length was insensitive to the choice of T_{strp}. However, that study was limited to a narrow range of T_{strp} from 16 to 19. For extremely low values of T_{strp}, the breakup time reduces significantly, resulting in faster breakup that slows down the vapor jet. This is probably the reason for the low computed vapor penetration length with T_{strp}=12. For the next subsequent computations, T_{strp}=18 is used.

To maintain consistency, the criteria used to determine the computed penetration lengths are the same as those used for the n-heptane spray. These criteria have been established by the ECN modeling groups for n-heptane sprays, and the extension of these criteria to n-dodecane sprays needs to be carefully evaluated. It is believed that the validation of computational models based on mixture fraction profiles is more appropriate to evaluate the performance of the computational models, since the mixture fraction is computed from fuel mass fraction, and therefore, does not depend on arbitrary criteria.

Figures 6.3 and 6.4 compare predictions for radial profiles of mean mixture fraction from the WSR model with experimental measurements at axial locations of z=25 and 45 mm at time t=1.5 ms after the start of injection. A standard $k-\epsilon$ turbulence model is used with $C_{\epsilon 1}$=1.52, 1.53, and 1.54. In absence of chemical reaction, the mixture fraction is defined as the fuel-vapor mass fraction. The radial profile for mean mixture fraction has its maximum value at the centerline of the jet and drops monotonically in the radially outward direction. The comparisons of profiles show that the radial profiles are sensitive to $C_{\epsilon 1}$. The higher the $C_{\epsilon 1}$, the higher is the centerline peak and the narrower the profile. This is consistent with the comparisons of vapor penetration length, which show higher vapor penetration length for higher $C_{\epsilon 1}$. Higher vapor penetration reduces the jet radial spread due to conservation of mass, and results in radially narrower profiles with higher centerline peak. The mean mixture fraction profile is observed to be more sensitive to the choice of $C_{\epsilon 1}$ near the injector (z=25 mm) than further downstream (z=45 mm). At z=45 mm, all the values of model constant produce similar results. Based on the overall agreement with the measurements, $C_{\epsilon 1}$=1.52 produces marginally better results than the other values.

The above sensitivity studies show that no single model constant exists that produces the best match in both vapor penetration and mixture fraction profiles. The vapor penetration is best captured with $C_{\epsilon 1}$=1.54, whereas the mixture fraction profile is best captured with $C_{\epsilon 1}$=1.52. For the PDF model, a value of 1.54 is employed here. However, for the reacting conditions the global ignition characteristics are also computed for $C_{\epsilon 1}$=1.52 and the differences between results for the two values of model constant are monitored.

Figures 6.5 and 6.6 compare predictions of radial profiles of mean mixture

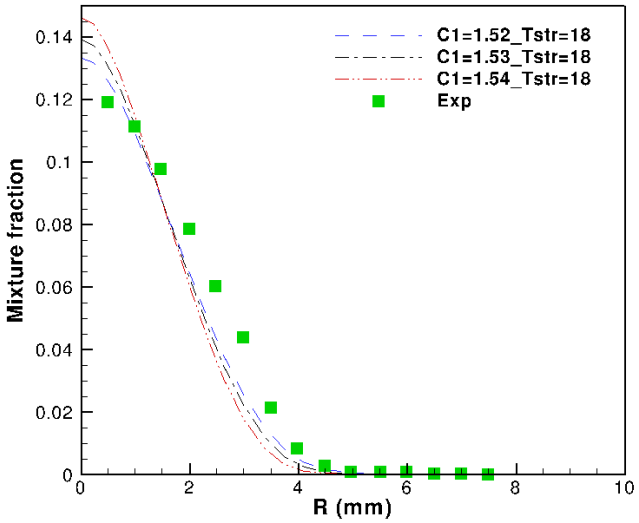

Figure 6.3. Sensitivity of computed radial profiles of mean mixture fraction at axial location z=25 mm at time t=1.5 ms after the start of injection to variations in turbulence model constant $C_{\epsilon 1}$. Three values of model constant have been used: $C_{\epsilon 1}$=1.52, 1.53, and 1.54. The breakup constant is T_{strp}=18.

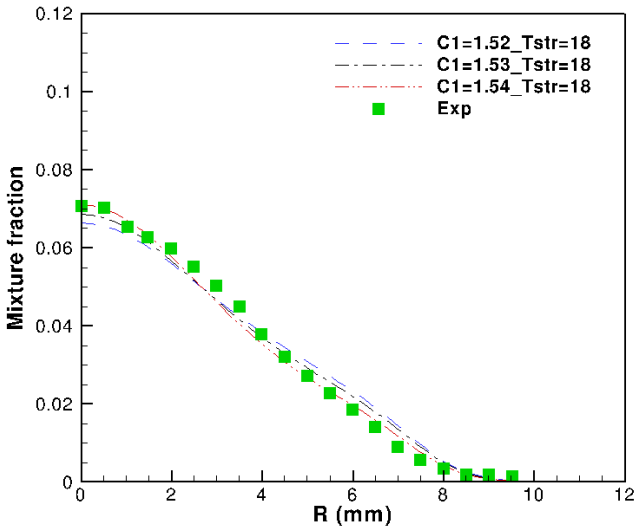

Figure 6.4. Sensitivity of computed radial profiles of mean mixture fraction at axial location z=45 mm at time t=1.5 ms after the start of injection to variations in turbulence model constant $C_{\epsilon 1}$. Three values of model constant have been used: $C_{\epsilon 1}$=1.52, 1.53, and 1.54. The breakup constant is T_{strp}=18.

fraction from the WSR and PDF models with experimental measurements at axial locations of z=25 and 45 mm from the injector at time t=1.5 ms after the start of injection. The turbulence and breakup model constants are $C_{\epsilon 1}$=1.54 and

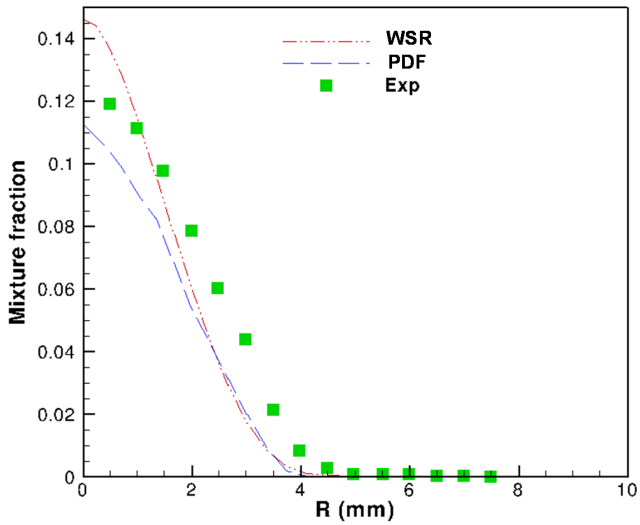

Figure 6.5. Comparison of radial profiles of mean mixture fraction at axial location z=25 mm at time t=1.5 ms after the start of injection for the WSR and PDF models, using the baseline model constants. For the PDF model, the IEM mixing model with C_{ϕ}=3.0 is used.

T_{strp}=18. At z=25 mm, the PDF model underpredicts the peak mean mixture fraction by approximately 8%, whereas the WSR model overpredicts the peak by approximately 16%. However, both the models underpredict the spread of the jet. At z=45 mm, the WSR model produces an excellent match with the measurements, whereas the PDF model underpredicts the data. This is similar to the n-heptane results, where at t=6.0 ms, the PDF model underpredicts the data for values of model constants that were calibrated using the WSR model.

6.2 Autoignition and Combustion for n-Dodecane Spray Flames

In this section, the model predictions are compared with the measurements over a range of conditions that include variations in initial temperatures. In contrast to

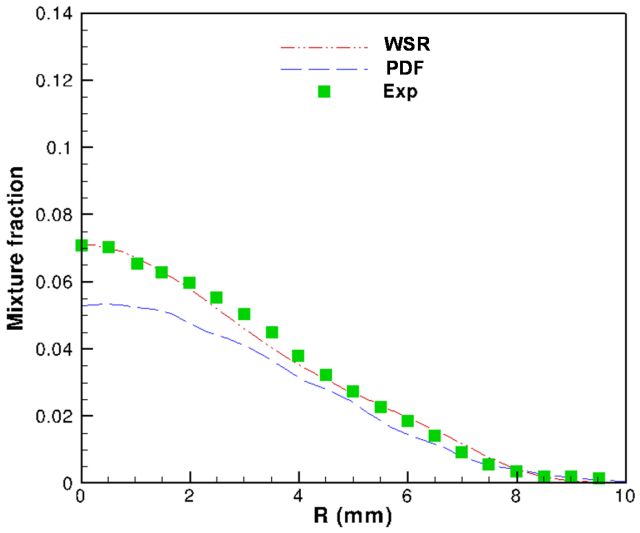

Figure 6.6. Comparison of radial profiles of mean mixture fraction at axial location z=45 mm at time t=1.5 ms after the start of injection for the WSR and PDF models, using the baseline model constants. For the PDF model, the IEM mixing model with C_ϕ=3.0 is used.

the n-heptane flames, the measured data for n-dodecane are limited to the 15% O_2 level only. Therefore, the comparisons of model predictions with the measurements are limited to variations in lift-off length and ignition delay with variations in initial temperature over a range of 800 to 1100 K.

The comparisons of ignition delay between the PDF and WSR models are shown over a temperature range of 800 to 1100 K in Fig. 6.7 using a 103-species, 370-reactions skeletal kinetic mechanism [3]. The PDF model shows significant improvement in prediction over the WSR model. For an initial temperature of 900 K, the predictions from the PDF model show remarkable agreement with the measurement data, whereas the WSR model predicts an ignition delay that is three times the measured value. For an initial temperature of 800 K, the WSR model fails to produce ignition, whereas the PDF model shows a clear two-stage ignition process (Fig. 6.9). Compared to n-heptane spray flames, the spray-A flames exhibit larger differences in global characteristics between the PDF and WSR models, with the PDF model results being in much better agreement with experiment. The general trends of the predictions are, however, similar to those

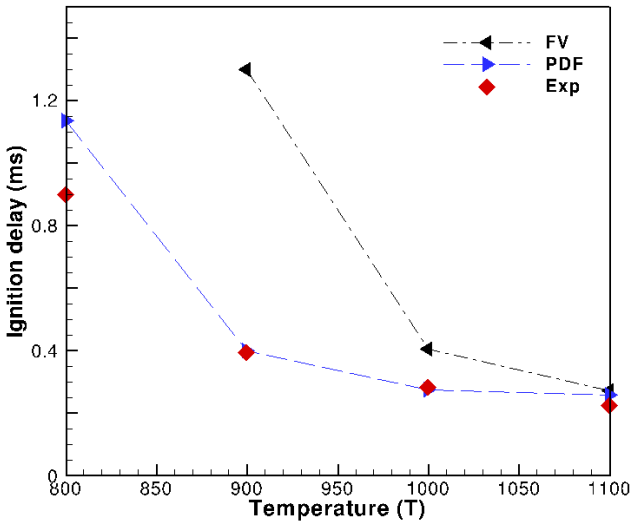

Figure 6.7. Computed and measured ignition delays versus initial temperature for the 15% O_2 n-dodecane flames using the WSR and PDF models. For the PDF model, IEM mixing is used with C_ϕ=3.0.

for n-heptane: both the PDF and WSR predictions deviate from measurements as the initial temperature drops, and they converge towards each other as the initial temperature increases. The comparisons of lift-off length between the two models over the same temperature range are shown in Fig. 6.8. The PDF model shows a better match in lift-off length with the measurements compared to the WSR model. This is different than what was found for n-heptane, where the WSR model showed somewhat better predictions of lift-off length. Comparisons of heat-release rates between the two models are presented in Fig. 6.10 for an initial temperature of 1000 K. The PDF model shows earlier autoignition compared to the WSR model. The higher peak in heat-release rate combined with later autoignition for the WSR model is consistent with the heat-release rate predictions for n-heptane flames.

The predictions from the computational models are compared for $C_{\epsilon 1}$=1.52 versus $C_{\epsilon 1}$=1.54 using the PDF/IEM model. The initial temperature is kept at 1100 K. With $C_{\epsilon 1}$=1.52, the computed ignition delay is 0.27 ms, whereas the ignition delay for $C_{\epsilon 1}$=1.54 is 0.26 ms. No appreciable differences are observed in computed lift-off lengths, either. The higher the $C_{\epsilon 1}$, the higher is the peak mean mixture fraction, and therefore the faster the mixture ignites. However, the

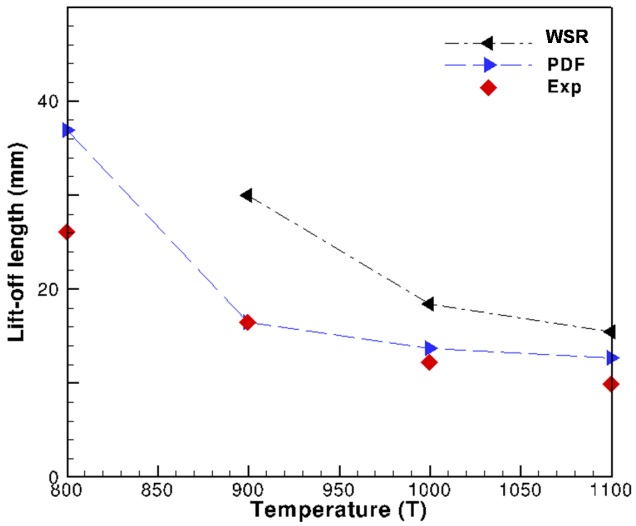

Figure 6.8. Computed and measured lift-off lengths versus initial temperature for the 15% O_2 n-dodecane flames using the WSR and PDF models. For the PDF model, IEM mixing is used with C_ϕ=3.0. For an initial temperature of 800 K, the WSR model fails to ignite.

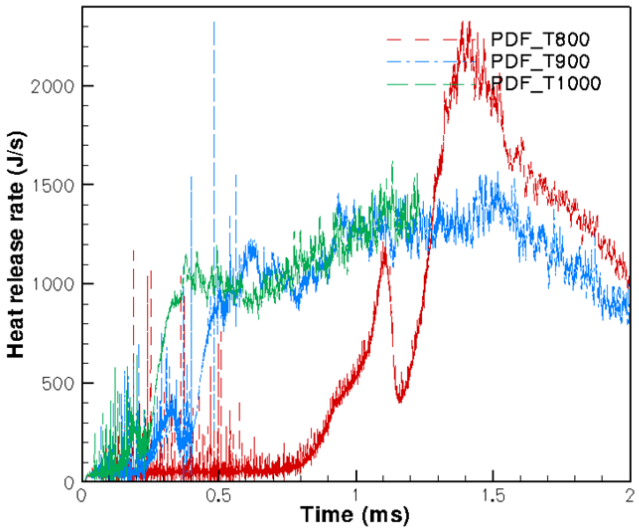

Figure 6.9. Computed heat-release rates versus time using the PDF/IEM model for the 15% O_2 n-dodecane flames for three initial temperature of 800, 900 and 1000 K.

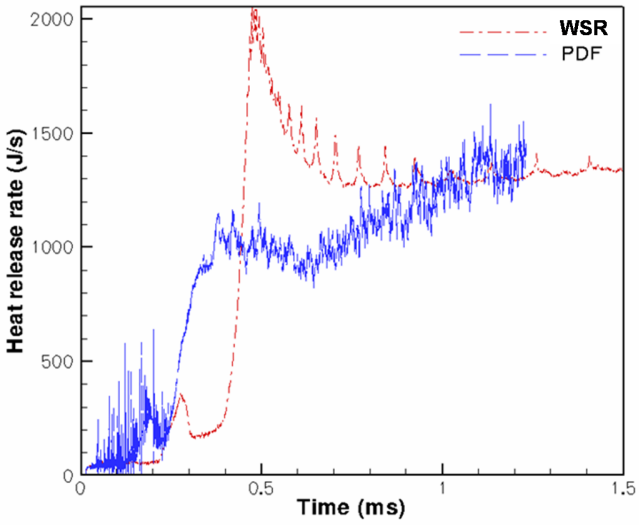

Figure 6.10. Computed heat-release rates versus time using the WSR and PDF models for the 15% O_2 n-dodecane flame for an initial temperature of 1000 K.

difference in predictions between the two values of the model constant ($C_{\epsilon 1}$) are small and can be neglected for all practical purposes.

The computed $\phi - T$ maps for the PDF and WSR models are compared in Fig. 6.11 for an initial temperature of 1000 K, initial O_2 mole fraction of 15%, and initial density of 22.8 kg/m^3. The primary difference between the results for the two models lies in the rich premixed zone of the flame. Compared to the n-heptane flame, the premixed rich combustion zone is shorter here. Difference in $\phi - T$ map between the two models diminish for temperatures higher than 1500 K on the fuel-rich side of the flame. On the ambient side of the flame, the predictions from the two models essentially overlap.

6.3 Computational Requirements

The PDF method is computationally intensive, and it is of interest to explore its scalability. A n-dodecane spray flame with an initial temperature of 1000 K, 15% O_2, and density of 22.8 kg/m^3 is used as the test case. The overall computational time required for the PDF model is compared with that for the WSR model in Table 6.3. The computational time required for the PDF model is approximately one

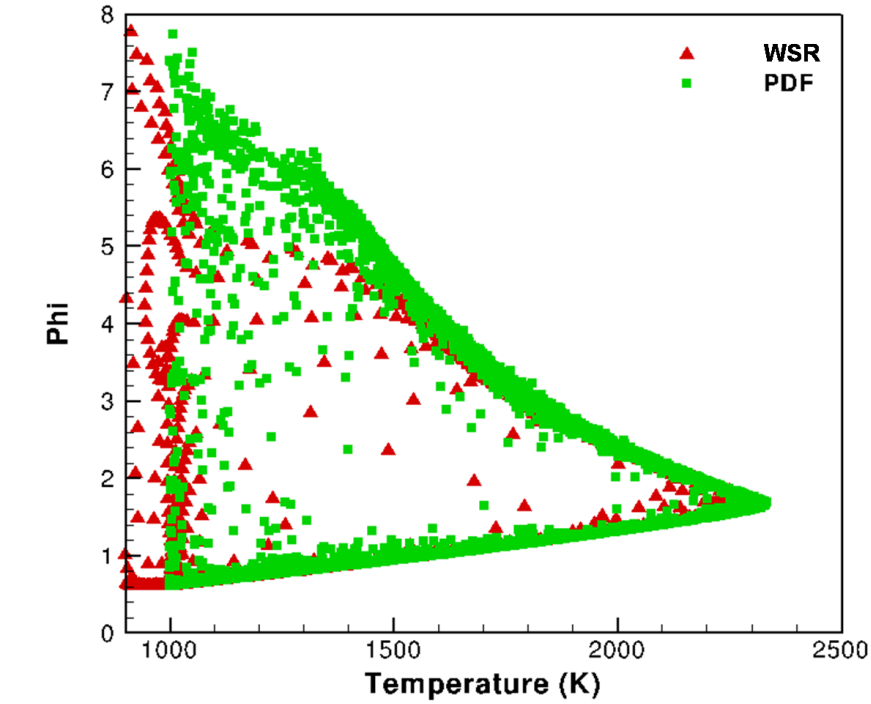

Figure 6.11. Comparisons of computed $\phi - T$ maps for the WSR and PDF models for n-dodecane with 15% O_2. For the PDF model, IEM mixing is used with C_ϕ=3.0.

order-of-magnitude more than the WSR model. It is noted that for this comparison the PDF model has been initialized with 20 particles per cell. The computational time for the PDF model increases linearly with the increase in number of particles per cell. The computational time required for the chemistry solver alone is also computed by comparing the overall computational time for the reacting spray flame with that of a non-reacting spray. It is observed that approximately 87% of the overall computational time is consumed in the chemistry computations. However, it should be emphasized that the fraction of overall time spent in solving for chemistry may change from one operating condition to other, and from one chemical mechanism to another.

The parallel scalability of the computational model using the PDF model is illustrated in Table 6.4. It is observed that the computational time scales approximately linearly with the number of processors up to eight processors. This is expected, since the PDF model parallelizes efficiently. This linear scale-up with

the number of processors holds the promise for computations with larger number of processors.

Table 6.3. Computational time for the PDF and WSR models using n-dodecane spray combustion.

	PDF	WSR
Number of processor	1	1
Wall time (hrs) per 100 time step	13.24	1.21

Table 6.4. Computational time and scalability for the PDF model using n-dodecane spray combustion.

Number of processors	1	2	4	8
Wall time (hrs) per 100 time step	13.24	6.5789	3.2628	1.6658
Speedup relative to one processor	1.00	2.01	4.06	7.95

Chapter 7

Conclusions and Recommendations

7.1 Conclusions

Low-temperature, high-pressure, globally fuel-lean and/or dilute combustion modes are of interest for next-generation compression-ignition engines to reduce emissions and improve fuel economy over a wide range of operating conditions. These combustion modes are very different from traditional diesel combustion, and modeling them requires improved physical models that can accommodate strong coupling between the spray, turbulence, and chemistry. Turbulence-chemistry interactions (TCI) in engine-relevant environments have been emphasized here. The turbulence-chemistry interactions are captured using a hybrid Lagrangian-particle/ Eulerian-mesh probability density function (PDF) model that allows for arbitrarily large gas-phase chemical mechanisms and detailed soot and radiation models. This research has focussed on understanding the extent to which TCI influence local flame structures and global autoignition characteristics under diesel-engine-like conditions.

The computational configuration is a constant-volume combustion chamber with well-defined initial conditions (ECN) [1]. Model results have been compared with ECN measurements for two single-component diesel fuel surrogates: n-heptane and n-dodecane. The effects of TCI have been evaluated for ignition delay, lift-off length, heat-release rate, species profiles, and soot volume fraction. The importance of radiation modeling on temperature and soot formation also has been investigated, using an optically-thin radiation model that captures the

turbulence-radiation interactions (TRI). A near-injector secondary breakup model and far-field dispersed-phase model have been used to account for liquid fuel injection and sprays.

The key findings for n-heptane spray flames are as follows:

- The predicted global autoignition characteristics (lift-off length and ignition delay) from the WSR and PDF models are similar at high initial temperatures, high initial O_2 concentrations, and/or high initial pressures. For these conditions, consideration of TCI does not contribute to any significant difference in computing the global autoignition characteristics.

- The differences in the computed global autoignition characteristics (lift-off length and ignition delay) from the WSR and PDF models increase at low initial temperatures, and/or low O_2 concentrations. For example, at 800 K, the PDF model underpredicts the ignition delay by approximately 5%, whereas the WSR model overpredicts the measurement by approximately 60%. For these conditions (low initial temperatures, and/or low O_2 concentrations), consideration of TCI contributes significantly in improving the computed ignition delay over the model that neglects TCI.

- For all the conditions, the WSR and PDF models produce significantly different flame structures. The differences between the two models increase for low initial temperatures and/or oxygen concentrations. The PDF model shows a more distributed turbulent flame brush that is more consistent with that observed in the experiment, whereas the WSR model shows a thin laminar-like flame structure. This shows that TCI are important in capturing realistic flame characteristics, although the global combustion characteristics with and without TCI may not show significant differences.

- The peak soot volume fraction is well captured by the PDF model ($\sim$ 1.2 ppm) compared to the WSR model; the latter predicts a peak soot volume fraction of 2.5 ppm, which is approximately twice that obtained from the measurements ($\sim$ 1.2 ppm). Although both the models predict the location of the peak soot volume fraction to be upstream of that observed in experiment,

consideration of TCI shows significant differences in the distribution of soot cloud compared to the WSR model (that neglects TCI).

- At low initial temperatures ($\leq$ 900 K) and/or low O_2 concentrations, the PDF model predicts a more distinct two-stage heat-release process than that predicted by the WSR model. The first stage of autoignition becomes more distinct at lower initial temperatures. The WSR model shows a higher peak for the main heat-release than that from the PDF model. Consideration of TCI results in earlier autoignition and significant differences in heat-release rate compared to the WSR model.

The computational models for n-heptane then were extended to n-dodecane sprays and spray flames, with the same models for turbulence and sprays. However, due to differences in evaporation, molecular properties and other thermodynamic properties the model constants were recalibrated from those used in the n-heptane sprays. The chemical mechanism for n-dodecane flames is a 103-species, 370-reaction skeletal mechanism [3] that has more detailed low-temperature chemistry pathway than the 40-species chemical mechanism [2] used for the n-heptane chemistry.

The key findings for n-dodecane spray flames are summarized below.

- Stronger differences are observed in the predicted global characteristics (ignition delay and lift-off length) between the PDF and WSR models compared to n-heptane flames, with the PDF results being in much better agreement with measurements. At an initial temperature of 900 K, while the WSR model predicts an ignition delay that is three times higher than the measured value, the PDF model prediction is within 5% of the measured data. At an initial temperature of 800 K, the WSR model fails to ignite, whereas the PDF model gives an ignition delay that matches reasonably with experiment. Clearly, consideration of TCI results in a significant improvement in the global combustion characteristics.

- The differences in heat-release rate between the WSR and PDF models are greater than those observed for n-heptane flames under the same initial conditions of temperature and O_2 concentration. For n-dodecane, the PDF model

shows distinct two-stage autoignition at all the temperatures, whereas the WSR model predicts a smaller first-stage heat-release zone, and higher peak heat-release rate. This shows that TCI contribute to stronger differences in heat-release rate when low-temperature chemistry is considered.

7.2 Recommendations

Based on the comparisons between the PDF and WSR models, the following recommendations are made for future research.

7.2.1 Configurations

The comparisons presented in this dissertation have been based on a simple constant-volume experimental configuration provided by the ECN Workshop using n-heptane and n-dodecane as the fuels. While a model that accounts for TCI demonstrated its strength in producing more realistic flame structures, and improved quantitative agreement with experiment, further investigation is needed. In the current work, the comparisons with experiment have been limited mainly to global ignition/combustion characteristics. More extensive validation with more exhaustive measurements is needed including profiles of mean temperature and species, and rms (root mean square) of scalar fluctuations at different locations. The ECN database is expected to grow in the future to include such measurements for n-dodecane and other fuels. The model comparisons need to be extended to other fuels, including multicomponent fuels and a wider range of operating conditions. Another possible extension of this work would be to simulate other geometric configurations, from other constant-volume devices and realistic engines. The ultimate goal is to apply this model to simulate turbulent combustion in real compression-ignition engines.

7.2.2 Physical Modeling

The quality of high-fidelity CFD predictions depends on the accuracy of the physical models that are used to capture the physical processes that control the combustion in turbulent spray flames. The ability of the physical models to reproduce the

physical processes accurately relies on physical understanding of the underlying processes that is derived from theoretical and experimental studies. Many of the key physical processes are not completely understood due to limited analytical and experimental data. The success of CFD predictions continues to depend on ongoing improvements in the physical models that need to be validated with exhaustive measurements with current state-of-the-art experimental diagnostics. Key areas of model improvement include sprays, chemical kinetics, soot, radiation, and turbulence/chemistry/soot/radiation interactions [125, 126, 200, 113]. Another possible direction is towards large-eddy simulation (LES), using a filtered density function (FDF) approach.

The near-injector spray modeling presented here is based on a secondary breakup model. The numerical model could be extended to include more detailed breakup models that account for both primary and secondary breakup. The dispersed-phase model for dilute sprays could be extended to multicomponent sprays with detailed evaporation models for each of the liquid species. For realistic engine-spray modeling at low-load conditions, spray-wall interactions may need to be considered.

The accuracy of the computational model depends on the spatial resolution of the computational mesh. For reliable CFD predictions, the solution should be independent of mesh. The spray model presented here depends on the mesh size, and therefore requires adjusting model constants to control the shape and penetration length of the spray. For realistic spray predictions in engine configuration, an adaptive meshing strategy may need to be considered to eliminate the mesh-dependent tuning of the spray model [201].

The combustion predictions are strongly influenced by the chemical kinetics. Accurate combustion predictions demand suitable chemical kinetics mechanisms that capture both the low- and high-temperature reaction pathways and that are computationally efficient with current state-of-the-art computational resources.

The soot modeling presented in the current work includes a semi-empirical two-equation soot model and a detailed soot model with a method of moments with interpolative closure for soot aerosol dynamics. The two-equation soot model depends on empirical rate coefficients that have been calibrated based on experimental data in specific flame configurations. The modeling parameters that control

the overall soot levels need to be investigated to improve the soot predictions for engine-relevant conditions. The MOMIC-based model, on the other hand, is a more fundamental approach. However, like the two-equation model, this model has not yet been explored for realistic engine conditions.

Here radiation has been modeled using an optically-thin model, and modest effects of radiation have been found. A possible extension of this work would be the implementation of more sophisticated radiation models, such as a photon Monte Carlo method [125, 126] that accurately accounts for both emission and absorption TRI in the context of PDF methods. A possible future direction would be to account for turbulence/chemistry/soot/radiation interactions. This requires detailed modeling and coupling of turbulence, chemistry, soot formation, and radiation effects.

Driven by more powerful computational resources, a promising future direction would be to move towards large-eddy simulation (LES) [200]. LES with PDF-based models for unresolved turbulent fluctuations has shown promise in laboratory flames.

7.2.3 Numerical Algorithms

High computational cost has been a major bottleneck for the PDF methods. To increase the computational speed, two possible strategies have been used in earlier studies: ISAT (*in-situ* adaptive tabulation) and parallelization with a "Round-Robin" algorithm. Eulerian PDF-based approaches have been reviewed recently, in the context of computational cost, and significant improvements in computational speed have been achieved with multi-environment probability density function (MEPDF) methods [113]. However, in the context of the particle PDF methods, further work is required to expedite the chemistry computations, which consume the major part of computational time.

Appendix A

n-Heptane Chemical Mechanism

For n-heptane the chemical kinetics for the 40-species, 165-reactions skeletal mechanism [2] is provided below. Units are cm-mole-sec-K for the pre-exponential Arrhenius coefficient and cal/mole for the activation energy. The coefficients are listed after the rate equation as pre-exponential, temperature exponent, and the activation energy.

```
ELEMENTS
    H      O      C      N
END
SPECIES
C7H16       O2          N2          CO2         H2O
CO          H2          OH          CH4         C2H2
C2H4        H2O2        HO2         H           O
CH3         CH3O        CH2         CH2O        CH3O2
CH4O2       HCO         C7H15-1     C7H15-2     C7H15O2
C7H14O2H    C7H14O2HO2  C7KET12     C6H12       C5H11CHO
C5H11CO     C5H11       C4H9        C3H7        C3H6
C3H5        C3H4        C2H3        C2H5        C2H6
END
```

REACTIONS

C7H16 + H	= C7H15-1 + H2	5.600E+07 2.0 7667.0!
C7H16 + H	= C7H15-2 + H2	4.380E+07 2.0 4750.0!
C7H16 + OH	= C7H15-1 + H2O	8.610E+09 1.10 1815.0!
C7H16 + OH	= C7H15-2 + H2O	4.500E+09 1.30 690.5!
C7H16 + HO2	= C7H15-1 + H2O2	1.120E+13 0.0 19300.0!
C7H16 + HO2	= C7H15-2 + H2O2	1.650E+13 0.0 16950.0!
C7H16 + O2	= C7H15-1 + HO2	2.500E+13 0.0 48810.0!
C7H16 + O2	= C7H15-2 + HO2	2.000E+14 0.0 47380.0!
C7H15-1 + O2	= C7H15O2	2.000E+12 0.0 0.0!
C7H15-2 + O2	= C7H15O2	2.000E+12 0.0 0.0!
C7H15O2	= C7H14O2H	6.000E+11 0.0 20380.0!
C7H14O2H + O2	= C7H14O2HO2	4.600E+11 0.0 0.0!
C7H14O2HO2	= C7KET12 + OH	1.000E+09 0.0 7480.0!
C7KET12	= C5H11CHO + CH2O + O	1.050E+16 0.0 4.110E+4! 16
C5H11CHO + O2	= C5H11CO + HO2	2.000E+13 0.5 4.220E+4!
C5H11CHO + OH	= C5H11CO + H2O	1.000E+13 0.0 0.000E+0!
C5H11CHO + H	= C5H11CO + H2	4.000E+13 0.0 4.200E+3!
C5H11CHO + O	= C5H11CO + OH	5.000E+12 0.0 1.790E+3!
C5H11CHO + HO2	= C5H11CO + H2O2	2.800E+12 0.0 1.360E+4!
C5H11CHO + CH3	= C5H11CO + CH4	1.700E+12 0.0 8.440E+3!
C5H11CHO + CH3O2	= C5H11CO + CH4O2	1.000E+12 0.0 9.500E+3!
C5H11CO	= C5H11 + CO	1.000E+11 0.0 9.600E+3!
C5H11	= C2H4 + C3H7	3.200E+13 0.0 28300.0!
C7H15-1	= C2H4 + C5H11	2.500E+13 0.0 28810.0!
C7H15-2	= C4H9 + C3H6	2.200E+13 0.0 28100.0!
C7H15-1	= C7H15-2	3.600E+16 0.0 80700.0!
C4H9	= C2H5 + C2H4	2.500E+13 0.0 28810.0!
C3H7	= C2H4 + CH3	9.600E+13 0.0 30950.0!
C3H7	= C3H6 + H	1.250E+14 0.0 36900.0!
C3H7 + O2	= C3H6 + HO2	1.000E+12 0.0 4980.0!
C3H6	= C2H3 + CH3	3.150E+15 0.0 85500.0!
C3H6 + H	= C3H5 + H2	5.000E+12 0.0 1500.0!
C3H6 + CH3	= C3H5 + CH4	9.000E+12 0.0 8480.0!
C3H5	= C3H4 + H	4.000E+13 0.0 69760.0!
C3H5 + H	= C3H4 + H2	1.000E+13 0.0 0.0!
C3H5 + O2	= C3H4 + HO2	6.000E+11 0.0 10000.0!
C3H4 + OH	= C2H3 + CH2O	1.000E+12 0.0 0.0!
C3H4 + OH	= C2H4 + HCO	1.000E+12 0.0 0.0!
CH3O + CO	= CH3 + CO2	1.570E+14 0.00 11800. !CGS 52
CH3O + M	= CH2O + H + M	1.000E+14 0.00 25000. !CGS 53
CH3O + H	= CH2O + H2	2.000E+13 0.00 0. !CGS 54
CH3O + OH	= CH2O + H2O	1.000E+13 0.00 0. !CGS 55
CH3O + O	= CH2O + OH	1.000E+13 0.00 0. !CGS 56
CH3O + O2	= CH2O + HO2	1.200E+11 0.00 2600. !CGS 57
CH3 + HO2	= CH3O + OH	5.000E+13 0.00 0. !CGS 58
CH3 + O2	= CH3O + O	4.670E+13 0.00 30000. !CGS 59
CH3 + O2	= CH2O + OH	3.800E+11 0.00 9000. !CGS 60
CH3 + O2	= CH3O2	3.020E+59 -15.0 17204. !CGS 61
CH3O2 + HO2	= CH4O2 + O2	4.630E+11 0.0 -2583. !CGS 24
CH3O2 + CH4	= CH4O2 + CH3	1.810E+11 0.0 18480. !CGS 25
CH3O2 + CH3	= CH3O + CH3O	2.410E+13 0.0 0. !CGS 26
CH3O2 + O	= CH3O + O2	3.610E+13 0.0 0. !CGS 27
CH3O2 + H	= CH3O + OH	9.640E+13 0.0 0. !CGS 28
CH3O2 + CH2O	= CH4O2 + HCO	1.000E+12 0.0 11665. !CGS 29
CH3O2 + C2H6	= CH4O2 + C2H5	2.950E+11 0.0 14944. !CGS 30
CH3O2 + CH3O2	= CH3O + CH3O + O2	2.800E+11 0.0 -780. !CGS 31
CH3O2 + H2O2	= CH4O2 + HO2	2.400E+12 0.0 10000. !CGS 32
CH4O2	= CH3O + OH	3.000E+16 0.0 42920. !CGS 33
CH3O2 + C2H4	= C2H3 + CH4O2	7.100E+11 0.0 17110. !CGS 34
CH4O2 + OH	= CH3O2 + H2O	1.000E+13 0.0 -258. !CGS 35
CH4O2 + O	= CH3O2 + OH	2.000E+13 0.0 4750. !
CH3 + O	= CH2O + H	8.000E+13 0.00 0. !CGS 36
CH3 + OH	= CH2 + H2O	7.500E+06 2.00 5000. !CGS 37
CH3 + OH	= CH2O + H2	4.000E+12 0.00 0. !CGS 38
CH3O + H	= CH3 + OH	1.000E+14 0.00 0. !CGS 39
CO + O + M	= CO2 + M	6.170E+14 0.00 3000. !CGS 40
CO + OH	= CO2 + H	3.510E+07 1.30 -758. !CGS 41
CO + O2	= CO2 + O	1.600E+13 0.00 41000. !CGS 42

```
HO2 + CO          = CO2 + OH                          5.800E+13 0.00 22930. !CGS 43
H2 + O2           = OH + OH                           1.700E+13 0.00 47780. !CGS 44
H2 + OH           = H2O + H                           1.170E+09 1.30 3626. !CGS 45
O + OH            = O2 + H                            4.000E+14 -0.50 0. !CGS 46
O + H2            = OH + H                            5.060E+04 2.67 6290. !CGS 47
H + HO2           = O + H2O                           3.100E+10 0.00 3590. !CGS 48
O + OH + M        = HO2 + M                           1.000E+16 0.00 0. !CGS 49
                  H2O/21./ CO2/5.0/ H2/3.3/ CO/2.0/
H + O2 + M        = HO2 + M                           3.600E+17 -0.72 0. !CGS 50
                  H2O/21./ CO2/5.0/ H2/3.3/ CO/2.0/
OH + HO2          = H2O + O2                          7.500E+12 0.00 0. !CGS 51
H + HO2           = OH + OH                           1.700E+14 0.0 875. !CGS 52
O + HO2           = O2 + OH                           1.400E+13 0.00 1073. !CGS 53
OH + OH           = O + H2O                           6.000E+08 1.30 0. !CGS 54
H + H + M         = H2 + M                            1.000E+18 -1.00 0. !CGS 55
                  H2/0./ H2O/0./ CO2/0./
H + H + H2        = H2 + H2                           9.200E+16 -0.60 0. !CGS 56
H + H + H2O       = H2 + H2O                          6.000E+19 -1.25 0. !CGS 57
H + H + CO2       = H2 + CO2                          5.490E+20 -2.00 0. !CGS 58
H + OH + M        = H2O + M                           1.600E+22 -2.00 0. !CGS 59
H + O + M         = OH + M                            6.200E+16 -0.60 0. !CGS 60
O + O + M         = O2 + M                            1.890E+13 0.00 -1788. !CGS 61
H + HO2           = H2 + O2                           1.250E+13 0.00 0. !CGS 62
HO2 + HO2         = H2O2 + O2                         2.000E+12 0.00 0. !CGS 63
H2O2 + M          = OH + OH + M                       4.300E+16 0.00 45500. !CGS 64
                  H2O/21./ CO2/5.0/ H2/3.3/ CO/2.0/
H2O2 + H          = HO2 + H2                          1.600E+12 0.00 3800. !CGS 65
H2O2 + OH         = H2O + HO2                         1.000E+13 0.00 1800. !CGS 66
H2O2 + H          = H2O + OH                          1.000E+13 0.00 3590. !CGS
H2O2 + O          = H2O + O2                          8.400E+11 0.00 4260. !CGS
H2O2 + O          = OH + HO2                          2.000E+13 0.00 5900. !CGS
H2 + HO2          = H2O + OH                          6.500E+11 0.00 18800. !CGS
CH2O + O2         = HCO + HO2                         6.200E+13 0.00 39000. !CGS
CH2O + O          = HCO + OH                          1.800E+13 0.00 3080. !CGS
CH2O + H          = HCO + H2                          2.190E+08 1.80 3000. !CGS
CH2O + OH         = HCO + H2O                         2.430E+10 1.20 -447. !CGS
CH2O + HO2        = HCO + H2O2                        3.000E+12 0.00 8000. !CGS
CH2O + M          = CO + H2 + M                       6.250E+15 0.00 69540. !CGS
CH2O + M          = HCO + H + M                       4.000E+23 -1.66 91120. !CGS
!H2 + CO          = CH2O                              4.300E+07 1.50 79600. !CGS
HCO + HCO         = CH2O + CO                         3.010E+13 0.00 0. !CGS
HCO + OH          = H2O + CO                          1.000E+14 0.00 0. !CGS
HCO + H           = H2 + CO                           1.190E+13 0.30 0. !CGS
HCO + O           = OH + CO                           3.000E+13 0.00 0. !CGS
HCO + O           = H + CO2                           3.000E+13 0.00 0. !CGS
HCO + O2          = HO2 + CO                          3.300E+13 -0.40 0. !CGS
HCO + M           = H + CO + M                        1.870E+17 -1.00 17000. !CGS
!HCO + H + M      = CH2O + M                          1.000E+12 0.48 -260. !CGS
HCO + HO2         = CO2 + OH + H                      3.000E+13 0.00 0. !CGS
CH4 + O2          = CH3 + HO2                         7.900E+13 0.00 56000. !CGS
!CH3 + HO2        = CH4 + O2                          1.000E+12 0.00 0. !CGS
CH4 + H           = CH3 + H2                          6.600E+08 1.60 10840. !CGS
CH4 + OH          = CH3 + H2O                         1.600E+06 2.10 2460. !CGS
CH4 + O           = CH3 + OH                          1.020E+09 1.50 8604. !CGS 99
CH4 + HO2         = CH3 + H2O2                        1.000E+13 0.00 18700. !CGS 100
CH4 + CH2         = CH3 + CH3                         4.000E+12 0.00 -570. !CGS 101
CH3 + CH2O        = CH4 + HCO                         5.500E+03 2.80 6000. !CGS 102
CH3 + HCO         = CH4 + CO                          1.200E+14 0.00 0. !CGS 103
CH3 + H           = CH4                               1.900E+36 -7.00 9050. !CGS 104
CH3 + H           = CH2 + H2                          9.000E+13 0.00 15100. !CGS 105
CH3 + CH3O        = CH4 + CH2O                        4.300E+14 0.00 0. !CGS 106
CH3 + CH3         = C2H6                              2.700E+53 -12.0 19400. !CGS
CH3 + CH3         = C2H5 + H                          4.990E+12 .100 10600. !CGS
```

```
!CH2 + H2          = CH3 + H          5.000E+05 2.00 7230. !CGS
CH2 + OH           = CH2O + H         2.500E+13 0.00 0. !CGS 107
CH2 + O2           = HCO + OH         4.300E+10 0.00 -500. !CGS 108
CH2 + O2           = CO2 + H2         6.900E+11 0.00 500. !CGS 109
CH2 + O2           = CO + H2O         2.000E+10 0.00 -1000. !CGS 110
CH2 + O2           = CH2O + O         5.000E+13 0.00 9000. !CGS 111
CH2 + O2           = CO2 + H + H      1.600E+12 0.00 1000. !CGS
CH2 + O2           = CO + OH + H      8.600E+10 0.00 -500. !
CH2 + CH2          = C2H2 + H2        1.200E+13 0.0 800. !
CH2 + CH2          = C2H2 + H + H     1.200E+14 0.0 800. !
CH2 + CO2          = CH2O + CO        1.000E+11 0.00 1000. !CGS 112
CH3 + HCO          = CH2O + CH2       3.000E+13 0.00 0. !CGS 113
CH3 + C2H4         = CH4 + C2H3       6.620E+00 3.70 9482. !CGS 114
CH3 + CH3          = C2H4 + H2        1.000E+15 0.00 31000. !CGS 115
CH3 + CH2          = C2H4 + H         3.000E+13 0.00 -570. !CGS 116
C2H4 + H           = C2H3 + H2        1.100E+14 0.00 8500. !CGS 117
C2H4 + O           = CH3 + HCO        1.600E+09 1.20 746. !CGS 118
C2H4 + O           = CH2O + CH2       3.000E+04 1.88 180. !CGS 119
C2H4 + O           = C2H3 + OH        1.510E+07 1.91 3790. !CGS 120
C2H4 + OH          = CH2O + CH3       6.000E+13 0.0 960. !CGS 121
C2H4 + HO2         = C2H3 + H2O2      7.100E+11 0.0 17110. !CGS 122
C2H4 + OH          = C2H3 + H2O       8.020E+13 0.00 5955. !CGS 123
C2H4 + M           = C2H2 + H2 + M    1.500E+15 0.00 55800. !CGS 124
C2H4 + M           = C2H3 + H + M     2.600E+17 0.0 96570. !CGS 125
C2H4 + H           = C2H5             2.600E+43 -9.25 52580. !CGS 126
C2H6 + O2          = C2H5 + HO2       1.000E+13 0.00 48960. !CGS 127
C2H5 + O2          = C2H4 + HO2       2.000E+10 0.0 -2200. !CGS 128
C2H4 + O2          = C2H3 + HO2       4.200E+14 0.00 57590. !CGS 128
C2H4 + C2H4        = C2H5 + C2H3      5.000E+14 0.0 64700. !CGS 129
C2H5 + HO2         = C2H4 + H2O2      3.000E+11 0.00 0. !CGS 130
C2H2 + O2          = HCO + HCO        4.000E+12 0.00 28000. !CGS
C2H2 + O           = CH2 + CO         1.020E+07 2.00 1900. !CGS 131
C2H2 + H + M       = C2H3 + M         5.540E+12 0.00 2410. !CGS 132
C2H3 + H           = C2H2 + H2        4.000E+13 0.00 0. !CGS 133
C2H3 + O2          = CH2O + HCO       4.000E+12 0.00 -250. !CGS 134
C2H3 + OH          = C2H2 + H2O       3.000E+13 0.00 0. !CGS 135
C2H3 + CH2         = C2H2 + CH3       3.000E+13 0.00 0. !CGS 136
C2H3 + HCO         = C2H4 + CO        6.034E+13 0.0 0. !CGS 137
C2H3 + C2H3        = C2H2 + C2H4      1.450E+13 0.0 0.0
C2H3 + O           = C2H2 + OH        1.000E+13 0.0 0.0
C2H2 + OH          = CH3 + CO         4.830E-04 4.00 -2000. !CGS 138
C2H3               = C2H2 + H         4.600E+40 -8.80 46200.
END
```

Appendix B

n-Dodecane Chemical Mechanism

For n-dodecane the chemical kinetics for the 103-species, 370-reactions skeletal mechanism [3] is provided below. Units are cm-mole-sec-K for the pre-exponential Arrhenius coefficient and cal/mole for the activation energy. The coefficients are listed after the rate equation as pre-exponential, temperature exponent, and the activation energy.

ELEMENTS
H C O N
END
SPECIES

N-C12H26	O2	N2	CO2	H2O
H	O	OH	CO	H2
HCO	CH3	CH4	HO2	H2O2
CH2O	CH3O	C2H6	C2H4	C2H5
C2H2	C2H3	CH3OH	CH2OH	CH2CO
HCCO	CH3CO	CH2CHO	CH3CHO	C3H6
N-C3H7	P-C4H9	CH3COCH2	C2H5CHO	C5H10-1
C5H11-1	C2H5O	CH3O2	C2H3O1-2	C2H3CO
C2H3CHO	C3H5O	C5H11O2-1	C5H10OOH1-3	C5H10OOH1-3O2
C3H5-A	CH2(S)	N-C5KET13	N-C3H7CHO	N-C3H7CO
CH2CH2COCH3	N-C4H9CHO	N-C4H9CO	C6H13-1	C6H12-1
C6H11	C7H15-1	N-C5H11CHO	N-C5H11CO	N-C4H9COCH2
C12H25-2	C12H25-4	C12H25-5	C12H25-6	C9H19-1
C8H17-1	C10H20-1	C8H16-4	C12H25O-5	C12H25O2-2
C12H25O2-4	C12H25O2-5	C12H25O2-6	C8H17O2-1	C12H25O2H-5
C12OOH2-4	C12OOH4-2	C12OOH5-7	C12OOH6-4	C12OOH6-8
C8OOH1-3	C12OOH2-4O2	C12OOH4-2O2	C12OOH5-7O2	C12OOH6-4O2
C12OOH6-8O2	C8OOH1-3O2	C12O2-4	C12O4-6	C8O1-3
C12KET2-4	C12KET4-2	C12KET5-7	C12KET6-4	C12KET6-8
C8KET1-3	N-C8H17CHO	N-C6H13CHO	N-C8H17CO	N-C6H13CO
C8H17COCH2	C6H13COCH2	C5H11COCH2		

END

```
REACTIONS
CH3+H(+m)       = CH4(+m)                          2.138e+15 -0.40 0.000E+00
                  lOw / 3.310E+30 -4.00 2108. /
                  trOe/0.0 1.E-15 1.E-15 40./
                  H2/2/ H2O/5/ CO/2/ CO2/3/
CH4+H           = CH3+H2                           1.727E+04 3.00 8.224E+03
                  rev / 6.610E+02 3.00 7.744E+03 /
CH4+OH          = CH3+H2O                          1.930E+05 2.40 2.106E+03
                  rev / 3.199E+04 2.40 1.678E+04 /
CH4+O           = CH3+OH                           3.150E+12 0.50 1.029E+04
                  rev / 5.296E+10 0.50 7.715E+03 /
C2H6+CH3        = C2H5+CH4                         1.510E-07 6.00 6.047E+03
                  rev / 9.649E-10 6.56 1.022E+04 /
HCO+OH          = CO+H2O                           1.020E+14 0.00 0.000E+00
                  rev / 2.896E+15 0.00 1.052E+05 /
CO+OH           = CO2+H                            1.400E+05 1.95 -1.347E+03
                  rev / 1.568E+07 1.95 2.099E+04 /
H+O2            = O+OH                             1.970E+14 0.00 1.654E+04
                  rev / 1.555E+13 0.00 4.250E+02 /
O+H2            = H+OH                             5.080E+04 2.67 6.292E+03
                  rev / 2.231E+04 2.67 4.197E+03 /
O+H2O           = OH+OH                            2.970E+06 2.02 1.340E+04
                  rev / 3.013E+05 2.02 -3.850E+03 /
OH+H2           = H+H2O                            2.160E+08 1.51 3.430E+03
                  rev / 9.352E+08 1.51 1.858E+04 /
HCO+m           = H+CO+m                           1.860E+17 -1.00 1.700E+04
                  rev / 6.467E+13 0.00 -4.420E+02 /
                  H2/2.5/ H2O/12/ CO/1.9/ CO2/3.8/
H2O2+OH         = H2O+HO2                          1.000E+12 0.00 0.000E+00
                  rev / 1.685E+11 0.33 3.146E+04 /
C2H4+O          = CH3+HCO                          1.020E+07 1.88 1.790E+02
                  rev / 2.851E+08 1.05 3.177E+04 /
H+C2H4(+m)      = C2H5(+m)                         1.081E+12 0.45 1.822E+03
                  lOw / 1.112E+34 -5.00 4.448E+03 /
                  trOe/1.0 1.000E-15 9.500E+01
                  2.000E+02/
                  H2/2/ H2O/5/ CO/2/ CO2/3/
CH3OH(+m)       = CH3+OH(+m)                       1.900E+16 0.00 9.173E+04
                  lOw / 2.95E+44 -7.35 9.546E+04 /
                  trOe/0.414 279. 5459. 1.00E+100/
                  H2/2/ H2O/16/ CO/2/ CO2/3/
```

```
C2H6+H          = C2H5+H2                                5.540E+02 3.50 5.167E+03
                rev / 1.355E-01 4.06 8.857E+03 /
CH3OH+HO2       = CH2OH+H2O2                             3.980E+13 0.00 1.940E+04
                rev / 1.096E+09 1.33 1.125E+04 /
C2H5+O2         = C2H4+HO2                               1.220E+30 -5.76 1.010E+04
                rev / 1.259E+30 -5.63 2.230E+04 /
C2H6+OH         = C2H5+H2O                               5.800E+07 1.73 1.160E+03
                rev / 6.142E+04 2.29 2.000E+04 /
C2H6+O          = C2H5+OH                                1.300E+07 2.13 5.190E+03
                rev / 1.397E+03 2.69 6.785E+03 /
CH3+HO2         = CH3O+OH                                1.100E+13 0.00 0.000E+00
                rev / 4.780E+14 -0.35 2.455E+04 /
CO+HO2          = CO2+OH                                 3.010E+13 0.00 2.300E+04
                rev / 6.435E+15 -0.33 8.461E+04 /
CH3+CH3(+m)     = C2H6(+m)                               9.214E+16 -1.17 6.358E+02
                lOw / 1.135E+36 -5.246 1.705E+03 /
                trOe/0.405 1120. 69.6 1.e+15/
                H2/2/ H2O/5/ CO/2/ CO2/3/
H2O+m           = H+OH+m                                 1.837E+27 -3.00 1.226E+05
                rev/ 2.250E+22 -2.00 0.000E+00 /
                H2/2.5/ H2O/12/ CO/1.9/ CO2/3.8/
H+O2(+m)        = HO2(+m)                                1.475E+12 0.60 0.000E+00
                lOw/ 3.500E+16 -0.41 -1.1160E+03 /
                trOe/5.0000E-01 1.0000E-30
                1.0000E+30 1.00E+100/
                H2/2.5/ H2O/12/ CO/1.9/ CO2/3.8/
CO+O(+m)        = CO2(+m)                                1.800E+10 0.00 2.384E+03
                lOw/ 1.350E+24 -2.788 4191. /
                H2/2.5/ H2O/12/ CO/1.9/ CO2/3.8/
CO+O2           = CO2+O                                  1.620E+13 0.00 4.770E+04
                rev / 1.433E+14 0.00 5.392E+04 /
HCO+H           = CO+H2                                  7.340E+13 0.00 0.000E+00
                rev / 4.813E+14 0.00 9.000E+04 /
HCO+O           = CO+OH                                  3.020E+13 0.00 0.000E+00
                rev / 8.697E+13 0.00 8.790E+04 /
CH2O+m          = HCO+H+m                                6.283E+29 -3.57 9.320E+04
                rev / 2.660E+24 -2.57 4.270E+02 /
CH2O+OH         = HCO+H2O                                3.430E+09 1.18 -4.470E+02
                rev / 1.186E+09 1.18 2.938E+04 /
CH2O+H          = HCO+H2                                 9.334E+08 1.50 2.976E+03
                rev / 7.453E+07 1.50 1.765E+04 /
CH2O+O          = HCO+OH                                 4.160E+11 0.57 2.762E+03
                rev / 1.459E+10 0.57 1.534E+04 /
CH3+OH          = CH2O+H2                                2.250E+13 0.00 4.300E+03
                rev / 6.756E+14 0.00 7.602E+04 /
CH3+O           = CH2O+H                                 8.000E+13 0.00 0.000E+00
                rev / 1.055E+15 0.00 6.963E+04 /
CH3+O2          = CH3O+O                                 1.995E+18 -1.57 2.921E+04
                rev / 3.585E+18 -1.59 -1.631E+03 /
CH2O+CH3        = HCO+CH4                                3.636E-06 5.42 9.980E+02
                rev / 7.584E-06 5.42 1.615E+04 /
HCO+CH3         = CH4+CO                                 1.210E+14 0.00 0.000E+00
                rev / 2.073E+16 0.00 9.048E+04 /
CH3O(+m)        = CH2O+H(+m)                             5.450E+13 0.00 1.350E+04
                lOw / 2.344E+25 -2.7 3.060E+04 /
C2H4(+m)        = C2H2+H2(+m)                            1.800E+13 0.00 7.600E+04
                lOw / 1.500E+15 0.00 5.5443E+04 /
HO2+O           = OH+O2                                  3.250E+13 0.00 0.000E+00
                rev / 7.857E+14 -0.33 5.539E+04 /
HCO+HO2         = CH2O+O2                                2.974E+10 0.33 -3.861E+03
                rev / 2.050E+13 0.00 3.895E+04 /
```

```
CH3O+O2          = CH2O+HO2                          5.500E+10 0.00 2.424E+03
                 rev / 1.318E+09 0.35 3.139E+04 /
CH3+HO2          = CH4+O2                            3.600E+12 0.00 0.000E+00
                 rev / 5.177E+15 -0.33 5.796E+04 /
HCO+O2           = CO+HO2                            7.580E+12 0.00 4.100E+02
                 rev / 9.029E+11 0.33 3.293E+04 /
HO2+H            = OH+OH                             7.080E+13 0.00 3.000E+02
                 rev / 1.352E+14 -0.33 3.957E+04 /
HO2+H            = H2+O2                             1.660E+13 0.00 8.200E+02
                 rev / 9.138E+14 -0.33 5.830E+04 /
HO2+OH           = H2O+O2                            2.890E+13 0.00 -5.000E+02
                 rev / 6.888E+15 -0.33 7.214E+04 /
H2O2+O2          = HO2+HO2                           5.942E+17 -0.66 5.315E+04
                 rev / 4.200E+14 0.00 1.198E+04 /
OH+OH(+m)        = H2O2(+m)                          1.236E+14 -0.37 0.000E+00
                 lOw / 3.041E+30 -4.63 2049. /
                 trOe /0.47 100. 2000. 1.0e+15/
                 H2/2.5/ H2O/12/ CO/1.9/ CO2/3.8/
H2O2+H           = H2O+OH                            2.410E+13 0.00 3.970E+03
                 rev / 7.750E+12 0.00 7.470E+04 /
CH4+HO2          = CH3+H2O2                          3.420E+11 0.00 1.929E+04
                 rev / 3.365E+11 -0.33 2.502E+03 /
CH2O+HO2         = HCO+H2O2                          5.820E-03 4.53 6.557E+03
                 rev / 1.194E-02 4.20 4.921E+03 /
OH+m             = O+H+m                             3.909E+22 -2.00 1.053E+05
                 rev / 4.720E+18 -1.00 0.000E+00 /
                 H2/2.5/ H2O/12/ CO/1.9/ CO2/3.8/
O2+m             = O+O+m                             6.473E+20 -1.50 1.215E+05
                 rev / 6.170E+15 -0.50 0.000E+00 /
                 H2/2.5/ H2O/12/ CO/1.9/ CO2/3.8/
H2+m             = H+H+m                             4.570E+19 -1.40 1.044E+05
                 rev/ 2.423E+15 -0.40 -3.040E+03 /
                 H2/2.5/ H2O/12/ CO/1.9/ CO2/3.8/
C2H3+H(+m)       = C2H4(+m)                          6.100E+12 0.27 2.800E+02
                 lOw / 9.800E+29 -3.86 3.320E+03 /
                 trOe /0.782 208. 2663. 6095./
C2H5+C2H3        = C2H4+C2H4                         5.765E+14 -0.63 2.490E+03
                 rev/ 4.820E+14 0.00 7.153E+04 /
C2H2+H(+m)       = C2H3(+m)                          3.110E+11 0.58 2.589E+03
                 lOw/ 2.254E+40 -7.269 6577. /
                 trOe/ 1.0 1.e-15 675. 1.e+15/
                 H2/2/ H2O/5/ CO/2/ CO2/3/
C2H4+H           = C2H3+H2                           8.420E-03 4.62 2.583E+03
                 rev / 5.723E-01 3.79 3.233E+03 /
C2H4+OH          = C2H3+H2O                          2.050E+13 0.00 5.950E+03
                 rev / 6.033E+15 -0.83 2.176E+04 /
C2H2+O2          = HCCO+OH                           2.000E+08 1.50 3.010E+04
                 rev / 2.232E+05 1.50 2.540E+04 /
CH3OH+OH         = CH2OH+H2O                         7.100E+06 1.80 -5.960E+02
                 rev / 3.293E+01 3.46 2.272E+04 /
CH3OH+H          = CH3O+H2                           3.600E+12 0.00 6.095E+03
                 rev / 7.467E+12 -0.02 7.825E+03 /
CH3OH+H          = CH2OH+H2                          1.440E+13 0.00 6.095E+03
                 rev / 1.543E+07 1.66 1.425E+04 /
CH3OH+CH3        = CH2OH+CH4                         3.190E+01 3.17 7.172E+03
                 rev / 8.927E-04 4.83 1.581E+04 /
CH3OH+O          = CH2OH+OH                          3.880E+05 2.50 3.080E+03
                 rev / 1.826E-01 4.16 9.143E+03 /
CH2OH+O2         = CH2O+HO2                          6.510E+05 2.27 -7.700E+02
                 rev / 3.020E+10 0.94 2.177E+04 /
CH2OH(+m)        = CH2O+H(+m)                        2.800E+14 -0.73 3.282E+04
                 lOw / 6.010E+33 -5.39 3.620E+04 /
                 trOe/ 0.96 67.6 1855. 7543./
C2H3+O2          = C2H2+HO2                          2.120E-06 6.00 9.484E+03
                 rev / 1.114E-07 6.33 1.757E+04 /
H2O2+O           = OH+HO2                            9.550E+06 2.00 3.970E+03
                 rev / 1.632E+05 2.33 1.818E+04 /
```

C2H2+O	= HCCO+H	1.430E+07 2.00 1.900E+03
	rev / 2.021E+05 2.00 1.331E+04 /	
C2H2+OH	= CH2CO+H	2.190E-04 4.50 -1.000E+03
	rev / 2.161E-03 4.50 1.966E+04 /	
CH2CO+H	= CH3+CO	1.100E+13 0.00 3.400E+03
	rev / 2.400E+12 0.00 4.020E+04 /	
CH2CO+O	= HCCO+OH	1.000E+13 0.00 8.000E+03
	rev / 1.432E+10 0.00 -1.255E+03 /	
CH2CO+OH	= HCCO+H2O	1.000E+13 0.00 2.000E+03
	rev / 1.412E+11 0.00 9.995E+03 /	
CH2CO+H	= HCCO+H2	2.000E+14 0.00 8.000E+03
	rev / 6.522E+11 0.00 8.400E+02 /	
HCCO+OH	= HCO+HCO	1.000E+13 0.00 0.000E+00
	rev / 2.411E+14 0.00 4.036E+04 /	
HCCO+H	= CH2(S)+CO	1.100E+14 0.00 0.000E+00
	rev / 2.046E+12 0.89 2.783E+04 /	
HCCO+O	= H+CO+CO	8.000E+13 0.00 0.000E+00
	rev / 0.000E+00 0.00 0.000E+00 /	
C2H6+O2	= C2H5+HO2	6.030E+13 0.00 5.187E+04
	rev / 2.679E+08 0.89 -1.922E+03 /	
C2H6+HO2	= C2H5+H2O2	1.320E+13 0.00 2.047E+04
	rev / 8.298E+10 0.24 7.852E+03 /	
CH3+C2H3	= CH4+C2H2	3.920E+11 0.00 0.000E+00
	rev / 2.962E+13 0.00 6.605E+04 /	
CH3+C2H5	= CH4+C2H4	1.950E+13 -0.50 0.000E+00
	rev / 2.895E+16 -0.70 7.017E+04 /	
CH3OH+CH2O	= CH3O+CH3O	3.835E+13 0.05 8.472E+04
	rev / 6.030E+13 0.00 0.000E+00 /	
CH2O+CH3O	= CH3OH+HCO	1.020E+11 0.00 2.980E+03
	rev / 3.926E+09 0.02 1.592E+04 /	
CH4+CH3O	= CH3+CH3OH	1.570E+11 0.00 8.842E+03
	rev / 2.897E+09 0.02 6.632E+03 /	
C2H6+CH3O	= C2H5+CH3OH	2.410E+11 0.00 7.090E+03
	rev / 2.842E+07 0.59 9.050E+03 /	
C2H3+H	= C2H2+H2	2.000E+13 0.00 2.500E+03
	rev / 1.331E+13 0.00 6.808E+04 /	
CH3O+CH3OH	= CH2OH+CH3OH	3.000E+11 0.00 4.074E+03
	rev / 1.549E+05 1.68 1.050E+04 /	
CH3OH+OH	= CH3O+H2O	1.000E+06 2.10 4.967E+02
	rev / 8.981E+06 2.08 1.738E+04 /	
C2H5+H	= CH3+CH3	3.610E+13 0.00 0.000E+00
	rev / 5.446E+16 -1.03 1.698E+04 /	
C2H3+O2	= CH2O+HCO	1.700E+29 -5.31 6.500E+03
	rev / 1.657E+29 -5.31 9.305E+04 /	
C2H6	= C2H5+H	2.783E+21 -1.56 1.038E+05
	rev / 3.610E+13 0.00 0.000E+00 /	
C2H4+CH3	= C2H3+CH4	6.620E+00 3.70 9.500E+03
	rev / 1.440E+00 4.02 5.472E+03 /	
CH3CO(+m)	= CH3+CO(+m)	3.000E+12 0.00 1.672E+04
	lOw / 1.200E+15 0.00 1.2518E+04 /	
CH3CHO	= CH3+HCO	2.614E+15 0.15 8.055E+04
	rev / 2.000E+13 0.00 0.000E+00 /	
CH3CHO+O2	= CH3CO+HO2	3.010E+13 0.00 3.915E+04
	rev / 8.552E+10 0.32 -1.940E+03 /	
CH3CHO+OH	= CH3CO+H2O	2.000E+06 1.80 1.300E+03
	rev / 1.354E+06 1.79 3.285E+04 /	
CH3CHO+H	= CH3CO+H2	1.340E+13 0.00 3.300E+03
	rev / 2.096E+12 -0.01 1.969E+04 /	
CH3CHO+O	= CH3CO+OH	5.940E+12 0.00 1.868E+03
	rev / 4.080E+11 -0.01 1.617E+04 /	
CH3CHO+HO2	= CH3CO+H2O2	3.010E+12 0.00 1.192E+04
	rev / 1.210E+13 -0.34 1.201E+04 /	
CH3CHO+CH3	= CH3CO+CH4	2.608E+06 1.78 5.911E+03
	rev / 1.066E+07 1.77 2.278E+04 /	

C3H5-A	= C2H2+CH3	2.397E+48 -9.90 8.208E+04
	rev / 2.610E+46 -9.82 3.695E+04 /	
C3H6	= C2H3+CH3	2.730E+62 -13.28 1.232E+05
	rev / 4.712E+59 -13.19 2.954E+04 /	
C3H6	= C3H5-A+H	2.010E+61 -13.26 1.185E+05
	rev / 4.887E+56 -12.25 2.808E+04 /	
C3H6+O	= CH2CO+CH3+H	2.500E+07 1.76 7.600E+01
	rev / 1.000E+00 0.00 0.000E+00 /	
C3H6+O	= C2H5+HCO	1.580E+07 1.76 -1.216E+03
	rev / 1.402E+05 1.88 2.651E+04 /	
C3H6+HO2	= C3H5-A+H2O2	1.500E+11 0.00 1.419E+04
	rev / 5.867E+05 1.33 9.759E+03 /	
C3H6+OH	= C3H5-A+H2O	3.120E+06 2.00 -2.980E+02
	rev / 6.194E+06 2.01 3.188E+04 /	
C2H4+O2	= C2H3+HO2	4.000E+13 0.00 5.820E+04
	rev / 4.939E+13 -0.50 1.368E+03 /	
CH2O+m	= CO+H2+m	1.826E+32 -4.42 8.712E+04
	rev / 5.070E+27 -3.42 8.435E+04 /	
N-C3H7	= CH3+C2H4	2.284E+14 -0.55 2.840E+04
	rev / 4.100E+11 0.00 7.204E+03 /	
N-C3H7	= H+C3H6	2.667E+15 -0.64 3.682E+04
	rev / 1.000E+13 0.00 2.500E+03 /	
N-C3H7+O2	= C3H6+HO2	3.000E+11 0.00 3.000E+03
	rev / 2.000E+11 0.00 1.750E+04 /	
C2H4+CH3O	= C2H3+CH3OH	1.200E+11 0.00 6.750E+03
	rev / 1.000E+10 0.00 9.000E+03 /	
C3H6+O	= C3H5-A+OH	5.240E+11 0.70 5.884E+03
	rev / 1.055E+11 0.71 2.082E+04 /	
C3H6+H	= C3H5-A+H2	1.730E+05 2.50 2.492E+03
	rev / 7.933E+04 2.51 1.952E+04 /	
C3H6+H	= C2H4+CH3	4.830E+33 -5.81 1.850E+04
	rev / 2.313E+33 -5.90 3.162E+04 /	
P-C4H9	= C2H5+C2H4	7.497E+17 -1.41 2.958E+04
	rev / 3.300E+11 0.00 7.200E+03 /	
CH3COCH2	= CH2CO+CH3	1.000E+14 0.00 3.100E+04
	rev / 1.000E+11 0.00 6.000E+03 /	
C2H5CHO	= C2H5+HCO	9.850E+18 -0.73 8.171E+04
	rev / 1.810E+13 0.00 0.000E+00 /	
C5H10-1	= C2H5+C3H5-A	9.173E+20 -1.63 7.399E+04
	rev / 4.000E+12 0.00 -5.960E+02 /	
C5H10-1+O	= P-C4H9+HCO	1.000E+11 0.00 0.000E+00
	rev / 0.000E+00 0.00 0.000E+00 /	
C5H10-1+O	= N-C3H7+CH3CO	1.000E+11 0.00 0.000E+00
	rev / 0.000E+00 0.00 0.000E+00 /	
C5H10-1+OH	= P-C4H9+CH2O	1.000E+11 0.00 0.000E+00
	rev / 0.000E+00 0.00 0.000E+00 /	
C5H10-1+OH	= N-C3H7+CH3CHO	1.000E+11 0.00 0.000E+00
	rev / 0.000E+00 0.00 0.000E+00 /	
H2O2+H	= H2+HO2	4.820E+13 0.00 7.950E+03
	rev / 1.875E+12 0.33 2.426E+04 /	
HCO+O	= CO2+H	3.000E+13 0.00 0.000E+00
	rev / 9.677E+15 0.00 1.102E+05 /	
CH3OH(+m)	= CH2OH+H(+m)	2.690E+16 -0.08 9.894E+04
	lOw / 2.34E+40 -6.33 1.031E+05 /	
	trOe/ 0.773 693. 5333. 1.00E+100/	
CH3CO+H	= CH2CO+H2	2.000E+13 0.00 0.000E+00
	rev / 5.626E+17 -1.13 6.370E+04 /	
CH3CO+O	= CH2CO+OH	2.000E+13 0.00 0.000E+00
	rev / 5.951E+18 -1.13 1.207E+05 /	
CH3CO+CH3	= CH2CO+CH4	5.000E+13 0.00 0.000E+00
	rev / 8.197E+17 -0.67 7.983E+04 /	
C2H4+O	= CH2CHO+H	3.390E+06 1.88 1.790E+02
	rev / 9.481E+06 1.79 1.605E+04 /	
C2H5+O	= CH3CHO+H	5.000E+13 0.00 0.000E+00
	rev / 5.505E+14 0.11 7.439E+04 /	
CH2OH+CH2O	= CH3OH+HCO	1.292E-01 4.56 6.596E+03
	rev / 9.630E+03 2.90 1.311E+04 /	
C5H11-1	= C2H4+N-C3H7	7.972E+17 -1.44 2.979E+04
	rev / 3.300E+11 0.00 7.200E+03 /	

```
C5H11-1          = H+C5H10-1                    3.483E+15 -0.66 3.788E+04
                 rev / 1.000E+13 0.00 2.900E+03 /
C5H11-1+O2       = C5H10-1+HO2                  3.000E-19 0.00 3.000E+03
                 rev / 2.000E-19 0.00 1.750E+04 /
C2H5O+m          = CH3+CH2O+m                   1.350E+38 -6.96 2.380E+04
                 rev / 6.442E+36 -6.99 1.685E+04 /
C2H5O+O2         = CH3CHO+HO2                   4.280E+10 0.00 1.097E+03
                 rev / 3.872E+08 0.44 3.188E+04 /
H2O2+O2          = HO2+HO2                      1.839E+14 -0.66 3.954E+04
                 rev / 1.300E+11 0.00 -1.629E+03 /
C2H3+O2          = CH2CHO+O                     3.500E+14 -0.61 5.260E+03
                 rev / 2.589E+12 0.12 6.459E+03 /
CH3O2+m          = CH3+O2+m                     4.343E+27 -3.42 3.047E+04
                 rev / 5.440E+25 -3.30 0.000E+00 /
C2H5+HO2         = C2H5O+OH                     3.200E+13 0.00 0.000E+00
                 rev / 3.075E+15 -0.32 2.749E+04 /
CH3O2+CH3        = CH3O+CH3O                    7.000E+12 0.00 -1.000E+03
                 rev / 2.971E+16 -0.93 2.831E+04 /
CH3O2+C2H5       = CH3O+C2H5O                   7.000E+12 0.00 -1.000E+03
                 rev / 6.569E+16 -0.90 3.126E+04 /
H2O2+OH          = H2O+HO2                      5.800E+14 0.00 9.560E+03
                 rev / 9.771E+13 0.33 4.102E+04 /
CH3O2+CH3O2      = CH2O+CH3OH+O2                3.110E+14 -1.61 -1.051E+03
                 rev / 0.000E+00 0.00 0.000E+00 /
CH3O2+CH3O2      = O2+CH3O+CH3O                 1.400E+16 -1.61 1.860E+03
                 rev / 0.000E+00 0.00 0.000E+00 /
C2H5O+m          = CH3CHO+H+m                   1.160E+35 -5.89 2.527E+04
                 rev / 3.063E+30 -4.78 6.100E+03 /
C2H3CO           = C2H3+CO                      3.043E+14 -0.46 3.051E+04
                 rev / 1.510E+11 0.00 4.810E+03 /
C2H3CHO+OH       = C2H3CO+H2O                   9.240E+06 1.50 -9.620E+02
                 rev / 2.147E+07 1.48 3.551E+04 /
C2H3CHO+H        = C2H3CO+H2                    1.340E+13 0.00 3.300E+03
                 rev / 7.191E+12 -0.02 2.462E+04 /
C2H3CHO+O        = C2H3CO+OH                    5.940E+12 0.00 1.868E+03
                 rev / 1.400E+12 -0.02 2.109E+04 /
C2H3CHO+HO2      = C2H3CO+H2O2                  3.010E+12 0.00 1.192E+04
                 rev / 4.152E+13 -0.35 1.694E+04 /
C2H3CHO+CH3      = C2H3CO+CH4                   2.608E+06 1.78 5.911E+03
                 rev / 3.656E+07 1.76 2.771E+04 /
C3H5O            = C2H3CHO+H                    1.000E+14 0.00 2.910E+04
                 rev / 7.714E+11 0.48 1.775E+04 /
C3H5O            = C2H3+CH2O                    2.028E+12 0.09 2.356E+04
                 rev / 1.500E+11 0.00 1.060E+04 /
C3H5O+O2         = C2H3CHO+HO2                  1.000E+12 0.00 6.000E+03
                 rev / 1.288E+11 0.00 3.200E+04 /
C3H5-A+HO2       = C3H5O+OH                     7.000E+12 0.00 -1.000E+03
                 rev / 2.041E+13 -0.16 1.226E+04 /
C3H5-A+CH3O2     = C3H5O+CH3O                   7.000E+12 0.00 -1.000E+03
                 rev / 1.994E+15 -0.74 1.702E+04 /
CH3+OH           = CH2(S)+H2O                   2.650E+13 0.00 2.186E+03
                 rev / 3.236E+10 0.89 1.211E+03 /
CH3OH+O2         = CH2OH+HO2                    2.050E+13 0.00 4.490E+04
                 rev / 3.989E+05 1.99 -4.424E+03 /
C5H11O2-1        = C5H11-1+O2                   1.956E+20 -1.50 3.581E+04
                 rev / 4.520E+12 0.00 0.000E+00 /
C5H11O2-1        = C5H10OOH1-3                  2.500E+10 0.00 2.045E+04
!                rev / 2.604E+09 -0.11 7.850E+03 /
C5H10OOH1-3O2    = C5H10OOH1-3+O2               8.039E+22 -2.30 3.797E+04
                 rev / 7.540E+12 0.00 0.000E+00 /
C5H10OOH1-3O2    = N-C5KET13+OH                 2.500E+10 0.00 2.140E+04
                 rev / 5.328E+03 1.35 4.470E+04 /
C3H6+O2          = C3H5-A+HO2                   4.000E+12 0.00 3.990E+04
                 rev / 3.332E+10 0.34 -5.560E+02 /
C3H6+CH3         = C3H5-A+CH4                   2.210E+00 3.50 5.675E+03
                 rev / 2.647E+01 3.51 2.318E+04 /
C3H6+C2H5        = C3H5-A+C2H6                  1.000E+11 0.00 9.800E+03
                 rev / 5.369E+05 1.33 1.644E+04 /
```

C3H5-A+HO2	= C2H3+CH2O+OH	1.000E-18 0.00 0.000E+00
	rev / 1.000E-30 0.00 0.000E+00 /	
C3H5-A+C2H5	= C2H4+C3H6	4.000E+11 0.00 0.000E+00
	rev / 6.937E+16 -1.33 5.280E+04 /	
C3H5-A+O2	= C2H3CHO+OH	2.470E+13 -0.44 2.302E+04
	rev / 1.903E+14 -0.80 7.488E+04 /	
C2H3O1-2	= CH3CO	8.500E+14 0.00 1.400E+04
	rev / 1.488E+14 -0.01 4.768E+04 /	
C2H3O1-2	= CH2CHO	1.000E+14 0.00 1.400E+04
	rev / 1.615E+15 -0.41 4.246E+04 /	
CH2CHO	= CH2CO+H	3.094E+15 -0.26 5.082E+04
	rev / 5.000E+13 0.00 1.230E+04 /	
CH2CHO+O2	= CH2O+CO+OH	2.000E+13 0.00 4.200E+03
	rev / 0.000E+00 0.00 0.000E+00 /	
N-C5KET13	= C2H5CHO+CH2CHO+OH	1.050E+16 0.00 3.900E+04
	rev / 0.000E+00 0.00 0.000E+00 /	
C3H5-A+O2	= CH2CHO+CH2O	7.140E+15 -1.21 2.105E+04
	rev / 4.944E+16 -1.40 8.862E+04 /	
C3H5-A+O2	= C2H2+CH2O+OH	9.720E+29 -5.71 2.145E+04
	rev / 0.000E+00 0.00 0.000E+00 /	
HCCO+O2	= CO2+HCO	2.400E+11 0.00 -8.540E+02
	rev / 1.474E+14 0.00 1.336E+05 /	
CH2CO+OH	= CH2OH+CO	3.730E+12 0.00 -1.013E+03
	rev / 9.430E+06 1.66 2.749E+04 /	
CH3+O2	= CH2O+OH	7.470E+11 0.00 1.425E+04
	rev / 7.778E+11 0.00 6.777E+04 /	
C2H4+H2	= CH3+CH3	3.767E+12 0.83 8.471E+04
	rev / 1.000E+14 0.00 3.200E+04 /	
N-C3H7CHO+O2	= N-C3H7CO+HO2	2.000E+13 0.50 4.220E+04
	rev / 1.000E+07 0.50 4.000E+03 /	
N-C3H7CHO+OH	= N-C3H7CO+H2O	2.690E+10 0.76 -3.400E+02
	rev / 1.852E+10 0.75 3.122E+04 /	
N-C3H7CHO+H	= N-C3H7CO+H2	4.000E+13 0.00 4.200E+03
	rev / 1.800E+13 0.00 2.400E+04 /	
N-C3H7CHO+O	= N-C3H7CO+OH	5.000E+12 0.00 1.790E+03
	rev / 1.000E+12 0.00 1.900E+04 /	
N-C3H7CHO+HO2	= N-C3H7CO+H2O2	2.800E+12 0.00 1.360E+04
	rev / 1.000E+12 0.00 1.000E+04 /	
N-C3H7CHO+CH3	= N-C3H7CO+CH4	1.700E+12 0.00 8.440E+03
	rev / 1.500E+13 0.00 2.800E+04 /	
N-C3H7CHO+CH3O	= N-C3H7CO+CH3OH	1.150E+11 0.00 1.280E+03
	rev / 3.000E+11 0.00 1.800E+04 /	
N-C3H7CO	= N-C3H7+CO	5.325E+15 -0.86 1.340E+04
	rev / 1.500E+11 0.00 4.800E+03 /	
CH2CH2COCH3	= C2H4+CH3CO	5.970E+12 0.00 2.073E+04
	rev / 2.110E+11 0.00 7.350E+03 /	
N-C4H9CHO+O2	= N-C4H9CO+HO2	2.000E+13 0.50 4.220E+04
	rev / 1.000E+07 0.00 4.000E+04 /	
N-C4H9CHO+OH	= N-C4H9CO+H2O	2.690E+10 0.76 -3.400E+02
	rev / 2.143E+10 0.73 3.124E+04 /	
N-C4H9CHO+H	= N-C4H9CO+H2	4.000E+13 0.00 4.200E+03
	rev / 1.800E+13 0.00 2.400E+04 /	
N-C4H9CHO+O	= N-C4H9CO+OH	5.000E+12 0.00 1.790E+03
	rev / 1.000E+12 0.00 1.900E+04 /	
N-C4H9CHO+HO2	= N-C4H9CO+H2O2	2.800E+12 0.00 1.360E+04
	rev / 1.000E+12 0.00 1.000E+04 /	
N-C4H9CHO+CH3	= N-C4H9CO+CH4	1.700E+12 0.00 8.440E+03
	rev / 1.500E+13 0.00 2.800E+04 /	
N-C4H9CHO+CH3O	= N-C4H9CO+CH3OH	1.150E+11 0.00 1.280E+03
	rev / 3.000E+11 0.00 1.800E+04 /	
N-C4H9CO	= P-C4H9+CO	1.000E+11 0.00 9.600E+03
	rev / 1.000E+11 0.00 0.000E+00 /	
CH2(S)+CH4	= CH3+CH3	4.000E+13 0.00 0.000E+00
	rev / 5.429E+15 -0.89 1.565E+04 /	
CH2(S)+C2H6	= CH3+C2H5	1.200E+14 0.00 0.000E+00
	rev / 1.041E+14 -0.33 1.982E+04 /	
CH2(S)+O2	= CO+OH+H	7.000E+13 0.00 0.000E+00
	rev / 0.000E+00 0.00 0.000E+00 /	

CH2(S)+H2	= CH3+H	7.000E+13 0.00 0.000E+00
	rev / 2.482E+17 -0.89 1.613E+04 /	
CH2(S)+O	= CO+H+H	3.000E+13 0.00 0.000E+00
	rev / 0.000E+00 0.00 0.000E+00 /	
CH2(S)+OH	= CH2O+H	3.000E+13 0.00 0.000E+00
	rev / 3.194E+18 -0.89 8.786E+04 /	
CH2(S)+CO2	= CH2O+CO	3.000E+12 0.00 0.000E+00
	rev / 2.852E+15 -0.89 6.552E+04 /	
CH2(S)+CH3	= C2H4+H	2.000E+13 0.00 0.000E+00
	rev / 2.671E+15 -0.06 6.884E+04 /	
CH2(S)+CH2CO	= C2H4+CO	1.600E+14 0.00 0.000E+00
	rev / 4.596E+15 -0.06 1.056E+05 /	
C6H13-1+O2	= C6H12-1+HO2	3.000E-19 0.00 3.000E+03
	rev / 2.000E-19 0.00 1.750E+04 /	
C6H13-1	= C2H4+P-C4H9	5.446E+17 -1.29 2.958E+04
	rev / 3.300E+11 0.00 7.200E+03 /	
C6H13-1	= C6H12-1+H	2.091E+16 -0.89 3.794E+04
	rev / 1.000E+13 0.00 2.900E+03 /	
C6H12-1+OH	= C6H11+H2O	3.000E+13 0.00 1.230E+03
	rev / 9.764E+14 -0.13 3.926E+04 /	
C6H12-1+H	= C6H11+H2	3.700E+13 0.00 3.900E+03
	rev / 2.781E+14 -0.13 2.677E+04 /	
C6H12-1+CH3	= C6H11+CH4	1.000E+12 0.00 7.300E+03
	rev / 1.964E+14 -0.13 3.065E+04 /	
C6H12-1+O	= C6H11+OH	2.120E+11 0.13 9.125E+03
	rev / 7.000E+11 0.00 2.990E+04 /	
C6H12-1+OH	= C5H11-1+CH2O	1.000E+11 0.00 -4.000E+03
	rev / 0.000E+00 0.00 0.000E+00 /	
C6H12-1+O	= C5H11-1+HCO	1.000E+11 0.00 -1.050E+03
	rev / 0.000E+00 0.00 0.000E+00 /	
C6H11	= C3H6+C3H5-A	2.500E+13 0.00 4.500E+04
	rev / 1.000E+10 0.00 1.700E+04 /	
C6H12-1	= N-C3H7+C3H5-A	1.000E+16 0.00 7.100E+04
	rev / 1.000E+13 0.00 0.000E+00 /	
C7H15-1	= C5H11-1+C2H4	8.157E+17 -1.42 3.084E+04
	rev / 1.000E+11 0.00 8.200E+03 /	
N-C5H11CHO+O2	= N-C5H11CO+HO2	2.000E+13 0.50 4.220E+04
	rev / 1.000E+07 0.00 4.000E+04 /	
N-C5H11CHO+OH	= N-C5H11CO+H2O	2.690E+10 0.76 -3.400E+02
	rev / 1.740E+10 0.76 3.120E+04 /	
N-C5H11CHO+H	= N-C5H11CO+H2	4.000E+13 0.00 4.200E+03
	rev / 1.800E+13 0.00 2.400E+04 /	
N-C5H11CHO+O	= N-C5H11CO+OH	5.000E+12 0.00 1.790E+03
	rev / 1.000E+12 0.00 1.900E+04 /	
N-C5H11CHO+HO2	= N-C5H11CO+H2O2	2.800E+12 0.00 1.360E+04
	rev / 1.000E+12 0.00 1.000E+04 /	
N-C5H11CHO+CH3	= N-C5H11CO+CH4	1.700E+12 0.00 8.440E+03
	rev / 1.500E+13 0.00 2.800E+04 /	
N-C5H11CHO+CH3O	= N-C5H11CO+CH3OH	1.150E+11 0.00 1.280E+03
	rev / 3.000E+11 0.00 1.800E+04 /	
N-C5H11CO	= C5H11-1+CO	1.000E+11 0.00 9.600E+03
	rev / 1.000E+11 0.00 0.000E+00 /	
N-C4H9COCH2	= P-C4H9+CH2CO	1.554E+18 -1.41 4.314E+04
	rev / 1.000E+11 0.00 1.160E+04 /	
C12H25-2+H	= N-C12H26	1.00e+14 0. 0.
C12H25-4+H	= N-C12H26	1.00e+14 0. 0.
C12H25-5+H	= N-C12H26	1.00e+14 0. 0.
C12H25-6+H	= N-C12H26	1.00e+14 0. 0.
C9H19-1+N-C3H7	= N-C12H26	8.00e+12 0. 0.
C8H17-1+P-C4H9	= N-C12H26	8.00e+12 0. 0.
C7H15-1+C5H11-1	= N-C12H26	8.00e+12 0. 0.
C6H13-1+C6H13-1	= N-C12H26	8.00e+12 0. 0.
N-C12H26+H	= C12H25-2+H2	2.600E+06 2.40 4.471E+03
	rev / 3.928E+03 2.74 1.126E+04 /	
N-C12H26+H	= C12H25-4+H2	2.600E+06 2.40 4.471E+03
	rev / 3.928E+03 2.74 1.126E+04 /	
N-C12H26+H	= C12H25-5+H2	2.600E+06 2.40 4.471E+03
	rev / 3.928E+03 2.74 1.126E+04 /	

N-C12H26+H	= C12H25-6+H2	2.600E+06 2.40 4.471E+03
	rev / 3.928E+03 2.74 1.126E+04 /	
N-C12H26+OH	= C12H25-2+H2O	9.400E+07 1.61 -3.500E+01
	rev / 6.148E+05 1.95 2.191E+04 /	
N-C12H26+OH	= C12H25-4+H2O	9.400E+07 1.61 -3.500E+01
	rev / 6.148E+05 1.95 2.191E+04 /	
N-C12H26+OH	= C12H25-5+H2O	9.400E+07 1.61 -3.500E+01
	rev / 6.148E+05 1.95 2.191E+04 /	
N-C12H26+OH	= C12H25-6+H2O	9.400E+07 1.61 -3.500E+01
	rev / 6.148E+05 1.95 2.191E+04 /	
N-C12H26+O	= C12H25-2+OH	9.540E+04 2.71 2.106E+03
	rev / 6.330E+01 3.05 6.798E+03 /	
N-C12H26+O	= C12H25-4+OH	9.540E+04 2.71 2.106E+03
	rev / 6.330E+01 3.05 6.798E+03 /	
N-C12H26+O	= C12H25-5+OH	9.540E+04 2.71 2.106E+03
	rev / 6.330E+01 3.05 6.798E+03 /	
N-C12H26+O	= C12H25-6+OH	9.540E+04 2.71 2.106E+03
	rev / 6.330E+01 3.05 6.798E+03 /	
N-C12H26+HO2	= C12H25-2+H2O2	1.120E+13 0.00 1.769E+04
	rev / 4.348E+11 0.01 8.165E+03 /	
N-C12H26+HO2	= C12H25-4+H2O2	1.120E+13 0.00 1.769E+04
	rev / 4.348E+11 0.01 8.165E+03 /	
N-C12H26+HO2	= C12H25-5+H2O2	1.120E+13 0.00 1.769E+04
	rev / 4.348E+11 0.01 8.165E+03 /	
N-C12H26+HO2	= C12H25-6+H2O2	1.120E+13 0.00 1.769E+04
	rev / 4.348E+11 0.01 8.165E+03 /	
N-C12H26+CH3	= C12H25-2+CH4	5.410E+04 2.26 7.287E+03
	rev / 2.135E+03 2.60 1.455E+04 /	
N-C12H26+CH3	= C12H25-4+CH4	5.410E+04 2.26 7.287E+03
	rev / 2.135E+03 2.60 1.455E+04 /	
N-C12H26+CH3	= C12H25-5+CH4	5.410E+04 2.26 7.287E+03
	rev / 2.135E+03 2.60 1.455E+04 /	
N-C12H26+CH3	= C12H25-6+CH4	5.410E+04 2.26 7.287E+03
	rev / 2.135E+03 2.60 1.455E+04 /	
N-C12H26+O2	= C12H25-2+HO2	4.000E+13 0.00 5.015E+04
	rev / 1.098E+09 0.67 -5.410E+02 /	
N-C12H26+O2	= C12H25-4+HO2	4.000E+13 0.00 5.015E+04
	rev / 1.098E+09 0.67 -5.410E+02 /	
N-C12H26+O2	= C12H25-5+HO2	4.000E+13 0.00 5.015E+04
	rev / 1.098E+09 0.67 -5.410E+02 /	
N-C12H26+O2	= C12H25-6+HO2	4.000E+13 0.00 5.015E+04
	rev / 1.098E+09 0.67 -5.410E+02 /	
N-C12H26+C2H3	= C12H25-2+C2H4	8.000E+11 0.00 1.680E+04
	rev / 2.000E+12 0.00 2.420E+04 /	
N-C12H26+C2H3	= C12H25-4+C2H4	8.000E+11 0.00 1.680E+04
	rev / 2.000E+12 0.00 2.420E+04 /	
N-C12H26+C2H3	= C12H25-5+C2H4	8.000E+11 0.00 1.680E+04
	rev / 2.000E+12 0.00 2.420E+04 /	
N-C12H26+C2H3	= C12H25-6+C2H4	8.000E+11 0.00 1.680E+04
	rev / 2.000E+12 0.00 2.420E+04 /	
N-C12H26+C2H5	= C12H25-2+C2H6	1.000E+11 0.00 1.040E+04
	rev / 1.000E+11 0.00 1.290E+04 /	
N-C12H26+C2H5	= C12H25-4+C2H6	1.000E+11 0.00 1.040E+04
	rev / 1.000E+11 0.00 1.290E+04 /	
N-C12H26+C2H5	= C12H25-5+C2H6	1.000E+11 0.00 1.040E+04
	rev / 1.000E+11 0.00 1.290E+04 /	
N-C12H26+C2H5	= C12H25-6+C2H6	1.000E+11 0.00 1.040E+04
	rev / 1.000E+11 0.00 1.290E+04 /	
N-C12H26+C12H25O2-5	= C12H25-2+C12H25O2H-5	1.000E+11 0.00 1.040E+04
	rev / 1.000E+11 0.00 1.290E+04 /	
N-C12H26+C12H25O2-5	= C12H25-4+C12H25O2H-5	1.000E+11 0.00 1.040E+04
	rev / 1.000E+11 0.00 1.290E+04 /	
N-C12H26+C12H25O2-5	= C12H25-5+C12H25O2H-5	1.000E+11 0.00 1.040E+04
	rev / 1.000E+11 0.00 1.290E+04 /	
N-C12H26+C12H25O2-5	= C12H25-6+C12H25O2H-5	1.000E+11 0.00 1.040E+04
	rev / 1.000E+11 0.00 1.290E+04 /	
C12H25-2	= C3H6+C9H19-1	6.00E+11 0.50 27650.0 !maNi

C12H25-4	= C5H10-1+C7H15-1	6.00E+11 0.50 27650.0 !maNi
C12H25-4	= C2H5+C10H20-1	6.00E+11 0.50 27650.0 !maNi
C12H25-5	= C6H12-1+C6H13-1	6.00E+11 0.50 27650.0 !maNi
C9H19-1	= C2H4+C7H15-1	9.12E+11 0.31 27238.0 !maNi
C8H17-1	= C2H4+C6H13-1	9.12E+11 0.31 27238.0 !maNi
C12H25-2	= C12H25-4	1.76e+09 0.76 3.47e+04
	rev / 1.76e+09 0.76 3.47e+04 /	
C12H25-2	= C12H25-5	3.22e+09 0.13 2.07e+04
	rev / 3.22e+09 0.13 2.07e+04 /	
C12H25-2	= C12H25-6	5.00e+11 -1.25 1.276e+04 ! estimated
	rev / 1.60e+10 -0.86 1.528e+04 /! estimated	
C12H25-4	= C12H25-5	9.587E+08 1.39 3.970E+04
	rev / 9.587E+08 1.39 3.970E+04 /	
C12H25-4	= C12H25-6	1.76e+09 0.76 3.47e+04
	rev / 3.50e+09 0.76 3.47e+04 /	
C12H25-4	= C12H25-6	3.22e+09 0.13 2.07e+04
	rev / 3.22e+09 0.13 2.07e+04 /	
C12H25-4	= C12H25-5	5.00e+11 -1.25 1.276e+04 ! estimated
	rev / 1.60e+10 -0.86 1.528e+04 / ! estimated	
C12H25-5	= C12H25-6	9.587E+08 1.39 3.970E+04
	rev / 9.587E+08 1.39 3.970E+04 /	
C12H25-5	= C12H25-6	1.76e+09 0.76 3.47e+04
	rev / 3.50e+09 0.76 3.47e+04 /	
C10H20-1+OH	= CH2O+C9H19-1	1.000E+11 0.00 -4.000E+03
	rev / 0.000E+00 0.00 0.000E+00 /	
C10H20-1+OH	= CH3CHO+C8H17-1	1.000E+11 0.00 -4.000E+03
	rev / 0.000E+00 0.00 0.000E+00 /	
C10H20-1+O	= CH2CHO+C8H17-1	1.000E+11 0.00 -1.050E+03
	rev / 0.000E+00 0.00 0.000E+00 /	
C8H16-4+OH	= N-C3H7CHO+P-C4H9	1.000E+11 0.00 -4.000E+03
	rev / 0.000E+00 0.00 0.000E+00 /	
C10H20-1	= C7H15-1+C3H5-A	1.000E+16 0.00 7.100E+04
	rev / 1.000E+13 0.00 0.000E+00 /	
C8H16-4	= C6H11+C2H5	1.000E+16 0.00 7.100E+04
	rev / 1.000E+13 0.00 0.000E+00 /	
C12H25O2-2	= C12H25-2+O2	1.357E+23 -2.36 3.767E+04
	rev / 7.540E+12 0.00 0.000E+00 /	
C12H25O2-4	= C12H25-4+O2	1.357E+23 -2.36 3.767E+04
	rev / 7.540E+12 0.00 0.000E+00 /	
C12H25O2-5	= C12H25-5+O2	1.357E+23 -2.36 3.767E+04
	rev / 7.540E+12 0.00 0.000E+00 /	
C12H25O2-6	= C12H25-6+O2	1.357E+23 -2.36 3.767E+04
	rev / 7.540E+12 0.00 0.000E+00 /	
C8H17O2-1	= C8H17-1+O2	2.657E+20 -1.67 3.540E+04
	rev / 4.520E+12 0.00 0.000E+00 /	
C12H25-5+C12H25O2-5	= C12H25O-5+C12H25O-5	7.000E+12 0.00 -1.000E+03
	rev / 7.570E+16 -1.12 3.160E+04 /	
C12H25-5+HO2	= C12H25O-5+OH	7.000E+12 0.00 -1.000E+03
	rev / 1.967E+18 -1.37 2.889E+04 /	
C12H25O2-2	= C12OOH2-4	2.500E+10 0.00 2.045E+04
C12H25O2-4	= C12OOH4-2	2.500E+10 0.00 2.045E+04
C12H25O2-5	= C12OOH5-7	2.500E+10 0.00 2.045E+04
C12H25O2-6	= C12OOH6-4	2.500E+10 0.00 2.045E+04
C12H25O2-6	= C12OOH6-8	2.500E+10 0.00 2.045E+04
C8H17O2-1	= C8OOH1-3	2.500E+10 0.00 2.045E+04
C12H25O2-5+HO2	= C12H25O2H-5+O2	1.750E+10 0.00 -3.275E+03
	rev / 5.974E+13 -0.85 3.490E+04 /	

C12H25O2-5+H2O2	= C12H25O2H-5+HO2	2.400E+12 0.00 1.000E+04
	rev / 2.400E+12 0.00 1.000E+04 /	
C12H25O2-5+CH3O2	= C12H25O-5+CH3O+O2	1.400E+16 -1.61 1.860E+03
	rev / 0.000E+00 0.00 0.000E+00 /	
C12H25O2-5 + C12H25O2-5	= C12H25O-5 + C12H25O-5 + O2	1.400E+16 -1.61 1.860E+03
	rev / 0.000E+00 0.00 0.000E+00 /	
C12H25O2H-5	= C12H25O-5+OH	1.250E+16 0.00 3.900E+04
N-C4H9CHO+C7H15-1	= C12H25O-5	1.00e+11 0. 12900.
C12OOH2-4	= C12O2-4+OH	7.500E+10 0.00 1.525E+04
	rev / 0.000E+00 0.00 0.000E+00 /	
C12OOH4-2	= C12O2-4+OH	7.500E+10 0.00 1.525E+04
	rev / 0.000E+00 0.00 0.000E+00 /	
C12OOH6-4	= C12O4-6+OH	7.500E+10 0.00 1.525E+04
	rev / 0.000E+00 0.00 0.000E+00 /	
C8OOH1-3	= C8O1-3+OH	7.500E+10 0.00 1.525E+04
	rev / 0.000E+00 0.00 0.000E+00 /	
C12OOH2-4	= OH+CH3CHO+C10H20-1	1.00E+13 0.00 3.0E+04
	rev / 0.000E+00 0.00 0.000E+00 /	
C12OOH4-2	= OH+C3H6+N-C8H17CHO	1.00E+13 0.00 3.0E+04
	rev / 0.000E+00 0.00 0.000E+00 /	
C12OOH6-4	= OH+C5H10-1+N-C6H13CHO	1.00E+13 0.00 3.0E+04
	rev / 0.000E+00 0.00 0.000E+00 /	
C12OOH6-8	= OH+N-C5H11CHO+C6H12-1	1.00E+13 0.00 3.0E+04
	rev / 0.000E+00 0.00 0.000E+00 /	
C12OOH2-4O2	= C12OOH2-4+O2	1.367E+23 -2.37 3.764E+04
	rev / 7.540E+12 0.00 0.000E+00 /	
C12OOH4-2O2	= C12OOH4-2+O2	1.367E+23 -2.37 3.764E+04
	rev / 7.540E+12 0.00 0.000E+00 /	
C12OOH5-7O2	= C12OOH5-7+O2	1.367E+23 -2.37 3.764E+04
	rev / 7.540E+12 0.00 0.000E+00 /	
C12OOH6-4O2	= C12OOH6-4+O2	1.367E+23 -2.37 3.764E+04
	rev / 7.540E+12 0.00 0.000E+00 /	
C12OOH6-8O2	= C12OOH6-8+O2	1.367E+23 -2.37 3.764E+04
	rev / 7.540E+12 0.00 0.000E+00 /	
C8OOH1-3O2	= C8OOH1-3+O2	1.367E+23 -2.37 3.764E+04
	rev / 7.540E+12 0.00 0.000E+00 /	
C12OOH2-4O2	= C12KET2-4+OH	1.250E+10 0.00 1.745E+04
C12OOH4-2O2	= C12KET4-2+OH	1.250E+10 0.00 1.745E+04
C12OOH5-7O2	= C12KET5-7+OH	1.250E+10 0.00 1.745E+04
C12OOH6-4O2	= C12KET6-4+OH	1.250E+10 0.00 1.745E+04
C12OOH6-8O2	= C12KET6-8+OH	1.250E+10 0.00 1.745E+04
C8OOH1-3O2	= C8KET1-3+OH	2.500E+10 0.00 2.100E+04
C12KET2-4	= OH+CH3COCH2+N-C8H17CHO	1.050E+16 0.00 3.900E+04
	rev / 0.000E+00 0.00 0.000E+00 /	
C12KET4-2	= OH+CH3CHO+C8H17COCH2	1.050E+16 0.00 3.900E+04
	rev / 0.000E+00 0.00 0.000E+00 /	
C12KET5-7	= OH+N-C4H9COCH2+N-C5H11CHO	1.050E+16 0.00 3.900E+04
	rev / 0.000E+00 0.00 0.000E+00 /	
C12KET6-4	= OH+N-C3H7CHO+C6H13COCH2	1.050E+16 0.00 3.900E+04
	rev / 0.000E+00 0.00 0.000E+00 /	
C12KET6-8	= OH+C5H11COCH2+N-C4H9CHO	1.050E+16 0.00 3.900E+04
	rev / 0.000E+00 0.00 0.000E+00 /	
C8KET1-3	= OH+CH2CHO+N-C5H11CHO	1.050E+16 0.00 3.900E+04
	rev / 0.000E+00 0.00 0.000E+00 /	
C12O2-4+OH	= CH3CO+C10H20-1+H2O	2.50e+12 0.00 0.00
	rev / 0.00 0.00 0.00 /	
C12O2-4+OH	= C3H6+N-C8H17CO+H2O	2.50e+12 0.00 0.00
	rev / 0.00 0.00 0.00 /	
C12O4-6+OH	= C5H10-1+N-C6H13CO+H2O	2.50e+12 0.00 0.00
	rev / 0.00 0.00 0.00 /	

```
C12O2-4+HO2          = CH3CO+C10H20-1+H2O2          5.000E+12 0.00 1.770E+04
                     rev / 0.00 0.00 0.00 /
C12O2-4+HO2          = C3H6+N-C8H17CO+H2O2          5.000E+12 0.00 1.770E+04
                     rev / 0.00 0.00 0.00 /
C12O4-6+HO2          = C5H10-1+N-C6H13CO+H2O2       5.000E+12 0.00 1.770E+04
                     rev / 0.00 0.00 0.00 /
C8O1-3+OH            = C2H4+N-C5H11CO+H2O           2.50e+12 0.00 0.00
                     rev / 0.00 0.00 0.00 /
C8O1-3+HO2           = C2H4+N-C5H11CO+H2O2          5.000E+12 0.00 1.770E+04
                     rev / 0.00 0.00 0.00 /
N-C8H17CHO+O2        = N-C8H17CO+HO2                2.000E+13 0.50 4.220E+04
                     rev / 1.000E+07 0.00 4.000E+04 /
N-C8H17CHO+OH        = N-C8H17CO+H2O                2.690E+10 0.76 -3.400E+02
                     rev / 1.740E+10 0.76 3.120E+04 /
N-C8H17CHO+H         = N-C8H17CO+H2                 4.000E+13 0.00 4.200E+03
                     rev / 1.800E+13 0.00 2.400E+04 /
N-C8H17CHO+O         = N-C8H17CO+OH                 5.000E+12 0.00 1.790E+03
                     rev / 1.000E+12 0.00 1.900E+04 /
N-C8H17CHO+HO2       = N-C8H17CO+H2O2               2.800E+12 0.00 1.360E+04
                     rev / 1.000E+12 0.00 1.000E+04 /
N-C8H17CHO+CH3       = N-C8H17CO+CH4                1.700E+12 0.00 8.440E+03
                     rev / 1.500E+13 0.00 2.800E+04 /
N-C8H17CHO+CH3O      = N-C8H17CO+CH3OH              1.150E+11 0.00 1.280E+03
                     rev / 3.000E+11 0.00 1.800E+04 /
N-C8H17CO            = C8H17-1+CO                   1.000E+11 0.00 9.600E+03
                     rev / 1.000E+11 0.00 0.000E+00 /
N-C6H13CHO+O2        = N-C6H13CO+HO2                2.000E+13 0.50 4.220E+04
                     rev / 1.000E+07 0.00 4.000E+04 /
N-C6H13CHO+OH        = N-C6H13CO+H2O                2.690E+10 0.76 -3.400E+02
                     rev / 1.740E+10 0.76 3.120E+04 /
N-C6H13CHO+H         = N-C6H13CO+H2                 4.000E+13 0.00 4.200E+03
                     rev / 1.800E+13 0.00 2.400E+04 /
N-C6H13CHO+O         = N-C6H13CO+OH                 5.000E+12 0.00 1.790E+03
                     rev / 1.000E+12 0.00 1.900E+04 /
N-C6H13CHO+HO2       = N-C6H13CO+H2O2               2.800E+12 0.00 1.360E+04
                     rev / 1.000E+12 0.00 1.000E+04 /
N-C6H13CHO+CH3       = N-C6H13CO+CH4                1.700E+12 0.00 8.440E+03
                     rev / 1.500E+13 0.00 2.800E+04 /
N-C6H13CHO+CH3O      = N-C6H13CO+CH3OH              1.150E+11 0.00 1.280E+03
                     rev / 3.000E+11 0.00 1.800E+04 /
N-C6H13CO            = C6H13-1+CO                   1.000E+11 0.00 9.600E+03
                     rev / 1.000E+11 0.00 0.000E+00 /
C8H17COCH2           = C8H17-1+CH2CO                2.000e+13 0.00 31000.
                     rev / 2.000e+11 0.00 7350. /
C6H13COCH2           = C6H13-1+CH2CO                2.000e+13 0.00 31000.
                     rev / 2.000e+11 0.00 7350. /
C5H11COCH2           = C5H11-1+CH2CO                2.000e+13 0.00 31000.
                     rev / 2.000e+11 0.00 7350. /
END
```

Bibliography

[1] Pickett, L. M. "Engine Combustion Network," in *Available at http://www.sandia.gov/ecn/index.php2011*, Sandia National laboratory.

[2] Golovitchev, V. I.
URL `http://http://www.tfd.chalmers.se/`

[3] Som, S., D. E. Longman, Z. Luo, M. Plomer, and T. Lu (Oct 9-12, 2011) "Three dimensional simulations of diesel Sprays using n-dodecane as a surrogate," in *Hosted by the University of Connecticut, Storrs, CT*, Fall Technical Meeting of the Eastern States Section of the Combustion Institute.

[4] (2007) "Basic research needs for clean and efficient combustion of 21st century transportation fuels. Report of the basic energy sciences workshop on basic research needs for clean and efficient combustion of 21st century transportation fuels, 29 October 1 November 2006," in *available at: http://www.sc.doe.gov/bes/reports/list.html*, Office of Science, U.S. Department of Energy.

[5] (2005) "US Census Bureau, International Data Base," Available at http://www.census.gov/ipc/.

[6] Drake, M. C. and D. C. Haworth (2007) "Advanced gasoline engine development using optical diagnostics and numerical modeling," *Proc. Comb. Inst.*, **31**, pp. 99 – 124.

[7] Fenger, J. (2009) "Air pollution in the last 50 years From local to global," *Atmospheric Environment*, **43**, pp. 13 – 22.

[8] Kromer, M. A., A. Bandivadekar, and C. Evans (2010) "Long-term greenhouse gas emission and petroleum reduction goals: Evolutionary pathways for the light-duty vehicle sector," *Energy*, **35**, pp. 387 – 397.

[9] Davis, S. C. and S. W. Diegel (2004) "Transportation Energy Data Book," in *Report ORNL-6973, Available at http://www-cta.ornl.gov*, 24th ed., Oak Ridge National Laboratory.

[10] "US Environmental Protection Agency," http://www.epa.gov/lawsregs/regulations/.

[11] Epping, K., S. M. Aceves, R. Bechtold, and J. E. Dec (2002) "The potential of HCCI combustion for high efficiency and low emissions," *SAE Technical Paper Series*, **2002-01-1923**.

[12] Zhao, F., T. W. Asmus, D. N. Assanis, J. E. Dec, J. A. Eng, and N. P. M. (2003) "Homogeneous Charge Compression Ignition (HCCI) Engines: Key Research and Development Issues," in *SAE International, Warrendale, PA*.

[13] Zhang, Y. Z. (2004) *"Hybrid particle/finite-volume PDF methods for three-dimensional time-dependent flows in complex geometries"*, Ph.D. thesis, The Pennsylvania State University, University Park, PA.

[14] Choi, H., M. Kim, K. Min, and J. Lee (2002) "The Stratified Combustion Model of Direct-Injection Spark-Ignition Engines," *Proc. Comb. Inst.*, **29**, pp. 695 – 701.

[15] Haworth, D. C., R. J. Blint, B. Guenot, and T. J. Poinsot (2000) "Numerical simulation of turbulent propaneair combustion with nonhomogeneous reactants," *Comb. and Flame*, **121**, pp. 395 – 417.

[16] (2006) "Energy Information Administration," in *Report No. DOE/EIA-0484*, Annual Energy Review, 2005.

[17] Knothe, G. (2010) "Biodiesel and renewable diesel: a comparison," *Prog. Energy Comb. Sc.*, **36**, pp. 364 – 373.

[18] Aatola, H., T. Sarjovaara, M. Larmi, and S. Mikkonen (2008) "Hydrotreated vegetable oil (HVO) as a renewable diesel fuel: trade-off between NOx, particulate emission, and fuel consumption of a heavy duty engine," *SAE Technical Paper Series*, **2008-01-2500**.

[19] Kokjohn, S., R. Hanson, D. Splitter, and R. Reitz (2009) "Experiments and Modeling of Dual-Fuel HCCI and PCCI Combustion Using In-Cylinder Fuel Blending," *SAE Technical Paper Series*, **2009-01-2647**.

[20] Splitter, D., S. Kokjohn, K. Rein, R. Hanson, S. Sanders, and R. Reitz (2010) "An Optical Investigation of Ignition Processes in Fuel Reactivity Controlled PCCI Combustion," *SAE Technical Paper Series*, **2010-01-0345**.

[21] Hanson, R., S. Kokjohn, D. Splitter, and R. Reitz (2010) "An Experimental Investigation of Fuel Reactivity Controlled PCCI Combustion in a Heavy-Duty Engine," *SAE Technical Paper Series*, **2010-01-0864**.

[22] Kokjohn, S. L., R. M. Hanson, D. A. Splitter, and R. D. Reitz (2011) "Fuel reactivity controlled compression ignition (RCCI): a pathway to controlled high-efficiency clean combustion," *Intl. J. Engine Res.*, **12**, pp. 209 – 226.

[23] Libby, P. A., K. N. C. Bray, and J. B. Moss (1979) "Effects of Finite Reaction Rate and Molecular Transport in Premixed Turbulent Combustion," *Comb. and Flame*, **34**, pp. 285 – 301.

[24] Bray, K. N. C. and J. B. Moss (1977) "A Unified Statistical Model of the Premixed Turbulent Flame," *Acta Astronaut*, **4**, pp. 291 – 319.

[25] Libby, P. A. and K. N. C. Bray (1981) "Counter Gradient Diffusion in Premixed Turbulent Flames," *AIAA J.*, **19**, pp. 205 – 213.

[26] Libby, P. A. (1985) "Theory of Normal Premixed Turbulent Flames Revisited," *Prog. Energy Comb. Sc.*, **11**, pp. 83 – 96.

[27] Abraham, J., F. A. Williams, and F. V. Bracco (1985) "Discussion of Turbulent Flame Structure in Premixed Charges," *SAE Technical Paper Series*, **850345**.

[28] Pope, S. B. (1985) "PDF methods for turbulent reactive flows,," *Prog. Energy Comb. Sc.*, **11**, pp. 119 – 192.

[29] Xu, J. and S. B. Pope (2000) "PDF calculations of turbulent nonpremixed flames with local extinction," *Comb. and Flame*, **123**, pp. 281 – 307.

[30] Tang, Q., J. Xu, and S. B. Pope (2000) "Probability density function calculations of local extinction and NO production in piloted-jet turbulent methane/air flames," *Proc. Comb. Inst.*, **28**, pp. 133 – 139.

[31] Cao, R. R. and S. B. Pope (2005) "The influence of chemical mechanisms on PDF calculations of nonpremixed piloted jet flames," *Comb. and Flame*, **143**, pp. 450 – 470.

[32] Cao, R. R., H. Wang, and S. B. Pope (2007) "The effect of mixing models in PDF calculations of piloted jet flames," *Proc. Comb. Inst.*, **31**, pp. 1543 – 1550.

[33] Haworth, D. C. (2010) "PDF methods for turbulent reactive flows,," *Prog. Energy Comb. Sc.*, **36**, pp. 168 – 259.

[34] (2011), "International workshop on measurement and computation of turbulent nonpremixed flames," .
URL `available at: http:/www.sandia.gov/ecn/refs.php`

[35] Jaishree, J. (2011) *"Lagrangian and Eulerian Probability Density Function methods for turbulent reacting flows"*, Ph.D. thesis, The Pennsylvania State University, University Park, PA.

[36] Coppalle, A. and D. Joyeux (1994) "Temperature and soot volume fraction in turbulent diffusion flames: measurements of mean and fluctuating values," *Comb. and Flame*, **96**, pp. 275 – 285.

[37] Kent, J. H. and D. Honnery (1987) "Modeling sooting turbulent jet flames using an extended flamelet technique," *Comb. Sc. Tech.*, **54**, pp. 383 – 397.

[38] Mehta, R. S. (2008) *"Detailed modeling of soot formation and turbulence-radiation interactions in turbulent jet flames"*, Ph.D. thesis, The Pennsylvania State University, University Park, PA.

[39] Kung, E. H. (2008) *"PDF-based modeling of autoignition and emissions for advanced directinjection engines"*, Ph.D. thesis, The Pennsylvania State University, University Park, PA.

[40] Zhang, Y. Z., E. H. Kung, and D. C. Haworth (2005) "A PDF method for multidimensional modeling of HCCI engine combustion: effects of turbulence/chemistry interactions on ignition timing and emissions," *Proc. Comb. Inst.*, **30**, pp. 2763 – 2771.

[41] Babajimopoulos, A., D. N. Assanis, D. L. Flowers, S. M. Aceves, and R. P. Hessel (2005) "A PDF method for turbulent mixing and combustion on three-dimensional unstructured deforming meshes," *Intl. J. Engine Res.*, **6**, pp. 497 – 512.

[42] Aceves, S., D. Flowers, F. Espinosa-Loza, A. Babajimopoulos, and D. A. Assanis (2005) "Analysis of Premixed Charge Compression Ignition Combustion With a Sequential Fluid Mechanics-Multizone Chemical Kinetics Model," *SAE Technical Paper Series*, **2005-01-0115**.

[43] Barths, H., C. Felsch, and N. Peters (2009) "Mixing models for the two-way-coupling of CFD codes and zero-dimensional multi-zone codes to model HCCI combustion," *Comb. and Flame*, **156**, pp. 130 – 139.

[44] Heywood, J. B. (1988) *Internal combustion engine fundamentals*, McGraw-Hill.

[45] William, J. P. and C. J. Mueller (2011) "Recent progress in the development of diesel surrogate fuels," *Prog. Energy Comb. Sc.*, **37**, pp. 330 – 350.

[46] Tao, F., R. D. Reitz, and D. E. Foster (2007) "Revisit of diesel reference fuel (n-Heptane) mechanism applied to multidimensional diesel ignition and combustion simulations," in *Multidimensional Engine Modeling Users' Group Meeting, Detroit, MI, April 15*.

[47] Turns, S. R. (2000) *An Introduction to Combustion: Concepts and Applications*, McGraw-Hill.

[48] Glassman, I. (1996) *Combustion*, 2 ed., Academic Press.

[49] Pfahl, U., K. Fieweger, and G. Adomett (1996) "Self-Ignition of Diesel-Relevant Hydrocarbon-Air Mixtures under Engine Conditions," *Proc. Comb. Inst.*, **26**, pp. 781 – 789.

[50] Westbrook, C. (2000) "Chemical Kinetics of Hydrocarbon Ignition in Practical Combustion Systems," *Proc. Comb. Inst.*, **28**, pp. 1563 – 1577.

[51] Higgins, B. and D. Siebers (2000) "Diesel-Spray Ignition and Premixed-Burn Behavior," *SAE Technical Paper Series*, **2000-01-0940**.

[52] Dec, J. E. and C. Espey (1998) "Chemiluminescence Imaging of Autoignition in a DI Diesel Engine," *SAE Technical Paper Series*, **982685**.

[53] Curran, H., P. Gaffuri, W. Pitz, and C. Westbrook (1998) "A Comprehensive Modeling Study of n-Heptane Oxidation," *Comb. and Flame*, **114**, pp. 149 – 177.

[54] Zhao, P. and C. K. Law (Oct 9-12, 2011) "NTC-affected ignition in non-premixed counterflow," in *Hosted by the University of Connecticut, Storrs, CT*, Fall Technical Meeting of the Eastern States Section of the Combustion Institute.

[55] Dec, J. E. (1997) "A Conceptual Model of DI Diesel Combustion Based on Laser-Sheet Imaging," *SAE Technical Paper Series*, **970873**.

[56] Chapman, E. M. (2008) *"NOx reduction strategies for compression ignition engines"*, Ph.D. thesis, The Pennsylvania State University, University Park, PA.

[57] Flynn, P. F., R. P. Durrett, G. L. Hunter, A. O. ZurLoye, O. C. Akinyemi, J. E. Dec, and C. K. Westbrook (1999) "Diesel combustion: An integrated view combining laser diagnostics, chemical kinetics, and empirical validation," *SAE Technical Paper Series*, **1999-01-0509**.

[58] Dec, J. E. (2009) "Advanced compression-ignition engines-understanding the in-cylinder processes," *Proc. Comb. Inst.*, **32**, pp. 2727 – 2742.

[59] Fenimore, C. (1970) "Formation of Nitric Oxide in Premixed Hydrocarbon Flames," *Proc. Comb. Inst.*, **13**, pp. 373 – 380.

[60] Leung, K. M., R. P. Lindstedt, and W. P. Jones (1991) "A simplified reaction mechanism for soot formation in nonpremixed flames," *Comb. and Flame*, **87**, pp. 289 – 305.

[61] Colket, M. B. and R. J. Hall (1991) "Description and discussion of a detailed model for soot formation in laminar premixed flames," in *Technical Report UTRC91-20*, United Technologies Research Center.

[62] Kennedy, I. M. (1997) "Models of soot formation and oxidation," *Prog. Energy Comb. Sc.*, **23**, pp. 95 – 132.

[63] Kamimoto, T. and M. Bae (1988) "High Combustion Temperature for the Reduction of Particulate in Diesel Engines," *SAE Technical Paper Series*, **880423**.

[64] Akihama, K., Y. Takatori, K. Inagaki, S. Sasaki, and A. M. Dean (2001) "Mechanism of the Smokeless Rich Diesel Combustion by Reducing Temperature," *SAE Technical Paper Series*, **2001-01-0655**.

[65] Kook, S., C. Bae, P. Miles, D. Choi, and L. M. Pickett (2005) "The Influence of Charge Dilution and Injection Timing on Low-Temperature Diesel Combustion and Emissions," *SAE Technical Paper Series*, **2005-01-3837**.

[66] Persson, H., O. Andersson, and R. Egnell (2011) "Fuel effects on flame lift-off under diesel conditions," *Comb. and Flame*, **158**, pp. 91 – 97.

[67] Hwang, W., J. E. Dec, and M. Sjöberg (2007) "Fuel Stratification for Low-Load HCCI Combustion: Performance and Fuel-PLIF Measurements," *SAE Technical Paper Series*, **2007-01-4130**.

[68] Dec, J. E. and M. Sjöberg (2003) "A Parametric Study of HCCI Combustion - the Sources of Emissions at Low Loads and the Effects of GDI Fuel Injection," *SAE Technical Paper Series*, **2003-01-0752**.

[69] Sweeney, M. S., S. Hochgreb, and R. S. Barlow (2011) "The structure of premixed and stratified low turbulence flames," *Comb. and Flame*, **158**, pp. 935 – 948.

[70] Dec, J. E., W. Hwang, and M. Sjöberg (2006) "An Investigation of Thermal Stratification in HCCI Engines Using Chemiluminescence Imaging," *SAE Technical Paper Series*, **2006-01-1518**.

[71] Babajimopoulos, A., G. A. Lavoie, and D. A. Assanis (2003) "Modeling HCCI Combustion With High Levels of Residual Gas Fraction - A Comparison of Two VVA Strategies," *SAE Technical Paper Series*, **2003-01-3220**.

[72] Ryan, T. and T. Callahan (1996) "Homogeneous Charge Compression Ignition of Diesel Fuel," *SAE Technical Paper Series*, **961160**.

[73] Gray, A. and T. Ryan (1997) "Homogeneous Charge Compression Ignition (HCCI) of Diesel Fuel," *SAE Technical Paper Series*, **971676**.

[74] Christensen, M., A. Hultqvist, and B. Johansson (1999) "Demonstrating the Multi Fuel Capability of a Homogeneous Charge Compression Ignition Engine with Variable Compression Ratio," *SAE Technical Paper Series*, **1999-01-3679**.

[75] Walter, B. and B. Gatellier (2002) "Development of the High Power NADI Concept Using Dual Mode Diesel Combustion to Achieve Zero NOx and Particulate Emissions," *SAE Technical Paper Series*, **2002-01-1744**.

[76] Sjöberg, M., J. E. Dec, and W. Hwang (2007) "Thermodynamic and Chemical Effects of EGR and Its Constituents on HCCI Autoignition," *SAE Technical Paper Series*, **2007-01-0207**.

[77] Maroteaux, F. and L. Noel (2006) "Development of a reduced n-heptane oxidation mechanism for HCCI combustion modeling," *Comb. and Flame*, **146**, pp. 246 – 267.

[78] Farrell, J. T., N. P. Cernansky, F. L. Dryer, D. G. Friend, C. A. Hergart, and L. C. K. et al. (2007) "Development of an experimental database and kinetic models for surrogate diesel fuels," *SAE Technical Paper Series*, **2007-01-0201**.

[79] Musculus, M. (2006) "Multiple Simultaneous Optical Diagnostic Imaging of Early-Injection Low-Temperature Combustion in a Heavy-Duty Diesel Engine," *SAE Technical Paper Series*, **2006-01-0079**.

[80] F., B.-L. (2008) "Detailed chemical kinetic models for the low-temperature combustion of hydrocarbons with application to gasoline and diesel fuel surrogates," *Prog. Energy Comb. Sc.*, **34**, pp. 440 – 498.

[81] Biet, J., M. H. Hakka, V. Warth, P. A. Glaude, and F. Battin-Leclerc (2008) "Experimental and modeling study of the low-temperature oxidation of large alkanes," *Energy and Fuels*, **22**, pp. 2258 – 2269.

[82] Westbrook, C. K., W. J. Pitz, O. Herbinet, H. J. Curran, and E. J. Silke (2009) "A detailed chemical kinetic reaction mechanism for n-alkane hydrocarbons from n-octane to nhexadecane," *Comb. and Flame*, **156**, pp. 181 – 199.

[83] Curran, H. J., P. Gaffuri, W. J. Pitz, and C. K. Westbrook (1998) "A comprehensive modeling study of n-heptane oxidation," *Comb. and Flame*, **114**, pp. 149 – 177.

[84] You, X., F. N. Egolfopoulos, and H. Wang (2009) "Detailed and simplified kinetic models of n-dodecane oxidation: the role of fuel cracking in aliphatic hydrocarbon combustion," *Proc. Comb. Inst.*, **32**, pp. 403 – 410.

[85] Zhang, H. R., E. G. Eddings, and A. F. Sarofim (2008) "A journey from n-heptane to liquid transportation fuels. 1. The role of the allylic radical and its related species in aromatic precursor chemistry," *Energy and Fuels*, **22**, pp. 945 – 953.

[86] Shen, H. S., J. Steinberg, J. Vanderover, and M. A. Oehlschlaeger (2009) "A shock tube study of the ignition of n-heptane, n-decane, n-dodecane, and n-tetradecane at elevated pressures," *Energy and Fuels*, **23**, pp. 2482 – 2489.

[87] Hentschel, W., K. P. Schindler, and O. Haahtela (1994) "European Diesel Research IDEA – Experimental Results from DI Diesel Engine Investigations," *SAE Technical Paper Series*, **941954**.

[88] Pitsch, H., , and N. Peters (1994) *Reduced Kinetics of Multicomponent Fuels to Describe the Auto-Ignition,Flame Propagation and Post Flame Oxidation of Gasoline and Diesel Fuels*, *Tech. Rep. 4th period*, Periodic Report,project FK.2, IDEA-EFFECT.

[89] CFD4C "Computational Fluid Dynamics for Combustion," in *http://www.iwr.uni-heidelberg.de/groups/reaflow/user/CFD4C/*, information and reports available online at.

[90] Sjöberg, M. and J. E. Dec (2007) "Comparing late-cycle autoignition stability for single- and two-stage ignition fuels in HCCI engines," *Proc. Comb. Inst.*, **31**, pp. 2895 – 2902.

[91] ——— (2008) "Influence of Fuel Autoignition Reactivity on the High-Load Limits of HCCI Engines," *SAE Technical Paper Series*, **2008-01-0054**.

[92] Peters, N., G. Paczko, R. Seiser, and K. Seshadri (2002) "Temperature cross-over and non-thermal runaway at two-stage ignition of n-heptane," *Comb. and Flame*, **128**, pp. 38 – 59.

[93] Ra, Y. and R. R. D. (2008) "A reduced chemical kinetic model for IC engine combustion simulations with primary reference fuels," *Comb. and Flame*, **155**, pp. 713 – 738.

[94] Patel, A., S. C. Kong, and R. D. Reitz (2004) "Development and Validation of a Reduced Reaction Mechanism for HCCI Engine Simulations," *SAE Technical Paper Series*, **2004-01-0558**.

[95] Lu, T., C. Law, C. Yoo, and J. Chen (2009) "Dynamic Stiffness Removal for Direct Numerical Simulations," *Comb. and Flame*, **156**, pp. 1542 – 1551.

[96] You, X. Q., F. N. Egolfopoulos, and H. Wang (2009) "Detailed and simplified kinetic models of n-dodecane oxidation: The role of fuel cracking in aliphatic hydrocarbon combustion," *Proc. Comb. Inst.*, **32**, pp. 403 – 410.

[97] Holley, A. T., X. Q. You, E. Dames, H. Wang, and F. N. Egolfopoulos (2009) "Sensitivity of propagation and extinction of large hydrocarbon flames to fuel diffusion," *Proc. Comb. Inst.*, **32**, pp. 1157 – 1163.

[98] Dagaut, P., A. El Bakali, and A. Ristori (2006) "The Combustion of Kerosene: Experimental Results and Kinetic Modeling Using 1- to 3-Component Surrogate Model Fuels," *Fuels*, **85**, pp. 944 – 956.

[99] Zeppieri, S. K., S. D. Klotz, and F. L. Dryer (2000) "Modeling Concepts for Larger Carbon Number Alkanes: A Partially Reduced Skeletal Mechanism for n-Decane Oxidation and Pyrolysis," *Proc. Comb. Inst.*, **28**, pp. 1587 – 1596.

[100] Zhao, A., J. Li, A. Kazakov, and F. L. Dryer (2005) "Burning Velocities and High Temperature Skeletal Kinetic Model for n-Decane," *Comb. Sc. Tech.*, **177**, pp. 89 – 106.

[101] Ristori, A., P. Dagaut, and M. Cathonnet (2001) "The Oxidation of n-Hexadecane: Experimental and Detailed Kinetic Modeling," *Comb. and Flame*, **125**, pp. 1128 – 1137.

[102] Fournet, R., F. Battin-Leclerc, P. A. Glaude, B. Judenherc, V. Warth, G. M. Cme, G. Scacchi, A. Ristori, G. Pengloan, P. Dagaut, and M. Cathonnet (2001) "The Gas Phase Oxidation of n-Hexadecane," *Int. J. Chem. Kin.*, **33**, pp. 574 – 586.

[103] Barlow, R. S. and J. H. Frank (1998) "Effects of turbulence on species mass fractions in methane/air jet flames," *Proc. Comb. Inst.*, **27**, pp. 1087 – 1095.

[104] Barlow, R. S. and A. Dreizler (2008) "Sandia/TUD Piloted CH4/Air Jet Flames," in *http://public.ca.sandia.gov/TNF/DataArch/FlameD.html*.

[105] Raman, V. and H. Pitsch (2007) "A consistent LES/filtered-density function formulation for the simulation of turbulent flames with detailed chemistry," *Proc. Comb. Inst.*, **31**, pp. 1711 – 1719.

[106] Mustata, R., L. Valino, C. Jimenez, J. W. P., and S. Bondi (2006) "A probability density function Eulerian Monte Carlo field method for large eddy simulations:application to a turbulent piloted methane/air diffusion flame (Sandia D)," *Comb. and Flame*, **145**, pp. 88 – 104.

[107] Subramaniam, S. and S. B. Pope (1998) "A mixing model for turbulent reactive flows based on Euclidean minimum spanning trees," *Comb. and Flame*, **115**, pp. 487 – 514.

[108] Dopazo, C. and E. E. OBrien (1974) "An approach to the autoignition of a turbulent mixture," *Acta Astronaut*, **1**, pp. 1239 – 1266.

[109] James, S., A. M. S., M. K. Razdan, and S. B. Pope (2001) "In situ detailed chemistry calculations in combustion flow analyses," *J. Engine Gas Turb. Power*, **123**, pp. 747 – 756.

[110] Wang, A., M. F. Modest, D. C. Haworth, and L. Wang (2008) "Monte Carlo simulation of radiative heat transfer and turbulence interactions in methane/air jet flames," *J. Quant Spectrosc. Rad. Transfer*, **109**, pp. 269 – 279.

[111] Sung, C. J., C. K. Law, and J. Y. Chen (1998) "An augmented reduced mechanism for methane oxidation with comprehensive global parametric validation," *Proc. Comb. Inst.*, **27**, pp. 295 – 304.

[112] Tang, Q., W. Zhao, M. Bockelie, and R. O. Fox (2007) "Multi-environment probability density function method for modelling turbulent combustion using realistic chemical kinetics," *Comb. Theory Modelling*, **11**, pp. 889 – 907.

[113] Jaishree, J. and D. C. Haworth (2012) "Comparisons of Lagrangian and Eulerian PDF methods in simulations of nonpremixed turbulent jet flames with moderate-to-strong turbulencechemistry interactions," *Comb. Theory and Modelling*, **16**(3), pp. 435 – 463.

[114] Liu, K., S. B. Pope, and D. A. Caughey (2005) "Calculations of bluff-body stabilized flames using a joint probability density function model with detailed chemistry," *Comb. and Flame*, **141**, pp. 89 – 117.

[115] Raman, V., H. Pitsch, and R. O. Fox (2005) "Hybrid large eddy simulation/Lagrangian filtereddensity-function approach for simulating turbulent combustion," *Comb. and Flame*, **143**, pp. 56 – 78.

[116] James, S., J. Zhu, and M. S. Anand (2006) "LES/FDF of turbulent flames using complex chemical kinetics," *AIAA Paper No.*, **2006-4746**.

[117] Masri, A. R., S. B. Pope, and B. B. Dally (2000) "PDF computations of a strongly swirling nonpremixed flame stabilised on a new burner," *Proc. Comb. Inst.*, **28**, pp. 123 – 131.

[118] Repp, S., A. Sadiki, C. Schneider, A. Hinz, T. Landenfeld, and J. Janicka (2002) "Prediction of swirling confined diffusion flame with a Monte Carlo and a presumed-PDF model," *Int. J. Heat Mass Transfer*, **45**, pp. 1271 – 1285.

[119] Cannon, S. M., B. S. Brewster, and L. D. Smoot (1999) "PDF modeling of lean premixed combustion using in situ tabulated chemistry," *Comb. and Flame*, **119**, pp. 233 – 252.

[120] Nandula, S. P., R. W. Pitz, R. S. Barlow, and G. J. Fiechtner (1996) "Rayleigh/Raman/LIF measurements in a turbulent lean premixed combustor," *AIAA Paper No.*, **960937**.

[121] Lindstedt, R. P. and E. M. Vaos (2006) "Transported PDF modeling of high-Reynolds-number premixed turbulent flames," *Comb. and Flame*, **145**, pp. 495 – 511.

[122] Stollinger, M. and S. Heinz (2007) "PDF modeling and simulation of premixed turbulent combustion," *Monte Carlo Methods Appl.*, **14**, pp. 311 – 329.

[123] Chen, Y. C., N. Peters, G. A. Schneemann, N. Wruck, U. Renz, and M. S. Mansour (1996) "The detailed flame structure of highly stretched turbulent premixed methaneair flames," *Comb. and Flame*, **107**, pp. 223 – 244.

[124] Lindstedt, R. P., S. A. Louloudi, and E. M. Vaos (2000) "Joint scalar probability density function modeling of pollutant formation in piloted turbulent jet diffusion flames with comprehensive chemistry," *Proc. Comb. Inst.*, **28**, pp. 149 – 156.

[125] Mehta, R. S., M. F. Modest, and D. C. Haworth (2010) "Radiation characteristics and turbulence-radiation interactions in sooting turbulent jet flames," *Comb. Theory and Modelling*, **14**(1), pp. 105 – 124.

[126] Mehta, R. S., D. C. Haworth, and M. F. Modest (2009) "An assessment of gas-phase reaction mechanisms and soot models for laminar atmospheric pressure ethylene-air flames," *Proc. Comb. Inst.*, **32**, pp. 1327 – 1334.

[127] Lindstedt, R. P., S. A. Louloudi, J. J. Driscoll, and V. Sick (2004) "Finite rate chemistry effects in turbulent reacting flows," *Flow Turb. Comb.*, **72**, pp. 407 – 426.

[128] Lindstedt, R. P., H. C. Ozarovsky, R. S. Barlow, and A. N. Karpetis (2007) "Progression of local extinction in high Reynolds number turbulent jet flames," *Proc. Comb. Inst.*, **31**, pp. 1551 – 1558.

[129] Kuan, T. S. and R. P. Lindstedt (2005) "Transported probability density function modeling of a bluff body stabilized turbulent flame," *Proc. Comb. Inst.*, **30**, pp. 767 – 774.

[130] James, S., J. Zhu, and M. S. Anand (2005) "Lagrangian PDF transport method for simulations of axisymmetric turbulent reacting flows," *AIAA Paper No.*, **2005-0156**.

[131] Merci, B., D. Roekaerts, B. Naud, and P. S. B. (2006) "Comparative study of micromixing models in transported scalar PDF simulations of turbulent nonpremixed bluff body flames," *Comb. and Flame*, **146**, pp. 109 – 130.

[132] Merci, B., B. Naud, and D. Roekaerts (2007) "Impact of turbulent flow and mean mixture fraction results on mixing model behavior in transported scalar PDF simulations of turbulent non-premixed bluff body flames," *Flow Turb. Comb.*, **79**, pp. 41 – 53.

[133] Merci, B., B. Naud, D. Roekaerts, and U. Maas (2009) "Joint scalar versus joint velocity-scalar PDF simulations of bluff-body stabilized flames with REDIM," *Flow Turb. Comb.*, **82**, pp. 185 – 209.

[134] Taut, C., C. Correa, O. Deutschmann, J. Warnatz, S. Einecke, and C. e. a. Schulz (2000) "Threedimensional modeling with Monte Carlo-probability density function methods and laser diagnostics of the combustion in a two-stroke engine," *Proc. Comb. Inst.*, **28**, pp. 1153 – 1159.

[135] Bianchi, G. M. and P. Pelloni (1999) "Modeling the Diesel Fuel Spray Break-up by Using a Hybrid Model," *SAE Technical Paper Series*, **1999-01-0226**.

[136] Huh, K. Y. and A. D. Gosman (1991) *A phenomenological model of Diesel spray atomization, Tech. Rep. (ICMF 91), Tsukuba, 24-27 September*, Proc. Int. Conf. on Multiphase Flows.

[137] Pilch, M. and C. A. Erdman (1987) "Use of breakup time data and velocity history data to predict the maximum size of stable fragments for acceleration-induced breakup of a liquid drop," *Int. J. Multiphase Flow*, **13**(6), pp. 741 – 757.

[138] Hsiang, L. P. and G. M. Faeth (1992) "Near-limit drop deformation and secondary breakup," *Int. J. Multiphase Flow*, **18**(5), pp. 635 – 652.

[139] Reitz, R. D. (1987) "Modeling Atomization Processes in High-Pressure Vaporizing Sprays," *Atom. and Spray Tech.*, **3**, pp. 309 – 337.

[140] Reitz, R. D. and R. Diwakar (1986) "Effect of drop breakup on fuel sprays," *SAE Technical Paper Series*, **860469**.

[141] Dukowicz, J. K. (1980) "A particle-fluid numerical model for liquid sprays," *J. Comp. Phys.*, **35**, pp. 229 – 253.

[142] Law, C. K. (1978) "Internal Boiling and Superheating in Vaporizing Multicomponent Droplets," *AIChE J.*, **24**, pp. 626 – 632.

[143] Randolph, A. L., A. Makino, and C. K. Law (1988) "Liquid-Phase Diffusional Resistance in Multicomponent Droplet Gasification," *Proc. Comb. Inst.*, **21**, pp. 601 – 608.

[144] Launder, B. E. and D. B. Spalding (1974) "The numerical computation of turbulent flows," *Comp. Meth. in Appl. Mech. and Eng.*, **3**, pp. 269 – 289.

[145] El Tahry, S. H. (1983) "k-ε equation for compressible reciprocating engine flows," *AIAA J. Energy*, **7**, pp. 345 – 353.

[146] Villermaux, J. and J. C. Devillon (1972) "Représentation de la coalescence et de la redispersion des domaines de ségrégation dans un fluide par un modéle d'interaction phénoménologique," in *Proc. of second int. symp. on chem. reaction eng.*, Elsevier, New York, pp. 1 – 13.

[147] Pope, S. B. (2003) *Turbulent Flows*, Cambridge University Press, Cambridge, UK.

[148] Fox, R. O. (2003) *Computational models for turbulent reacting flows*, Cambridge University Press, Cambridge, UK.

[149] Masri, A. R., S. Subramaniam, and S. B. Pope (1996) "A mixing model to improve the PDF simulation of turbulent diffusion flames," *Proc. Comb. Inst.*, **26**, pp. 49 – 57.

[150] Curl, R. L. (1963) "Dispersed phase mixing: I. Theory and effects of simple reactors," *AIChE J.*, **9**, pp. 175 – 181.

[151] Janicka, J., W. Kolbe, and W. Kollmann (1977) "Closure of the transport equation for the probability density function of turbulent scalar fields," *J. Non-Equilib. Thermodyn.*, **4**, pp. 47 – 66.

[152] Pope, S. B. (1982) "An improved turbulent mixing model," *Comb. Sci. Tech.*, **28**, pp. 131 – 145.

[153] Haworth, D. C. and S. H. ElTahry (1991) "A PDF approach for multidimensional turbulent flow calculations with application to in-cylinder flows in reciprocating engines," *AIAA J.*, **29**, pp. 208 – 218.

[154] Muradoglu, M., P. Jenny, S. B. Pope, and D. A. Caughey (1999) "A consistent hybrid finite volume/particle method for the PDF equations of turbulent reactive flows," *J. Comp. Phys.*, **154**, pp. 342 – 371.

[155] Merryman, E. and A. Levy (1975) "Nitrogen Oxide Formation in Flames: The roles of NO2 and fuel nitrogen," *Proc. Comb. Inst.*, **15**, pp. 1073 – 1083.

[156] Meunier, P., M. Costa, and M. Carvalho (1998) "The formation and destruction of NO in turbulent propane diffusion flames," *Fuels*, **77**, pp. 1705 – 1714.

[157] Miller, J. and C. Bowman (1989) "Mechanism and Modeling of Nitrogen Chemistry in Combustion," *Prog. Energy Comb. Sc.*, **15**, pp. 287 – 338.

[158] Frenklach, M. (2002) "Method of moments with interpolative closure," *Chem. Eng. Sci.*, **57**, pp. 2229 – 2239.

[159] Raju, M. S. (2005) "Numerical investigation of various atomization models in the modeling of a spray flame," in *Technical Report NASA/CR-2005-214033*, NASA Glenn Research Center.

[160] Cha, C. M., J. Zhu, K. Rizk, and M. S. Anand (2005) "A comprehensive liquid fuel injection model for CFD simulations of gas turbine combustors," *AIAA Paper No.*, **2005-0349**.

[161] Bilger, R. W. (2011) "A mixture fraction framework for the theory and modeling of droplets and sprays," *Comb. and Flame*, **158**, pp. 191 – 202.

[162] Lippert, A. M. and R. D. Reitz (1997) "Modeling of multicomponent fuels using continuous distributions with application to droplet evaporation and sprays," *SAE Technical Paper Series*, **972882**.

[163] Wu, K. J., R. D. Reitz, and F. V. Bracco (1986) "Measurements of drop size at the spray edge near the nozzle in atomizing liquid jets," *Phys. Fluids*, **29**, pp. 941 – 951.

[164] Martinelli, L., , F. V. Bracco, and R. D. Reitz (1984) "Comparisons of computed and measured dense spray jets," *Prog. Astronautics and Aeronautics*, **95**, pp. 484 – 512.

[165] O'Rourke, P. J. and A. A. A. (1987) "The TAB method for numerical calculation of spray droplet breakup," *SAE Technical Paper Series*, **872089**.

[166] Faeth, G. M. (1983) "Evaporation and combustion of sprays," *Prog. Energy Comb. Sc.*, **9**, pp. 1 – 76.

[167] Sirignano, W. A. (1983) "Fuel droplet vaporization and spray combustion theory," *Prog. Energy Comb. Sc.*, **9**, pp. 291 – 322.

[168] Abramzon, B. and W. A. Sirignano (1989) "Adaptive grid refinement using cell-level and global imbalances," *Int. J. Heat Mass Transfer*, **32**, pp. 1605 – 1618.

[169] Gosman, A. D. and S. I. Ioannides (1983) "Aspects of computer simulation of liquid-fuelled combustors," *AIAA J. Energy*, **7**, pp. 482 – 490.

[170] Ge, H. W. and E. Gutheil (2008) "Simulation of a turbulent spray flame using coupled PDF gas phase and spray flamelet modeling," *Comb. and Flame*, **153**, pp. 173 – 185.

[171] Barlow, R. S., N. S. A. Smith, J. Y. Chen, and R. W. Bilger (1999) "Nitric oxide formation in dilute hydrogen jet flames: isolation of the effects of radiation and turbulence-chemistry submodels," *Comb. and Flame*, **117**, pp. 4 – 31.

[172] Frank, J. H., R. S. Barlow, and C. Lundquist (2000) "Radiation and nitric oxide formation in turbulent non-premixed jet flames," *Proc. Comb. Inst.*, **28**, pp. 447 – 454.

[173] Zhu, X. L., J. P. Gore, A. N. Karpetis, and R. S. Barlow (2001) "Scalar profiles and NO formation in laminar opposed-flow partially premixed methane/air flames," *Comb. and Flame*, **127**, pp. 2102 – 2118.

[174] ——— (2002) "The effects of self-absorption of radiation on an opposed flow partially premixed flame," *Comb. and Flame*, **129**, pp. 342 – 345.

[175] Modest, M. F. (2003) *Radiative heat transfer*, 2 ed., Academic Press.

[176] Guo, H., F. Liu, and G. J. Smallwood (2004) "Soot and NO formation in counterflow ethylene/oxygen/nitrogen diffusion flames," *Comb. Theory and Modelling*, **8**(3), pp. 475 – 489.

[177] STAR-CD (2001) *Computational Fluid Dynamics Software*, CD-adapco, NY.

[178] Issa, R. I. (1986) "Solution of the implicitly discretised fluid flow equations by operator-splitting," *J. Comp. Phys.*, **62**, pp. 40 – 65.

[179] Kee, R. J., F. M. Rupley, E. Meeks, and J. A. Miller (1996) *Chemkin III: A fortran chemical kinetics package for the analysis of gas-phase chemical and plasma kinetics*, *Tech. Rep. 94551-0969*, Sandia National Laboratories, Livermore, CA.

[180] Subramaniam, S. V. and D. C. Haworth (2000) "A PDF method for turbulent mixing and combustion on three-dimensional unstructured deforming meshes," *Intl. J. Engine Res.*, **1**, pp. 171 – 190.

[181] Zhang, Y. Z. and D. C. Haworth (2004) "A general mass consistency algorithm for hybrid particle/finite-volume PDF methods," *J. Comp. Phys.*, **194**, pp. 156 – 193.

[182] Chang, S. and D. C. Haworth (1997) "Adaptive grid refinement using cell-level and global imbalances," *Int. J. Numer. Methods Fluids*, **24**, pp. 375 – 392.

[183] Kung, E. H. and D. C. Haworth (2008) "Transported probability density function (tPDF) modeling for direct-jnjection internal combustion engines," *SAE Technical Paper Series*, **2008-01-0969**.

[184] Pope, S. B. (1995) "Particle method for turbulent flows: integration of stochastic model equations," *J. Comp. Phys.*, **117**, pp. 332 – 349.

[185] Siebers, D. L. (1998) "Liquid-phase fuel penetration in diesel sprays," *SAE Technical Paper Series*, **980809**.

[186] Naber, J. D. and D. L. Siebers (1996) "Effects of Gas Density and Vaporization on Penetration and Dispersion of Diesel Sprays," *SAE Technical Paper Series*, **960034**.

[187] Idicheria, C. A. and L. M. Pickett (2005) "Soot formation in diesel combustion under high-EGR conditions," *SAE Technical Paper Series*, **2005-01-3834**.

[188] Siebers, D. L. and B. Higgins (2001) "Flame lift-off on direct-injection diesel sprays under quiescent conditions," *SAE Technical Paper Series*, **2001-01-0530**.

[189] Higgins, B. and D. L. Siebers (2001) "Measurement of the flame lift-off location on DI diesel sprays using OH chemiluminescence," *SAE Technical Paper Series*, **2001-01-0918**.

[190] Musculus, M. P. B. and L. M. Pickett (2005) "Diagnostic considerations for optical laser-extinction measurements of soot in high-pressure transient combustion environments," *Comb. and Flame*, **141**, pp. 371 – 391.

[191] Borghesia, G., E. Mastorakos, C. B. Devaud, and R. W. Bilger (2011) "Modelling evaporation effects in Conditional Moment Closure for spray autoignition," *Comb. Theory and Modelling*, **15**(5), pp. 725 – 752.

[192] Bekdemir, C., E. Rijk, B. Somers, and P. DeGoey (2010) "On the Application of the Flamelet Generated Manifold (FGM) Approach to the Simulation of an Igniting Diesel Spray," *SAE Technical Paper Series*, **2010-01-0358**.

[193] Novella, R., A. Garca, J. M. Pastor, and V. Domenech (2011) "The role of detailed chemical kinetics on CFD diesel spray ignition and combustion modelling," *Mathematical and Computer Modelling*, **54**, pp. 1706 – 1719.

[194] Bajaj, C., J. Abraham, and L. M. Pickett (2011) "Modeling Atomization Processes in High-Pressure Vaporizing Sprays," *Atom. and Sprays*, **21**, pp. 411 – 426.

[195] Golovitchev, V. I., N. Nordin, R. Jarnicki, and J. Chomiak (2000) "3-D Diesel spray simulations using a new detailed chemistry turbulent combustion model," *SAE Technical Paper Series*, **2000-01-1891**.

[196] Zeuch, T., G. Morac, S. S. Ahmed, and F. Mauss (2008) "A comprehensive skeletal mechanism for the oxidation of n-heptane generated by chemistry-guided reduction," *Comb. and Flame*, **155**, pp. 651 – 674.

[197] Seiser, R., H. Pitsch, K. Seshadri, W. J. Pitz, and H. J. Curran (2000) "Extinction and autoignition of n-heptane in counterflow configuration," *Proc. Comb. Inst.*, **28**, pp. 2029 – 2037.

[198] Pei, Y., E. Hawkes, and S. Kook (2011) "N-heptane spray modelling in a constant volume chamber with the Lagrangian probability density function approach," in *University of Newcastle, Newcastle, NSW*, Proc. of the Australian Combustion Symposium.

[199] Johnson, T. (2008) "Diesel engine emissions and their control," *Platinum Metals Rev.*, **52**, pp. 23 – 37.

[200] Gupta, A., M. Modest, and D. Haworth (2009) "Large-eddy simulation of turbulence-radiation interactions in a planar turbulent channel flow," *Int. J. Heat Transfer*, **131**, pp. 061704–1 – 061704–8.

[201] Lippert, A., S. Chang, S. Are, and D. Schmidt (2005) "Mesh Independence and Adaptive Mesh Refinement For Advanced Engine Spray Simulations," *SAE Technical Paper Series*, **2005-01-0207**.

Vita

Subhasish Bhattacharjee

The Pennsylvania State University 2007 - 2012. Doctor of Philosophy in Mechanical Engineering; Graduate Research Assistant under Dr. Daniel C. Haworth.

General Electric 2005 - 2007. Worked as Engineer at Bangalore Office.

Indian Institute of Technology, Kharagpur 2003 - 2005. Masters of Technology in Mechanical Engineering.

Haldia Petrochemicals Limited 2002 - 2003. Worked as Engineer in Maintenance of plant equipments.

Jadavpur University 1998 - 2002. Bachelor of Engineering in Mechanical Engineering.